Professorship for Sensors

technische universität
dortmund

Silver-Based Grating Structures for Biomolecule Detection

Design, Fabrication, and Sensing Performance

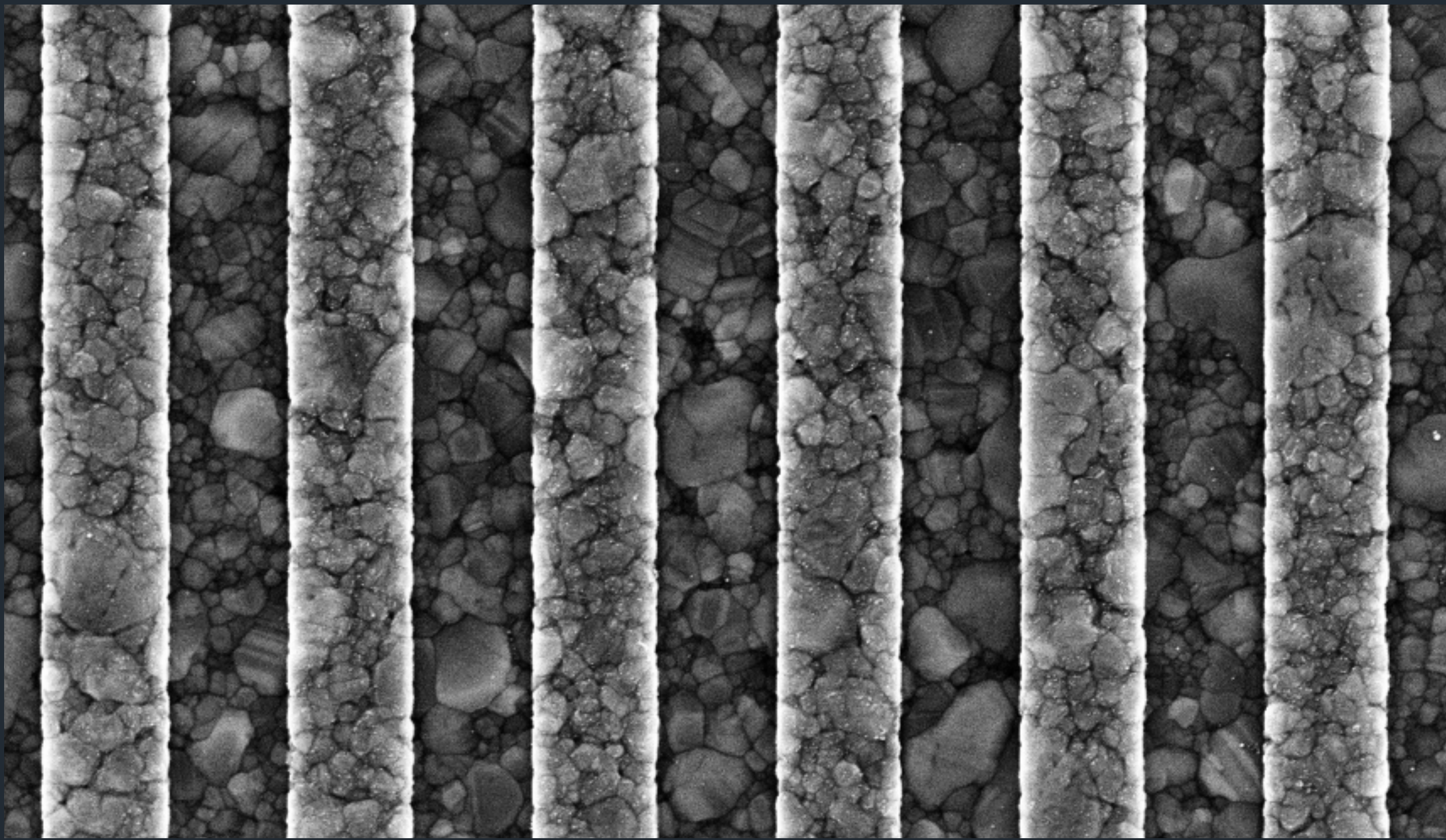

Pongsak Sarapukdee

Silver-Based Grating Structures for Label-Free Biomolecule Detection

A thesis approved for the academic degree of
Doktor der Ingenieurwissenschaften (Dr.-Ing.)

at the

Faculty of Electrical Engineering and Information Technology
TU Dortmund University

by
Pongsak Sarapukdee, M.Sc.

Supervisor: Prof. Stefan Palzer, PhD, Technische Universität Dortmund
Co-Advisor: Prof. Dr. Jürgen Wöllenstein, Albert-Ludwigs-Universität Freiburg

Date of Oral Examination: 18.09.2025

Cover image: A scanning electron micrograph of a 1-D silver grating (400 nm line width, 800 nm period) fabricated on a 100 nm Ag base with 50 nm ridge height, illustrating the periodic plasmonic architecture used for label-free biomolecule sensing.

Silver-Based Grating Structures for Label-Free Biomolecule Detection – A dissertation submitted in partial fulfillment of the requirements for the degree of Doctoral of Engineering in Faculty of Electrical Engineering and Information Technology, TU Dortmund University

This dissertation is available online on the website of the University Library:
https://ub.tu-dortmund.de

Professorship for Sensors, TU Dortmund University
This document was typeset using LATEX, and BibLatex processed the bibliography.

Contents

Abstract

Addressing global healthcare challenges, including emerging diseases, antibiotic resistance, and environmental threats, requires innovative diagnostic tools. Biosensors based on label-free detection have gained attention for their rapid, sensitive, and cost-effective analysis. Among them, Surface Plasmon Resonance (SPR) stands out as a powerful technique for real-time biomolecular interaction monitoring. However, traditional prism-based SPR systems face limitations in integration and portability, spurring interest in grating-based alternatives.

This thesis explores the theoretical, computational, fabrication, and experimental aspects of grating-based SPR systems for label-free biosensing. It introduces key principles including surface plasmon polaritons (SPPs), and grating-coupling mechanisms. A literature review covers recent advances in plasmonic materials, microfabrication methods, and performance optimization.

Finite-Difference Time-Domain (FDTD) simulations are used to design grating structures, evaluate refractive index sensitivity, and validate results experimentally. Gratings are fabricated using electron beam lithography and deposition on CMOS-compatible substrates, with microchannel integration enabling real-time biosensing. Experimental results show high sensitivity and strong agreement with simulation.

The study also investigates 2D and gradient grating period (GGP) structures for multiplexed sensing and evaluates durability enhancements like protective coatings. Inverted gratings on glass offer environmental resilience but exhibit reduced coupling efficiency.

In summary, this work advances grating-based SPR sensor technology through modeling, fabrication, and experimental validation. The findings support their potential for compact, sensitive, and versatile biosensing, with future integration into semiconductor-based systems promising further miniaturization.

CHAPTER 1

Introduction

The world is currently facing numerous global health challenges, particularly in healthcare systems, infectious diseases, and the threat of widespread pandemics. The rapid global spread of infectious and its evolving variants highlights the critical need for rapid and accurate detection of bio-threats to prevent widespread disruption [1, 2]. Beyond immediate outbreaks, antibiotic resistance jeopardizes the effectiveness of bacterial infection treatments [3]. Non-communicable diseases such as heart disease, diabetes, and cancer are rising due to aging populations and lifestyle change. Additionally, healthcare disparities persist, with many low-income regions lacking access to essential medical services, vaccines, and clean water [4]. Climate change further exacerbates health risks by worsening air pollution, accelerating the spread of vector-borne diseases, and increasing food and water insecurity [5]. Addressing these interconnected challenges demands global collaboration, investment in healthcare infrastructure, and advancements in medical research and technology.

Innovations in biosensing technology present powerful solutions across multiple domains, including disease detection and control, the development of novel therapeutics, and the need for affordable, portable diagnostic tools to expand healthcare access in remote and underserved regions [6]. Biosensors significantly enhance diagnostic speed and accuracy [7], contribute to environmental safety, and improve access to clean and safe food [8]. Their role is pivotal in addressing both present and future global health crises.

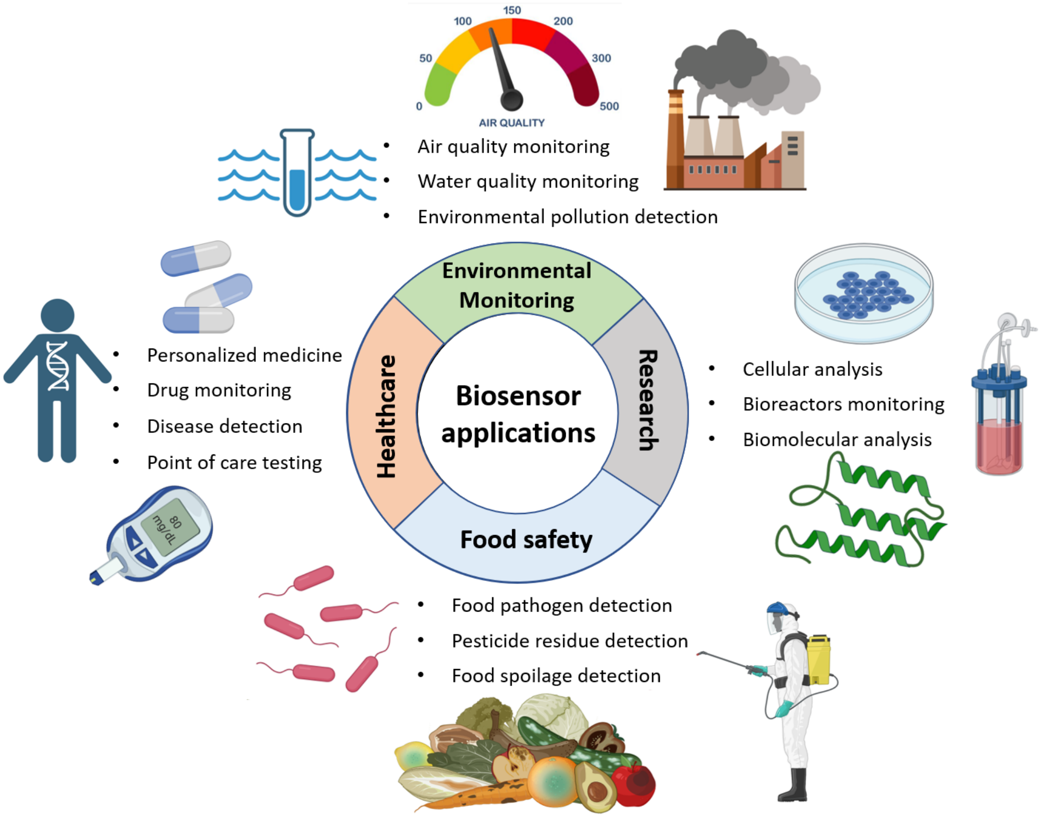

Figure 1.1.: Illustration of biosensor uses in a variety of fields, including environmental monitoring, healthcare, food safety, and research. Representative examples are provided to demonstrate the variety and potential effect of biosensor technology. (Created in Biorender)

Biosensors are analytical devices that integrate biological recognition elements with physical or chemical transducers to detect specific biological or chemical substances [9]. As illustrated in Fig. 1.1, they are applied across diverse fields, revolutionizing industries such as healthcare [10], environmental monitoring [11], food safety [12], and biotechnology [13]. In medical diagnostics, biosensors play a crucial role in detecting diseases

[14, 15], monitoring glucose levels in diabetic patients [16], and identifying biomarkers for conditions such as cancer and infectious diseases [17, 18]. Their ability to provide rapid and accurate results has significantly improved point-of-care testing [19], enabling early disease detection and personalized medicine. In environmental monitoring, biosensors are employed for detecting pollutants, toxins, and hazardous substances in air, water, and soil, contributing to sustainable environmental management and public health protection [6]. The food industry also benefits from biosensors, where they are used for detecting pathogens, contaminants, and allergens, ensuring food quality and safety [20]. In biotechnology and pharmaceutical research, biosensors facilitate drug discovery and development by analyzing biomolecular interactions, screening potential drug candidates, and optimizing therapeutic formulations [21].

Furthermore, integrating biosensors with microsystem technology plays a crucial role in developing portable, scalable, and affordable diagnostic devices. The miniaturization of these sensors not only significantly reduces production costs but also facilitates seamless integration into existing systems and simplifies maintenance requirements. These features make biosensors particularly well-suited for resource-limited settings [9, 22]. Importantly, deploying biosensors in low-income countries presents substantial opportunities to effectively address critical healthcare and environmental issues [23].

Biosensors function by translating biological interactions into measurable electrical, optical, or mechanical signals. The general working principle of biosensors involves a sequence of highly coordinated stages that enable the detection of target analytes [24]. As schematically illustrated in Fig. 1.2, The process begins with analyte recognition. A specific bioreceptor, such as enzymes, antibodies, or nucleic acids, interacts selectively with the target analyte, ensuring high specificity. This interaction triggers a bio-recognition event, leading to biochemical changes such as variations in pH, electron transfer, or molecular mass, which serve as indicators of the presence and concentration of the analyte. These biochemical changes are then converted into a measurable output through signal transduction, where a transducer element translates the molecular interactions into an electrical [25], optical [26], or mechanical signal [27]. Subsequently, the signal undergoes

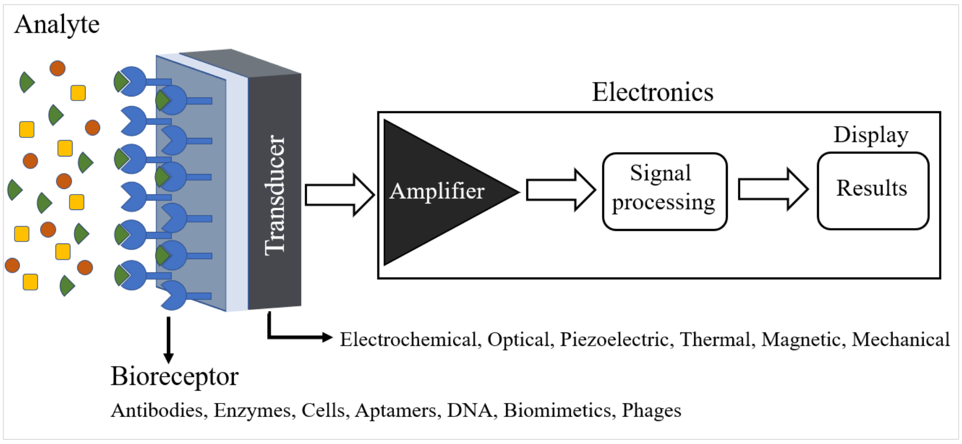

Figure 1.2.: Schematic representation of a biosensor. The analyte of interest interacts with a bioreceptor, which is specific to the target molecule. This interaction is then transduced into a measurable signal by a transducer element. The signal is subsequently amplified and processed by electronic circuitry, ultimately generating a readable output.

processing, involving amplification, filtering, and conversion into digital format to enhance its clarity and precision. Finally, the data display stage presents the processed signal in an interpretable format, such as a numerical value or graphical output, enabling real-time monitoring and analysis of the detected analyte. This systematic approach ensures high sensitivity and reliability.

Biosensors can be broadly classified according to their detection methodologies into optical, electrochemical, and mechanical biosensors [28]. Optical biosensors detect changes in light properties, electrochemical biosensors measure electrical signals such as current or impedance, and mechanical biosensors sense nanoscale mass variations. Additionally, biosensors can be categorized based on whether they require external labeling for detection, distinguishing between label-free and labeled biosensors, as illustrated in Fig. 1.3 [29]. Label-free biosensors directly detect biomolecular interactions by measuring intrinsic properties such as mass, refractive index, or electrical conductivity, eliminating the need for fluorescent, radioactive, or enzymatic labels [30]. A prominent example is Surface Plasmon Resonance (SPR), an optical method that measures refractive index changes upon analyte binding [31]. SPR is particularly advantageous due to its capability for real-time monitoring, high sensitivity, and non-invasive nature, thus preserving the natural state of biomolecules and minimizing experimental artifacts. Another example of a label-free biosensor is the quartz crystal microbalance (QCM), a mechanical method that detects mass shifts resulting from analyte interactions [32]. These methods enable real-time, high-sensitivity analysis, preserving the natural state of biomolecules and minimizing potential artifacts. Conversely, labeled biosensors rely on externally attached tags, such as fluorescent dyes or nanoparticles, to amplify detection signals.

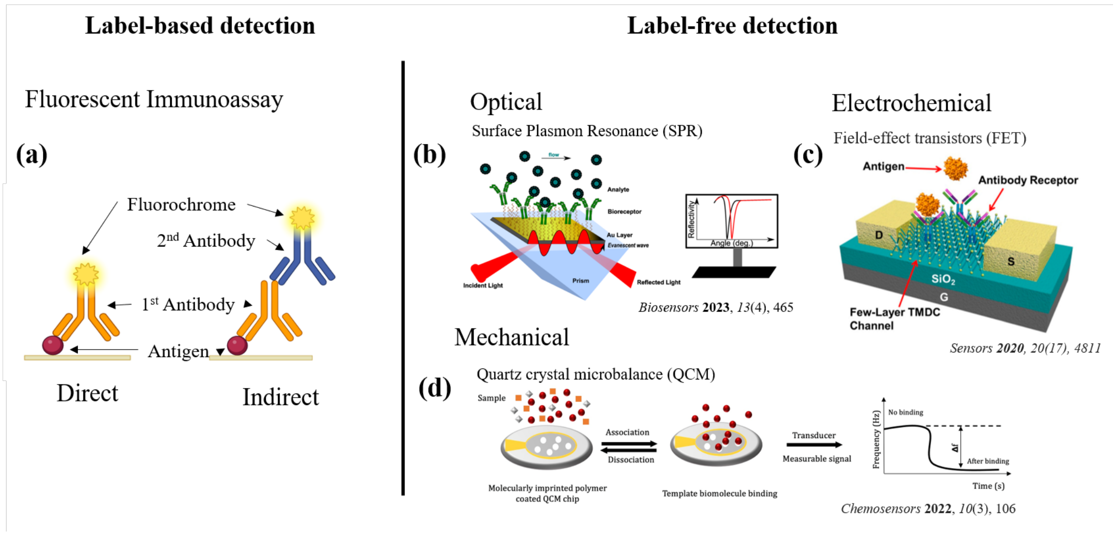

Figure 1.3.: Comparison of label-based and label-free detection methods in biosensors: (a) Label-based fluorescent immunoassay, (b) Surface Plasmon Resonance (SPR) [33], (c) Field-Effect Transistor (FET) sensor [34], (d) Quartz Crystal Microbalance (QCM) sensor [35]. Adapted from [36] under the terms of the Creative Commons CC-BY license.

Although labeled techniques, such as enzyme-linked immunosorbent assays (ELISA) [37] and fluorescence resonance energy transfer (FRET) [38], provide high specificity, they often require extensive sample preparation and additional reagents, increasing complexity [39]. Among sensing methods, electrochemical biosensors measure electrical signals like current or impedance, whereas optical biosensors detect light variations, and mechanical biosensors identify nanoscale mass changes. While labeled biosensors are advantageous for high-throughput screening, label-free biosensors are gaining prominence due to their ability to provide rapid, real-time, and cost-effective analysis without interfering with the biomolecular interactions being studied [40].

There are several label-free methods for detecting biomolecular interactions. These include the use of Surface Plasmon Resonance (SPR) among other techniques, as shown in Fig. 1.4. SPR utilizes the advancement of plasmonics technology, which holds great potential for increasing the processing speed of future integrated circuits by bridging the gap between electronics and photonics. SPR, a plasmonic-based approach, plays an important part in label-free biosensors. While traditional methods may face limitations in speed, sensitivity, or the need for labeling, SPR offers the potential for real-time, highly sensitive detection of biomolecular interactions, mirroring the advantages plasmonics offers in chip technology. This ability makes SPR a powerful tool for understanding biomolecular processes in their native environment.

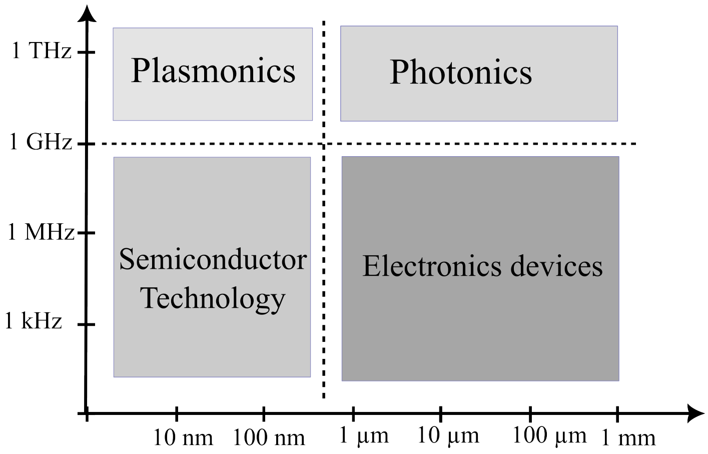

Figure 1.4.: Comparison of operating speeds and critical dimensions of different chip-scale device technologies. Plasmonics offers a unique combination of high speed and small size, potentially bridging the gap between electronics and photonics. Adapted from [41] under the terms of the Creative Commons CC-BY license.

Surface Plasmon Resonance is a technique that detects changes in the refractive index near a metal-dielectric interface. By measuring the angle or wavelength at which SPR occurs, binding events between target molecules and ligands immobilized on the sensing surface can be detected and quantified [42–48].

Table 1.1.: Comparison of prism-based and grating-based SPR techniques.

Techniques	Advantages	Limitations
Prism-based	Simple, widely used Established instrumentation High sensitivity	Prism coupling limits Sensitivity affected by surface roughness Limited multiplexing
Grating-based	Enhanced sensitivity, localized field Increased interaction volume Precise control of grating parameters Flexible design	Complex fabrication Precise control of plasmons Sensitivity depends on grating properties Angular dependence due to diffraction

Nowadays, prism-based surface plasmon resonance is a common and widely used technique for biosensing. However, it has limitations in terms of bulkiness, cost, and complexity [49, 50]. To overcome these drawbacks, researchers are turning to grating-based SPR are investigated as an alternative approach. Comparison between two techniques is shown in Table 1.1. Grating-based SPR offers advantages in miniaturization, integration, and cost-effective fabrication. It eliminates the need for bulky prism configurations, enabling the development of compact and portable biosensing devices. Grating-based SPR shows great promise in surpassing the limitations of prism-based SPR [51, 52].

While grating-based SPR offers numerous advantages, it also has certain limitations that currently prevent its widespread use in biosensors. However, it is important to highlight that grating-based SPR has immense potential for improvement and integration into real-world applications [53]. While addressing the challenges of sensitivity, fabrication complexity, angular sensitivity, and biomolecule immobilization, several key solutions can enhance the performance of grating-based SPR and bring it closer to practical implementation [54].

One of the critical factors for improving sensitivity in grating-based SPR is optimizing the structure design [55, 56] and metal layer properties [57]. Employing nanotechnology, this research focuses on the careful engineering of grating parameters at the nanoscale, including period, depth, and profile, and the selection of appropriate metals with enhanced plasmonic properties, resulting in significantly enhanced sensitivity. Also, advanced computer modeling techniques can play a vital role in predicting the performance of different grating designs, reducing the number of physical sample fabrications, and accelerating the development process.

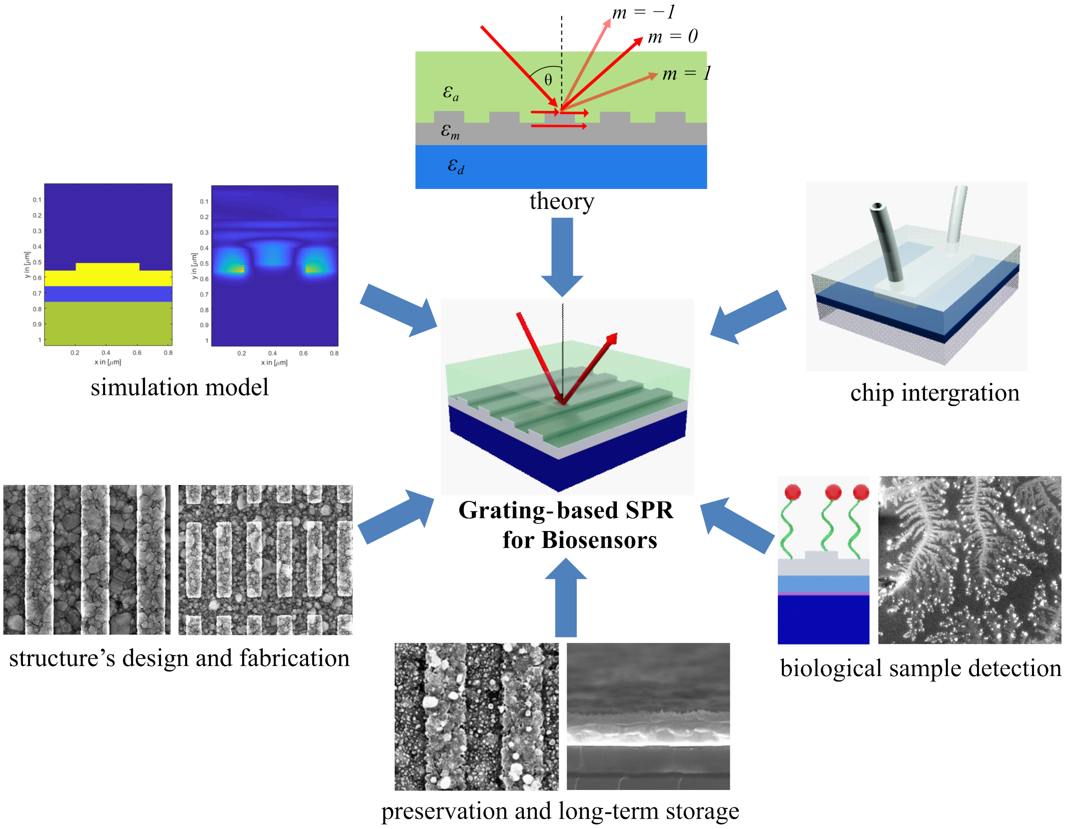

Figure 1.5.: Exploration of grating-based SPR research from several perspectives for usage in biosensor platforms, including theoretical analysis, simulation modeling, structure design and fabrication, chip integration, biological sample detection, and preservation and long-term storage.

Furthermore, the stability and long-term use of grating-based SPR can be improved by incorporating novel structure designs. This research, introducing protective coatings can enhance the durability and resistance to environmental changes, ensuring reliable and reproducible measurements over extended periods. Additionally, integrating microfluidic flow cells and automated sample handling systems can improve stability by maintaining a constant flow of analytes [58], minimizing fluctuations due to manual sample introduction.

The ultimate goal of this thesis is to remove existing restrictions and improve the overall efficacy of grating-based SPR, allowing it to be used in a variety of crucial biosensing applications. The research intends to improve the system's performance, broaden its operational scope, and enable the full realization of its promise in multiple biosensing domains by incorporating these developments. Fig. 1.5 depicts in detail the primary topic of inquiry for this comprehensive thesis, offering a clear demarcation of the scope and context of the research.

This thesis comprehensively explores surface plasmons and their applications. It begins by establishing the theoretical foundation in *Chapter 2*, covering surface plasmon principles, metal permittivity, and excitation techniques using prisms and gratings. *Chapter 3* then examines the current landscape of surface plasmon resonance (SPR) biosensors, including materials, basic setups, and technological advancements. *Chapter 4* details the computational modeling employed in this research, followed by *Chapter 5*, which outlines both conventional and inverted grating fabrication methods. *Chapter 6* presents and analyzes the characteristics and optimization of grating structures under varying parameters, including simulation and biological testing results. Finally, *Chapter 7* summarizes the key findings, acknowledges limitations, and proposes future research directions.

CHAPTER 2

Theoretical Background and Conception

This chapter delves into the theoretical foundations essential for understanding grating-based surface plasmon resonance (SPR) systems used for label-free biomolecule detection. It begins with a detailed discussion of the Maxwell's equations, outlining the fundamental principles governing electromagnetic field interactions. These principles serve as a basis for deriving the electromagnetic propagation of surface plasmons in various structures. The chapter explores the frequency-dependent permittivity of metals using Drude model, introducing critical concepts such as the plasma frequency and the complex dielectric function, which are pivotal for understanding plasmons behavior. Subsequently, the chapter provides an in-depth analysis of surface plasmons, emphasizing their electromagnetic nature at the interface of metals and dielectrics. The derivation of the surface plasmon dispersion relation is presented, highlighting the conditions necessary for the generation of these excitations. Furthermore, the compounded nature of surface plasmon polaritons (SPPs) is discussed, along with their evanescent field characteristics and dispersion properties. The chapter concludes with a comprehensive overview of various excitation methods for surface plasmon polaritons. Special attention is given to prism and grating-based coupling techniques, where the principles of phase matching and momentum transfer are applied to achieve efficient SPPs excitation. This foundation sets the stage for optimizing SPR-based biosensing platforms.

2.1. Electromagnetic Properties of the Materials

The interaction of metals with electromagnetic fields is well-described by the classical framework provided by Maxwell's equations. The classical approach remains valid even for metallic nanostructures with dimensions down to the nanometer scale [59]. Consequently, the optical properties of metals are appropriately treated within the framework of classical theory. It is well-established experience that metals exhibit high reflectivity for frequencies up to the visible range, preventing the propagation of electromagnetic waves. At low frequencies, metals reflect electromagnetic waves, with negligible penetration. Approaching near-infrared and visible frequencies, penetration and dissipation increase significantly, hindering size scaling of photonic devices [60]. In the ultraviolet range, metals become dielectric-like, allowing wave propagation with varying attenuation depending on the band structure [61]. Alkali metals show ultraviolet transparency, while noble metals (e.g., gold, silver) exhibit strong absorption due to interband transitions [62].

Metal dispersion is described by a complex dielectric function $\varepsilon(\omega)$, which underlies all discussed phenomena. This frequency dependence is shown to arise from the phase shift between induced currents and the driving field near the electron relaxation time τ [59]. The macroscopic Maxwell's equations simplify the electromagnetic response by averaging over microscopic interactions [63].

Maxwell's macroscopic electromagnetic equations describe the fundamental relationships between dielectric displacement **D**, magnetic field strength **H**, electric field strength **E** and magnetic flux density **B**. These fields depend explicitly on external electric charge density ρ_{ext} and external current density $\mathbf{J}_{ext}$. Mathematically, these relationships are represented by the following set of equations [64]:

$$\nabla \cdot \mathbf{D} = \rho_{ext} \tag{2.1}$$

$$\nabla \cdot \mathbf{B} = 0 \tag{2.2}$$

$$\nabla \times \mathbf{E} = -\frac{\partial \mathbf{B}}{\partial t} \tag{2.3}$$

$$\nabla \times \mathbf{H} = \frac{\partial \mathbf{D}}{\partial t} + \mathbf{J}_{ext} \tag{2.4}$$

A distinction is made between external and internal charge and current densities, where $\rho_{tot} = \rho_{ext} + \rho_{int}$ and $\mathbf{J}_{tot} = \mathbf{J}_{ext} + \mathbf{J}_{int}$ rather than the traditional free/bound division, to provide a clearer approach, particularly for metallic interfaces [65].

The four macroscopic fields can also be linked through the polarization **P** and magnetization **M**:

$$\mathbf{D} = \varepsilon_0 \mathbf{E} + \mathbf{P} \tag{2.5}$$

$$\mathbf{H} = \frac{1}{\mu_0}\mathbf{B} - \mathbf{M}, \tag{2.6}$$

where ε_0 and μ_0 are the permittivity[1] and permeability[2] of vacuum, respectively. For non-magnetic media, the magnetization **M** is negligible.

The polarization **P** represents the electric dipole moment per unit volume induced by the alignment of microscopic dipoles with the electric field. It is related to the internal charge

---

[1] $\varepsilon_0 \approx 8.854 \times 10^{-12}$ F/m

[2] $\mu_0 \approx 1.257 \times 10^{-6}$ H/m

density ρ_{int} via $\nabla \cdot \mathbf{P} = -\rho_{int}$. Charge conservation, expressed as $\nabla \cdot \mathbf{J}_{int} = -\partial \rho_{int}/\partial t$, implies a connection between the internal charge and current densities:

$$\mathbf{J}_{int} = \frac{\partial \mathbf{P}}{\partial t}. \tag{2.7}$$

The macroscopic electric field, as defined through **D**, incorporates all polarization effects, encompassing both external and induced fields. Substituting Eq. (2.5) into Eq. (2.1) yields:

$$\nabla \cdot \mathbf{E} = \frac{\rho_{tot}}{\varepsilon_0}. \tag{2.8}$$

where ρ_{tot} represents the total charge density (external and internal). For isotropic, non-magnetic media, the constitutive relations are:

$$\mathbf{D} = \varepsilon_0 \varepsilon \mathbf{E} \tag{2.9}$$

and

$$\mathbf{B} = \mu_0 \mu \mathbf{H}, \tag{2.10}$$

where ε is the relative permittivity (or dielectric function) and μ is the relative permeability. The linear relationship between **D** and **E** can also be expressed using the electric susceptibility χ, which explains the linear connection between **P** and **E** through [66]:

$$\mathbf{P} = \varepsilon_0 \chi \mathbf{E}. \tag{2.11}$$

Combining Eqs. (2.5), (2.9), and (2.11) leads to the relation: $\varepsilon = 1 + \chi$. For a linearly conductive medium with conductivity σ, the current density is:

$$\mathbf{J} = \sigma \mathbf{E}. \tag{2.12}$$

The macroscopic electromagnetic behavior of isotropic linear materials is described by four fundamental linear relationships. Since it is obviously that metals exhibit frequency-dependent optical responses. Therefore, to account for nonlocality in both time and space, the constitutive relations can be generalized as convolution integrals:

$$\mathbf{D}(\mathbf{r}, t) = \varepsilon_0 \int dt' d\mathbf{r}' \varepsilon(\mathbf{r} - \mathbf{r}', t - t')\mathbf{E}(\mathbf{r}', t') \tag{2.13}$$

$$\mathbf{J}(\mathbf{r}, t) = \int dt' d\mathbf{r}' \sigma(\mathbf{r} - \mathbf{r}', t - t')\mathbf{E}(\mathbf{r}', t'). \tag{2.14}$$

Transforming these equations into the frequency domain via Fourier transforms [67] yields:

$$\mathbf{D}(\mathbf{k}, \omega) = \varepsilon_0 \varepsilon(\mathbf{k}, \omega)\mathbf{E}(\mathbf{k}, \omega) \tag{2.15}$$

$$\mathbf{J}(\mathbf{k}, \omega) = \sigma(\mathbf{k}, \omega)\mathbf{E}(\mathbf{k}, \omega). \tag{2.16}$$

Eqs. (2.15) and (2.16) connect macroscopic fields with frequency-dependent material properties. However, the intrinsic optical characteristics are revealed by examining the relationship between frequency and the dielectric function, effectively removing the influence of macroscopic field stimuli [68]. Combining Eq. (2.7) with (2.16) gives:

$$-i\omega\mathbf{P}(\mathbf{k}, \omega) = \sigma(\mathbf{k}, \omega)\mathbf{E}(\mathbf{k}, \omega). \tag{2.17}$$

Similarly, using Eqs. (2.5) and (2.15), yields:

$$\mathbf{P}(\mathbf{k}, \omega) = \varepsilon_0[\varepsilon(\mathbf{k}, \omega) - 1]\mathbf{E}(\mathbf{k}, \omega) \tag{2.18}$$

From Eqs. (2.17) and (2.18), the dielectric function is expressed as:

$$\varepsilon(\mathbf{k}, \omega) = 1 + \frac{i\sigma(\mathbf{k}, \omega)}{\omega\varepsilon_0}. \tag{2.19}$$

When light interacts with metals, if the light's wavelength is much larger than the size of the unit cell or free path of the electrons, the dielectric response simplifies to a spatially local form: $\varepsilon(\mathbf{k} = \mathbf{0}, \omega) = \varepsilon(\omega)$. This approximation remains valid even into the ultraviolet range. The dielectric constant $\varepsilon(\omega)$, and conductivity $\sigma(\omega)$, are both complex quantities that depend with frequency (ω). These two quantities are related by the dielectric function in Eq. (2.19).

In the optical frequency range, the dielectric function $\varepsilon(\omega)$, can be expressed as

$$\varepsilon(\omega) = \varepsilon_1(\omega) + i\varepsilon_2(\omega). \tag{2.20}$$

The complex value can be determined through the complex refractive index $n(\omega)$, which is also frequency-dependent and expressed as

$$n(\omega) = n_1(\omega) + i\kappa(\omega), \tag{2.21}$$

where $\kappa(\omega)$ is the extinction coefficient, which quantifies optical absorption. The relationship between the complex refractive index and the dielectric function is given by $n(\omega) = \sqrt{\varepsilon(\omega)}$.

2.2. Permittivity of Metals: Drude Model

The Drude model [69] provides a good approximation of the optical behavior of metals across a broad range of frequencies. It treats the metal as a gas of free electrons with number density N moving against a background of stationary positive ions. This simplification is applicable to metals, even into the ultraviolet range [64]. However, for noble metals, interband transitions initiate in the visible range, limiting the applicability of the free electron model at higher energies [70]. The Drude model simplifies the complex interactions within the metal by neglecting details of the lattice potential and electron-electron interactions.

When considering dynamic current density **J** and electric field **E**, the conductivity σ becomes frequency-dependent. The Drude model predicts a complex, frequency-dependent conductivity [71]:

$$\sigma = \frac{\sigma_0}{1 + i\omega\tau}, \tag{2.22}$$

where σ_0 represents the low-frequency conductivity, and τ is the scattering time. For frequencies $\omega \ll 1/\tau$, the conductivity simplifies to $\sigma \approx \sigma_0$, becoming real and independent of frequency [64].

For a medium with a free-space-like dielectric permittivity ($\varepsilon = \varepsilon_0$), substituting Eq. (2.22) into the appropriate relationship between conductivity and permittivity (Eq. (2.19)) yields an effective relative permittivity:

$$\varepsilon(\omega) = 1 + \frac{\omega_p^2}{-\omega^2 + i\omega/\tau} = 1 + \frac{\omega_p^2}{-\omega^2 + i\omega\gamma_d}, \tag{2.23}$$

where $\gamma_d = 1/\tau$ is the scattering rate. The plasma frequency ω_p is defined as:

$$\omega_p = \sqrt{\frac{\sigma_0}{\varepsilon_0\tau}}, \tag{2.24}$$

and the corresponding free-space plasma wavelength λ_p is [71]:

$$\lambda_p = \frac{2\pi c_0}{\omega_p}, \tag{2.25}$$

where c_0 is the speed of light[3] in free space. Lossless materials exhibit a residual, frequency-independent relative permittivity $1 + \chi_m$ that persists even at frequencies $\omega \gg \omega_p$. For these materials, the relative permittivity (Eq. (2.23)) becomes:

$$\varepsilon(\omega) = 1 + \chi_m + \frac{\omega_p^2}{-\omega^2 + i\omega\gamma_d}. \tag{2.26}$$

The Drude model can be related to the Lorentz oscillator model [72], which describes the

---

[3] approximately 299,792,458 m/s

motion of a bound electron as a harmonic oscillator. The Drude model, which describes the behavior of free electrons in a material, can be understood as a special case of the more general Lorentz oscillator model. In the Drude model, however, the electrons are considered free, meaning the restoring force that would bind them is zero. This translates to an elastic constant $\kappa = 0$, and consequently, a resonance frequency $\omega_0 = 0$. When the Lorentz model's equation of motion is simplified with these conditions, it leads to a polarization density $\mathbf{P}$ that is related to the applied electric field $\mathbf{E}$. This relationship is expressed through a susceptibility $\chi(\omega)$, which is given by

$$\chi(\omega) = \frac{\mathbf{P}}{\varepsilon_0 \mathbf{E}} = \frac{\omega_p^2}{-\omega^2 + i\omega\gamma_d}, \tag{2.27}$$

where ω_p is the plasma frequency, defined as

$$\omega_p = \sqrt{\frac{Ne^2}{\varepsilon_0 m}}. \tag{2.28}$$

with N is the electron density, e is the electron charge, m is the electron mass, and ε_0 is the vacuum permittivity. This expression for susceptibility is obtained by considering an oscillating electric field with frequency ω. By relating this susceptibility to the permittivity, one recovers the Drude model's conductivity, provided that the conductivity σ_0 is given by

$$\sigma_0 = \frac{Ne^2\tau}{m}. \tag{2.29}$$

Thus, the Drude model's susceptibility represents a specific form of the Lorentz model's susceptibility with with $\omega_0 = 0$ and $\gamma_d = \Delta\omega = 2\pi\Delta\nu$, where $\Delta\nu$ is the spectral width. A comparison of the frequency dependence of the real and imaginary parts of the relative permittivity for the Lorentz and Drude models is shown in Fig. 2.1.

High-Frequency Drude Model: In the high-frequency regime, where the angular frequency ω significantly exceeds the scattering rate γ_d (or equivalently, $\omega \gg 1/\tau$), the damping term in the Drude model can be neglected. This simplification leads to a purely imaginary conductivity, $\sigma(\omega) \approx \sigma_0/i\omega\tau$, derived from Eq. (2.22). Consequently, the

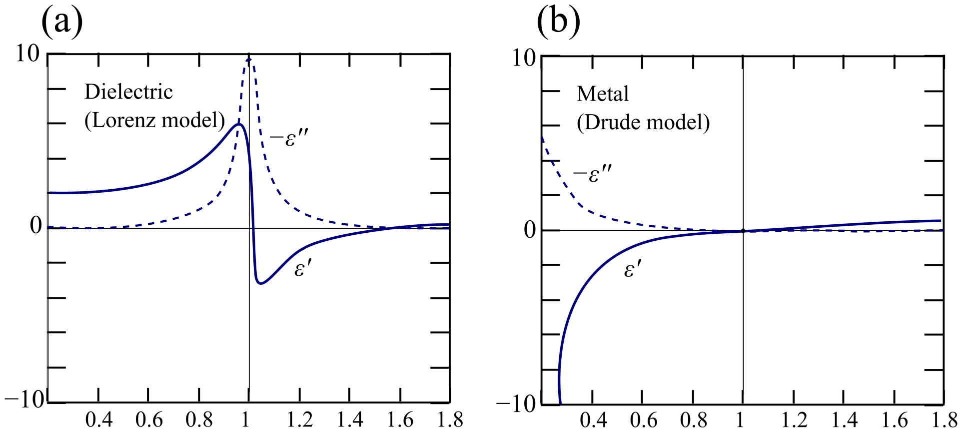

Figure 2.1.: The frequency dependence of relative permittivity $\varepsilon = \varepsilon' + i\varepsilon''$, with real (solid) and imaginary (dashed) parts. (a) Lorenz model for a dielectric resonance with ω_0, $Q = 10$, and $\chi_0 = 1$. (b) Drude model for a metal with ω_p, $\omega_p\tau = 10$, and $\varepsilon = \varepsilon_0$. The real permittivity is negative when frequency is below ω_p. Reproduced with permission from [73]. Copyright 2019, John Wiley & Sons, Inc..

effective permittivity (Eq. (2.26) with $\chi_m = 0$) for this simplified model becomes real:

$$\varepsilon(\omega) \approx 1 - \frac{\omega_p^2}{\omega^2}. \tag{2.30}$$

This equation shows how conductivity reduces the permittivity below the free-space value ε_0 and introduces a frequency dependence that varies inversely with the square of the frequency.

The simplified Drude model effectively captures the optical behavior of metals in the near-infrared and visible spectral regions. For wavelengths shorter than approximately $1\,\mu$m (corresponding to $\omega = 2\pi\nu = 1.9 \times 10^{15}$ rad/s), the condition $\omega \gg \gamma_d$ is valid for the metals listed in Tab. 2.1. In summary, at sufficiently high frequencies ($\omega \gg 1/\tau$), the simplified Drude model for metals becomes a specialized case of the Lorentz model for dielectric materials, lacking both restoring force $\kappa = 0$ and damping $\gamma_d = 0$. The permittivity, as given by Eq. (2.30), is real. It exhibits negative values below the plasma frequency ω_p, characterizing the metal as a Single Negative (SNG) medium[4], and positive

---

[4] Single Negative (SNG) medium: a medium with a negative dielectric constant.

Table 2.1.: Plasma frequency ω_p, free-space plasma wavelength λ_p, scattering time τ, and damping coefficient rate $\gamma_d = 1/\tau$ for various metals [74].

Metal	ω_p (rad/s)	λ_p (nm)	τ (fs)	γ_d (s^{-1})
Ag	1.30×10^{16}	144	30.9	0.32×10^{14}
Au	1.28×10^{16}	146	9.27	1.08×10^{14}
Cu	1.26×10^{16}	148	6.88	1.45×10^{14}
Li	0.93×10^{16}	203	50.8	0.197×10^{14}
Na	0.85×10^{16}	222	17.3	0.578×10^{14}
Al	1.73×10^{16}	109	51.2	0.195×10^{14}
In	1.84×10^{16}	102	14.2	0.704×10^{14}
Zn	1.45×10^{16}	129	21.3	0.469×10^{14}
Cd	1.28×10^{16}	147	18.8	0.532×10^{14}

values above ω_p, indicating Double Positive (DPS) medium[5] behavior.

Wave propagation within a simplified Drude medium is described by a propagation constant $\beta = n\mathbf{k}_0 = (\omega/c_0)\sqrt{\varepsilon(\omega)}$ and a dispersion relation:

$$\beta(\omega) = \frac{\omega}{c_0}\sqrt{1 - \frac{\omega_p^2}{\omega^2}}, \tag{2.31}$$

as depicted in Fig. 2.2. The figure also shows the corresponding relative permittivity $\varepsilon(\omega)$, refractive index n, and attenuation coefficient α.

Forbidden Band ($\omega < \omega_p$): At frequencies below the plasma frequency ω_p, the effective permittivity $\varepsilon(\omega)$ of the metal becomes negative. This makes the metal behave as a Single Negative (SNG) medium. The wavenumber k becomes imaginary $k = i\omega\sqrt{|\varepsilon(\omega)|\mu_0}$ leading to attenuation without propagation of the electromagnetic wave. This region is termed a "forbidden band"because light cannot propagate through it. The attenuation coefficient $\alpha = 2k_0\sqrt{\frac{\omega_p^2}{\omega^2} - 1}$ decreases as frequency increases, reaching zero at the plasma frequency ω_p. At the plasma frequency, free electrons in the metal undergo longitudinal collective oscillations known as plasmons. Plasmons are the quanta of plasma waves, analogous to photons being the quanta of electromagnetic waves. The negative permitti-

---

[5] Double Positive (DPS) medium: a conventional medium with both a positive dielectric constant and positive magnetic permeability.

vity results in an imaginary impedance, causing total reflection at the boundary between the metal and a Double Positive (DPS) medium, provided the free space wavelength is greater than the plasma wavelength ($\lambda_0 > \lambda_p$). Doped semiconductors do not exhibit reflection in the visible region because their plasma frequency lies in the infrared. This is due to their lower free-electron density N (see Eq. (2.28)) compared to metals.

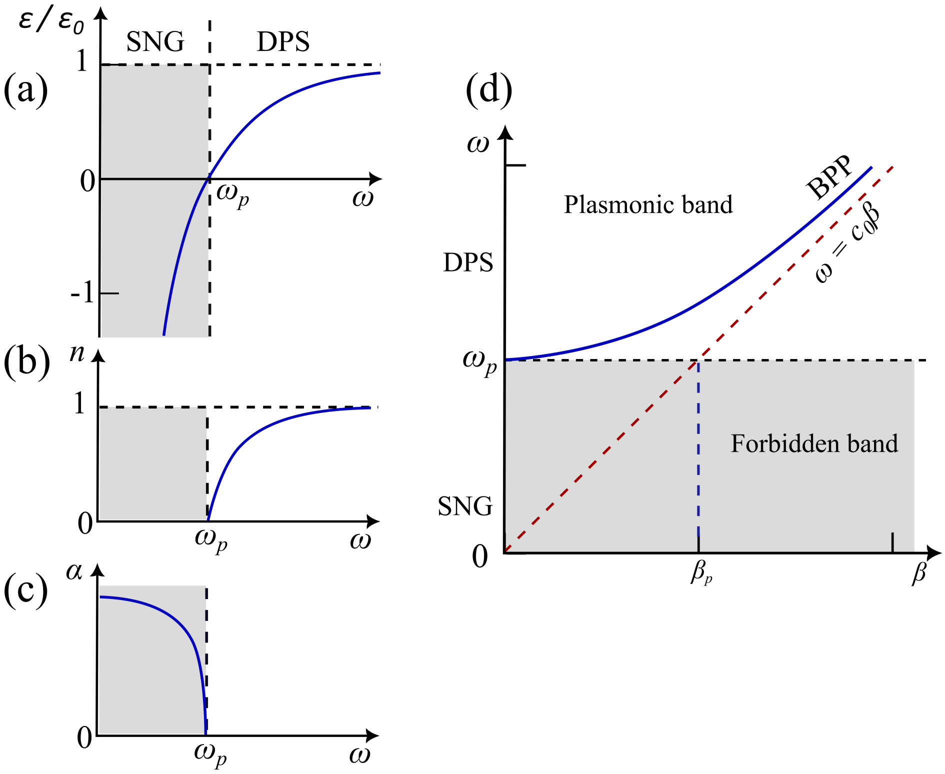

Figure 2.2.: On the left, the effects of frequency on (a) the relative permittivity $\varepsilon(\omega)/\varepsilon_0$, (b) the refractive index n, and (c) the attenuation α in the simplified Drude model. On the right (d), the relationship between frequency and wavevector with the equation $\omega = \sqrt{\omega_p^2 + c_0^2\beta^2}$. It is demonstrated that bulk plasmon polaritons (BPPs) in metals can be found only at frequencies exceeding the plasma frequency ($\omega > \omega_p$). Reproduced with permission from [73]. Copyright 2019, John Wiley & Sons, Inc.

Plasmonic Band ($\omega > \omega_p$): At frequencies above the plasma frequency, the effective permittivity $\varepsilon(\omega)$ is positive and real. The medium behaves like a lossless dielectric, but with unique dispersion properties. The propagation constant is given by $\beta = \sqrt{\omega^2 - \omega_p^2}/c_0$, and the refractive index, $n = \sqrt{1 - \omega_p^2/\omega^2}$, is less than unity, approaching zero near ω_p.

This frequency range is known as the plasmonic band, and the propagating waves are called bulk plasmon polaritons (BPPs).

2.3. Surface Plasmon Polaritons

The previous section discussed electromagnetic properties of materials and examined the dielectric functions of the Drude and Drude-Lorentz models. Under certain conditions, regular electric-charge oscillations on the metal surface can be produced and driven by external electromagnetic fields to form surface plasmon polaritons (SPPs). This section provides the fundamental principles of SPPs at a single, flat interface, beginning with a discussion of electromagnetic wave propagation and then focusing on the specific characteristics of SPPs.

2.3.1. Electromagnetic Wave Propagation at an Interface

To understand SPPs, the propagation of electromagnetic waves along the interface between a dielectric and a conductor is first examined. These surface waves are formed by the coupling of electromagnetic fields to the oscillations of the electron plasma in the conductor. Building upon the description of the electron plasma, Maxwell's equations can be employed to analyze the behavior of electromagnetic waves at this planar interface.

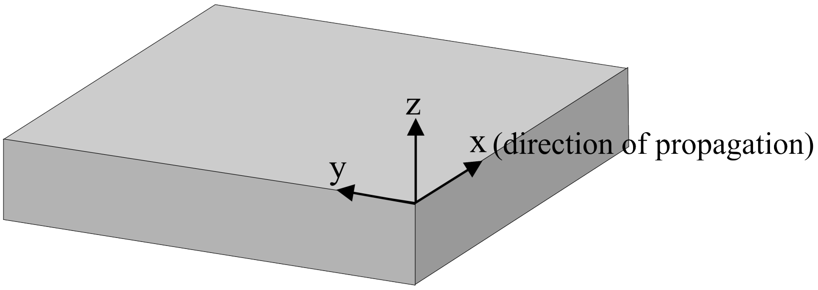

Figure 2.3.: Geometry of a planar waveguide. In a Cartesian coordinate system, wave propagation is directed along the x-axis.

The propagation of electromagnetic waves is described by the wave equation. When a time-harmonic electric field of the form $\mathbf{E}(\mathbf{r}, t) = \mathbf{E}(\mathbf{r})e^{-i\omega t}$ is assumed, the wave equation is reduced to the *Helmholtz equation* [75]:

$$\nabla^2\mathbf{E} + k_0^2\varepsilon\mathbf{E} = 0, \tag{2.32}$$

where $k_0 = \omega/c$ is defined as the wave number in vacuum.

To study confined propagating waves, a one-dimensional system is considered where the permittivity ε is varied only along the z-direction. Wave propagation is assumed to occur along the x-axis, with no variation in the y-direction (refer to Fig. 2.3), resulting in $\varepsilon = \varepsilon(z)$. For surface waves, the interface is defined as the $z = 0$ plane. The electric field can then be expressed as $\mathbf{E}(x, y, z) = \mathbf{E}(z)e^{i\beta x}$, where $\beta = k_x$ represents the *propagation constant* of the traveling waves. Upon substituting this expression into Eq. (2.32), the following equation is obtained:

$$\frac{\partial^2\mathbf{E}(z)}{\partial z^2} + (k_0^2\varepsilon(z) - \beta^2)\mathbf{E}(z) = 0. \tag{2.33}$$

An analogous equation applies to the magnetic field $\mathbf{H}$.

For wave propagation along the x-direction ($\frac{\partial}{\partial x} = i\beta$) and homogeneity in the y-direction ($\frac{\partial}{\partial y} = 0$), Maxwell's equations can be simplified. This simplified system supports two distinct types of solutions, categorized by their polarization:

Transverse Magnetic (TM) modes are characterized by non-zero field components E_x, E_z, and H_y. Transverse Electric (TE) modes are characterized by non-zero field components H_x, H_z, and E_y.

For TM modes, the governing equations are given by:

$$E_x = -i\frac{1}{\omega\varepsilon_0\varepsilon}\frac{\partial H_y}{\partial z} \tag{2.34}$$

$$E_z = -\frac{\beta}{\omega\varepsilon_0\varepsilon}H_y \tag{2.35}$$

and the wave equation is expressed as:

$$\frac{\partial^2 H_y}{\partial z^2} + (k_0^2\varepsilon - \beta^2)H_y = 0. \tag{2.36}$$

For TE modes, the corresponding equations are given by:

$$H_x = i\frac{1}{\omega\mu_0}\frac{\partial E_y}{\partial z} \tag{2.37}$$

$$H_z = \frac{\beta}{\omega\mu_0}E_y \tag{2.38}$$

and the wave equation is expressed as:

$$\frac{\partial^2 E_y}{\partial z^2} + (k_0^2\varepsilon - \beta^2)E_y = 0. \tag{2.39}$$

These equations form the foundation for analyzing and understanding surface plasmon polaritons.

p- and s-polarization

The interaction of light with a surface depends strongly on its polarization. This arises from the fundamental relationship between the electric field of light and the orientation of the surface. Specifically, the component of the electric field **E** parallel to the surface plays a critical role. From the wave equations, the orientation of the electric field is crucial for wave propagation. To illustrate this, consider the following definitions and Fig. 2.4:

p-polarization[6] (Fig. 2.4(a)): The electric field vector **E** lies within the plane of incidence. This plane is defined by the incident wave vector ($\mathbf{k}_i$) and the surface normal. In this configuration, the electric field has a component parallel to the surface.

---

[6] 'p' stands for 'parallel' and is also known **Transverse Magnetic (TM) mode**

s-polarization[7] (Fig. 2.4(b)): The electric field vector **E** is perpendicular to the plane of incidence. In this case, the electric field has no component parallel to the surface.

These two polarization states exhibit distinct behaviors upon reflection due to the different orientations of their electric field vectors relative to the plane of incidence.

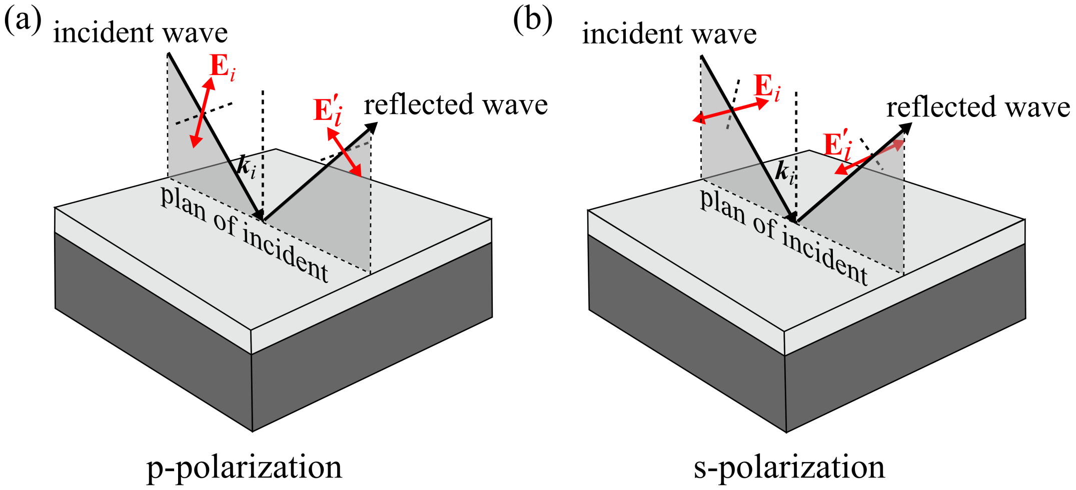

Figure 2.4.: (a) p-polarization: The electric field vector $\mathbf{E}_i$ lies in the plane of incidence, defined by the incident wave vector $\mathbf{k}_i$ and the surface normal. (b) s-polarization: The electric field vector $\mathbf{E}_i$ is perpendicular to the plane of incidence.

2.3.2. Surface Plasmon Polaritons at a Single Interface

The simplest geometry supporting Surface Plasmon Polaritons (SPPs) is considered to be a single, planar interface (Fig. 2.5) between a dielectric, non-absorbing half-space ($z > 0$) with a positive, real dielectric constant ε_2 and an adjacent conducting half-space ($z < 0$) characterized by a dielectric function $\varepsilon_1(\omega)$. The metallic behavior of the conductor requires $\mathrm{Re}[\varepsilon_1] < 0$, a condition that is satisfied for metals at frequencies below the bulk plasma frequency ω_p. Propagating wave solutions confined to the interface, exhibiting evanescent decay in the perpendicular (z) direction, are sought.

---

[7] 's' stands for 'senkrecht' meaning perpendicular, also known as **Transverse Electric (TE) mode**

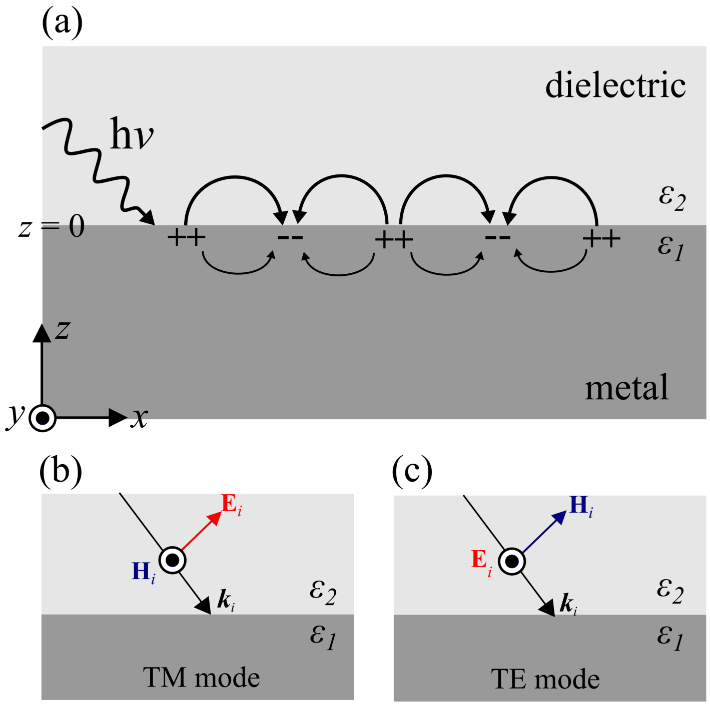

Figure 2.5.: Illustration of Surface Plasmon Polaritons (SPP) excitation and modes at a metal-dielectric interface. (a) SPP excitation at a metal-dielectric interface. (b) TM mode field orientation and (c) TE mode.

Transverse Magnetic (**TM** or p) solutions are first examined. The equations derived in the previous section are applied to both half-spaces, yielding the following field components: For $z > 0$ (dielectric):

$$H_y(z) = A_2 e^{i\beta x} e^{-k_2 z} \tag{2.40}$$

$$E_x(z) = iA_2 \frac{1}{\omega\varepsilon_0\varepsilon_2} k_2 e^{i\beta x} e^{-k_2 z} \tag{2.41}$$

$$E_z(z) = -A_2 \frac{\beta}{\omega\varepsilon_0\varepsilon_2} e^{i\beta x} e^{-k_2 z} \tag{2.42}$$

For $z < 0$ (metal):

$$H_y(z) = A_1 e^{i\beta x} e^{k_1 z} \tag{2.43}$$

$$E_x(z) = -iA_1 \frac{1}{\omega\varepsilon_0\varepsilon_1} k_1 e^{i\beta x} e^{k_1 z} \tag{2.44}$$

$$E_z(z) = -A_1 \frac{\beta}{\omega\varepsilon_0\varepsilon_1} e^{i\beta x} e^{k_1 z} \tag{2.45}$$

Here, $k_i \equiv k_{z,i}$ $(i = 1, 2)$ represents the wave vector component perpendicular to the interface in each medium. A_1 and A_2 describe the intensity of the field decaying away from the interface. The inverse of its magnitude, $\hat{z} = 1/|k_z|$, defines the evanescent decay length, which quantifies the wave's confinement. At the interface $(z = 0)$, the tangential components of the electric and magnetic fields must be continuous. This means that H_y and E_z must be equal on both sides of the interface, leading to $A_1 = A_2$ and

$$\frac{k_2}{k_1} = -\frac{\varepsilon_2}{\varepsilon_1}. \tag{2.46}$$

With the chosen sign convention in Eqs. (2.40)-(2.45), confinement necessitates $\mathrm{Re}[\varepsilon_1] < 0$ when $\varepsilon_2 > 0$. SPPs are found to exist only at interfaces between materials with opposing signs of the real part of their permittivities (i.e., a conductor and an insulator). The wave equation (Eq. (2.36)) for H_y is applied, yielding:

$$k_1^2 = \beta^2 - k_0^2\varepsilon_1 \tag{2.47}$$

$$k_2^2 = \beta^2 - k_0^2\varepsilon_2. \tag{2.48}$$

Combining these with Eq. (2.46) gives the SPP dispersion relation:

$$\beta = k_0\sqrt{\frac{\varepsilon_1\varepsilon_2}{\varepsilon_1 + \varepsilon_2}} = \frac{\omega}{c}\sqrt{\frac{\varepsilon_1\varepsilon_2}{\varepsilon_1 + \varepsilon_2}}. \tag{2.49}$$

This relation is noted to be valid for both lossless and lossy conductors.

At low frequencies, specifically in the mid-infrared range or lower, the real part of the metal's permittivity becomes large and negative ($\varepsilon_1 \to -\infty$), the wavevector associated with surface plasmon polaritons (SPPs) can be approximated by:

$$\beta = \frac{\omega}{c} \lim_{\varepsilon_1 \to -\infty} \sqrt{\frac{\varepsilon_1 \varepsilon_2}{\varepsilon_1 + \varepsilon_2}} \approx \frac{\omega}{c} \sqrt{\varepsilon_2}.$$

This result indicates that the wavevector is nearly identical to the propagation constant of light, k_0, within the dielectric medium. Additionally, when ε_1 approaches ε_2, the frequency ω converges to a specific value given by:

$$\omega_{sp} = \frac{\omega_p}{\sqrt{1 + \varepsilon_2}},$$

where ω_{sp} represents the plasma frequency, which characterizes the oscillation frequency of bulk plasmons.

Transverse Electric (**TE** or s) modes on the interface between the dielectric and metal. The field components are given as: For $z > 0$ (dielectric):

$$E_y(z) = A_2 e^{i\beta x} e^{-k_2 z} \tag{2.50}$$

$$H_x(z) = -iA_2 \frac{1}{\omega \mu_0} k_2 e^{i\beta x} e^{-k_2 z} \tag{2.51}$$

$$H_z(z) = A_2 \frac{\beta}{\omega \mu_0} e^{i\beta x} e^{-k_2 z} \tag{2.52}$$

For $z < 0$ (metal):

$$E_y(z) = A_1 e^{i\beta x} e^{k_1 z} \tag{2.53}$$

$$H_x(z) = iA_1 \frac{1}{\omega \mu_0} k_1 e^{i\beta x} e^{k_1 z} \tag{2.54}$$

$$H_z(z) = A_1 \frac{\beta}{\omega \mu_0} e^{i\beta x} e^{k_1 z} \tag{2.55}$$

Continuity of E_y and H_x at the interface requires equal on both sides of the interface and $A_1(k_1 + k_2) = 0$. Since confinement requires $\mathrm{Re}[k_1] > 0$ and $\mathrm{Re}[k_2] > 0$, this condition is only satisfied if $A_1 = 0$, implying $A_2 = 0$. Therefore, it is concluded that no wave exits with TE modes. Surface plasmon polaritons are only present with TM polarization.

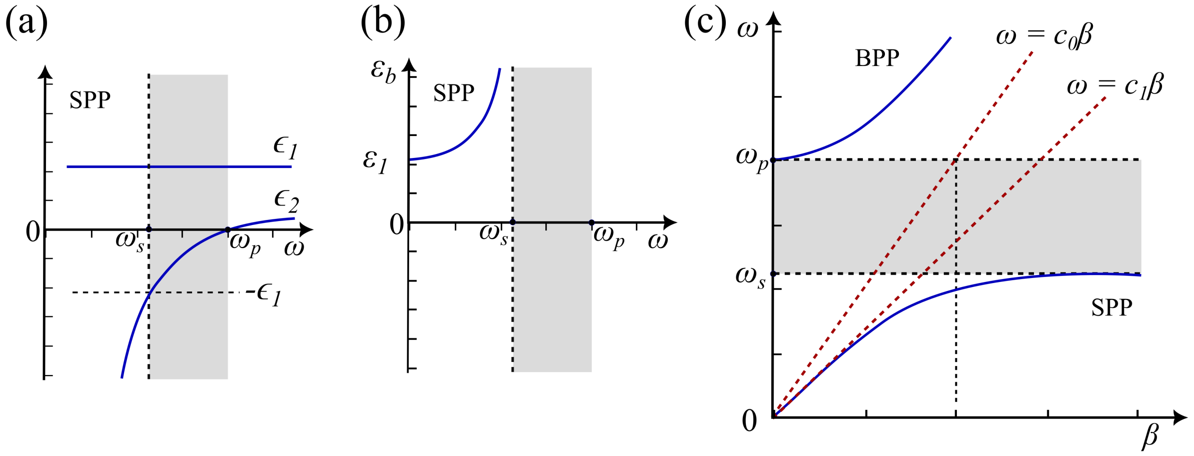

Figure 2.6.: Surface plasmon polariton (SPP) wave propagating along the interface between a metal and a dielectric, these plots were generated from Eqs. (2.31) and (2.49). (a) The variation of the permittivities of the dielectric ε_1 and metallic ε_2 materials with frequency ω. The SPP wave exists required $|\varepsilon_2| > \varepsilon_1$, is satisfied for frequencies $\omega < \omega_s$. (b) The effective permittivity ε_b of the SPP wave as a function of frequency. The wave velocity is given by c_0/n_b, where $n_b = \sqrt{\varepsilon_b/\varepsilon_0}$. (c) Dispersion curves for bulk plasmon polaritons (BPP) and SPP waves. The dispersion of light in a vacuum and within the bulk dielectric medium is indicated by dotted red lines. Reproduced with permission from [73]. Copyright 2019, John Wiley & Sons, Inc.

SPP wave at a metal-dielectric boundary

The dispersion relation of surface plasmon polaritons (SPPs) is illustrated in Fig. 2.6, based on Eq. (2.49).

For $\omega < \omega_s$, the metal behaves as a medium with a negative dielectric constant (i.e. $\varepsilon < 0$, while $\mu > 0$) under the Drude model, allowing SPPs to propagate along its interface with a dielectric. This frequency range lies within the metal's forbidden band ($0 < \omega < \omega_p$), where bulk wave propagation is prohibited. The SPP properties are governed by the ratio $|\varepsilon_2|/\varepsilon_1$, which decreases monotonically as ω/ω_s increases, approaching unity at ω_s. Compared to bulk dielectric waves, SPPs exhibit lower velocity (c_0/n_b) and a shorter plasmon wavelength (λ_0/n_b), as seen in Fig. 2.6(c), where $\beta > \omega/c_1$. The penetration depth in the metal ($d_2 = 1/|k_2|$) is smaller than in the dielectric ($d_1 = 1/|k_1|$), and both are shorter than the bulk dielectric wavelength. As ω/ω_s increases, the SPP slows, its wavelength decreases, and it becomes more confined to the interface. At $\omega/\omega_s = 1$, where $\varepsilon_1 + \varepsilon_2 = 0$, the SPP velocity reaches zero.

For $\omega_s < \omega < \omega_p$, the metal still exhibits a negative dielectric constant (with $\varepsilon < 0$), but SPPs cannot form since $|\varepsilon_2| < \varepsilon_1$, leading to total reflection of dielectric bulk waves at the interface between a negative-ε medium and a positive-ε dielectric.

For $\omega > \omega_p$, the metal transitions to a conventional medium with both a positive dielectric constant and positive magnetic permeability (i.e. $\varepsilon > 0$ and $\mu > 0$), precluding SPPs at interfaces between similar materials. However, bulk plasmon polaritons (BPPs) can propagate, and wave interactions at the metal-dielectric boundary follow standard dielectric refraction and reflection laws, including total internal reflection for incidence angles beyond the critical threshold.

2.4. Excitation of Surface Plasmons

In the Sec. 2.3.2, it was established that the wavevector of surface plasmon polaritons (SPPs) on a flat metal-dielectric interface is mismatched with that of free-space light at the same frequency ($\omega = ck$). This mismatch, which is evident from the SPP dispersion relation, precludes the direct excitation of SPPs by illumination of a smooth metal surface ($\beta > k$). To excite SPPs using free-space light, the wavevector k of the incident light must be modified [59]. This wavevector modification can be achieved by employing a three-layer system composed of a thin metal film placed between two insulators with different dielectric constants. In this section, the most common techniques utilized for SPP excitation, such as prism coupling and grating coupling, are reviewed.

2.4.1. Prism Coupling

A widely used method for surface plasmon excitation is prism coupling, which utilizes the attenuated total reflection (ATR) method. Two ATR configurations are commonly employed: the Kretschmann geometry [59, 76] and the Otto geometry [77]. In the Kretschmann configuration, a high-index prism with refractive index n_p is interfaced with a metal-dielectric waveguide. This waveguide consists of a thin metal film with permittivity ε_m and a semi-infinite dielectric with refractive index n_d, where $n_d < n_p$, as illustrated in Fig. 2.7.

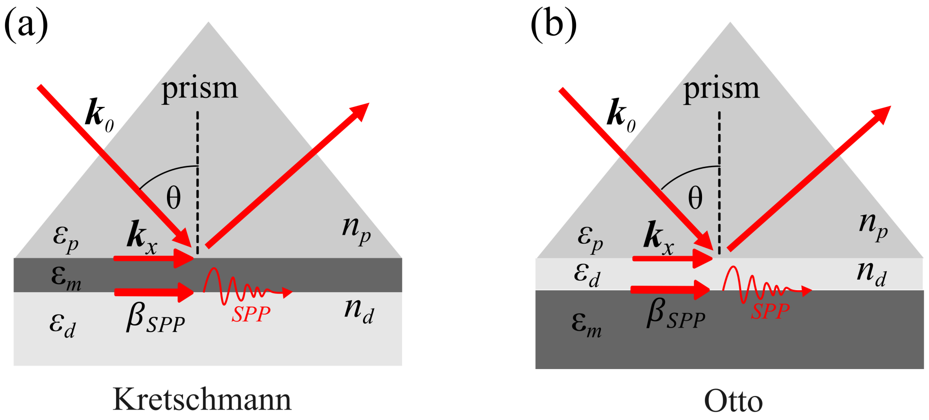

Figure 2.7.: Excitation of surface plasmons polaritons (SPP). (a)The Kretschmann and (b)Otto configuration of the attenuated total reflection (ATR) method.

When light incident from the prism strikes the metal film, it is partially reflected and partially transmitted into the metal as an inhomogeneous, evanescent wave. If the metal film is sufficiently thin, the evanescent wave penetrates through the film and couples to a surface plasmon at the outer metal-dielectric boundary. The propagation constant of the surface plasmon, β_{SPP}, is influenced by the presence of the dielectric and can be expressed as:

$$\beta_{SPP} = \frac{\omega}{c}\sqrt{\frac{\varepsilon_d \varepsilon_m}{\varepsilon_d + \varepsilon_m}}, \tag{2.56}$$

where β_{SPP} represents the propagation constant of the surface plasmon polaritons propagating the metal-dielectric interface in the absence of the prism. Efficient coupling between the evanescent wave (k_x) and the surface plasmon polaritons (β_{SPP}) requires phase-matching, which is achieved when:

$$\frac{2\pi}{\lambda}\sqrt{\varepsilon_p}\sin\theta = k_x = \mathrm{Re}\{\beta_{SPP}\} = \mathrm{Re}\left\{\frac{2\pi}{\lambda}\sqrt{\frac{\varepsilon_d\varepsilon_m}{\varepsilon_d+\varepsilon_m}}\right\}. \tag{2.57}$$

In the Otto geometry, a high-index prism with refractive index n_p is interfaced with a dielectric-metal waveguide. This waveguide comprises a thin dielectric film with refractive index n_d ($n_d < n_p$), and a semi-infinite metal with permittivity ε_m, as depicted in Fig. 2.8.

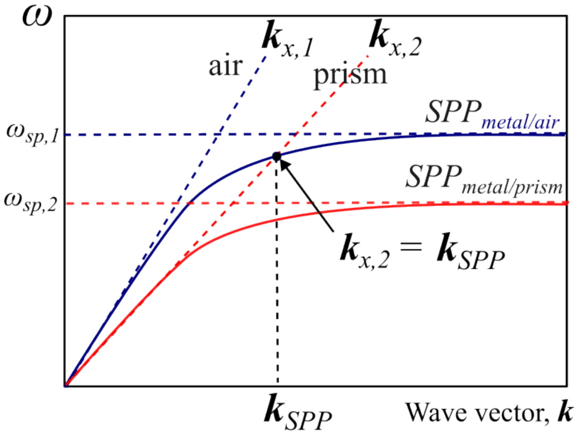

Figure 2.8.: The dispersion relation of SPP and free-space light in the prism and dielectric material (air).

In this configuration, a light wave incident on the prism-dielectric film interface at an angle exceeding the critical angle generates an evanescent wave that propagates along the interface. If the thickness of the dielectric layer is appropriately chosen (typically on the order of a few microns), the evanescent wave can couple to a surface plasmon at the dielectric-metal interface.

2.4.2. Grating Coupling

A diffraction grating is an optical device used to split an incident plane wave into multiple plane waves traveling in different directions. This property is crucial for exciting surface plasmon polaritons.

A diffraction grating modifies the phase or amplitude of an incoming wave periodically. This can be achieved using either a transparent plate with a periodic thickness variation

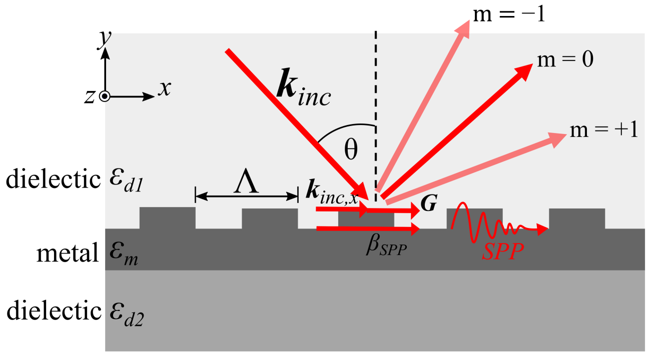

Figure 2.9.: Excitation of surface plasmons by light diffraction on a grating.

or a refractive index that changes periodically. Additionally, periodic structures such as apertures, obstacles, or absorbing components can be used. A reflection diffraction grating is typically made by applying a thin, periodically ruled metal film onto a glass substrate.

A reflection diffraction grating consists of a thin metal plate located in the $y = 0$ plane, where the surface profile varies periodically in the x-direction with a period Λ (see Fig. 2.9). When a plane wave of wavelength $\lambda \ll \Lambda$ strikes the grating at a small incident angle θ_{inc}, it gives rise to multiple diffracted plane waves that propagate at various angles relative to the y-axis.

A more general analysis, valid beyond the paraxial approximation, shows that the angles θ_m of the diffracted orders satisfy:

$$\sin\theta_m = \sin\theta_{inc} + m\frac{\lambda}{\Lambda} \tag{2.58}$$

This relationship is obtained by representing the grating's periodic transmission function $t(x, y)$ as a Fourier series composed of components $\exp(-jm2\pi x/\Lambda)$, where $m = 0, \pm1, \pm2, \ldots$.

The incident plane wave $\exp(-jkx\sin\theta_{inc})$, when modulated by the harmonic term $\exp(-jm2\pi x/\Lambda)$, generates a plane wave at angle θ_m, represented as

$$\exp(-jkx\sin\theta_m) \propto \exp(-jkx\sin\theta_{inc})\exp(-jm2\pi x/\Lambda). \tag{2.59}$$

This follows the phase-matching condition

$$k\sin\theta_m = k\sin\theta_{inc} + m\frac{2\pi}{\Lambda}, \tag{2.60}$$

which simplifies to Eq. (2.58) by substituting $k = 2\pi/\lambda$.

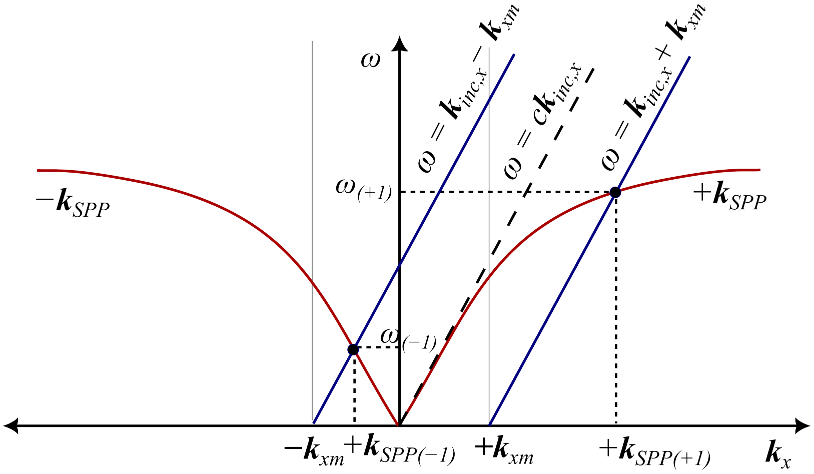

Figure 2.10.: Grating coupling of surface plasmons. The x-component of the incident light wavevector ($\mathbf{k}_{inc,x}$) is shown as a dashed grey line. Light scattering by the grating results in lines $\mathbf{k}_{inc,x} + \mathbf{k}_{xm}$ and $\mathbf{k}_{inc,x} - \mathbf{k}_{xm}$. For simplicity, only the first-order (±1) diffracted light is displayed. Surface plasmons are excited at the intersections of these lines with the plasmon dispersion curves $\mathbf{k}_{SPP}$ and $-\mathbf{k}_{SPP}$.

Considering all this, a diffraction grating generates multiple wavevectors by introducing a periodic phase modulation, enforcing momentum conservation along the grating plane. This allows light to be diffracted into discrete orders, with the diffraction angles determined by the grating period and incident wavelength, provide the necessary additional momentum to couple incident light into surface plasmon polaritons. In the surface plasmon excitation by grating, a light wave incident from a dielectric medium with permittivity

ε_d interacts with a metal grating of permittivity ε_m and period Λ (see Fig. 2.9). When a light wave with wavevector $\mathbf{k}_{inc}$ strikes the grating, it generates multiple diffracted wavevectors k_m [78–80], given by:

$$\mathbf{k}_m = \mathbf{k}_{inc} + m\mathbf{G}, \tag{2.61}$$

where m is the diffraction order, and $\mathbf{G}$ is the grating vector, which lies in the grating plane (x-z plane in Fig. 2.9), perpendicular to the grooves. The magnitude of the grating vector is:

$$\mathbf{G} = \frac{2\pi}{\Lambda}. \tag{2.62}$$

Due to diffraction, the wavevector component perpendicular to the grating remains unchanged, while the in-plane component follows:

$$\mathbf{k}_{xm} = \mathbf{k}_x + m\frac{2\pi}{\Lambda}. \tag{2.63}$$

Surface plasmons are excited when the in-plane wavevector component $\mathbf{k}_{xm}$ matches the surface plasmon propagation constant β_{SPP} (see Fig. 2.10). This matching condition is given by:

$$\frac{2\pi}{\lambda}\sqrt{\varepsilon_d}\sin\theta + m\frac{2\pi}{\Lambda} = k_{xm} = \pm\mathrm{Re}\{\beta_{SPP}\}, \tag{2.64}$$

where

$$\beta_{SPP} = \frac{\omega}{c}\sqrt{\frac{\varepsilon_d\varepsilon_m}{\varepsilon_d + \varepsilon_m}} \tag{2.65}$$

is the propagation constant for a smooth metal-dielectric interface. This condition can be rewritten as:

$$\sqrt{\varepsilon_d}\sin\theta + m\frac{\lambda}{\Lambda} = \pm\mathrm{Re}\left\{\sqrt{\frac{\varepsilon_d\varepsilon_m}{\varepsilon_d + \varepsilon_m}}\right\}. \tag{2.66}$$

To determine the angle at which a surface plasmon is excited on a grating, can use Eq. (2.66) in the following formula:

$$\theta = \sin^{-1}\left(\frac{1}{\sqrt{\varepsilon_d}}\left(\sqrt{\frac{\varepsilon_d \varepsilon_m}{\varepsilon_d + \varepsilon_m}} - m \cdot \frac{2\pi}{\Lambda}\right)\right) \tag{2.67}$$

By modifying the diffraction order, grating pitch, and incident angle, various resonance conditions can be achieved for surface plasmon excitation.

2.5. Theoretical Considerations for Grating-Coupled SPR Biosensors

Theories regarding surface plasmons and grating structures have been provided, demonstrating their potential for biosensing applications. It has been shown that surface plasmon resonance (SPR) enhances the sensitivity of optical biosensors by facilitating strong light-matter interactions at metal-dielectric interfaces. Among the different coupling mechanisms, grating-based SPR has been recognized as particularly advantageous, as it eliminates the need for bulkier prism-based coupling and allows for precise biomolecular detection. Theoretical studies have indicated that the performance of grating SPR biosensors can be improved by optimizing structural and material parameters, as outlined in the following key design considerations.

Momentum Matching Optimization

The excitation of surface plasmon polaritons (SPPs) via grating coupling is examined based on Eq. (2.66). It is demonstrated that one of the critical parameters directly influencing SPP excitation is the grating period (Λ) and the groove depth (h). These parameters must be carefully considered to ensure efficient coupling, particularly when the incident light has a wavelength (λ) smaller than the grating period ($\lambda < \Lambda$). This condition is essential for fulfilling the phase-matching requirement in SPP excitation, given by the relation in Eq. (2.60). Furthermore, the grating geometry, including the groove profile, duty cycle, and modulation depth, represents another crucial factor requiring clarification, as it can significantly alter the electromagnetic field distribution and the efficiency of SPP excitation. Different grating profiles (e.g., sinusoidal, rectangular, or triangular) influence the diffraction efficiency and localized field enhancement, thereby affecting the overall coupling efficiency.

Recent studies [81–83] have demonstrated that optimizing these parameters enhances the SPP excitation and propagation, leading to improved performance in plasmonic devices and sensing applications.

Resonance Wavelength Sensitivity

The geometry of the grating should be adjusted to maximize shifts in resonance wavelength resulting from molecular binding, thereby improving detection limits. A sharper resonance peak has been found to enhance the sensor's ability to detect small variations in the refractive index.

Choice of Metal

Plasma frequency (ω_p), free-space plasma wavelength (λ_p), scattering time (τ), and scattering rate ($\gamma_d = 1/\tau$) for various metals such as gold or silver (see Tab. 2.1) have been shown to exhibit significant differences that strongly influence plasmon propagation length, field enhancement, and stability. The choice of metal is primarily determined by the specific application and intended purpose. Metals with lower scattering rates and longer scattering times tend to support longer plasmon propagation lengths, enhancing the efficiency of plasmonic devices [84–86]. The dependence of these parameters on the electronic structure and interband transitions of metals further affects their suitability for particular applications.

Minimizing Radiative Losses

Radiative losses can be minimized by optimizing the grating structure, which enhances the quality factor of the plasmonic resonance. This optimization leads to improved signal contrast and greater detection accuracy.

By applying these theoretical principles, the performance of grating-based SPR biosensors can be significantly enhanced. Greater sensitivity, improved selectivity, and higher detection accuracy can be achieved.

CHAPTER 3

Plasmonic Grating Biosensors - State-of-the-art

This chapter provides a comprehensive review of the latest advancements in SPR technology, focusing on grating-based SPR for biosensing applications. It discusses recent developments in plasmonic materials, grating fabrication techniques, and different SPR configurations, including conventional prism-based SPR, localized surface plasmon resonance (LSPR), backside illumination SPR sensors, and grating coupler SPR measurement setups. Sensitivity enhancement strategies, such as coupling with electrical readouts, microfluidic integration, and AI-driven signal processing, are explored. Additionally, the integration of grating-based SPR with emerging technologies and applications in industrial and clinical biosensing is reviewed. Performance parameters, including Sensitivity, Figure of Merit (FOM), full-width at half-maximum (FWHM), and Coupling Efficiency (CE), are introduced as key metrics for evaluating sensor performance. This chapter sets the stage for a detailed discussion of state-of-the-art techniques and novel configurations, offering insights into the critical parameters that influence grating-based SPR biosensing. By addressing these aspects, the chapter provides a comprehensive foundation for understanding and advancing SPR technologies.

3.1. Plasmonic Materials for Grating-Based SPR Sensors

Plasmonic materials have gained significant attention in recent years due to their ability to support surface plasmon resonances (SPRs), which enable enhanced light-matter interactions. These materials, primarily composed of noble metals, transition metal nitrides, and some semiconductors, exhibit unique optical properties that are useful in applications such as biosensing, photonics.

As discussed in theoretical chapter, a plasmonic metamaterial is a material whose optical properties are derived from surface plasmons, collective oscillations of free electrons at the interface between a metal and a dielectric. The efficiency of this coupling depends on factors such as material conductivity, quality factor, and fabrication feasibility.

Noble Metals

Noble metals, such as gold (Au), silver (Ag), and aluminum (Al), are frequently employed in plasmonic applications due to their high electrical conductivity and ability to support long propagation distances of surface plasmon polaritons (SPPs) [87]. Silver (Ag) offers the lowest optical losses and longest propagation distances in the visible spectrum, making it the most efficient plasmonic material [87], though it is susceptible to oxidation. Gold (Au), while exhibiting higher optical losses in the visible range, is preferred for biomedical and long-term plasmonic applications due to its excellent chemical stability [88]. Aluminum (Al) provides a cost-effective alternative with strong plasmonic activity in the ultraviolet (UV) spectrum, but its performance is affected by oxidation and surface roughness.

Alternative Plasmonic Materials

Beyond noble metals, alternative plasmonic materials are being explored, including transition metal nitrides (TiN, ZrN, CuN) [89–91], two-dimensional (2D) materials like graphene and transition metal dichalcogenides (TMDs) [92]. Titanium nitride (TiN) offers high-temperature stability and optical properties comparable to gold. Graphene provides tunable plasmonics in the mid-infrared (MIR) and terahertz (THz) ranges, making it advantageous for integrated photonics. Alkali metals (Na, K) exhibit the smallest optical losses and high-quality factors [93], but fabrication and processing challenges hinder their practical use. Despite this variety, silver remains the top performer for plasmonic quality factors in Localized Surface Plasmon Polariton (LSPP) and SPP applications within the visible and near-infrared (NIR) spectrums [87, 94].

Plasmonic Properties of Silver

Paul R. West and his team [94] analyzed the optical properties of various plasmonic materials based on their quality factors, propagation lengths, and optical losses. Their study highlights that, although no single plasmonic material is optimal for all applications, silver remains the best-performing material for most use cases. Fig. 3.1 illustrates the propagation distances of SPPs for different metals as a function of wavelength. This simulation demonstrates that silver exhibits the lowest losses in the Drude model and the longest propagation length in the visible spectrum [87]. Moreover, Fig. 3.2 compares the quality factors of different metals commonly used in plasmonics. Quality factors [94] provide a quantitative measure of the performance of plasmonic materials. It shows that silver (Ag) exhibits the highest quality factors among the metals considered, particularly in the visible and near-infrared regions, which corresponds to optical frequencies.

Challenges of Using Silver

While silver offers superior plasmonic properties, its rapid oxidation in air significantly alters its optical behavior, making it less than ideal for long-term plasmonic devices [94]. This oxidation issue has spurred research into several solutions: protective coatings like silicon dioxide (SiO_2) [95] and graphene layers to prevent oxidation [96]; bimetallic structures (Ag-Au, Ag-Al) [97] designed to enhance stability while preserving plasmonic

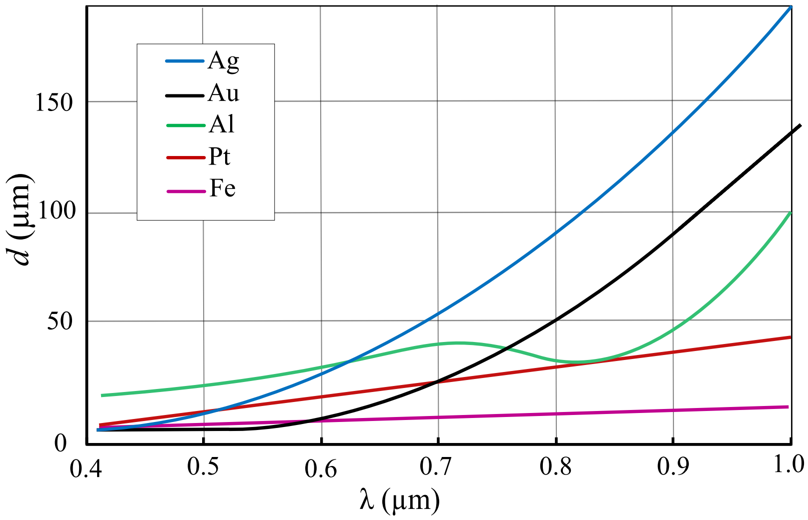

Figure 3.1.: The propagation distances of SPP in different metals as a function of the wavelength in μm. Adapted from [87], a license has been granted by Cambridge University Press.

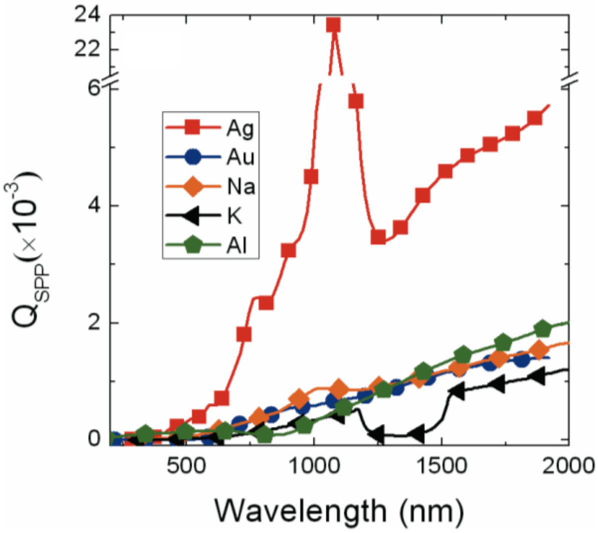

Figure 3.2.: Comparison of the surface plasmon resonance quality factor (Q_{SPP}) for different metals (Ag, Au, Na, K, Al) as a function of wavelength. Silver (Ag) exhibits the highest Q_{SPP}, particularly in the visible and near-infrared regions, indicating its superior performance for plasmonic applications. Reproduced with permission from.[94] Copyright 2007, WILEY - VCH VERLAG GMBH

efficiency; and nanostructuring techniques aimed at improving performance and reducing susceptibility to oxidation.

Conclusion, although multiple materials can be employed for plasmonic applications, silver remains the optimal choice due to its low optical losses and long propagation distances. Even though silver is susceptible to oxidation, recent advancements in protective coatings, bimetallic alloys, and fabrication techniques have significantly improved its durability. As a result, silver continues to be the leading plasmonic material for applications in biosensing, photonics, and high-performance optical devices.

3.2. Grating Fabrication Techniques for SPR Sensors

Grating structures are essential components in Surface Plasmon Resonance (SPR) sensors, as they enable the coupling of incident light to surface plasmon waves. The fabrication of these gratings requires precise control over periodicity, depth, and uniformity to enhance sensor sensitivity and ensure repeatability. Different fabrication techniques offer varying levels of resolution, scalability, cost-effectiveness, and material compatibility, influencing the performance of SPR sensors.

This section explores key fabrication methods, detailing their principles, working mechanisms, achievable grating sizes, and limitations. Additionally, it justifies why Electron Beam Lithography (EBL) is chosen in this research for precise and high-performance grating fabrication.

Interference Lithography (IL)
Interference lithography (IL) is a maskless photolithographic technique that utilizes two or more coherent laser beams to create an interference pattern on a photosensitive material. This interference generates periodic light and dark fringes, exposing the photoresist in a pattern corresponding to the desired grating structure [98]. The fabrication process as shows in Fig. 3.3, involves four steps: substrate preparation, where a substrate (silicon, quartz, or glass) is coated with photoresist; exposure, where overlapping laser beams create the interference pattern; development, where the exposed photoresist forms the periodic grating pattern; and optionally, etching, where the pattern is transferred to the substrate using reactive ion etching (RIE). IL allows for grating periodicities typi-

cally between 200 nm and 5 μm [97, 99], controlled by laser wavelength and interference angle, and grating depths from 50 nm to 1 μm, dependent on etching conditions. The resolution limit is 100-500 nm [100], constrained by diffraction. IL's advantages include high uniformity over large areas (cm^2-scale) and high-speed processing suitable for mass production. However, it has limitations, primarily its limited flexibility to create only sinusoidal gratings and its fixed periodicity, dependent on the interference angle.

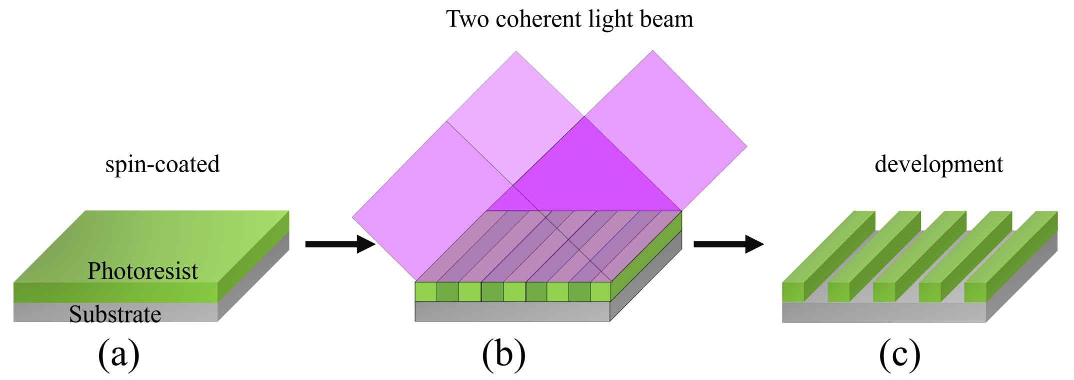

Figure 3.3.: Grating fabrication via Interference Lithography. (a) A photoresist is spin-coated onto a substrate. (b) Two coherent light beams interfere, creating a periodic intensity pattern on the photoresist. (c) Development removes the exposed photoresist, revealing a patterned structure.

Nanoimprint Lithography (NIL)

Nanoimprint lithography (NIL) is a technique that employs mechanical deformation to transfer nanoscale patterns onto a substrate [101]. This is achieved by pressing a pre-patterned mold (master stamp) into a soft polymer layer and subsequently curing or solidifying the material [102]. The fabrication process as shows in Fig. 3.4, includes mold fabrication, where a high-precision master mold (made of silicon, quartz, or metal) is created using electron beam lithography (EBL) [103] or photolithography [104]; imprinting, where the mold is pressed onto a thermoplastic or UV-curable polymer; curing and separation, where the polymer is hardened via UV exposure [105] or heat [106], and the mold is removed, leaving the grating pattern; and finally, metal deposition, where a thin metal film (e.g., Au, Ag) is deposited over the structured surface. NIL allows for grating periodicities from 50 nm to 1 μm [107], limited by the master mold resolution, and grating depths from 10 nm to 200 nm, controlled by imprint pressure and mold depth. With high-quality molds, NIL can achieve a resolution down to 10-100 nm [100].

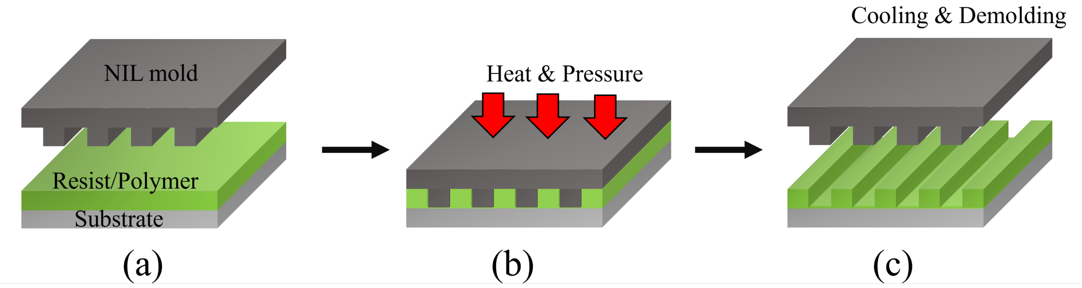

Figure 3.4.: Schematic Illustration of Thermal Nanoimprint Lithography (T-NIL) for a grating fabrication. (a) A mold with patterned features is brought into contact with a polymer resist layer coated on a substrate. (b) Heat and pressure are applied, forcing the mold features into the softened polymer. (c) After cooling and demolding, the pattern is transferred to the polymer resist.

UV Lithography

UV lithography is a mask-based photolithographic process that uses a photomask to define patterns on a light-sensitive material. The photomask, with its opaque and transparent regions, allows UV light to selectively expose the photoresist, thus creating grating structures [108]. The fabrication process as shows in Fig. 3.5, involves several steps: substrate preparation, where a silicon or glass substrate is coated with photoresist; exposure, where a UV light source shines through the pre-designed photomask, exposing the photoresist in the defined pattern; development, where the exposed photoresist is developed, revealing the grating structure; and finally, etching and metal deposition, where the grating pattern is transferred onto the substrate, and a plasmonic metal (e.g., Au, Ag) is deposited. UV lithography allows for grating periodicities ranging from 1 μm to 100 μm [109], limited by UV diffraction effects, and grating depths from 50 nm to 10 μm, dependent on the etching process. The resolution limit is 300-500 nm [100], constrained by mask design and light diffraction. While UV lithography is fast and widely used in industrial settings, and suitable for micron-scale gratings, its resolution is diffraction-limited, and its mask dependency limits flexibility.

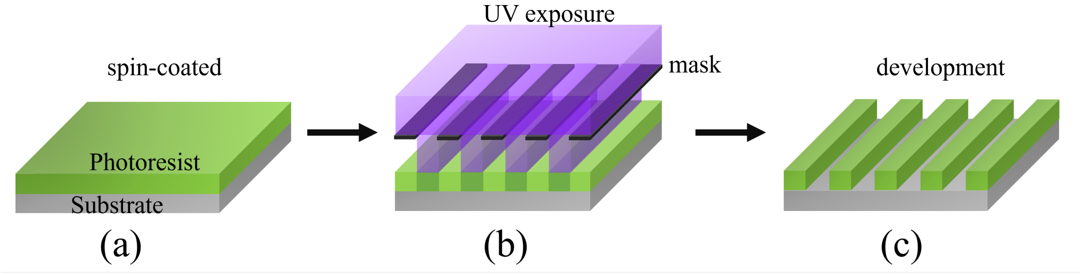

Figure 3.5.: Schematic of UV lithography Process. (a) A photoresist layer is spin-coated onto a substrate. (b) The photoresist is selectively exposed to UV light through a mask, defining the desired pattern. (c) Development removes the exposed photoresist, revealing the pattern on the substrate.

Electron Beam Lithography (EBL) – The Preferred Technique

Electron Beam Lithography (EBL) is a direct-write nanolithography technique that utilizes a highly focused electron beam to expose a resist layer, enabling the fabrication of extremely fine grating structures [110]. The process as shows in Fig. 3.6, begins with substrate coating, where a substrate (silicon, quartz, or polymer) is coated with an electron-sensitive resist (e.g., PMMA) [111]. Direct writing follows, where a high-energy electron beam scans the resist in a computer-controlled pattern to define the grating structure. The exposed resist is then chemically developed, revealing the grating pattern. Finally, the pattern is transferred to the substrate, and a thin metallic film (e.g., Au, Ag, or Al) is deposited. EBL offers unparalleled flexibility with grating periodicities ranging from 5 nm to 1 μm [82, 112, 113], and grating depths from 5-500 nm [100], precisely controlled via etching. Its resolution limit of less than 10 nm makes it the highest-resolution technique available.

To summarize, as shows in Tab. 3.1, the selection of a grating fabrication technique depends on resolution, scalability, cost, and design flexibility. While Interference Lithography (IL) and Nanoimprint Lithography (NIL) are effective for mass production, they lack the nanometer-scale precision required for optimal SPR performance. Electron beam lithography (EBL) is chosen for its superior resolution, precise control, and ability to fabricate highly customized grating structures, making it the best choice for high-sensitivity SPR applications.

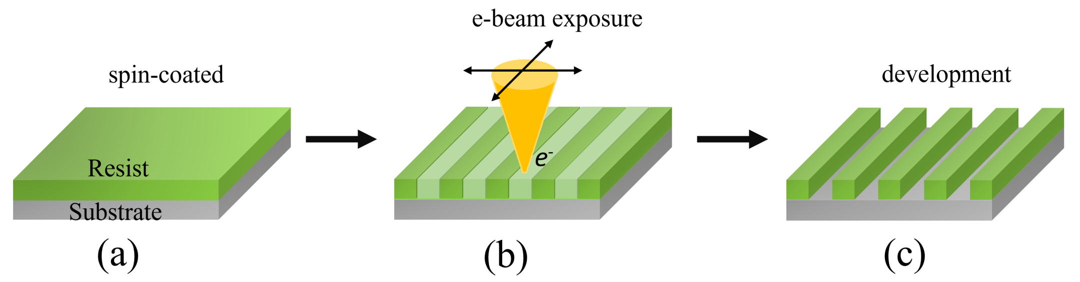

Figure 3.6.: Schematic of Electron Beam Lithography Process. (a) A resist layer is spin-coated onto a substrate. (b) The resist is selectively exposed to an electron beam (e-beam), defining the desired pattern. (c) Development removes the exposed resist, revealing the pattern on the substrate.

Table 3.1.: Comparison of different grating fabrication techniques based on key parameters.

Feature	Interference Lithography (IL)	Nanoimprint Lithography (NIL)	UV Lithography	Electron Beam Lithography (EBL)
Resolution Limit	∼500 nm	20 nm	∼500 nm	<10 nm
Grating Periodicity	200 nm – 5 μm	50 nm – 1 μm	1 μm – 100 μm	5 nm – 1 μm
Grating Depth	50 nm – 1 μm	10 nm – 200 nm	50 nm – 10 μm	5 nm – 500 nm
Pattern Flexibility	Sinusoidal patterns	Limited to mold design	Mask-dependent	Fully customizable
Scalability	High	High	High	Low
Fabrication Speed	Fast	Fast	Very fast	Slow
Cost	Low	Medium	Low	High
Mass Production	Excellent	Excellent	Excellent	Poor
Material Compatibility	Glass, silicon, quartz	Polymers, glass, metals	Glass, silicon, photoresist	Glass, silicon, polymers
SPR Sensors	Moderate sensitivity	Moderate to high sensitivity	Low to moderate sensitivity	High sensitivity

3.3. Measurement Configurations of Grating-Based SPR Sensors

The measurement configuration plays a crucial role in optimizing the efficiency and accuracy of grating-coupled SPR sensors. Unlike the conventional prism-based setup, grating-based SPR relies on the diffraction of incident light to excite surface plasmons. Several measurement configurations exist, each with distinct advantages and limitations.

Angular Interrogation (Chosen Method for This Thesis)

Angular interrogation, the method chosen for this thesis, measures the angle at which Surface Plasmon Resonance (SPR) occurs, identified by the minimum reflected light intensity. The setup as shows in Fig. 3.7, comprises a laser source (e.g., He-Ne laser at 632.8 nm [82, 114] or a diode laser at 637 nm [115]), a collimating lens to focus the beam for angular variation, a polarizer to ensure p-polarized light, a motorized rotational stage for precise incident angle adjustment (±0.01° precision), and a detector (photodiode [116] or CCD camera [114]) to measure reflectivity. The measurement output is the SPR angle shift (°) per refractive index unit (RIU). This method typically achieves a sensitivity of 40–160°/RIU [100, 114, 117] with high resolution (±0.01°). Its advantages include high sensitivity to RI variations (making it ideal for biosensing), a wide dynamic range (detecting from 1.33–1.40 RIU) [82], simple data interpretation (due to the linear relationship between RI change and angle shift), and low-cost optics compared to wavelength inter-

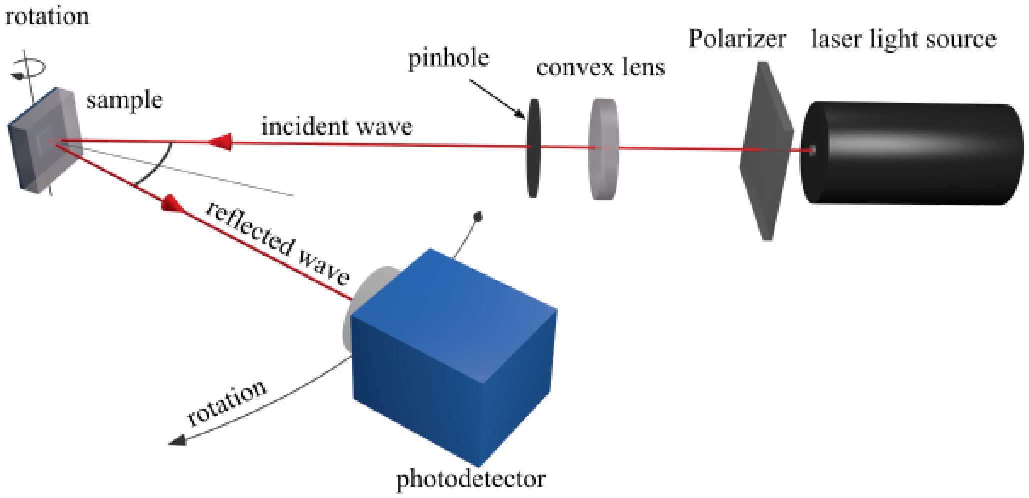

Figure 3.7.: Schematic of angular interrogation setup. A laser light source emits a beam that is polarized and focused by a convex lens through a pinhole. The resulting incident wave is directed onto a sample, which is mounted on a rotation stage. The reflected wave is then measured by a photodetector, also mounted on a rotation stage. (Image adapted from Sarapukdee et al. [82] under the Creative Commons Attribution (CC BY) license.)

rogation. However, angular interrogation also has limitations: slower measurement speed due to mechanical scanning and bulky instrumentation due to the rotating components.

Wavelength Interrogation

Wavelength interrogation, an alternative SPR measurement technique, measures the shift in the SPR resonance wavelength rather than the angle. The setup as shows in Fig. 3.9, includes a broadband light source (such as a halogen lamp [118] or supercontinuum laser [119]), a diffraction grating to select specific wavelengths, and a spectrometer to detect intensity changes across the spectrum. The measurement output is the resonance wavelength shift (nm/RIU), and the sensitivity typically ranges from 400–1200 nm/RIU [100, 120]. Wavelength interrogation offers the advantages of fast measurements due to the absence of mechanical movement and easier miniaturization for portable devices. However, it also has limitations, including lower sensitivity compared to angular interrogation, complex data processing requiring precise wavelength calibration, and higher equipment costs due to the spectrometer.

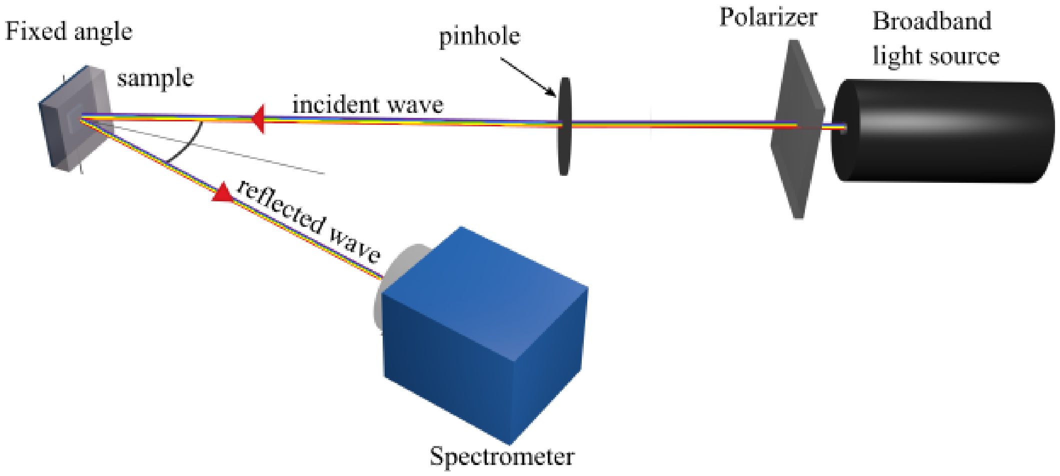

Figure 3.8.: Schematic of wavelength interrogation setup. A broadband light source emits light that is polarized and passes through a pinhole. The resulting incident wave is directed onto a sample at a fixed angle. The reflected wave is then analyzed by a spectrometer.

Phase Interrogation

Phase interrogation is another SPR technique that measures the phase shift or polarization change in reflected light [121]. The setup as shows in Fig. 3.9, typically includes a monochromatic laser source, a beam splitter and rotating analyzer to control the polarization state, and a CMOS camera to capture the interference pattern [122]. The measurement output is the phase shift, measured in degrees (°/RIU). This method offers extremely high sensitivity, up to 300°/RIU [121, 123], making it ideal for single-molecule detection. While advantageous for its high sensitivity and potential for single-molecule detection, phase/polarization interrogation also has limitations. It requires complex optical alignment [100] is sensitive to environmental noise (such as temperature and vibrations), and has a limited dynamic range compared to angular or wavelength methods.

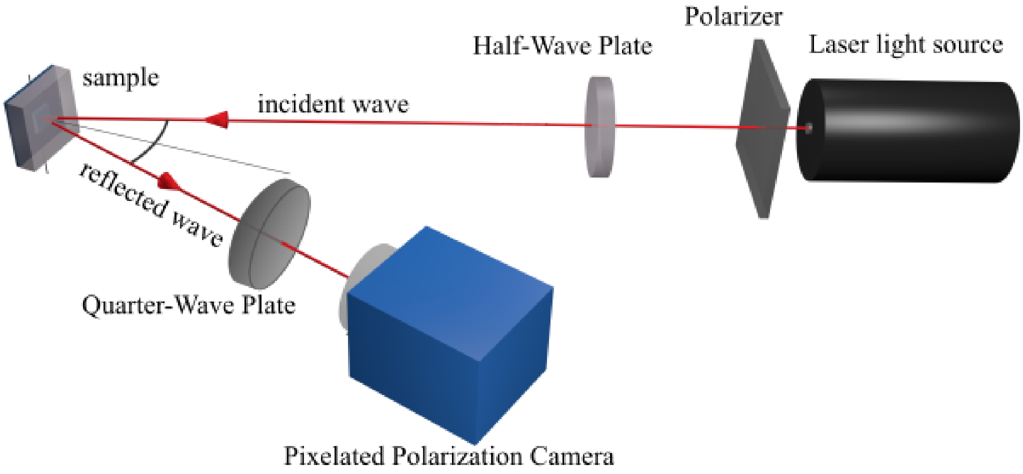

Figure 3.9.: Schematic of a phase interrogation setup. A laser light source emits a beam that is polarized by a polarizer. A half-wave plate is used to control the polarization state of the incident wave. The beam is directed onto a sample, and the reflected wave passes through a quarter-wave plate before being detected by a pixelated polarization camera.

3.4. Performance Evaluation Metrics in SPR Biosensing

Performance evaluation metrics are critical for assessing the efficacy of SPR biosensors. Key metrics such as sensitivity, figure of merit (FoM), full-width at half-maximum (FWHM), and Coupling Efficiency (CE) are critical. Sensitivity quantifies the ability to detect small changes in refractive index. The FoM integrates sensitivity and spectral resolution, ensuring optimal sensor performance. FWHM represents the sharpness of the resonance peak, directly impacting detection accuracy. This section provides these evaluation metrics, their mathematical formulations, and their significance in improving SPR biosensing technology.

Sensitivity (S)

Sensitivity measures the ability of the SPR sensor to detect small changes in the refractive index (RI) of the sensing medium [124]. It is expressed as the shift in resonance angle or wavelength per unit change in RI:

$$S = \frac{\Delta\theta}{\Delta n} \quad \text{or} \quad S = \frac{\Delta\lambda}{\Delta n} \tag{3.1}$$

where:

S = Sensitivity

$\Delta\theta$ = Change in resonance angle (°)

$\Delta\lambda$ = Change in resonance wavelength (nm)

Δn = Change in refractive index (RIU)

A higher sensitivity value indicates a better-performing sensor.

Full-Width at Half-Maximum (FWHM)

FWHM represents the width of the SPR resonance peak at half of its maximum intensity [125]. It is defined as the difference between the two x-values (in this case, angles) at which the measured value (here, reflectivity) falls to half of its maximum value. For a reflectivity curve $R(\theta)$ with a maximum value $R_{\max}$, the FWHM is given by the angular range between the two points where:

$$R(\theta_1) = R(\theta_2) = \frac{1}{2} R_{\max}, \tag{3.2}$$

so that:

$$\text{FWHM} = \theta_2 - \theta_1. \tag{3.3}$$

A narrower FWHM results in a sharper peak, improving sensor resolution.

Figure of Merit (FoM)

The Figure of Merit (FoM) [126] evaluates the overall sensor performance by considering both sensitivity and resolution:

$$FoM = \frac{S}{\text{FWHM}} \tag{3.4}$$

where:
S = Sensitivity
$FWHM$ = Full-width at half-maximum of the resonance curve
A higher FoM indicates better sensor resolution and detection capabilities.

Coupling Efficiency (CE)

The assessment of coupling efficiency (CE) [82] involved computations that hinged on signal attributes, specifically involving the interrelation of the full-width at half-maximum (FWHM) of the excitation angle peak and the relative reflectivity R_{rel}. The CE was quantified using the formula:

$$CE = \frac{(1 - R_{rel})}{\text{FWHM}} \tag{3.5}$$

where: R_{rel} = Relative reflectivity $FWHM$ = Full-width at half-maximum of the excitation angle peak A higher CE value signifies a more effective coupling of incident light into the SPR mode, optimizing sensor performance.

3.5. Conventional SPR Biosensing

Conventional Surface Plasmon Resonance (SPR) biosensing is as a powerful and widely adopted technique for real-time monitoring of biomolecular interactions. Notably, SPR holds the largest market share within the label-free biosensor sector [127], a testament to its reliability and versatility. Its significant applications span diverse fields, including biological research, pharmaceutical development, clinical diagnostics, and environmental monitoring. Commercially available SPR instruments [128], such as those offered by Biacore (Cytiva), Reichert Technologies, and Nicoya Lifesciences, provide users with robust platforms for conducting these analyses. These systems vary in throughput, sensitivity, and automation, catering to a wide range of experimental needs and budgets.

Working Principle of Conventional SPR Sensors

Conventional SPR biosensors operate by utilizing a thin metal film, typically gold or silver, coated onto a glass prism. The prism optically couples with a sample solution containing the target analyte. Light is directed onto the metal film at an angle slightly above the resonance angle, exciting surface plasmons. The reflected light is then collected and analyzed using a photodetector to determine shifts in resonance conditions, which correlate with biomolecular interactions.

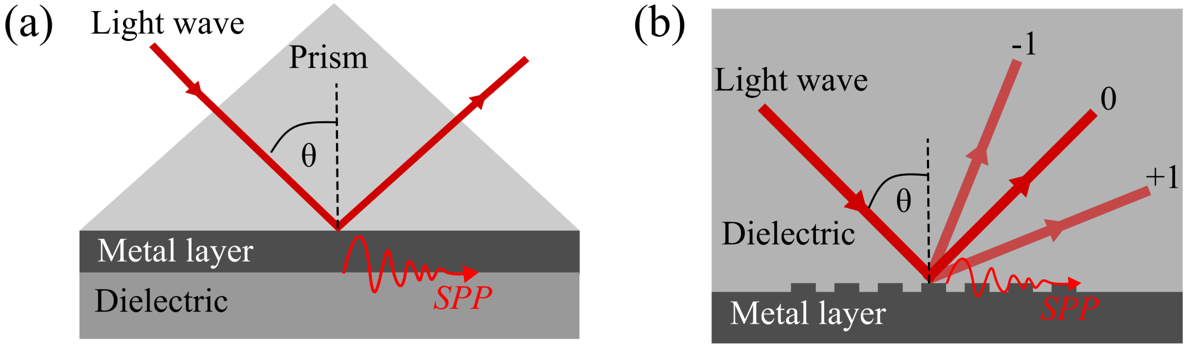

Figure 3.10.: Various SPR sensor configurations using different light coupling approaches for SPR biosensing, including (a) prism coupling-based Kretschmann configuration, (b) grating coupling.

In the most commonly used Kretschmann configuration [76], shown in Fig. 3.10(a), light is directed through a high-refractive-index prism onto a thin metal film. When the momentum of the incident photons matches the surface plasmon wave, resonance occurs, leading to a measurable dip in the reflected light intensity. This resonance condition shifts in response to molecular binding events at the metal surface, allowing quantitative analysis of biomolecular interactions.

SPR Signal Analysis and Real-Time Monitoring

The data for angular detection can be analyzed using two primary methods: angular scanning of incident light as shows in Fig. 3.11(b) or monitoring angular changes over time as shows in Fig. 3.11(c).

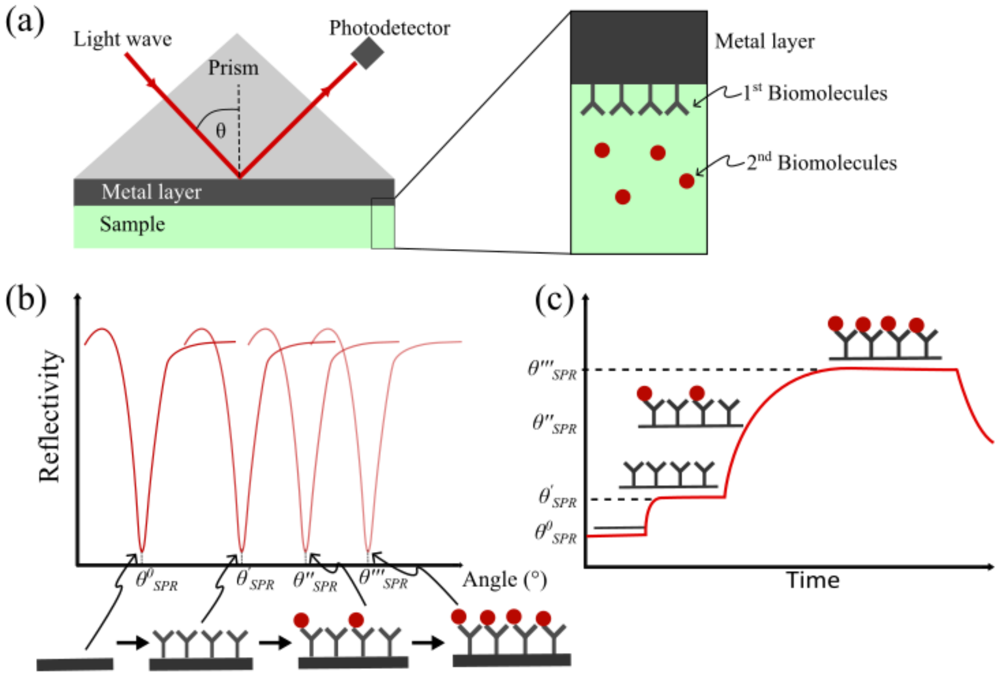

Figure 3.11.: (a) Diagram of an SPR setup in the Kretschmann configuration. Light wave is transferred to surface plasmons at a certain angle, resulting in a minimum intensity in the angular scanning, as shown in (b). (c) SPR angle variation as a function of time enables real-time monitoring of the antibody-antigen interaction.

Fig. 3.10b illustrates angular scanning for different scenarios:

- A pure gold sensor with an initial resonance angle θ^0_{SPR}.

- A sensor with immobilized antibodies, shifting the resonance angle to θ'_{SPR}.

- A sensor detecting target antigens, shifting the angle further to θ''_{SPR}, which eventually saturates at θ'''_{SPR} when binding reaches equilibrium.

In real-time detection, as shown in Fig. 3.11c, the SPR angle fluctuation over time allows for continuous monitoring of biomolecular interactions. This method is widely used to calculate kinetic parameters [129] such as binding curves, association rate constants, dissociation rate constants, and equilibrium constants (affinity).

Advantages and Challenges of Conventional SPR Biosensing

Conventional SPR biosensors offer several key advantages [130]. They allow for label-free detection [29], eliminating the need for fluorescent or radioactive labels, which simplifies experimental procedures and avoids potential interference with analyte behavior. Real-time monitoring is another benefit, enabling continuous observation of kinetic interactions, particularly valuable for studying rapid binding and dissociation processes [131, 132]. Finally, their high sensitivity allows for the detection of even minute changes in refractive index caused by molecular interactions, making them highly effective for biomolecular studies [133]. However, conventional SPR biosensing also has limitations. It is surface sensitive, primarily detecting interactions within a few nanometers of the metal surface [134, 135], which restricts its applicability to some biological systems where interactions occur further away. Non-specific binding is another concern, as direct contact between the sample and the metal surface can lead to fouling or non-specific interactions [136, 137], requiring careful experimental design and surface regeneration strategies. Lastly, the high initial investment and maintenance costs of the equipment can limit accessibility in resource-limited settings.

3.6. Advances in SPR Biosensing Systems and Technologies

SPR has evolved significantly, with new configurations and sensing mechanisms improving its sensitivity and applicability. Beyond conventional prism-based SPR, localized surface plasmon resonance (LSPR) and backside illumination techniques have enabled more flexible and enhanced biosensing approaches. This section covers the latest advances in SPR biosensing, with a focus on different SPR configurations and sensing methodologies. It begins with a discussion of principle, followed by an examination of advanced technologies and associated challenges.

Localized Surface Plasmon Resonance (LSPR)

LSPR biosensors operate based on the interaction between light and the collective oscillation of conduction electrons, known as surface plasmons [138]. When noble metal nanoparticles [139] are irradiated with light at a specific wavelength, the free electrons at the nanoparticle surface undergo resonant oscillations, resulting in enhanced light absorption and scattering, as illustrated in Fig. 3.12(a). This localized surface plasmon resonance (LSPR) phenomenon is highly sensitive to changes in the refractive index of the surrounding medium [140], making it a powerful tool for biosensing applications [141].

The resonance wavelength, λ_{res}, of LSPR is highly dependent on the refractive index, n, of the surrounding medium. The shift in resonance wavelength due to changes in the refractive index, Δn, is given by [142, 143]:

$$\Delta\lambda_{\text{max}} = m\Delta n \left[1 - \exp\left(\frac{-2d}{l_d}\right)\right]. \tag{3.6}$$

Here, m is the bulk refractive-index response of the nanoparticle(s), Δn is the change in refractive index induced by the adsorbate, d is the effective adsorbate layer thickness, and l_d is the characteristic electromanetic field decay length. The extinction cross-section,

C_{ext}, for nanoparticles in the quasi-static approximation based on Mie theory can be expressed as [142, 143]:

$$C_{\text{ext}} = \frac{24\pi^2 R^3}{\lambda} \frac{\epsilon_m^{3/2}\,\text{Im}(\epsilon)}{[\text{Re}(\epsilon) + 2\epsilon_m]^2 + \text{Im}(\epsilon)^2}, \tag{3.7}$$

where R is the radius of the nanoparticle, ϵ_m is the dielectric constant of the surrounding medium, and ϵ is the complex dielectric function of the metal.

LSPR-based biosensors offer high sensitivity to molecular interactions due to the strong localization of the plasmonic field. These sensors work by detecting shifts in the resonance wavelength when biomolecules bind to the nanostructure surface.

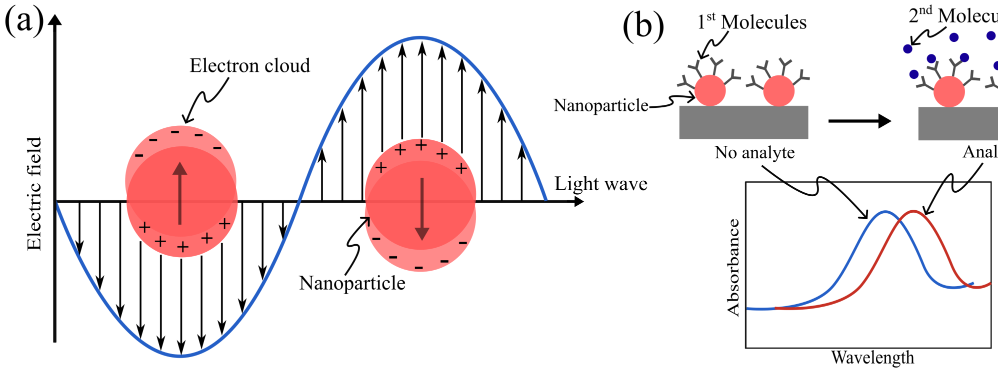

Figure 3.12.: Schematic diagram illustrating the localized surface plasmon on a nanoparticle surface. (a) The localized surface plasmon resonance (LSPR) of plasmonic nanoparticles and (b) absorbance spectra obtained for binding events on nanoparticles.

Comparison Between LSPR and Conventional SPR

While both LSPR and Surface Plasmon Resonance (SPR) operate based on plasmonic principles, their mechanisms and applications differ significantly. Tab. 3.2 summarizes key differences between the two techniques.

Advantages and Challenges of LSPR Biosensing

Localized Surface Plasmon Resonance (LSPR) biosensors offer key advantages due to their tunable optical properties, which can be precisely controlled by adjusting the nanoparticle size, shape, and material composition [144]. This adaptability enhances sensi-

Table 3.2.: Comparison between SPR and LSPR

Feature	LSPR	SPR
Resonance Mode	Localized at nanoparticle surface	Propagating along metal-dielectric interface
Excitation Source	Direct light illumination	Requires prism, grating, or waveguide coupling
Sensing Depth	Few nanometers (highly localized)	Hundreds of nanometers (bulk interactions)
Sensitivity	High for surface interactions	High for bulk refractive index changes
Miniaturization	Compatible with portable devices	Requires complex optical components
Multiplexing Potential	Moderate (limited by spectral overlap)	High (better spectral separation)

tivity and enables multiplexed detection of multiple biomolecules in a single experiment [145]. Unlike conventional Surface Plasmon Resonance (SPR) sensors that rely on complex optical setups such as prisms or gratings, LSPR sensors can be directly excited by light, simplifying the sensor design. Additionally, the localized nature of LSPR near the nanoparticle surface enhances sensitivity to small environmental changes, making these sensors ideal for portable and point-of-care diagnostic applications [146–148]. Despite these benefits, LSPR sensors face certain challenges. Broad spectral linewidths reduce detection specificity and complicate peak shift measurements [149, 150]. Stability and reproducibility can be affected by nanoparticle aggregation and surface fouling, leading to inconsistencies in sensor performance. Furthermore, spectral overlap in multiplexed LSPR detection limits the ability to distinguish between different analytes [151]. The high cost of noble metal nanoparticles [152], such as gold and silver, also poses a barrier to large-scale commercialization.

Backside Illumination SPR Sensors

Backside illumination SPR sensors involve directing incident light from the substrate side rather than the typical front-side illumination through the sensing medium. This approach [153, 154] optimizes the coupling mechanism, leading to enhanced sensitivity and reduced optical noise.

In addition, the backside illumination grating structure SPR coupling offers flexibility in sensor chip fabrication. It can be implemented on various materials, including silicon, glass [154, 155], or polymers [153], allowing for compatibility with different sample environments and applications. The fabrication techniques for the grating structure are well-established and can be readily incorporated into existing microfabrication processes.

The study from [156, 157] suggests a grating arrangement for effective backside illumination SPR coupling for use in tiny SPR sensors. The alignment is shown in Fig. 3.13. An embedded grating structure with a flat surface in contact with the sample was created. Using bulk micromachining, a 300 nm thick SOI top layer was used as a completely embeddable grating amid an SU-8 substrate. The simulations show that the suggested structure has a good SPR coupling efficiency and may be used with an SPR sensor. The experimentally determined optical response of the built device revealed that efficient SPR coupling is achievable.

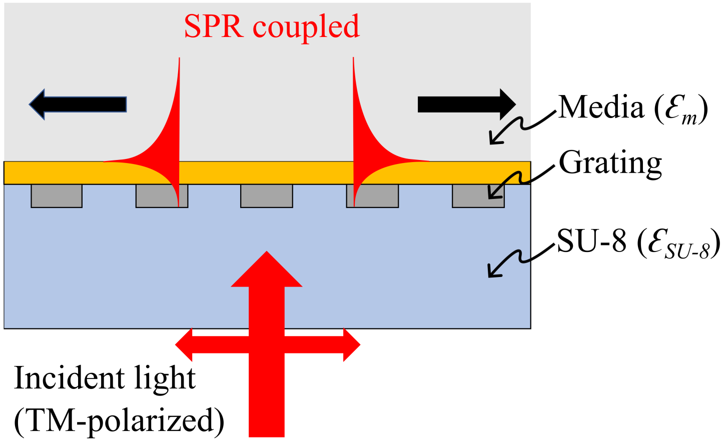

Figure 3.13.: A backside lighting device with an SPR coupling structure, consisting of an Au film, a Si grating area, and an Al thin film region on an SU-8 substrate. The surface of the Au grating acts as the sensor surface. To activate the SPR, the Au portion works as the anode electrode and the aluminum electrode as the cathode electrode, and the incident light must be transverse magnetic (TM) polarized in the plane of incidence. Adapted with permission from [157]. Copyright ©2021, IEEE.

Advantages and Challenges of Backside Illumination SPR Sensors

Backside illumination grating-coupled SPR sensors offer significant advantages for precise refractive index measurements. By directing light through the substrate, this configuration minimizes signal interference from the sample medium, enhancing sensitivity and stability [158]. Protecting the sensing surface from direct light exposure reduces photodamage and thermal effects [159], ensuring robust performance. Furthermore, the compatibility with diverse substrates and potential for miniaturization enables integration into advanced microfluidic [160, 161] and portable biosensing systems.

However, realizing the full potential of this technology requires addressing several challenges. The fabrication process demands precise optical alignment for optimal light coupling, and the increased angular sensitivity can lead to narrower resonance curves, requiring careful calibration. Additionally, the limited dynamic range and scalability considerations necessitate the development of refined manufacturing processes [162], alignment methodologies, and calibration procedures. Overcoming these challenges will pave the way for broader applications in advanced biosensing.

SPR Coupling with Electrical Readout

An optical prism and a photodetector are used in the most typical SPR observation setup. Recent advancements have integrated electrical readout mechanisms [163] to enhance signal processing, miniaturization, and portability. The coupling of SPR with electrical detection [164, 165] not only simplifies instrumentation but also facilitates seamless integration with existing electronic circuits and microfluidic systems [164]. Electrical readout mechanisms in SPR systems leverage various transduction methods, including capacitive sensing [164], CMOS photodetector [165, 166], electrochemical detection [167], and field-effect transistor (FET)-based readouts [168]. These approaches allow the direct conversion of optical resonance shifts into electrical signals, improving detection sensitivity and real-time monitoring capabilities.

The study from [165, 169, 170] proposes an electrical readout SPR sensor utilizing an Au diffraction grating with a submicrometer pitch, capable of coupling visible light at a 700-nm wavelength with SPR. This wavelength is carefully chosen to minimize water absorption while maximizing optical coupling efficiency. The grating geometry was designed using the rigorous coupled-wave analysis (RCWA) method [171] to produce large optical absorption nearing unity, with sharp resonant characteristics due to SPR in visible light. The device was fabricated using nanofabrication technology to incorporate Au diffraction gratings on an n-type silicon (n-Si) substrate.

SPRs on the grating were generated by light irradiation from the Au grating side, and the SPR could be read out electrically via the Schottky junction formed at the Au/n-Si interface [169]. The working principle relies on the generation of hot electrons in the Au film, which overcome the Schottky barrier and inject into the n-Si substrate, allowing SPR detection as a photocurrent signal. Measurements were performed using air, pure water, and aqueous glucose solutions to confirm the feasibility of refractive index measurements. The SPR modes observed in these experiments were consistent with theoretical predictions, and the measurable refractive index resolution was derived from noise evaluation, demonstrating the sensor's capability for high-precision detection.

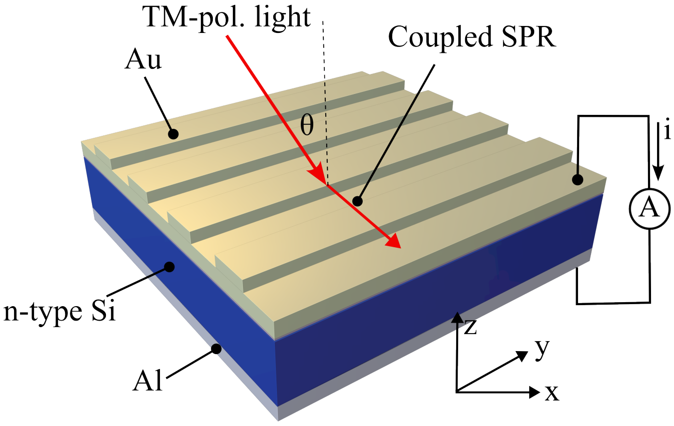

Figure 3.14.: Semiconductor-based SPR sensors with electrical sensor readouts. The incident light's energy is absorbed during SPR. Due to the absorbed energy of the incident light, hot electrons in the Au film can overcome the Schottky barrier and are injected into the n-Si substrate, allowing SPR to be read out as a photocurrent. Adapted with permission from [170], Copyright 2022, IEEE.

Advantages and Challenges of SPR Coupling with Electrical Readout

Semiconductor-based surface plasmon resonance (SPR) sensors with electrical readouts present a promising avenue for compact, high-performance sensing [163], but face challenges including electrical noise, limited dynamic range compared to optical methods, fabrication complexities, and material compatibility issues. To mitigate these limitations, advanced signal processing, optimized interface design, precision nanofabrication, and surface functionalization are crucial. Further advancements, such as hybrid platforms incorporating graphene and 2D materials, alongside electrostatic modulation and conductive nanostructures, are being explored to enhance sensitivity and tunability. The integration of SPR with electronic readouts is driving the development of next-generation lab-on-chip devices and portable biosensors.

Microfluidics-Based SPR Biosensors

Microfluidics enables precise manipulation of minute fluid volumes through submillimeter channels, offering an ideal platform for ultrasensitive chemical detection [172, 173] and cell [174] manipulation in biomedical research. Advanced microfluidic systems simplify assays and reduce processing time by replacing conventional techniques. Integrated with on-chip sensors, simple microfluidic devices enhance biological testing, while innovations in high-throughput and miniaturization support cost-effective biosensors [175].

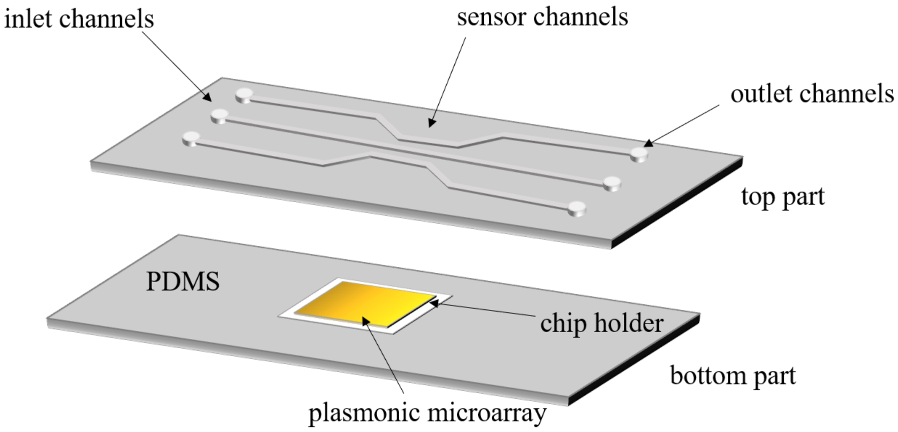

Figure 3.15.: The PDMS top slab contains three microfluidic channels: inlet, sensor channels interfacing with the plasmonic chip, and outlet. The bottom PDMS slab secures the chip and connects to the top layer. Adapted from [176] under the CC BY NC ND license.

Combining microfluidic chips with plasmonic biosensors integrates lab-on-chip advantages with SPR technology [177], enabling portable, multiplex biomolecule detection. Onur Tokel et al. [178] developed a low-cost, disposable microfluidic-SPR biosensor for pathogen detection. A gold-coated substrate, functionalized with antibodies, is centrally positioned in a microchannel with inlet and outlet ports. The Kretschmann configuration underpins the SPR system, where a CMOS sensor captures reflected LED light from the semiconductor surface. Fig. 3.15 illustrates the compact arrangement of the light source, sensor, and related optics.

Advantages and Challenges of Microfluidic Integration

Microfluidic integration enhances SPR biosensors by enabling low-volume analysis, controlled flow, automation, and multiplexing, facilitating portable diagnostics. However, issues such as sensor surface fouling, complex fabrication [179], and data processing persist. Future efforts focus on advanced surface functionalization and improved sensor stability. The transition to practical point-of-care applications requires affordable [180], user-friendly devices. While microprocessor integration enhances portability, miniaturizing optical components into a single platform remains an engineering challenge. Overcoming these hurdles is critical for widespread adoption in clinical and field applications.

Summary

The versatility of SPR biosensors allows for the characterization of biomolecular interactions, measurement of binding constants and kinetics, and concentration analysis without the need for labeling. The first practical application of SPR sensors for biomolecular detection was reported in 1983 [181], and since then, they have undergone rapid development, becoming a valuable platform for qualitative and quantitative measurements of biomolecular interactions [182]. The advantages of high sensitivity, selection of diverse target molecules, and real-time detection have made SPR sensors indispensable in the fields of biology, food safety, and medical diagnostics.

While numerous SPR sensors have been reported in various applications, traditional SPR devices are often associated with expensive equipment, complex optics, and precise component alignment, which hampers their portability. However, recent advancements have led to the development of portable SPR devices [183, 184], although they still require a portable computer to operate and are approximately the size of a lunch box.

Looking ahead, continued advancements in SPR technology hold great promise for further expanding its applications, improving portability, and enhancing its capabilities in various fields, leading to more accessible and efficient biosensing platforms. Previous literature lacks a comprehensive analysis of the intricate relationship between various critical parameters, leaving a significant gap in understanding. This research aims to close the gap by thoroughly investigating the impact of fundamental parameters such as grating size, silver layer thickness, long-term preservation techniques, the implementation of a new configuration, and the reliability of computer model predictions. By these issues being addressed, a more comprehensive and holistic understanding of the complex dynamics underlying grating SPR for biomolecules can be gained.

CHAPTER 4

Model and Simulation of Grating-Based SPR

This chapter presents the development, implementation, and validation of a computational model for simulating grating coupled surface plasmon resonance (SPR) sensors. The simulation is based on the Finite Difference Time Domain (FDTD) method, incorporating the Drude model for metal dispersion, Perfectly Matched Layers (PML) for boundary absorption, Periodic Boundary Conditions (PBC) for simulating periodic structures, and the Total Field Scattered Field (TF SF) method for wave excitation. The model is validated through convergence analysis and comparison with experimental reflectance data. It is then used to analyze the sensor's response to changes in refractive index and to investigate the influence of different grating geometries on plasmon excitation[8]. Simulation

---

[8] Portions of this section have been previously published as: P. Sarapukdee, C. Spenner, D. Schulz, and S. Palzer, "Optimizing stability and performance of silver-based grating structures for surface plasmon resonance sensors," *Sensors*, vol. 23, no. 15, 2023. DOI: 10.3390/s23156743.

results demonstrate strong agreement with measured data and highlight the potential of the model as a predictive and optimization tool for SPR sensor design and analysis[9].

4.1. Simulation Concept

The primary advantage of using simulations for grating-coupled SPR biosensors is their ability to predict and optimize grating structures across multiple configurations, significantly reducing the time required for experimental iterations. Recent studies [160, 185–187] on surface plasmon resonance (SPR) have heavily relied on simulations due to the challenges associated with fabricating large-area nanometer-scale gratings.

Building a computational model is particularly beneficial as it enables precise predictions of plasmonic interactions, optimization of grating geometry for enhanced sensitivity, and consideration of fabrication limitations that may impact experimental outcomes. However, while simulations provide strong predictive capabilities, they must be validated against experimental data to refine parameters and ensure accuracy. By integrating real-world constraints and continuously optimizing grating designs, simulation models play a crucial role in advancing the development of highly sensitive and reliable SPR biosensors.

The computer modeling process used in this study is illustrated in Fig. 4.1. It consists of three main steps:

1. Model Development – A computer model is built using theoretical data.
2. Validation – The simulation results are compared with experimental data from laboratory measurements.

---

[9] Portions of this section have been previously published as: P. Sarapukdee, D. Schulz, and S. Palzer, "Concept, simulation, and fabrication of inverted grating structures for surface plasmon resonance sensors," *Journal of Sensors and Sensor Systems*, vol. 13, no. 2, pp. 157–166, 2024. DOI: 10.5194/jsss-13-157-2024.

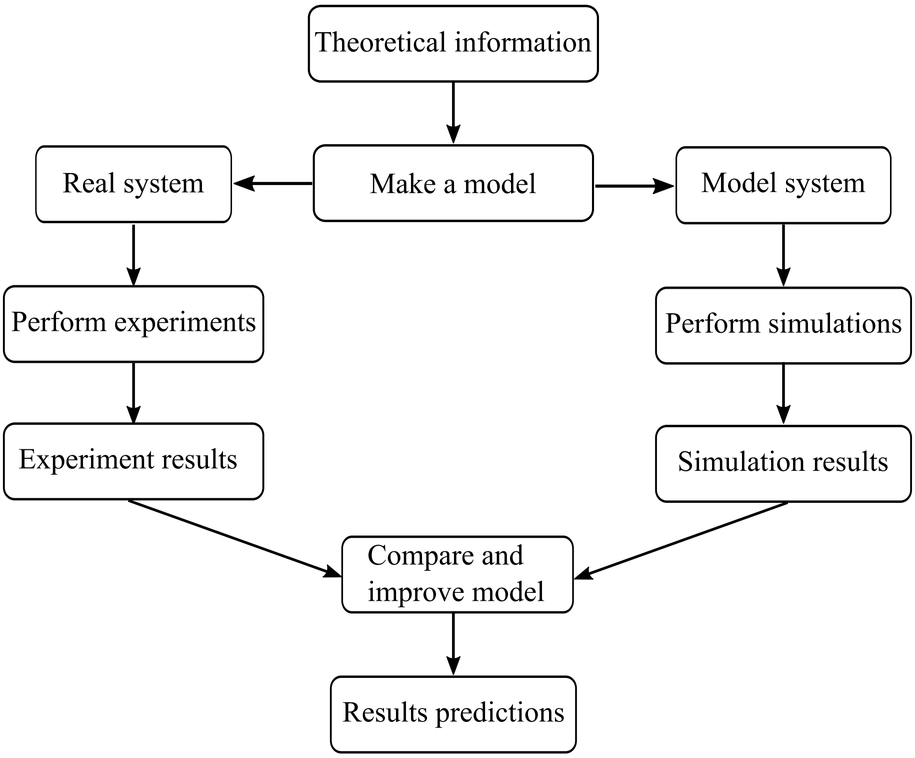

Figure 4.1.: Construction of a computer model to predict the plasmon excitation angle in grating structures with different geometries and materials. (Image from Sarapukdee, P., et al. [155], is licensed under CC BY 4.0.)

3. Parameter Optimization – The model parameters are iteratively adjusted to minimize discrepancies between the simulation and experiment. This process can be repeated with new experimental results to continuously improve accuracy.

The Finite-Difference Time-Domain (FDTD) method is particularly well-suited for simulating grating-based SPR due to its ability to accurately handle complex geometries and material dispersion. By discretizing both space and time, the FDTD method allows for time-domain analysis of electromagnetic field interactions, making it essential for understanding the transient behavior and resonant excitation of surface plasmons.

Additionally, FDTD can readily incorporate the Drude model for metals, enabling precise modeling of the frequency-dependent permittivity of plasmonic materials such as gold and silver. Moreover, the FDTD method can be combined with Perfectly Matched Layer (PML) boundary conditions to simulate an unbounded space, effectively preventing spurious reflections at simulation boundaries. This is critical for accurately predicting the SPR angle and resonance characteristics.

4.2. Structural Overview and Applied Models

The investigated structure, depicted in Fig. 4.2, consists of multiple layers, each designed to support the excitation and propagation of surface plasmon resonance (SPR). The plasmonic layer is formed by a silver (Ag) film embedded within a dielectric SiO_2 environment, which facilitates SPR excitation by providing the necessary interface for plasmonic wave coupling. The silver layer is structured with a periodic grating to enhance coupling efficiency, enabling strong field confinement at the metal-dielectric interface.

The surrounding SiO_2 layers serve multiple purposes. They provide optical confinement, ensuring efficient wave propagation, and help stabilize the refractive index environment, which is crucial for maintaining sensor sensitivity. Beneath these layers, a silicon (Si) substrate acts as a support structure, contributing to overall stability and assisting in light reflection and guiding.

The dielectric medium (air) above the plasmonic layer interacts directly with the propagating surface plasmons. In practical biosensing applications, this layer represents the sensing region, where biomolecular interactions cause shifts in the local refractive index, leading to measurable changes in the SPR signal.

To ensure accurate simulation of SPR in this layered structure, multiple computational techniques are employed. The Drude model is used to describe the dispersive nature of silver, accounting for the frequency-dependent permittivity of metals, which is crucial for accurately capturing plasmonic behavior. To prevent unwanted reflections at the simulation boundaries, Perfectly Matched Layer (PML) boundary conditions are implemented at the top and bottom of the computational domain. These artificial absorbing layers simulate an infinite space, ensuring that outgoing waves do not interfere with the simulated SPR response. Additionally, the periodic nature of the grating structure ne-

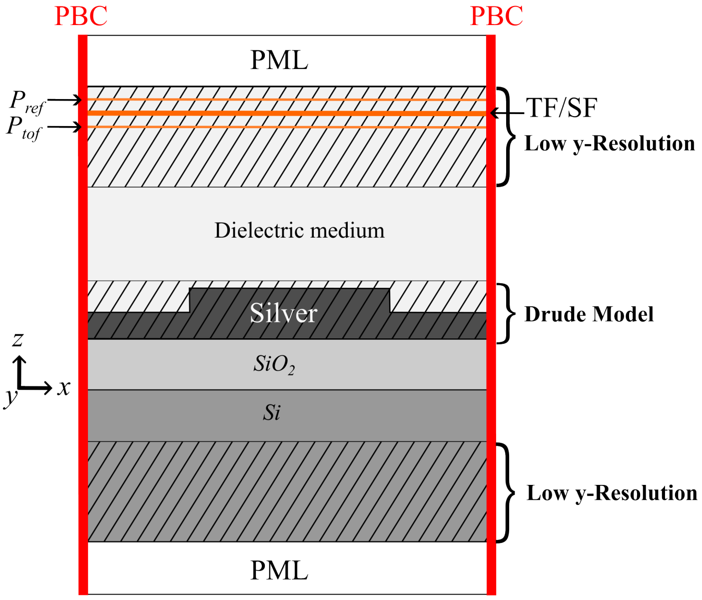

Figure 4.2.: The structure used for validating the chosen model, highlighting the regions with Perfectly Matched Layers (PML), periodic boundary conditions (PBC), and the Total-Field/Scattered-Field (TF/SF) method implementation. The Drude model is applied to the plasmon excitation region to account for the frequency-dependent permittivity of silver, ensuring accurate modeling of the plasmonic response.

cessitates the use of Periodic Boundary Conditions (PBC) along the lateral boundaries. This approach reduces computational cost while ensuring that a single period of the structure is sufficient to model the infinitely repeating grating with correct wave propagation. Furthermore, the Total-Field/Scattered-Field (TF/SF) method is employed to efficiently introduce an incident electromagnetic wave into the simulation. By separating the total electromagnetic field into its incident and scattered components, this method allows precise control over wave excitation and its interaction with the plasmonic grating. Together, these computational techniques enhance the accuracy and reliability of the SPR simulation, ensuring that the model effectively represents real-world plasmonic interactions.

Each of these computational models plays a vital role in ensuring accurate simulation results and realistic representation of SPR behavior. In the following sections, each of these models will be discussed in detail, including their theoretical foundations, implementation techniques, and their impact on the accuracy of the simulations.

4.3. Finite-Difference Time-Domain (FDTD) Modeling

The Finite-Difference Time-Domain (FDTD) method is widely employed due to its ability to handle complex, dispersive materials and geometries. This section introduces the fundamental equations governing FDTD simulations, focusing on the transverse magnetic (TM) mode, and discusses the implementation of essential boundary conditions such as Perfectly Matched Layers (PML) and Periodic Boundary Conditions (PBC). The incorporation of the Drude model for metal dispersion is explored, along with the Total-Field/Scattered-Field (TF/SF) approach for wave excitation. The combination of these techniques ensures accurate modeling of plasmonic wave interactions in periodic grating structures

FDTD Determination Equations

For the derivation of the FDTD determination equations, only the TM mode where the magnetic field is entirely perpendicular to the plane, with the field components $\mathbf{E}_x$, $\mathbf{E}_z$, and $\mathbf{H}_y$ are shown (see Sec. 2.3). The relevant Maxwell equations for the TM-mode simplify to

$$\frac{\partial \mathbf{E}_x}{\partial t} = \frac{1}{\varepsilon}\frac{\partial \mathbf{H}_y}{\partial z} \tag{4.1}$$

$$\frac{\partial \mathbf{E}_z}{\partial t} = -\frac{1}{\varepsilon}\frac{\partial \mathbf{H}_y}{\partial x} \tag{4.2}$$

$$\frac{\partial \mathbf{H}_y}{\partial t} = \frac{1}{\mu}(\frac{\partial \mathbf{E}_z}{\partial x} - \frac{\partial \mathbf{E}_x}{\partial z}). \tag{4.3}$$

These equations are derived from Maxwell's equations, specifically using only Faraday's Law and Ampère's Law. The divergence equations (Gauss's Laws) are not explicitly used because they are automatically satisfied when the curl equations are properly discretized.

When discretizing the equations, the derivatives are formed by dividing the difference between two adjacent points. Consequently, a linear progression of the field value is assumed between these points. However, this assumption is only valid between the points and not at the actual locations of the points. This holds true for both time and local derivatives. Discretization is essential because Maxwell's equations are continuous differential equations that cannot be solved numerically without approximating derivatives using finite differences.

Therefore, the 1960s-developed Yee-Grid is implemented [188], in which magnetic fields are shifted against each other in time and space by a half-step width. This staggered arrangement ensures numerical stability and accuracy by enabling a leapfrog update scheme, where electric and magnetic fields are computed alternately. The half-step offset also minimizes numerical dispersion and improves the convergence of the FDTD algorithm. This is demonstrated in Fig. 4.3.

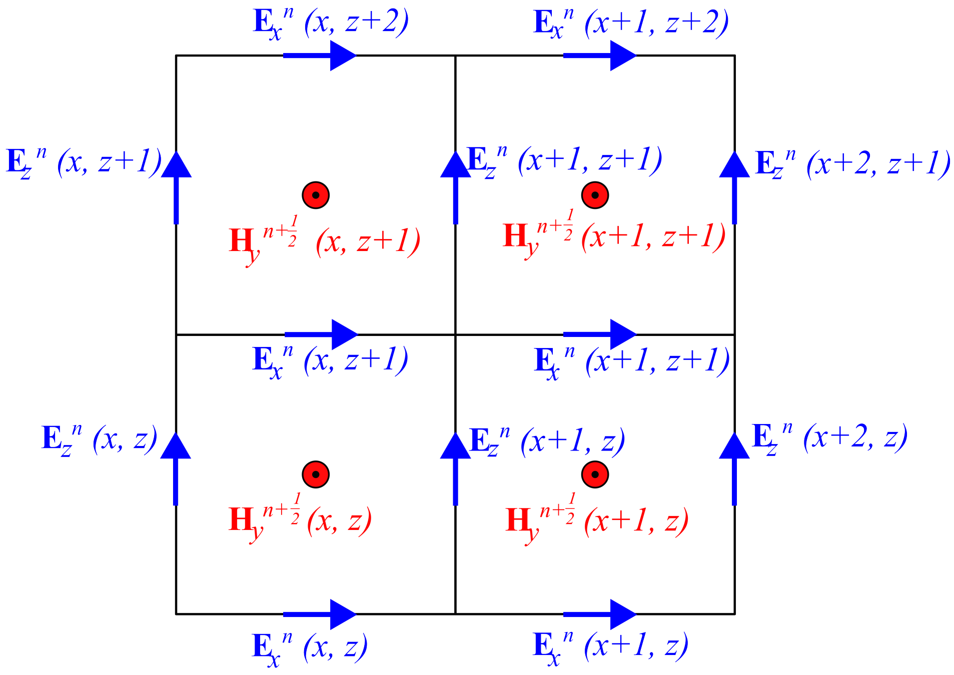

Figure 4.3.: Representation of the Yee-Grid, the electric and magnetic field values are shifted against each other by half a time step.

$$\mathbf{E}_x^{n+1}(x,z) = \mathbf{E}_x^{n}(x,z) + \frac{\triangle t}{\varepsilon}\left(\mathbf{H}_y^{n+1/2}(x,z+1) - \mathbf{H}_y^{n+1/2}(x,z)\right)\frac{1}{\triangle z} \tag{4.4}$$

$$\mathbf{E}_z^{n+1}(x,z) = \mathbf{E}_z^{n}(x,z) - \frac{\triangle t}{\varepsilon}\left(\mathbf{H}_y^{n+1/2}(x+1,z) - \mathbf{H}_y^{n+1/2}(x,z)\right)\frac{1}{\triangle x} \tag{4.5}$$

$$\begin{aligned}\mathbf{H}_y^{n+1/2}(x,z) &= \mathbf{H}_y^{n-1/2}(x,z) \\ &\quad + \frac{\triangle t}{\mu}\left((\mathbf{E}_z^{n}(x,z) - \mathbf{E}_z^{n}(x-1,z))\frac{1}{\triangle x} - (\mathbf{E}_x^{n}(x,z) - \mathbf{E}_x^{n}(x,z-1))\frac{1}{\triangle z}\right)\end{aligned} \tag{4.6}$$

The discretization of the simplified Maxwell equations leads to the determination of TM mode equations. Here, n represents the current time step and $n+1$ the subsequent one. In the simulations conducted for this study,ε and z are location-dependent, whereas $\triangle t, \triangle x$, and μ remain constant across the computational domain. Each new field value in the three-dimensional depends on the value at the same location one step earlier as well as the four surrounding field values that existed half a time earlier. In the simplest case, $\triangle x$ and $\triangle z$ are selected to have the same size, resulting in an orthogonal grid. This has the disadvantage that the local resolution is the same everywhere, requiring unnecessarily intensive computations in regions that do not require discretization at the highest resolution. This global time discrepancy t is thereby calculated via the formula

$$\triangle t = \frac{\triangle x}{c_0} \cdot \frac{1}{\sqrt{\triangle x^2 + \triangle y^2 + \triangle z^2}} \tag{4.7}$$

In a one-time step, the electromagnetic wave in a vacuum cannot propagate further than the maximum distance between two points in space. Due to the slower propagation speed in the dielectric, this case is not critical for stability.

Inclusion of the Drude Model

The Drude model is incorporated to simulate the behavior of electromagnetic fields in thin metal layers. This implementation follows the approach described in [189], utilizing the polarization current density $\mathbf{J}_P$. The electrical susceptibility χ (refer to Sec. 2.2) required for this purpose is first expressed as:

$$\chi = \frac{\omega_p^2}{j\omega(j\omega + \gamma_d)} \tag{4.8}$$

This susceptibility is then rewritten and transformed into the definition formula for the polarization current density:

$$\mathbf{J}_P = j\omega\varepsilon_0\chi\mathbf{E} \tag{4.9}$$

Substituting χ into Eq. (4.9) yields:

$$\mathbf{J}_P = j\omega\varepsilon_0 \frac{\omega_p^2}{j\omega(j\omega + \gamma_d)}\mathbf{E} \tag{4.10}$$

which can be further simplified to:

$$\gamma_d\mathbf{J}_P + j\omega\mathbf{J}_P = \varepsilon_0\omega_p^2\mathbf{E} \tag{4.11}$$

This expression can be transformed into the time domain, resulting in:

$$\gamma_d\mathbf{J}_P + \frac{\delta}{\delta t}\mathbf{J}_P = \varepsilon_0\omega_p^2\mathbf{E} \tag{4.12}$$

To discretize this equation using the finite difference approximation, the derivative is evaluated between two successive time steps n and $n+1$. Consequently, the terms without derivatives must be time-averaged. This leads to the discrete-time difference equation:

$$\gamma_d\frac{\mathbf{J}_P^{n+1} + \mathbf{J}_P^n}{2} + \frac{\mathbf{J}_P^{n+1} - \mathbf{J}_P^n}{\triangle t} = \varepsilon_0\omega_p^2\frac{\mathbf{E}^{n+1} + \mathbf{E}^n}{2}. \tag{4.13}$$

Since only time derivatives are discretized in the Drude model calculations, spatial dependence is not explicitly considered here. This formulation results in the following recursive equation for the polarization current density:

$$\mathbf{J}_P^{n+1} = \frac{\varepsilon_0 \cdot \omega_p^2}{\gamma_d + \frac{2}{\Delta t}} \cdot \left(\mathbf{E}^{n+1} + \mathbf{E}^n\right) + \frac{\frac{2}{\Delta t} - \gamma_d}{\frac{2}{\Delta t} + \gamma_d} \cdot \mathbf{J_P}^n. \tag{4.14}$$

The computed current density is incorporated into Maxwell's equations via the fourth Maxwell equation. The material-dependent factor of permittivity is represented by ε_∞, which takes the value ε_d in dielectric regions where the Drude model is not applied, and corresponds to the Drude parameter in metallic regions. The time-averaged formulation of the current density leads to:

$$\varepsilon_0 \varepsilon_\infty \frac{\mathbf{E}^{n+1} - \mathbf{E}^n}{\Delta t} + \frac{\mathbf{J}^{n+1} + \mathbf{J}^n}{2} = \nabla \times \mathbf{H}^{n+\frac{1}{2}}. \tag{4.15}$$

Solving for $\mathbf{E}^{n+1}$ gives:

$$\mathbf{E}^{n+1} = \mathbf{E}^n + \frac{\triangle t}{\varepsilon_0 \varepsilon_\infty} \left(\nabla \times \mathbf{H}^{n+\frac{1}{2}} - \frac{\mathbf{J}^{n+1} + \mathbf{J}^n}{2}\right). \tag{4.16}$$

By substituting Eq. (4.14) into (4.16), we obtain:

$$\frac{1}{2} \cdot \frac{\varepsilon_0 \cdot \omega_p^2}{\gamma_d + \frac{2}{\Delta t}} \cdot \left(\mathbf{E}^{n+1} + \mathbf{E}^n\right) + \frac{1}{2} \cdot \left(1 + \frac{\frac{2}{\Delta t} - \gamma_d}{\frac{2}{\Delta t} + \gamma_d}\right) \cdot \mathbf{J}_P^n. \tag{4.17}$$

This results in the final governing equation for the electric field incorporating the Drude model:

$$\mathbf{E}^{n+1} = \frac{\varepsilon_0 \varepsilon_\infty - \frac{\Delta t}{2} \cdot \frac{\varepsilon_0 \cdot \omega_p^2}{\gamma_d + \frac{2}{\Delta t}}}{\varepsilon_0 \varepsilon_\infty + \frac{\Delta t}{2} \cdot \frac{\varepsilon_0 \cdot \omega_p^2}{\gamma_d + \frac{2}{\Delta t}}} \cdot \mathbf{E}^n + \frac{\Delta t}{\varepsilon_0 \varepsilon_\infty + \frac{\Delta t}{2} \cdot \frac{\varepsilon_0 \cdot \omega_p^2}{\gamma_d + \frac{2}{\Delta t}}} \cdot (\nabla \times \mathbf{H}) - \frac{\frac{\Delta t}{2} \cdot \left(1 + \frac{\frac{2}{\Delta t} - \gamma_d}{\frac{2}{\Delta t} + \gamma_d}\right)}{\varepsilon_0 \varepsilon_\infty + \frac{\Delta t}{2} \cdot \frac{\varepsilon_0 \cdot \omega_p^2}{\gamma_d + \frac{2}{\Delta t}}} \cdot \mathbf{J}^n. \tag{4.18}$$

The term $\nabla \times \mathbf{H}$ is computed as described in Sec. 4.3, depending on whether $\mathbf{E}_x$ or $\mathbf{E}_y$ is being evaluated. Since the current density is nonzero only in regions where the parameter ω_p is greater than zero, computations related to current density and its associated prefactor are performed only in metallic regions to optimize computational efficiency. The prefactor applied to $\mathbf{E}^n$ is used globally in the governing equations. In non-metallic regions, where $\omega_p = 0$, this prefactor simplifies to one, ensuring consistency in the calculations. When implementing this in the simulation, the old electric field values are stored before updating them. The new field values are then computed using the governing equations, incorporating the prefactor. In metallic regions, the current density from the previous time step is also included in the update process. Finally, Eq. (4.14) is applied in these metallic regions to determine the current density at the current time step.

Perfectly Matched Layer

To ensure accurate simulations within a finite computational domain, it is essential to prevent artificial reflections at the simulation boundaries. The concept of the Perfectly Matched Layer (PML), first introduced in [190], addresses this issue by introducing an absorbing boundary region that minimizes wave reflections. The PML material's permittivity matches that of the surrounding medium, effectively absorbing outgoing waves while minimizing reflections. Additionally, the PML exhibits damping properties that further attenuate the wave amplitude at the domain edges.

To implement the PML, the magnetic field components are decomposed into $\mathbf{H}_{yx}$ and $\mathbf{H}_{yz}$. This introduces an additional field component, which slightly increases computational complexity. Losses in the form of electric conductivity σ and magnetic conductivity $\sigma^\star$ are incorporated into Maxwell's equations for the transverse magnetic (TM) mode, leading to the following formulations:

$$\varepsilon \frac{\partial \mathbf{E}_x}{\partial t} + \sigma \mathbf{E}_x = \frac{\partial \mathbf{H}_y}{\partial z} \tag{4.19}$$

$$\varepsilon \frac{\partial \mathbf{E}_z}{\partial t} + \sigma \mathbf{E}_z = -\frac{\partial \mathbf{H}_y}{\partial x} \tag{4.20}$$

$$\mu \frac{\partial \mathbf{H}_y}{\partial t} + \sigma^\star \mathbf{H}_y = \left(\frac{\partial \mathbf{E}_z}{\partial x} - \frac{\partial \mathbf{E}_x}{\partial z} \right). \tag{4.21}$$

If the following condition holds:

$$\frac{\sigma}{\varepsilon} = \frac{\sigma^\star}{\mu}, \tag{4.22}$$

then the characteristic field impedance within the PML remains identical to that of the surrounding medium, ensuring a seamless transition without reflections.

To formulate the governing equations for field components, the magnetic field and introduced conductivities are separated into x- and z-components, yielding:

$$\frac{\partial \mathbf{E}_x}{\partial t} + \sigma_z \mathbf{E}_x = \frac{1}{\varepsilon}\frac{\partial(\mathbf{H}_{yx} + \mathbf{H}_{yz})}{\partial z} \tag{4.23}$$

$$\frac{\partial \mathbf{E}_z}{\partial t} + \sigma_x \mathbf{E}_z = -\frac{1}{\varepsilon}\frac{\partial(\mathbf{H}_{yx} + \mathbf{H}_{yz})}{\partial x} \tag{4.24}$$

$$\frac{\partial \mathbf{H}_{yx}}{\partial t} + \sigma_x^\star \mathbf{H}_{yx} = -\frac{1}{\mu}\frac{\partial \mathbf{E}_z}{\partial x} \tag{4.25}$$

$$\frac{\partial \mathbf{H}_{yz}}{\partial t} + \sigma_z^\star \mathbf{H}_{yz} = \frac{1}{\mu}\frac{\partial \mathbf{E}_x}{\partial z} \tag{4.26}$$

These equations are normalized by the material constants, assuming $\sigma_x = \sigma_x^\star$ and $\sigma_z = \sigma_z^\star$ as per Eq. (4.22). In the discretized formulation, time-averaging is applied similarly to the Drude model. The resulting update equations for the field components are:

$$\mathbf{E}_x^{n+1}(i,k) = \frac{1 - \frac{\Delta t \cdot \sigma_z}{2}}{1 + \frac{\Delta t \cdot \sigma_z}{2}} \cdot \mathbf{E}_x^n(i,k) + \frac{1}{1 + \frac{\Delta t \cdot \sigma_z}{2}} \cdot \frac{\Delta t}{\varepsilon}\left(\frac{\partial(\mathbf{H}_{yx} + \mathbf{H}_{yz})}{\partial z}\right) \tag{4.27}$$

$$\mathbf{E}_z^{n+1}(i,k) = \frac{1 - \frac{\Delta t \cdot \sigma_x}{2}}{1 + \frac{\Delta t \cdot \sigma_x}{2}} \cdot \mathbf{E}_z^n(i,k) - \frac{1}{1 + \frac{\Delta t \cdot \sigma_x}{2}} \cdot \frac{\Delta t}{\varepsilon}\left(\frac{\partial(\mathbf{H}_{yx} + \mathbf{H}_{yz})}{\partial x}\right) \tag{4.28}$$

$$\mathbf{H}_{yx}^{n+1}(i,k) = \frac{1 - \frac{\Delta t \cdot \sigma_x^\star}{2}}{1 + \frac{\Delta t \cdot \sigma_x^\star}{2}} \cdot \mathbf{H}_{yx}^n(i,k) - \frac{1}{1 + \frac{\Delta t \cdot \sigma_x^\star}{2}} \cdot \frac{\Delta t}{\mu}\left(\frac{\partial \mathbf{E}_z}{\partial x}\right) \tag{4.29}$$

$$\mathbf{H}_{yz}^{n+1}(i,k) = \frac{1 - \frac{\Delta t \cdot \sigma_z^\star}{2}}{1 + \frac{\Delta t \cdot \sigma_z^\star}{2}} \cdot \mathbf{H}_{yz}^n(i,k) + \frac{1}{1 + \frac{\Delta t \cdot \sigma_z^\star}{2}} \cdot \frac{\Delta t}{\mu}\left(\frac{\partial \mathbf{E}_x}{\partial z}\right) \tag{4.30}$$

For periodic boundary conditions, only σ_z is required, simplifying the system. The equations described in Sec. 4.3 are incorporated by multiplying the described prefactors by the PML prefactors.

Periodic Boundary Conditions

Periodic boundary conditions (PBCs) are essential for simulating lattice-periodic structures. By imposing PBCs, it is sufficient to model only a single unit cell of length equal to the lattice period, thereby capturing the behavior of an infinitely periodic structure. However, this assumption does not hold at the boundary regions of periodic lattices, where discontinuities may arise. In the absence of PBCs, simulating a large number of lattice periods would be necessary to accurately represent the structure's behavior. Additionally, PML is not required at periodic edges, as reflections are naturally avoided.

To implement periodic boundary conditions, field values at the simulation domain's edges, which would normally fall outside the computational area, are retrieved from the corresponding values at the opposite edge. This ensures continuity and maintains periodicity. When simulating a plane wave with a variable incidence angle, it is necessary to account for the phase difference between corresponding points at opposite edges. This is achieved by introducing a phase correction factor:

$$\exp(-i \cdot \mathbf{k}_x \cdot x) \tag{4.31}$$

where $\mathbf{k}_x$ is the wave vector component of the incident wave along the displacement direction, and x represents the distance between the periodic edges. This adjustment ensures that wave propagation is correctly modeled across the periodic boundaries.

When implementing PBCs, the computation inherently handles complex numbers. However, if using a programming language that lacks support for complex arithmetic, an alternative approach known as the sine-cosine method [191] can be used. In this method, the real and imaginary components of the field are represented separately in two distinct computational domains. Consequently, the number of arithmetic operations per time step is doubled, increasing computational overhead.

It is important to note that phase compensation can only be accurately applied to a single wavelength. As a result, the broadband nature of the Finite-Difference Time-Domain (FDTD) method is lost when using periodic boundary conditions, limiting its applicability in multi-wavelength simulations.

Total Field/Scattered Field Method

The Total Field/Scattered Field (TF/SF) method is employed to introduce incident waves into the simulation domain. This method divides the computational domain into two distinct regions: the Total Field region, where both the incident and scattered fields are present, and the Scattered Field region, which contains only the fields scattered by the structure under investigation. The boundary between these two regions serves as a directed source, which can take on various forms. However, in a rectangular simulation domain with periodic boundary conditions, it is practical to orient this boundary orthogonally to the periodic edges.

For the TF/SF division to be effective, reflections from the Scattered Field region back into the Total Field region must be minimized. This can be achieved by incorporating a Perfectly Matched Layer (PML) at the boundaries of the Scattered Field region. In Finite-Difference Time-Domain (FDTD) simulations, fields can be excited using either a hard or a soft source. A hard source directly imposes the excitation field at specified points, which leads to unwanted reflections. In contrast, a soft source superimposes the excitation field onto the existing field, preventing reflections at the source location.

The excitation occurs just beneath the TF/SF boundary. When computing the field values in the Scattered Field region above this boundary, the contribution from the additional excitation must be subtracted. For the 2D simulations performed in this study, where the transverse magnetic (TM) mode with field components $\mathbf{E}_x$, $\mathbf{E}_z$, and $\mathbf{H}_y$ is considered, the excitation field $\mathbf{E}_{in}$ is softly added to the $\mathbf{E}_x$ field values along the TF/SF boundary. Half a time step later, when updating the $\mathbf{H}_y$ field above the boundary, the added contribution is subtracted using the equation:

$$\mathbf{H}_y^{t+\frac{\Delta t}{2}}(x,z) = \mathbf{H}_y^{t+\frac{\Delta t}{2}}(x,z) - \sqrt{\frac{\varepsilon}{\mu}} \cdot \mathbf{E}_{x,in}^{t+\frac{\Delta t}{2}+\frac{\sqrt{\varepsilon}\Delta z}{2c_0}}(x,z) \tag{4.32}$$

The temporal and spatial discretization of the Yee grid (see Sec. 4.3) ensures proper alignment of the excitation points. Each grid point below the TF/SF boundary is initialized with the excitation field. If the wave is introduced using a complex function, such as in a computer simulation, applying a filter function at the onset helps to gradually increase the field values. Without this filtering, high-frequency disturbances may arise, leading to prolonged transient effects and increased settling times.

In the simulations conducted for this study, the incident excitation field $\mathbf{E}_{in}$ is modeled as a plane wave impinging on the simulation domain at an angle θ. In 3D simulations, the azimuthal angle ϕ can also be adjusted to control the wave's orientation within the computational space.

4.4. Computer Model Verification

To validate this approach, a convergence analysis is conducted, followed by a comparison of numerical results with experimental data. Initially, the structure and numerical setup of the simulations are presented. The model verification then proceeds in two steps. The first step involves performing convergence analyses to examine how changes in spatial discretization in the x-direction affect the simulation results. The second step is a plausibility check, where simulation results are compared with measurement data.

Simulation Conditions

The resolution remains uniform in the x-direction. However, in the y-direction, a region with lower resolution is introduced, extending to the PML. This approach is particularly crucial for analyzing long-range modes, as their fields extend significantly into the dielectric. By utilizing a thick dielectric layer with reduced resolution, computational efficiency is significantly improved without compromising accuracy.

To determine the reflectivity, the power density is evaluated just above and below the TF/SF boundary. Since the electric (**E**) and magnetic (**H**) fields are both temporally and spatially offset, this displacement must be considered in calculations. The power density is computed at each time step and integrated along the x-axis to obtain the total power. Once the simulation reaches a steady state, the average power over a designated time period is calculated. Using the obtained average power values, the reflectivity is determined as follows:

$$R = \frac{P_{\text{ref}}}{P_{\text{ges}} - P_{\text{ref}}} \tag{4.33}$$

where P_{ref} represents the average power above the TF/SF boundary, and P_{ges} denotes the total average power below the TF/SF boundary over the same time period. When periodic boundary conditions are applied, only the power component perpendicular to these boundaries is considered, as only this component effectively radiates outward. To ensure accuracy, power values are measured a few points above and below the TF/SF boundary, assuming that the wave propagation direction remains consistent in both cases, preserving the ratio of total powers.

The steady-state condition is also defined in terms of power stability. Specifically, the average power of the most recent time interval is compared with that of the preceding interval at predefined time steps. This criterion ensures that the simulation has reached equilibrium before extracting final reflectivity values.

Convergence Analysis

To evaluate the impact of resolution in the x-direction, reflectance spectra are computed for different discretization widths Δx, as illustrated in Fig. 4.4. It is observed that as resolution increases, the dip between nine and ten degrees shifts to the right. This shift occurs due to reduced discretization errors in the grid period at finer resolutions. The selected example represents a worst-case scenario with the highest discretization error. While slight variations in the shape and depth of the dips are observed between resolutions of 1 nm and 2 nm, the differences are minimal. Considering that computational time increases cubically with finer resolutions in both spatial directions, owing to the required reduction in time step size, a resolution of 2 nm is adopted for this study.

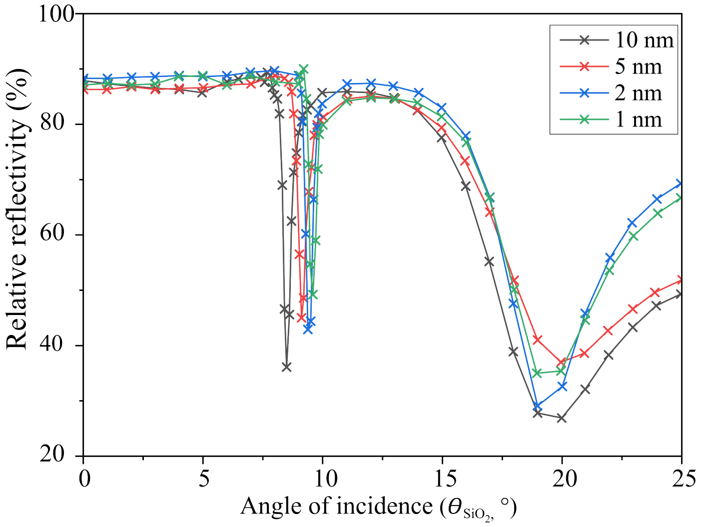

Figure 4.4.: Simulation results demonstrating the impact of varying the resolution in the x-direction. The y-direction resolution is set at 2 nm, the dielectric layer thickness is 1100 nm, and the PML width is 50 points. The results indicate that resolution significantly influences accuracy.

The impact of resolution variation in the y-direction is shown in Fig. 4.5. Increasing the resolution from 2 nm to 1 nm results in only minor changes in dip depths, while the overall trends remain nearly identical. However, significant deviations appear at lower resolutions, where dip depths vary considerably. This discrepancy arises because, at a

5 nm resolution, the silver layer is represented by only six points, while at a 10 nm resolution, it is represented by only three points.

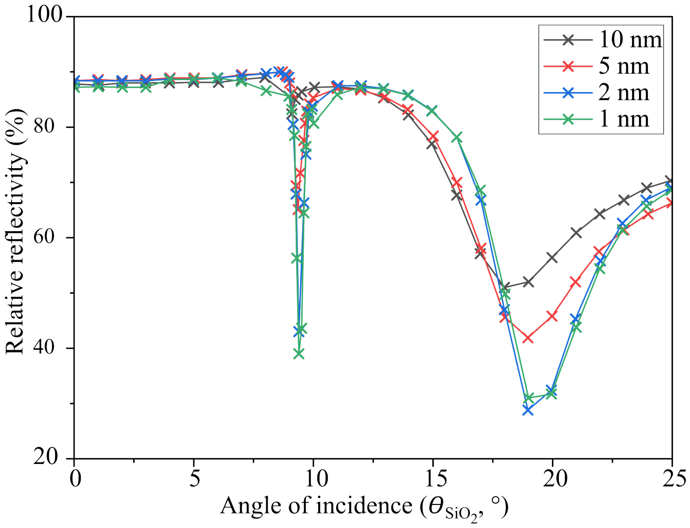

Figure 4.5.: Simulation results illustrating the effect of varying the resolution in the y-direction. The x-direction resolution is maintained at 2 nm, the dielectric layer thickness is 1100 nm, and the PML width is 50 points.

Fig. 4.6 investigates the influence of dielectric layer thickness on the reflectance spectrum. While the dip angle remains unchanged, minor variations in dip depth are observed. Since these variations are smaller than the deviations introduced by the 2 nm resolution limitation, a dielectric width of 1100 nm is chosen as the optimal parameter for this study.

Model Verification with Experiment Results

To ensure the accuracy of the computational model beyond convergence analysis, verification is performed by comparing simulation results with experimental measurement data. A plausibility check is conducted by analyzing the simulated reflectance spectrum against measured results. Fig. 4.7b illustrates a fabricated grating periodic structure for which measurement data is available.

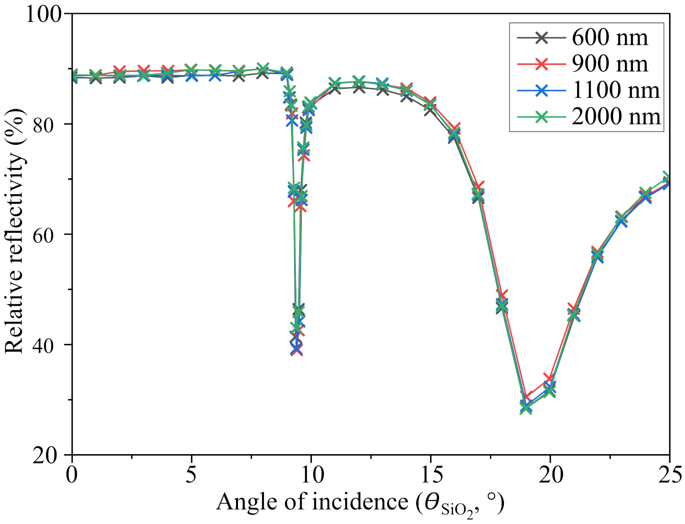

Figure 4.6.: Simulation results depicting the influence of dielectric layer thickness variation. The x-direction resolution is set to 2 nm, and the PML width is 50 points.

The material properties were carefully implemented in the model. Specifically, the nickel layer was assigned a dielectric constant of -11.4 at a wavelength of 632.8 nm. For silver, an initial permittivity value of -19 was used, which was then adjusted to optimize the fit between the simulation and experimental results. As shown in Fig. 4.7, the reflectance spectrum exhibits two distinct dips: the first at 16° and the second at 30.2°. These dips correspond to the diffraction orders of the grating structure.

Additionally, the simulation accurately captures the relative reflectance signal dip. The ratio of penetration depths between the two dips in both the simulation and experiment is also found to be comparable. This agreement indicates that the simulated values reliably approximate practical experimental results, confirming the model's validity.

4.5. Simulation of Measurement Scenarios

A computational model for simulating grating structures was developed and subsequently validated through comparison with experimental data. After optimizing the model parameters to achieve close agreement with experimental observations, it was utilized to

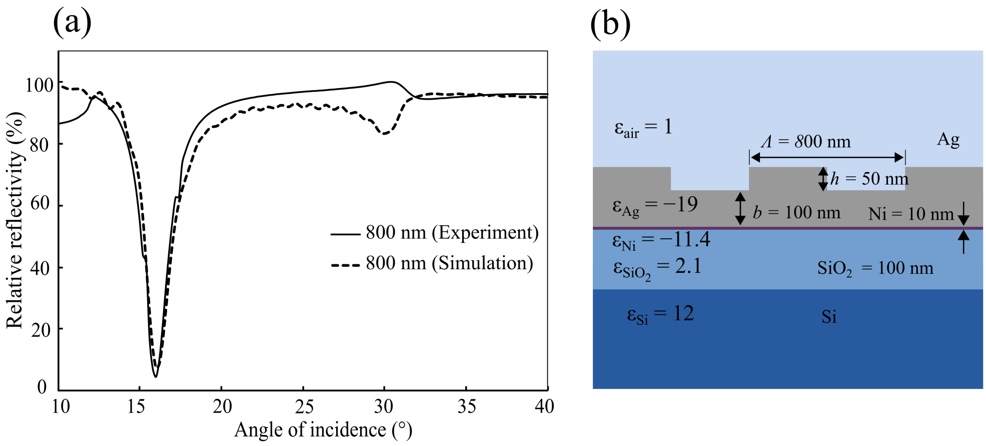

Figure 4.7.: Comparison of simulation and experimental result for grating period of 800 nm. (a) Comparison between the simulated reflectance spectrum and experimental results. (b) Schematic of the grating structure used in the simulation, with material layers from top to bottom: air ($\varepsilon_{air} = 1$), silver (Ag, $\varepsilon_{Ag} = -19$, $h = 50nm$), nickel (Ni, $\varepsilon_{Ni} = -11.4$, 10 nm), silicon oxide (SiO$_2$, $\varepsilon_{SiO_2} = 2.1$, 100 nm), and silicon (Si, $\varepsilon_{Si} = 12$).

predict the grating's behavior under ideal, noise-free conditions. This validated model was then applied to determine the refractive index of an unknown sample by analyzing the simulated and measured diffraction patterns.

4.5.1. Refractive Index Calculation

Based on the coefficient and refractive index (RI) of materials, the simulation model was modified to fit the experimental data. After modification, the model was used for the proposed sensor to analyze a sample over a grating structure with different refractive index values. Using the improved computer model from Sec. 4.4, the RI of an analyte layer over the grating structure was calculated. First, the grating was adjusted in accordance with the geometry depicted in Fig. 4.8. The computer model was then simulated by varying the RI value of the analyte layer from 1.0 to 1.7, which corresponds to the biomolecules typically employed in biomedical applications, as shown in Tab. 4.1. The obtained plasmon excitation angle values were plotted against the RI values after running the model. This graph can be used to calculate the RI or excitation angle for plasmons in

Table 4.1.: List of approximate values for refractive index of biological samples. (Table from Sarapukdee, P., et al. [82], licensed under CC BY 4.0.)

Medium	Refractive index	Reference
Water, PBS	1.33, 1.332	[192]
Extra, Intra -cellular fluid	1.34-1.35, 1.35-1.36	[193]
Proteins, Lipids, DNA	1.40, 1.42, 1.44	[194]
Skin, Muscle, Adipose	1.36, 1.39, 1.46	[195]
Blood plasma	1.335	[196]
Hemoglobin	1.354	[197]

future experiments. Fig. 4.9 depicts the resulting simulation signals of the analyte layer with RI. The RI values ranged from 1.0 to 1.7 with a 0.1 step. The results demonstrate that the analyte layer with an RI value greater than 1.2 exhibited a weak dip signal but no narrow-band signal. Consequently, it was quite challenging to analyze the data from RI values 1.2 to 1.7. While the RI values of 1.0 and 1.1 indicated a distinct and significant dip signal. After that, the simulation results plotted the relationship between a plasmon excitation angle and a RI is shown in Fig. 4.10. Moreover, the straight-line of the simulation results showed the equation of $y = 19.048x - 1.4643$ with yielded a coefficient of determination $R^2 = 0.9554$. With this equation, the RI can be calculated from the measured angle according to this equation:

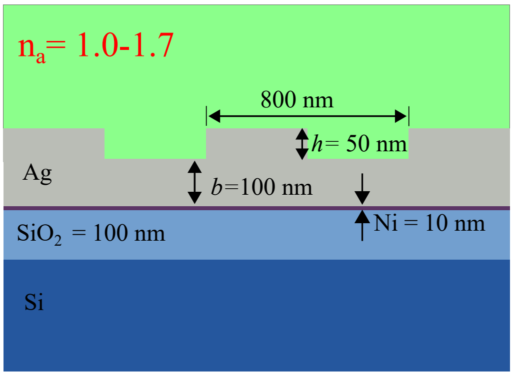

Figure 4.8.: Using the computer model to calculate the refractive index of 1.0-1.7.

$$x = \frac{y + 1.4643}{19.048} \tag{4.34}$$

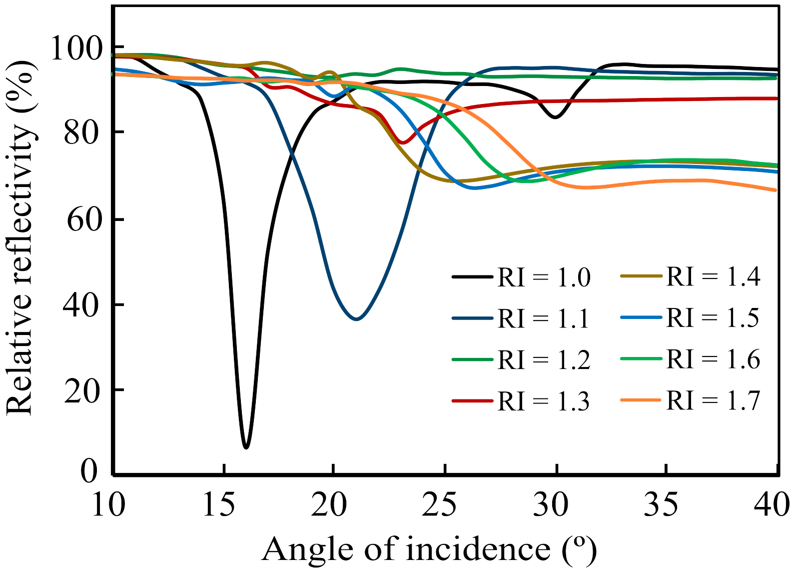

Figure 4.9.: The relative reflection results(a-h) of the samples with the refractive index of 1.0-1.7 are calculated using the computer model.

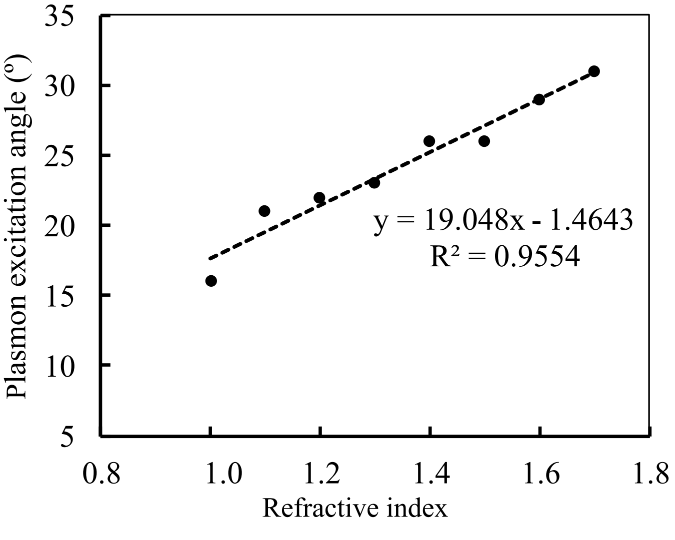

Figure 4.10.: The relation of the plasmon excitation and refractive index of 1.0-1.7 was calculated using the computer model.

where x is a RI and y is a plasmon excitation angle.

4.5.2. Sensitivity of the Grating-Based SPR Sensors

In Sec. 4.5.1, the computer model was executed to predict the plasmon excitation angle of the analysts in the refractive index range of 1.0 to 1.7, with a step size of 0.1. In this experiment, we used the refractive index range of 1.32 to 1.46, which is the range of refractive indices (RIs) that have been reported for biological samples in theoretical and experimental studies in Tab. 4.1, in increments of 0.05 to assess the high resolution of sensor detection. Fig. 4.11(a) demonstrates the outcomes. The spectrum profiles demonstrate that three dip angles existed. This structure refers a first, second and third-diffraction order grating. According to Eq. (2.67), θ varies with refractive index n_a, and thus the grating configuration can be used as a refractive index sensor. The sensor's sensitivity S is defined as Eq. (3.1). Fig. 4.11(b) shows that the proposed sensor can be a potential candidate for sensing the analyte of refractive indexes ranging from 1.32 to 1.46. SPR response of the sensor with various refractive indexes of the analysts is shown in Fig. 4.11(a). The first range of the refractive index is varying from 1.32 to 1.37. It found that dip strength is about $30 - 70\%$, the plasmon excitation angle as a function of the refractive index is shown as a positive trend for $+1$ diffraction order but shown a negative trend for the -2 diffraction order, as shown in Fig. 4.11(b), and the sensitivity of the proposed sensor is 22.86°/RIU and 35.43°/RIU for $+1$ and -2 diffraction order, respectively.

Fig. 4.11(a) shows the second range of the refractive index, which was investigated from 1.37 to 1.46. Unlike the study conducted on the refractive index range of 1.32 to 1.37, the result only shows the presence of the -2 diffraction order and the $+3$ diffraction order. The results show the larger sensitivity of sensor 35.58°/RIU and 128.85°/RIU for -2 and $+3$ diffraction order, respectively. Moreover, the outcomes were compared to those of other surface plasmon sensor experiments. Comparatively to the other studies in Tab. 4.2, the outcomes were relatively low. Therefore, it can be concluded that in order to improve the computer model, additional experimental data on samples in solution form with different RIs is required.

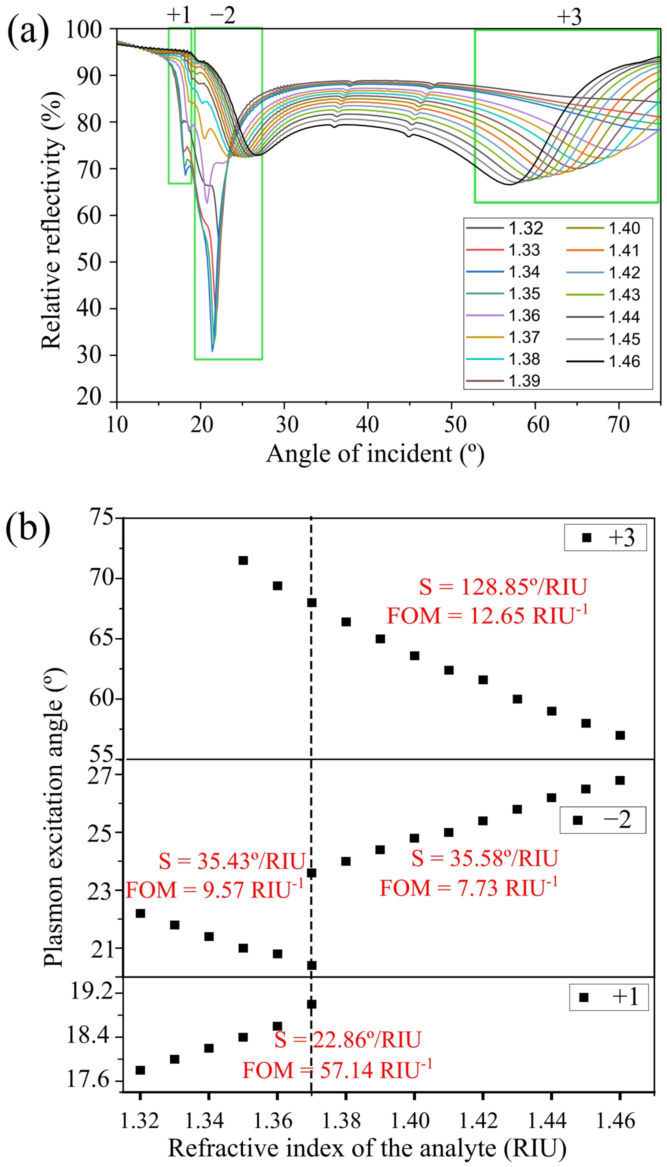

Figure 4.11.: (a)Relative reflectivity profile of the grating structures with various refractive index of 1.32-1.46 and the plasmon excitation angles as a function of refractive indexes for first order, second order, and third order of diffraction. (Adapted from Sarapukdee, P., et al. [82], is licensed under CC BY 4.0.)

4.5.3. Simulation of alternative grating structures

The experimental investigation of the influence of different grating shapes on plasmon excitation angles was conducted. Six distinct grating structures were designed based on established fabrication techniques and their constraints, each representing a unique shape.

Table 4.2.: Comparison of sensor performance with other previous works. (Table from Sarapukdee, P., et al. [82], is licensed under CC BY 4.0.)

Structure configuration	Methods	Coating	Wavelength (nm)	Sensitivity (°/RIU)	References
Prism	Sim.	Ag-Au	632.8	54.84	[198]
Prism	Sim.	Graphene-hybrid	633	56.34-60.62	[199]
Prism with air gap	Sim.	Ag-graphene	633	61.54-68.03	[200]
Grating integrated prism	Sim.	Ag-graphene	633	220.67	[201]
Bimetallic grating	Sim.	Al-Au	900	187.2	[202]
Bimetallic grating	Sim.	Ag-Au	920	346	[203]
2D bimetallic alloy grating	Sim.	Ag, Au, Cu, Pd, Pt	700	152-161	[204]
Grating with phase-interrogation	Exp.	Au	633	300	[123]
Multilayers grating	Sim.	Al-Au grating	900	279.6	[205]
Grating	Exp./Sim.	Ag	632.8	22.86-128.85	This work

Note: Exp. = Experiment, Sim. = Simulation

The shapes included, rectangular, sinusoidal, triangular, rectangular with rounded edges, blazed grating on the left side, and blazed grating on the right side.

All grating shapes are depicted in Fig. 4.12. To isolate the effect of grating profile on plasmon excitation, several parameters were maintained constant across all shapes. The grating period, grating height, thickness of the grating elements, and material properties were kept consistent, enabling a direct comparison of the impact of the grating structure shape on the excitation angle while minimizing confounding variables.

The range of incident angles was varied from 10° to 40°, encompassing a broad spectrum of potential excitation scenarios. By maintaining a constant wavelength, the scattered light intensity was measured and analyzed as a function of the incident angle for each grating shape. This comprehensive approach enabled the determination of the plasmon excitation angle associated with each structure, with results presented in Fig. 4.13.

The performance of each grating shape is summarized in Tab. 4.3. The assessment of coupling efficiency (CE) involved computations based on signal attributes, specifically involving the interrelation of the full-width at half-maximum (FWHM) of the excitation angle peak and the relative reflectivity R_{rel}. The CE was quantified using the Eq. (3.5).

This formulation underscores that diminished spectral broadening and reduced reflectivity yield an augmented portion of incoming light being effectively channeled into the

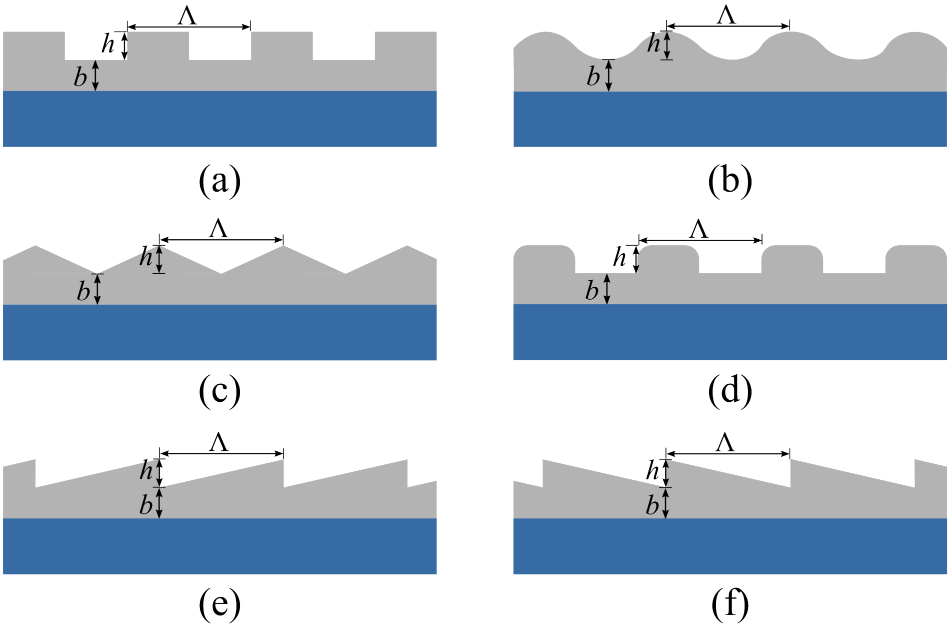

Figure 4.12.: Six different shapes of grating structures analyzed: (a) Rectangular, (b) Sinusoidal, (c) Isosceles triangular, (d) Rectangular with rounded edges, (e) Blazed grating on the right side, (f) Blazed grating on the left side.

grating structure, culminating in heightened overall efficiency.

Table 4.3.: Results of plasmon excitation angle and relative reflection of six different grating structures.

Grating Structure	**Excitation Angle (°)**	**Reflectivity**	**FWHM (°)**	**CE**
(a) Rectangular	16.0	0.073	1.80	0.52
(b) Sinusoidal	13.6	0.363	0.84	0.76
(c) Isosceles triangular	13.6	0.414	0.76	0.77
(d) Rectangular with round edge	15.4	0.195	1.22	0.66
(e) Blazed (right)	14.2, 32.4	0.677, 0.575	0.85, 1.45	0.38, 0.37
(f) Blazed (left)	15.0, 31.4	0.460, 0.369	0.99, 1.56	0.43, 0.41

Ensuring consistency in crucial parameters such as period size, height, and thickness across all gratings, the grating profile significantly influences plasmon-related characteristics such as excitation angles, reflectivity, FWHM, coupling efficiency, and sensitivity. The results show a variety of excitation angles from 13.6° to 16.0°, each with different reflectance properties. Notably, the blazed grating shapes (e, f) displayed a secondary dip in the excitation angle, adding complexity to the interplay between grating structure and plasmonic responses.

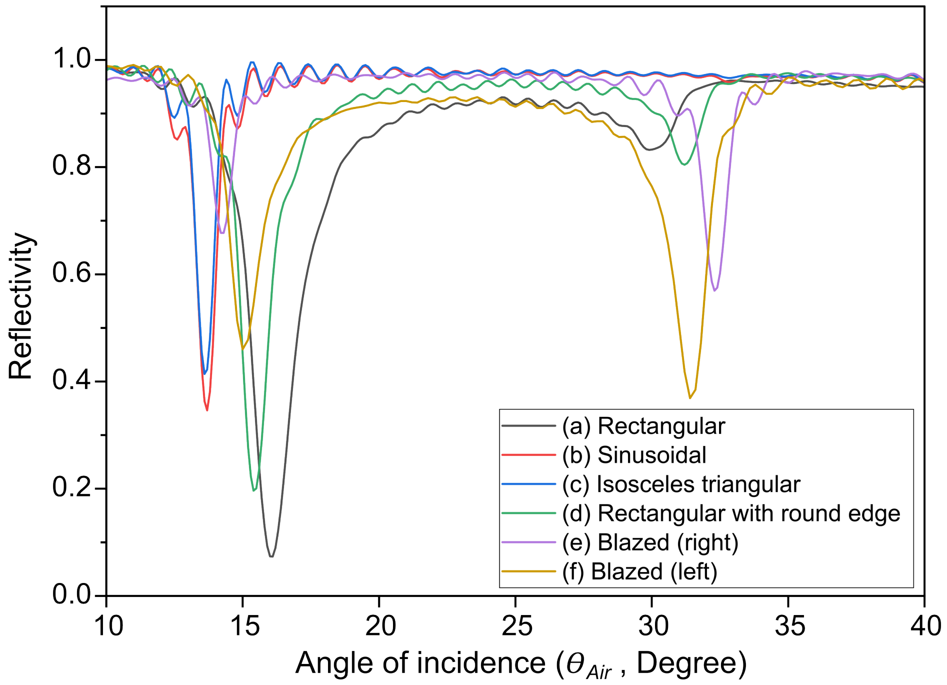

Figure 4.13.: Simulation of various structures with equal periodicity under variation of the grating shapes. The considerable effect of grating geometry on performance is apparent.

The basic rectangular form (a) had the greatest reduction in reflection at 0.073, demonstrating the interplay between grating shape and plasmonic resonances. Surprisingly, the isosceles triangle shape had the highest coupling efficiency at 0.77, closely followed by the sinusoidal shape at 0.76. These findings emphasize the critical relevance of selecting the right grating structure shape to strategically improve plasmonic coupling efficiency, particularly for specialized applications.

4.5.4. Simulation of Inverted Grating Structure

In this experiment, the grating was designed with a glass substrate and inverted. The manufacturing parameters must be verified beforehand. Hence, the developed and improved model, and the permittivity of material was set in the geometry, as shown in Fig. 4.14 with the following parameter range: the grating period of 500-800 nm, the grating size of 250-400 nm, the grating height of 20-40 nm, and the silver layer on top of 50 nm.

In the same manner as Sec. 4.4, the permittivity of materials was set in the model. For instance, the permittivity of glass was set to 2.1, that of silver to −19, and that of air to 1. The optimal structure was determined by a plasmon excitation angle ranging from 10° to 40°, in accordance with the suggested angle based on the measuring station and sensor limitations (see Sec. 6.2).

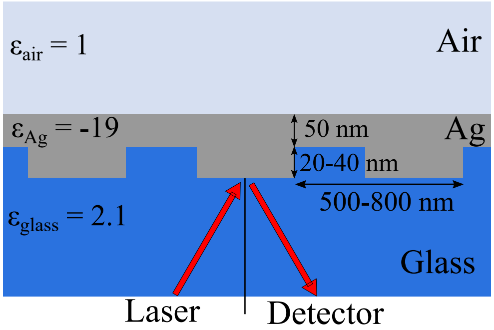

Figure 4.14.: Sketch of inverted geometry for the computer model, with the grating period range of 500-800 nm, the grating height range of 20-40 nm, and the silver layer on top thickness of 50 nm.

The simulation results, which include a relative reflection profile and a plasmon excitation angle, are displayed in Fig. 4.15 (the whole set of results is available in Appendix A.3). When grating periods of 600, 700, and 800 nm are contrasted with those of the 500 nm grating structure, the latter exhibits a higher coupling efficiency.

In order to fully clarify the structural characteristics, Fig. 4.16(a) shows the reflection profile and plasmon excitation angles for a 500 nm grating period. The plasmon excitation angles, spanning from 10 to 70 degrees, are explicated in detail. Not only do these modeling results provide good candidates for the upcoming fabrication efforts, but they also highlight how important careful nanostructuring is in order to achieve sensitive and repeatable devices. Fig. 4.16(b) subsequently presents the coupling efficiency (CE). This illustration discloses two configurations that manifest optimal outcomes: one characterized by a silver base thickness b of 50 nm and a height h of 30 nm, and another featuring $b = 50$ nm and $h = 20$ nm. These configurations evince commendable coupling

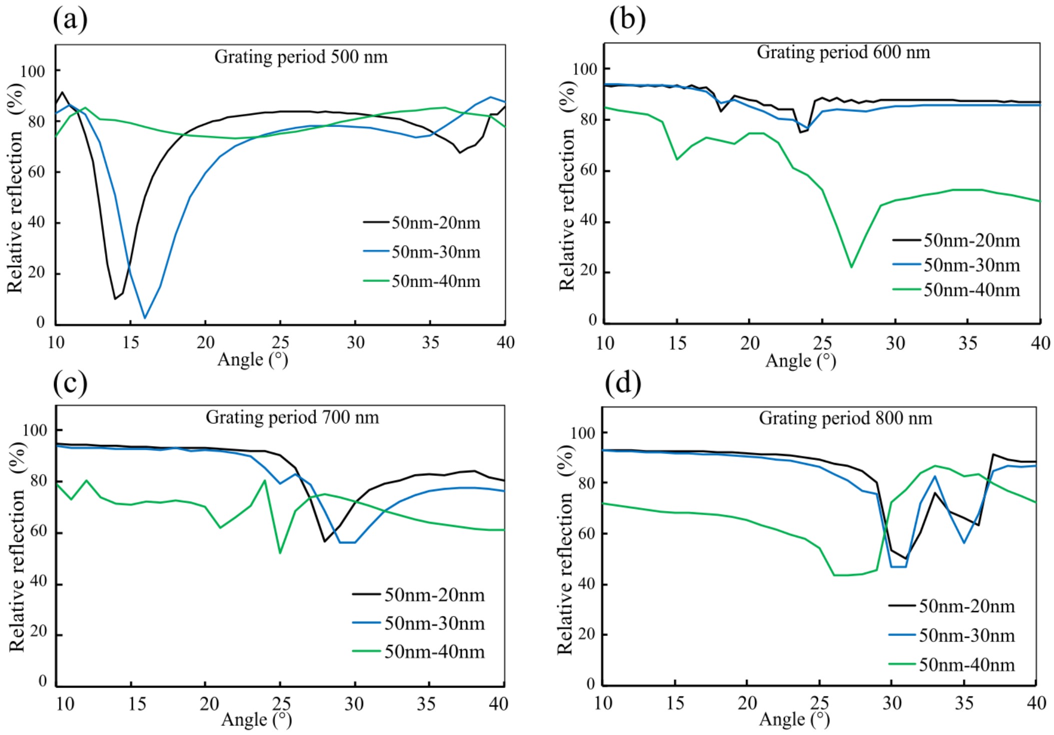

Figure 4.15.: Simulation results of the inverted grating model, (a)the grating period of 500 nm with the grating height of 20 nm and 30 nm presents the optimum dip signal at 9° and 16°. (b)The grating period of 600 nm with the grating height of 40 nm presents the dip angle at 26°. (c, d) The 700 nm and 800 nm gating periods do not show a significantly strong dip signal.

efficiency, thereby delineating pivotal benchmarks for informed decision-making in design considerations.

Under close inspection, the excellent coupling efficiency present in both configurations is revealed in the complex interplay between fabrication and performance details. Nevertheless, after careful analysis, the arrangement with b = 50 nm and h = 30 nm is the best option. This specific structural combination achieves an excellent balance, delivering outstanding performance attributes and at the same time enabling a relatively simple production procedure. It is hence the best choice for the intended inverted grating design concept.

Notably, despite variations in the refractive index, the dips remained fairly consistent. This can be attributed to the fact that SPR is likely being excited at the silver-substrate

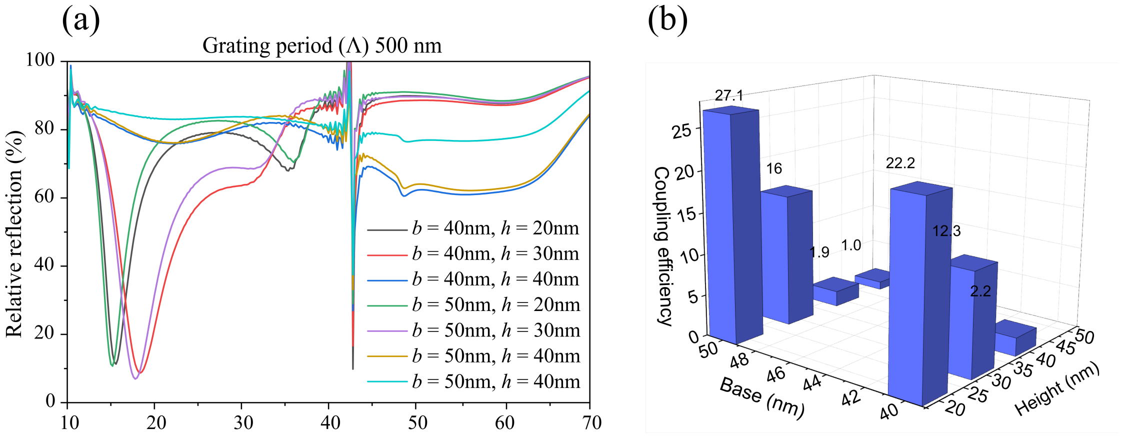

Figure 4.16.: (a) Example simulation results for the inverted grating model with grating periodicity = 500 nm and changing grating heights of 20 nm, 30 nm, and 40 nm. The relative reflection decreases dramatically as the height exceeds 30 nm. (b) With a base thickness of 50 nm and a grating height of 20 nm, the greatest coupling efficiency is 27.1. (Image from Sarapukdee, P., et al. [155], is licensed under CC BY 4.0.)

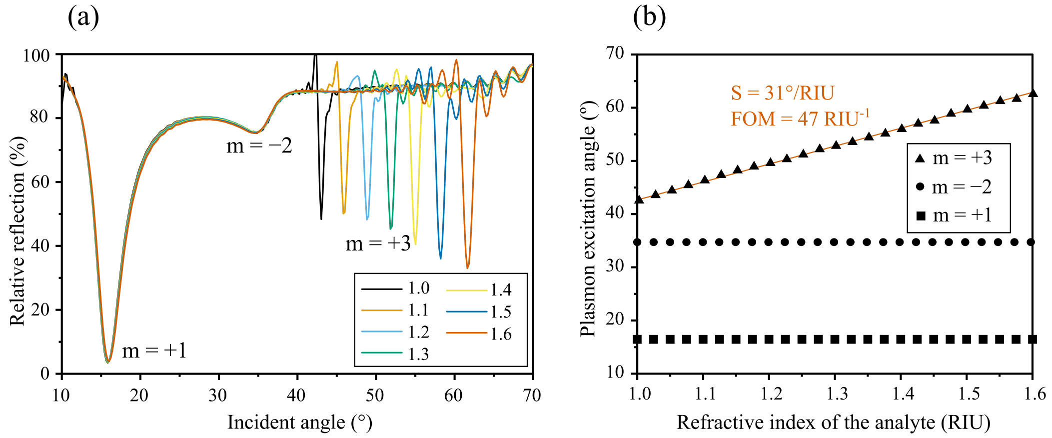

Figure 4.17.: The impact of the sample's refractive index on plasmon excitation highlights the sensitivity of inverted structures in first ($m = +1$), second ($m = -2$), and third ($m = +3$) order coupling. (b) The graph shows the relationship between plasmon excitation angle and refractive index units: the first and second-order angles show minimal variation with changes in refractive index, while the third-order (S = 31°/RIU, FOM = 47 RIU^{-1}) demonstrates noticeable shifts. (Image from Sarapukdee, P., et al. [155], is licensed under CC BY 4.0.)

interface, with the excitation angle remaining unaffected by changes in the analyte layer. In contrast, the +3 order SPR dip exhibited a more dynamic response, highly sensitive to changes in the refractive index. It demonstrated a sensitivity of 31°/RIU, with a figure of merit (FOM) of 47 RIU^{-1}. The shift in the excitation angle directly correlates with changes in the surrounding medium, indicating its potential as an effective tool for tracking alterations in analyte properties.

CHAPTER 5

Fabrication of the Grating-Based SPR

This chapter presents the development and fabrication processes of grating structures optimized for Surface Plasmon Resonance (SPR) sensors. Three primary structures were fabricated: conventional grating[10], two-dimensions grating[11], grating integrated with polydimethylsiloxane (PDMS) microchannels[12], and an innovative inverted grating on a glass substrate for backside illumination[13]. These structures were tailored for CMOS compatibility and enhanced optical properties, utilizing planar technology and silicon

---

[10] Portions of this section have been previously published as: P. Sarapukdee, C. Spenner, D. Schulz, and S. Palzer, "Optimizing stability and performance of silver-based grating structures for surface plasmon resonance sensors," *Sensors*, vol. 23, no. 15, 2023. DOI: 10.3390/s23156743.

[11] Portions of this section have been previously published as: P. Sarapukdee, D. Schulz, and S. Palzer, "Grating structures for silver-based surface plasmon resonance sensors with adjustable excitation angle," *Sensors*, vol. 24, no. 14, 2024. DOI: 10.3390/s24144538.

[12] Portions of this section have been previously published as: P. Sarapukdee, D. Schulz, and S. Palzer, "Silver-based plasmonic grating with PDMS microchannel for biological sensors," *Proceedings*, vol. 97, no. 1, 2024. DOI: 10.3390/proceedings2024097192.

[13] Portions of this section have been previously published as: P. Sarapukdee, D. Schulz, and S. Palzer, "Concept, simulation, and fabrication of inverted grating structures for surface plasmon resonance sensors," *Journal of Sensors and Sensor Systems*, vol. 13, no. 2, pp. 157–166, 2024. DOI: 10.5194/jsss-13-157-2024.

or glass substrates. The fabrication process involved advanced techniques such as electron beam lithography, thermal evaporation, and reactive ion etching. Nickel adhesive layers were implemented to enhance the adhesion and uniformity of silver deposition. Dose testing optimized electron beam parameters, ensuring precise patterning with minimal defects. The fabrication methods were validated through SEM imaging, confirming uniformity, sharp edge structures, and reproducibility. Additionally, the PDMS microchannel integration enables applications with liquid analytes, and the inverted grating structure facilitates backside measurements, demonstrating versatility in sensor configurations. This work highlights the potential of grating-based SPR structures for label-free biomolecular detection, providing a robust foundation for experimental applications and future optimizations.

5.1. Construction of the Grating Structures

This section details the construction of grating structures, categorized into three primary configurations, as illustrated in Fig. 5.1: (i) conventional grating structures, (ii) grating structures integrated with a polymer (PDMS), and (iii) inverted grating structures. The fabrication methodology, including the selection of suitable technologies and preliminary testing to determine the optimal grating design, is discussed. The obtained test results will inform the development of future structures. Furthermore, optical measurement data and fabrication conclusions of plasmonic gratings are presented.

To facilitate plasmon excitation via light radiation, a coupler is developed. As on-chip integration is essential for future applications, grating structures are preferred over other coupling methods, such as microprism couplers, which require specialized micromechanical processes incompatible with CMOS fabrication. Grating structures offer advantages over prism couplers by maintaining CMOS compatibility and simplifying the manufacturing process.

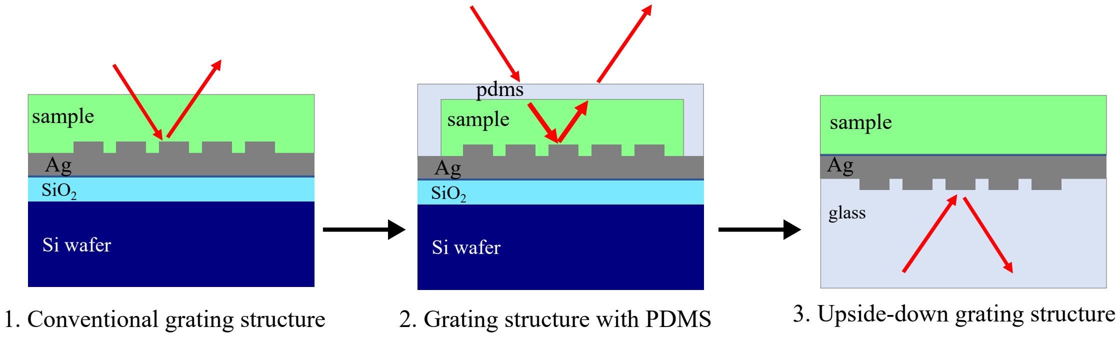

Figure 5.1.: The three primary grating structures include: (i) a conventional surface grating, (ii) a grating structure integrated with PDMS, and (iii) an inverted grating approach.

The grating structure comprises a straightforward layer configuration, which can be fabricated effectively using planar technology. A silicon wafer serves as the base material, undergoing thermal oxidation to form a silicon oxide layer beneath the plasmon-supporting metal layer. The metal layer, deposited via vapor deposition, is processed using e-beam lithography and patterning techniques.

Fig. 5.2 presents the cross-sectional dimensions of the fabricated grating. The grating period is initially aligned with the helium-neon laser wavelength (632.8 nm) used in experiments and is subsequently adjusted within the 700-900 nm range (see Sec. 2.4.2). The metal layer thickness varies from 25 to 100 nm. These parameters are optimized to enhance surface plasmon excitation and maximize performance.

5.2. Fabrication Process

This section outlines the procedures and tools used to construct the grating structure. The fabrication begins with the selection of a suitable substrate, which serves as the base for subsequent planar processing steps. Next, the metallization process is described in detail. Finally, the electron beam lithography (EBL) process, along with the role of the electron beam writer, is elaborated.

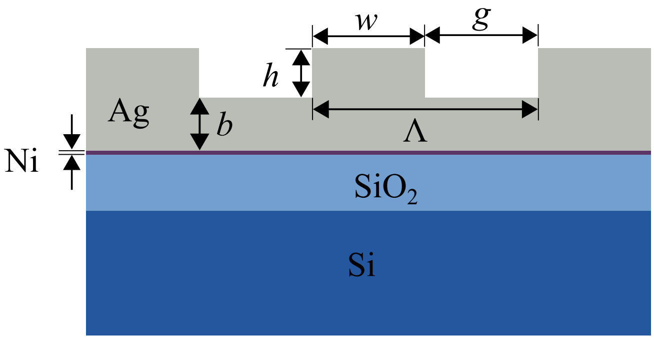

Figure 5.2.: Fabrication details of the grating structure: a silicon wafer with a 100 nm thermally grown oxide layer serves as the substrate. A nickel adhesion layer (10-15 nm) supports the silver layer, ensuring optimal adhesion. Additional parameters include the grating period Λ, silver base layer thickness b, grating height h, grating width w, and gap size g.

Fig. 5.3 illustrates the fabrication workflow, starting with the design phase in KLayout software [14] and continuing with the actual fabrication on a silicon wafer. The central region of the wafer, where the grating structure is patterned, is examined using a scanning electron microscope (SEM).

5.2.1. Substrate

The complete fabrication process is substrate dependent. Planar techniques were applied to generate the grating structure, with silicon, a standard material in semiconductor manufacturing, as the primary component. Surface plasmon excitation demands a three-layer configuration. Silicon's natural oxide layer exhibits desirable insulating behavior, and it allows for thermal oxidation to yield silicon dioxide.

Fig. 5.4 illustrates the preparation of the grating substrate. The silicon dioxide layer was thermally grown on the silicon wafer, serving as the dielectric beneath the metal grating, while ambient air completed the required three-layer system. The wafer underwent a dry oxidation process, resulting in a 100 nm-thick oxide layer. The thickness of the silicon oxide layer was measured using an ellipsometer (M-2000, J.A. Woollam Co., US).

---

[14] Strasser, Matthias. KLayout. https://www.klayout.de.

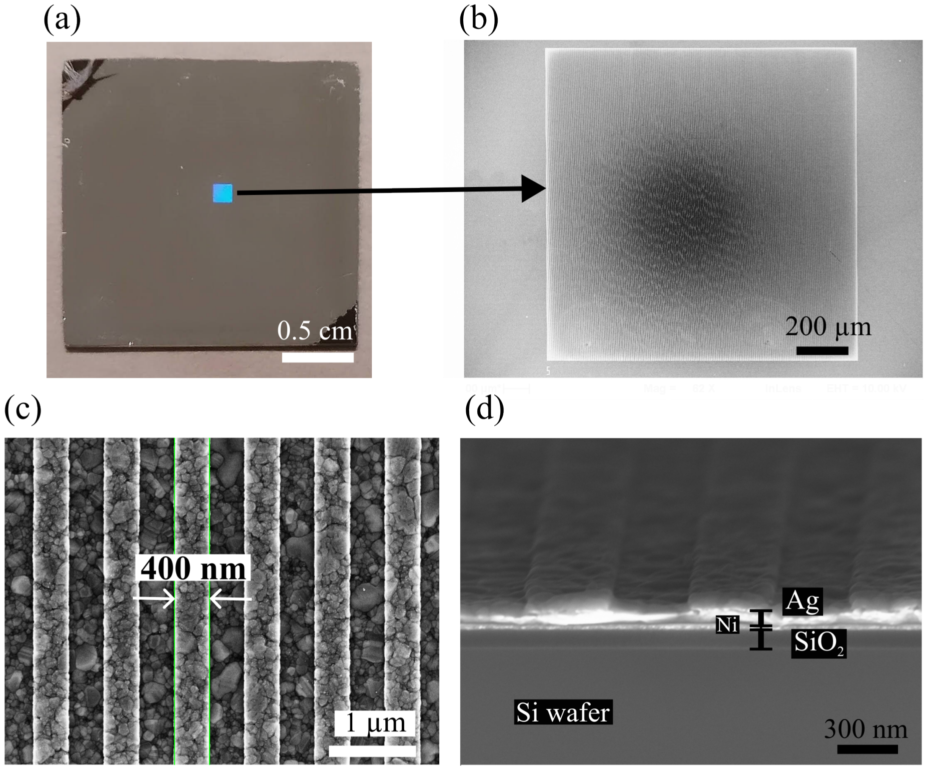

Figure 5.3.: (a) the grating's construction on a (2 × 2) cm wafer, (b) an SEM image of the (1.2×1.2) mm grating region, (c) the silver grating, specifying a 400 nm size and approximately 800 nm period, and (d) a cross-sectional view of the grating's structure. (Image from Sarapukdee, P., et al. [82], is licensed under CC BY 4.0.)

Due to economic constraints, fabricating the grating structures directly on 4-inch wafers was deemed impractical. Additionally, the electron beam writer was unable to accommodate full 4-inch wafers. Consequently, the oxidized wafers were diced into smaller (2 × 2) cm pieces using the wafer dicing saw (ESEC 8003, ESEC, CH).

To ensure surface cleanliness and optimal adhesion during the metallization process, the diced wafer fragments underwent a rigorous cleaning procedure. Initially, they were immersed in a peroxymonosulfuric acid solution composed of sulfuric acid (H_2SO_4) and hydrogen peroxide (H_2O_2) to remove organic contaminants. This was followed by the standard RCA cleaning protocol [206], designed to eliminate both organic residues and ionic contaminants. The samples were sequentially cleaned with acetone and isopropyl

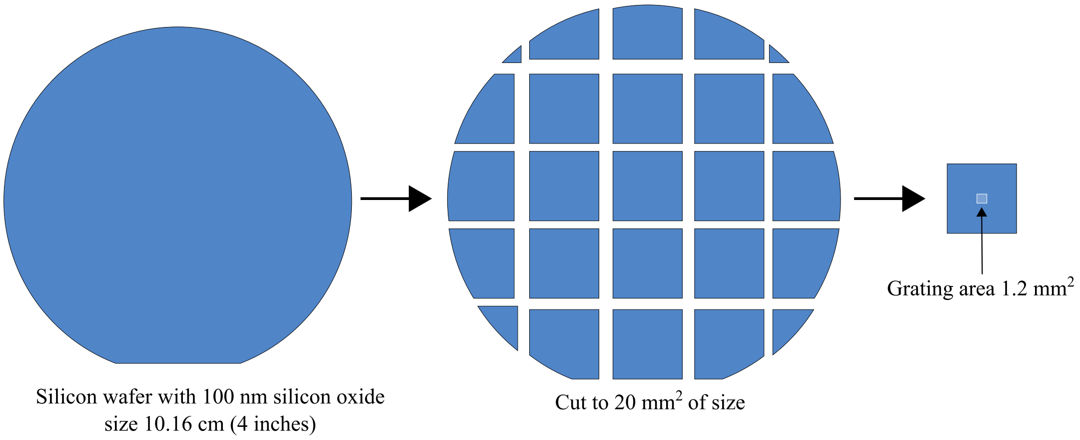

Figure 5.4.: A 100 mm silicon wafer, coated with a 100 nm silicon oxide layer, is diced into (2 × 2) cm pieces. A (1.2 × 1.2) mm grating structure is fabricated at the center. (Adapted from Sarapukdee, P., et al. [82], is licensed under CC BY 4.0.)

alcohol (IPA), rinsed with deionized (DI) water, and finally dried using nitrogen gas. This thorough cleaning ensured the elimination of impurities, thereby preventing adhesion issues during subsequent metallization steps.

5.2.2. Nickel Adhesive Layer

A nickel layer serves as an adhesive intermediary beneath a silver layer during the fabrication of plasmonic silver gratings. This facilitates the deposition of a more uniform silver layer with a smoother surface, enhancing its structural integrity [207]. Fig. 5.5 illustrates the surface morphology of silver layers deposited with and without a nickel seed layer on silicon.

The deposition of the nickel layer was conducted using the pulsed DC magnetron sputtering technique (PlasmaLab System 400, Oxford Instrument, UK). This method intermittently interrupts the fluctuating voltage to mitigate the risk of arc discharge, which could otherwise compromise the integrity of the deposited film. Additionally, this approach contributes to a more homogeneous layer formation.

During the sputtering process, the deposition was performed dynamically, wherein the substrate plate moved in circular trajectories beneath the target material. This motion ensured that deposition occurred solely when the substrate was directly positioned beneath the target, promoting greater uniformity in the resultant layer.

The thickness of the nickel layer was minimized to reduce its impact on the dispersion relation. For this reason, static deposition is preferred over dynamic deposition. In dynamic deposition, the typical nickel layer thickness ranges from 10 to 15 nm, with a sputtering rate of several nanometers per second. However, achieving precise control over film thickness becomes challenging at such low sputtering durations, as the final thickness is highly sensitive to the initial substrate alignment.

The sputtering parameters were set to a power of 1,000 W, under conditions of an argon (Ar) flow rate of 25 sccm and a chamber pressure of 1×10^{-4} Torr. Prior to the actual deposition, the target was pre-cleaned to eliminate any potential contamination from preceding processes. The airlock's mechanical components and the entire deposition process were regulated automatically by a control computer to ensure consistency and precision.

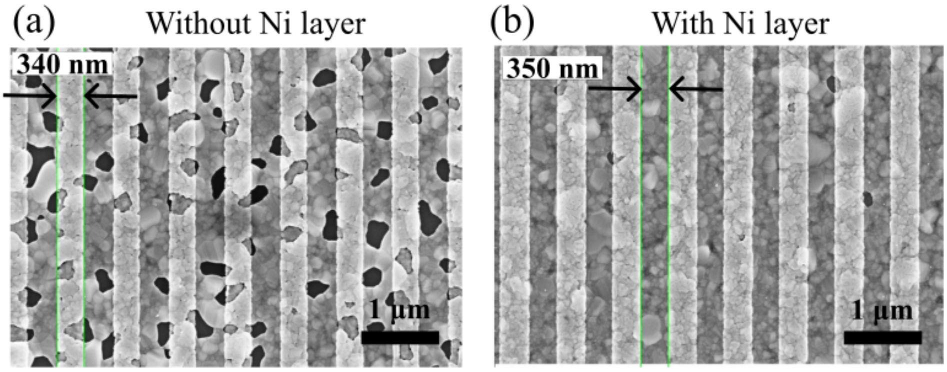

Figure 5.5.: Comparison of grating structures with (a) and without (b) a nickel seeding layer. The schematic on the right illustrates the layer arrangement. The SEM image of the silver grating surface without a nickel layer exhibits numerous voids, indicating the inability of silver to effectively adhere to the underlying silicon oxide (SiO_2).

5.2.3. Silver Deposition

The silver layer was deposited using a thermal evaporation system. This system enables the thermal evaporation of metals by heating them in a tungsten crucible through which a high current flows. High-purity silver wire (Ag, 99.99%, 1.0 mm diameter, Kurt J. Lesker Company Ltd., UK) was prepared as the raw material. It was trimmed to the appropriate size and positioned firmly within the crucible. The crucible, bolted securely between two electrodes at the process chamber's base, was then filled with the silver.

The samples were attached to the sample holder using a vacuum- and heat-resistant adhesive (Kapton adhesive tape, CMC Klebetechnik GmbH, GE), ensuring the surface to be coated faced downward toward the crucible (bottom-down method). To prevent contamination, a high vacuum was created within the process chamber using a combination of a scroll pump and a turbomolecular pump, achieving a pressure in the range of $1 - 3 \times 10^{-6}$ mbar.

A high current was gradually applied to the crucible, melting the silver. As the temperature increased, the liquid silver evaporated and condensed onto the samples. To monitor the deposition process in real-time, an oscillating quartz sensor (Intellemetrics IL820, Intellemetrics Ltd., UK) measured the film thickness. Careful control of the current was essential; a rapid increase could cause the silver to boil and spill from the crucible, contaminating the chamber. For a uniform and dense layer, the deposition rate was maintained below 0.2 nm/s.

5.2.4. Electron-Beam Lithography

Electron-beam lithography (EBL) is a crucial technique in semiconductor fabrication, enabling the patterning of highly precise nanostructures. In this thesis, EBL was utilized to optimize the grating structure by varying its geometric parameters.

The mask layout was designed using computer-aided design (CAD) software, Klayout (GNU public license), ensuring precise geometric information for the desired structure.

The data from the layout were processed into control commands by the electron beam writer's post-processor, facilitating direct writing onto the substrate.

A substrate coated with an electron-sensitive photoresist, typically polymethylmethacrylate (PMMA), was exposed to a highly focused electron beam in a serial writing process. Given its time-consuming nature, this method is primarily used for research prototypes or small-scale production, while it plays a significant role in mask fabrication for parallel lithographic processes. The PMMA resist (PMMA; 4% 950 K, 679.04, Allresist GmbH, Strausberg, Germany) was selected, with a coating thickness of approximately 250 nm, ensuring reliable lift-off of metal layers for structures with heights between 25–100 nm.

To achieve the desired resist thickness, PMMA was diluted with chlorinated resins, allowing improved viscosity and flow when applied using a resist spinner (Polos, SPS-Europe, GE). According to the manufacturer's specifications [208], a 250 nm thick PMMA layer was obtained by spinning at 4,000 RPM for 60 seconds, followed by a baking step at 180 °C for 90 seconds to remove residual solvents. The resist development was performed using a solution of isopropanol and deionized water (3:1) for 45 seconds, with a subsequent 15-second rinse in pure isopropanol to halt development.

The patterning was conducted using an electron beam writer (Pioneer, Raith GmbH, GE). The writing process required configuration of aperture size, acceleration voltage, and working distance to optimize beam focus and resolution. The beam deflection within the writing field was controlled by digital-to-analog converters, with the minimum step size determined by the writing field edge length and the converter resolution.

The area dose required for exposure was calculated as:

$$Area\,dose = \frac{Beam\ current\ \times\ Area\ dwell\,time}{Step\ size\ \times\ Line\ spacing} \tag{5.1}$$

Optimal resolving power was achieved with a working distance of 6 mm, a writing field size of $(100 \times 100)\mu m$, an aperture of 30 μm, and an accelerating voltage of 10 kV. Given the grating structure dimensions of (1.2 × 1.2) mm, the mask layout was divided into multiple contiguous writing fields, managed by the Raith operating system software.

This methodology ensured high-precision structuring of the plasmonic grating, critical for applications requiring submicron feature definition.

Dose Testing

The development of a process follows the principle of bottom-up development. Tests must be conducted to establish process parameters. The parameters determined the quality and reproducibility of the structures to be produced. Dose tests were used to determine the process parameters for electron beam lithography. The exposed and chemically developed profile in this process depends on the resist and electron beam parameters. Consequently, starting parameters are necessary as a method for initiating tests. This work uses a 250 nm thick PMMA resist to prepare the sample. For this experiment, a grating period of 800 nm was chosen. The grating height of the silver-based material was 50 nm. According to the areas that the beam spot must cover (see Appendix A.1), the structural area of the grating was (1.2 × 1.2) mm. The parameters are shown in Tab. 5.1. The evaluation of the grating size with a scanning electron microscope as shows in Fig. 5.6, revealed that the radiation dose performed (Tab. 5.1) was in good condition of 50-55 μC/cm^2 for 10 kV energy and 95-100 μC/cm^2 for 20 kV. On the other hand, low and high doses can

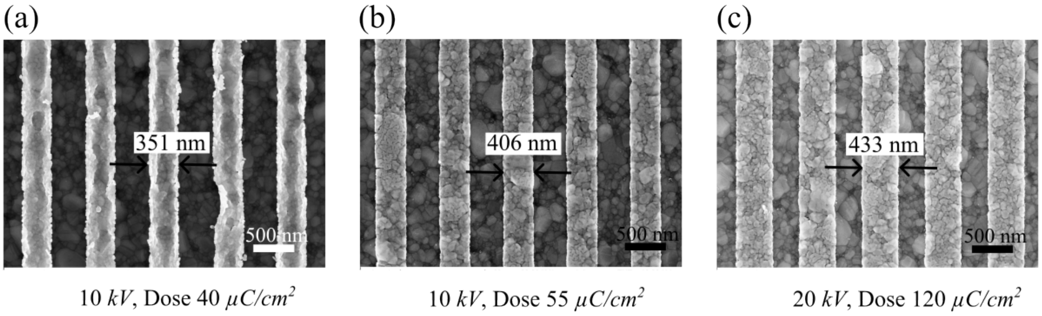

10 kV, Dose 40 $\mu C/cm^2$ 10 kV, Dose 55 $\mu C/cm^2$ 20 kV, Dose 120 $\mu C/cm^2$

Figure 5.6.: SEM images compare the results of e-beam lithography in different doses, and the results show the under dose (a), optimum dose(b), and overdose(c).

Table 5.1.: Parameters of dose test and results of expected a grating period of 800 nm, grating size 400 nm, according to the computer design.

Ebeam enegy	Aperture	Writing field	Step size	Dose (μC/cm^2)	Grating size (nm)	SD
10 kV	20 μm	100 μm	0.016 μm	40	351	9
				45	361	7
				50	390	5
				55	406	4
				60	411	5
20 kV	20 μm	100 μm	0.016 μm	95	393	4
				100	389	4
				110	418	4
				115	420	5
				120	433	10

manifest as under- and overdose, respectively. At a radiation dose of 55 μC/cm^2 and 10 kV, the optimal structure has achieved a grating structure close to 400 nm. This dose test was also ideal for patterning by the lift-off method, as the photoresist can be eliminated without leaving a residue. Consequently, subsequent experiments were conducted under this condition.

5.2.5. Lift-Off

A silver grating was fabricated using the lift-off technique. First, a layer of photoresist was applied to the samples, followed by exposure using an electron beam writer. The exposed samples were then developed, transferring the designed structure onto the photoresist. Subsequently, a thermal evaporation system was used to deposit a silver layer onto the patterned surface.

To remove the excess metal, the samples underwent a lift-off process. They were initially submerged in acetone for 10 to 15 minutes. This was followed by ultrasonic treatment in an acetone bath to facilitate the dissolution of the top resist layer. After cleaning, the optical structure was examined. If any resist residues remained, the procedure was repeated for an additional 10 minutes. Finally, the samples were immersed in isopropanol to remove any remaining impurities, ensuring the complete removal of resist and unwanted silver particles.

Upon completion of the lift-off process, the photoresist-defined regions representing the grating's indentation were entirely eliminated, leaving behind the structured silver grating.

5.3. Fabrication of Grating Structures

Following the foundational overview of fabrication techniques in the previous section, this section provides a detailed description of the specific fabrication processes for various grating structures. It includes subsections on the fabrication of conventional grating structures, grating structure integrated with PDMS microchannels, and inverted grating structures.

5.3.1. Conventional Grating Structure

The verification of grating structures was conducted using two different fabrication techniques, differing primarily in their process sequence (Fig. 5.7). However, both methods were executed under identical conditions. The primary distinction lies in the thermal vapor deposition of a silver layer.

In Method A, silver was deposited as a base layer on top of a nickel layer, whereas in Method B, a photoresist was applied directly onto the nickel layer. Despite this difference, the subsequent fabrication steps were identical for both methods. The process began with electron beam lithography, followed by chemical development to remove broken polymers. After development, thermal vapor deposition of silver was performed, followed by a lift-off process to remove the photoresist.

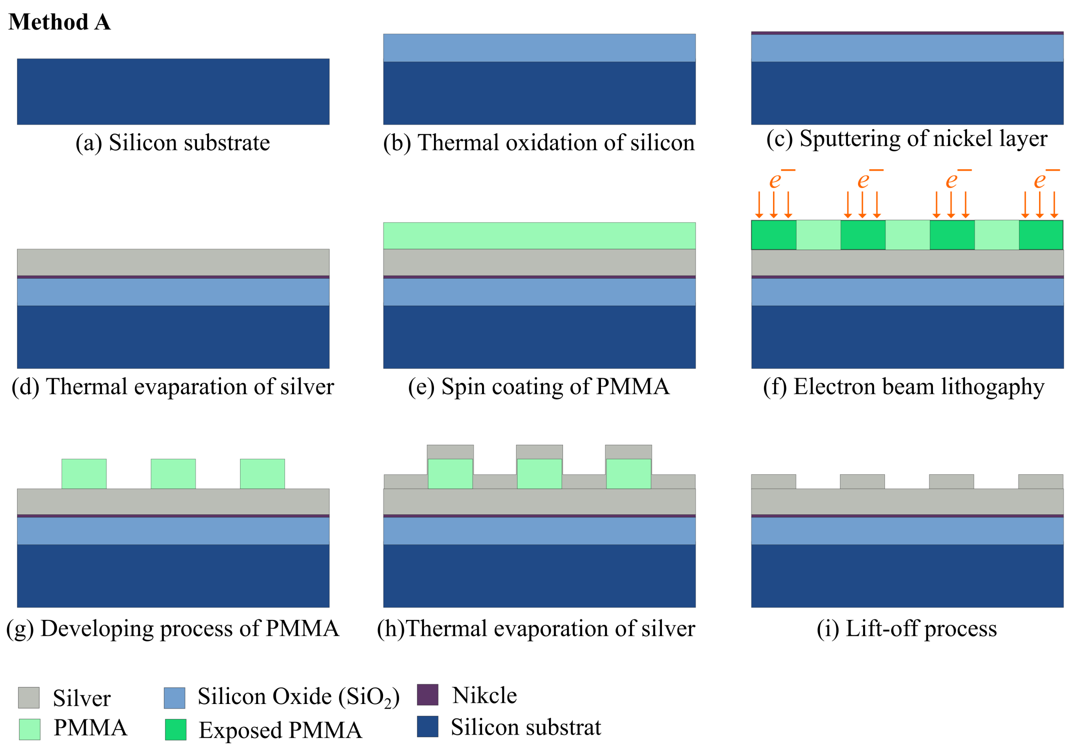

Figure 5.7.: Schematic of grating structure fabrication on Silicon substrate (Method A). (a) A silicon substrate is prepared. (b) A silicon oxide layer is grown on the substrate via thermal oxidation. (c) A nickel layer is deposited by sputtering. (d) A silver layer is deposited by thermal evaporation. (e) PMMA resist is spin-coated on top. (f) E-beam lithography defines the grating pattern in the PMMA. (g) Development removes the exposed PMMA. (h) A second silver layer is thermally evaporated. (i) Lift-off removes the remaining PMMA and excess silver, leaving the patterned silver grating structure. (Adapted from Sarapukdee, P., et al. [82], is licensed under CC BY 4.0.)

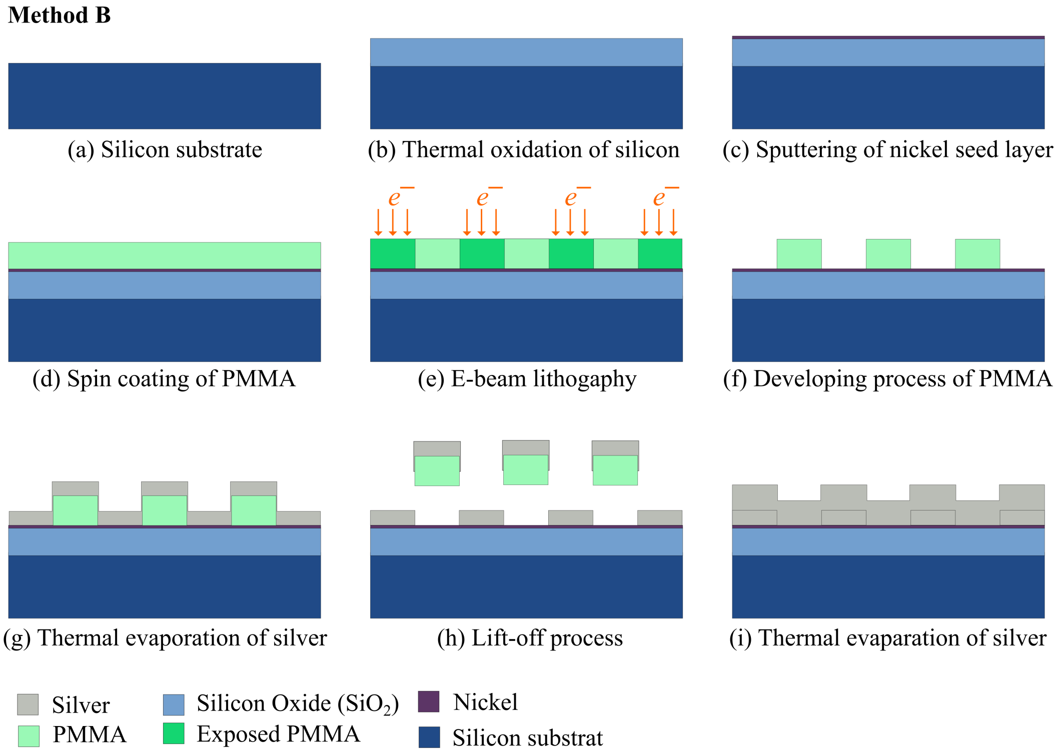

Figure 5.8.: Schematic of grating coupler fabrication on Silicon substrate (Method B). (a) A silicon substrate is prepared. (b) A silicon oxide layer is grown on the substrate via thermal oxidation. (c) A nickel seed layer is deposited by sputtering. (d) PMMA resist is spin-coated on top. (e) E-beam lithography defines the grating pattern in the PMMA. (f) Development removes the exposed PMMA. (g) Silver is thermally evaporated onto the patterned surface. (h) Lift-off removes the remaining PMMA and excess silver, leaving the patterned silver grating. (i) A second layer of silver is thermally evaporated to form the final grating coupler structure.

Scanning electron microscope images demonstrated that both techniques created grating structures. However, Method B, lacking a base layer, required an additional thermal evaporation step to address this deficiency. The scanning electron microscope comparison, illustrated in Fig. 5.9, indicated that Method A yielded structures with more defined edges, resulting in superior optical measurement outcomes.

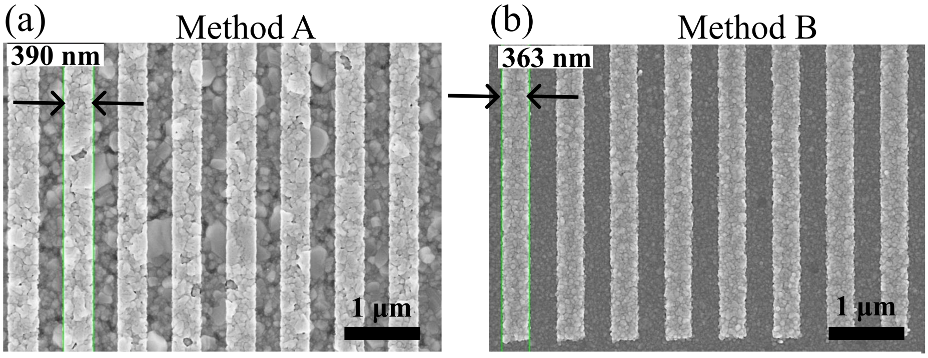

Figure 5.9.: Scanning electron microscope (SEM) images comparing grating structures fabricated using two different methods: (a) Method A, resulting in a grating period of 390 nm, and (b) Method B, yielding a grating period of 363 nm.

5.3.2. Grating Structure Integrated with PDMS Microchannels

Fig. 5.10 illustrates the fabrication process for integrating a grating structure with PDMS microchannels, which is essential for applications involving fluidic transport over a structured optical surface.

The process began by fabricating the grating structure on a silicon wafer using electron beam lithography (EBL), followed by chemical development and thermal vapor deposition of silver to form the metal layer. The lift-off process was employed to remove excess photoresist and achieve precise grating features.

Subsequently, the PDMS microchannels were fabricated and integrated onto the grating structure. The desired channel height of approximately 150 μm was achieved by using adhesive tapes as molds. These tapes were cut into the required dimensions (1.5 × 0.7 cm^2) and placed at the bottom of a heat-resistant container.

Next, PDMS (polydimethylsiloxane) was prepared and poured over the grating structure. The volume of PDMS was carefully controlled to ensure a final thickness of approximately 2 mm. To remove trapped air bubbles, the PDMS was degassed in a vacuum chamber before curing in an oven at 60°C for 30 minutes.

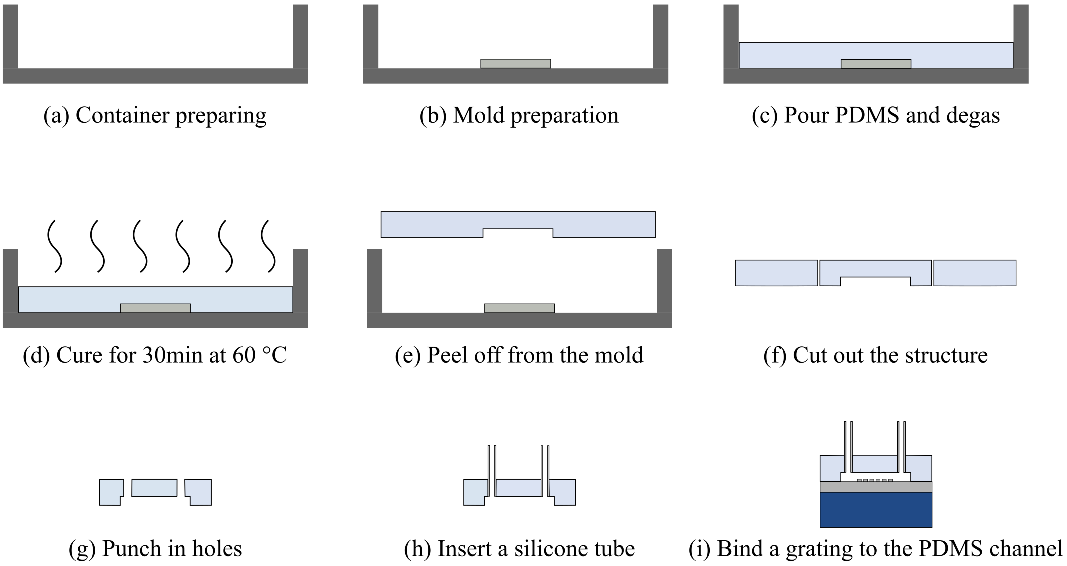
(a) Container preparing (b) Mold preparation (c) Pour PDMS and degas

(d) Cure for 30min at 60 °C (e) Peel off from the mold (f) Cut out the structure

(g) Punch in holes (h) Insert a silicone tube (i) Bind a grating to the PDMS channel

Figure 5.10.: Schematic of a microfluidic channel fabrication process using PDMS. (a) A container is prepared. (b) A mold is prepared with the desired microchannel design. (c) PDMS is poured into the mold and degassed to remove air bubbles. (d) The PDMS is cured at 60°C for 30 minutes. (e) The cured PDMS is peeled off from the mold. (f) The PDMS structure is cut out. (g) Holes are punched for inlets and outlets. (h) Silicone tubes are inserted into the holes. (i) A grating is bound to the PDMS channel.

5.3.3. Inverted Grating Structures

The inverted grating structure was fabricated on a transparent glass substrate, enabling measurements where backlight passes through the substrate to the grating structure without interference from the analyte layer. The process began with the spin-coating of 250 nm PMMA resist onto the glass substrate, followed by 40 nm Electra 9 (AR-PC 5090.02, Allresist GmbH, Germany), a conductivity-enhancing layer, to improve SEM image resolution. Electron beam lithography was then performed, followed by deep reactive ion etching (RIE, Oxford PlasmaLab 80 Plus, Oxford Instruments, UK) to transfer the pattern onto the glass substrate. Next, two silver layers were sequentially deposited. The first silver layer was deposited at a thickness corresponding to the etching depth, followed by a lift-off process to remove excess material. The second silver layer was then deposited to complete the top layer. Finally, an optional protective coating was applied to enhance durability. By utilizing electron lithography and reactive ion etching, this approach enabled precise control over grating dimensions, ensuring high fidelity in structural replication and improved performance in optical applications.

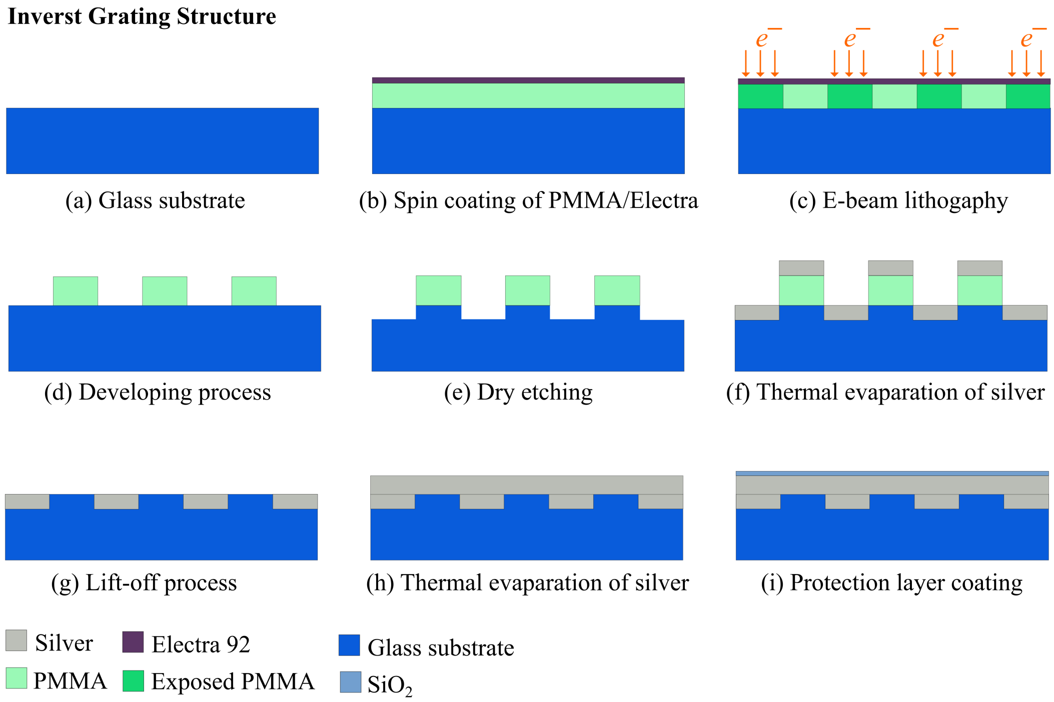

Figure 5.11.: Schematic of the inverted grating fabrication process. (a) A glass substrate is coated with PMMA. (b) A layer of Electra 92 is spin-coated on top of the PMMA. (c) E-beam lithography defines the grating pattern in the Electra 92 layer. (d) Development removes the exposed Electra 92 and PMMA. (e) Dry etching transfers the pattern to the underlying PMMA layer. (f) Silver is thermally evaporated onto the patterned surface. (g) Lift-off removes the remaining PMMA and excess silver, leaving the patterned silver grating. (h) A second layer of silver is thermally evaporated. (i) A protective layer is coated on top. (Adapted from Sarapukdee, P., et al. [155], is licensed under CC BY 4.0.)

CHAPTER 6

Characteristics of Grating-Based SPR

This chapter examines key features of grating-based Surface Plasmon Resonance (SPR) systems, focusing on their structural, optical, and functional aspects for label-free biomolecule detection. It provides insights into the optimization of multilayer gratings, including metal layer measurements and software analyses to fine-tune parameters. The impact of grating period variations and silver layer thickness on SPR excitation angles is systematically explored[15], emphasizing their role in optimizing sensor performance. Experimental results reveal that precise tuning of grating dimensions and silver thickness produces high-performance sensors with narrow reflection profiles and low full width at half maximum (FWHM) values. Advanced designs, such as two-dimensional gratings, enhance flexibility in plasmon excitation angles, offering improved sensitivity for diverse sensing applications. Gradient grating period (GGP) structures are also introduced, demonstrating

---

[15] Portions of this section have been previously published as: P. Sarapukdee, C. Spenner, D. Schulz, and S. Palzer, "Optimizing stability and performance of silver-based grating structures for surface plasmon resonance sensors," *Sensors*, vol. 23, no. 15, 2023. DOI: 10.3390/s23156743.

multi-angle plasmon excitation for dynamic and multiplex biosensing[16]. Grating-based SPR sensors are validated through experiments detecting Protein A and immunoglobulin G (IgG) solutions, showing their effectiveness in measuring analyte layers via plasmon angle shifts. Incorporating polydimethylsiloxane (PDMS) microchannels enables real-time, solution-based detection[17]. Challenges related to the durability of silver-based gratings are addressed through surface reconditioning techniques and protective silicon oxide and silicon nitride coatings, ensuring prolonged sensor stability[18]. These insights pave the way for robust and versatile SPR sensors in biosensing and beyond. The chapter also explores inverted grating-based SPR sensors as an alternative to conventional configurations, emphasizing their advantages in reduced light absorption and enhanced environmental resistance[19]. Simulations identify optimal geometric parameters such as grating period, height, and silver thickness for maximizing plasmon coupling efficiency. Experimental comparisons highlight the suitability of 1 mm thick glass substrates for minimal signal interference and high reflectivity.

6.1. Metal Layer Measurement

The scanning electron microscope (SEM; Raith GmbH, GE) was used to analyze the grating structure. To examine the cross-section, the sample was broken 1 mm adjacent to the grating structure. Fig. 6.1 presents the multilayer structure of the grating, with SEM software used to measure both shape and thickness. The intended design parameters

---

[16] Portions of this section have been previously published as: P. Sarapukdee, D. Schulz, and S. Palzer, "Grating structures for silver-based surface plasmon resonance sensors with adjustable excitation angle," *Sensors*, vol. 24, no. 14, 2024. DOI: 10.3390/s24144538.

[17] Portions of this section have been previously published as: P. Sarapukdee, D. Schulz, and S. Palzer, "Silver-based plasmonic grating with PDMS microchannel for biological sensors," *Proceedings*, vol. 97, no. 1, 2024. DOI: 10.3390/proceedings2024097192.

[18] Portions of this section have been previously published as: P. Sarapukdee, M. Pech, D. Schulz, "Surface Reconditioning of Silver-Based Gratings for Surface Plasmon Biosensors," *Biophotonics Congress 2021.*, 12–16 April 2021, Washington, DC, United States. DOI: 10.1364/BODA.2021.DTu1A.2.

[19] Portions of this section have been previously published as: P. Sarapukdee, D. Schulz, and S. Palzer, "Concept, simulation, and fabrication of inverted grating structures for surface plasmon resonance sensors," *Journal of Sensors and Sensor Systems*, vol. 13, no. 2, pp. 157–166, 2024. DOI: 10.5194/jsss-13-157-2024.

include a grating height of 50 nm, a silver-based layer of 100 nm, and a nickel adhesive layer of 10–15 nm.

Tab. 6.1 summarizes the measured layer thicknesses. The results indicate a deviation from the expected values, yet they provide critical insights for parameter optimization in future samples. Additionally, evaluations confirm the successful growth of the Si/SiO_2 layers and silver deposition. SEM images serve as an effective tool for determining both the shape and thickness of the sample.

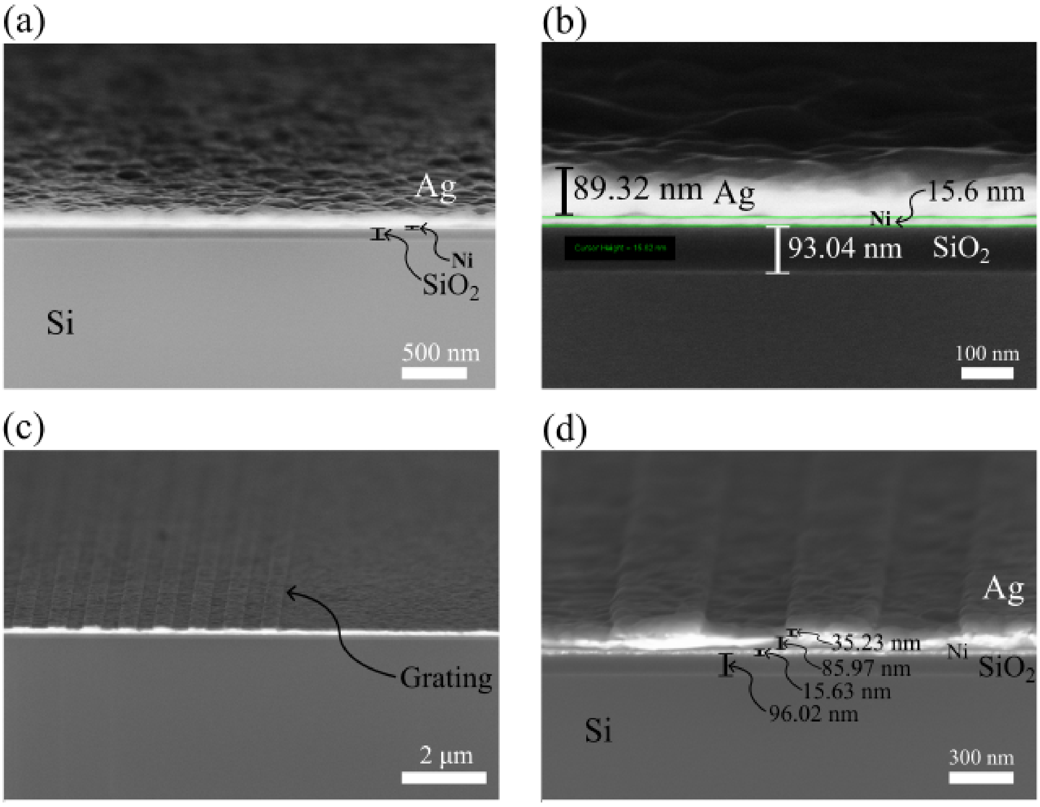

Figure 6.1.: SEM images of the sample cross-section: (a) The multi-layer structure on the silicon substrate without a grating structure. (b) Measurement results showing 93.04 nm of Si/SiO_2 and 89.32 nm of the silver layer. (c) The grating structure with multilayer measurements: 96.02 nm of Si/SiO_2, 15.63 nm of the nickel layer, 85.97 nm of the silver base, and a grating height of 35.23 nm. (Adapted from Sarapukdee, P., et al. [82], is licensed under CC BY 4.0.)

Fig. 6.2(a) presents an SEM cross-section of the grating structure, detailing key dimensions such as height (h), base (b), width (w), and gap (g). The measured grating dimensions

Table 6.1.: Summary of measured thickness values for sample layers.

Sample No.	SiO_2 (nm)	Nickel (nm)	Silver Base (b) (nm)	Silver Height (h) (nm)
1	93	16	93	51
2	93	17	99	42
3	103	15	89	49
4	95	18	107	51
5	96	16	86	35
Mean	96	16	95	46
Standard Deviation (SD)	4	1	8	6

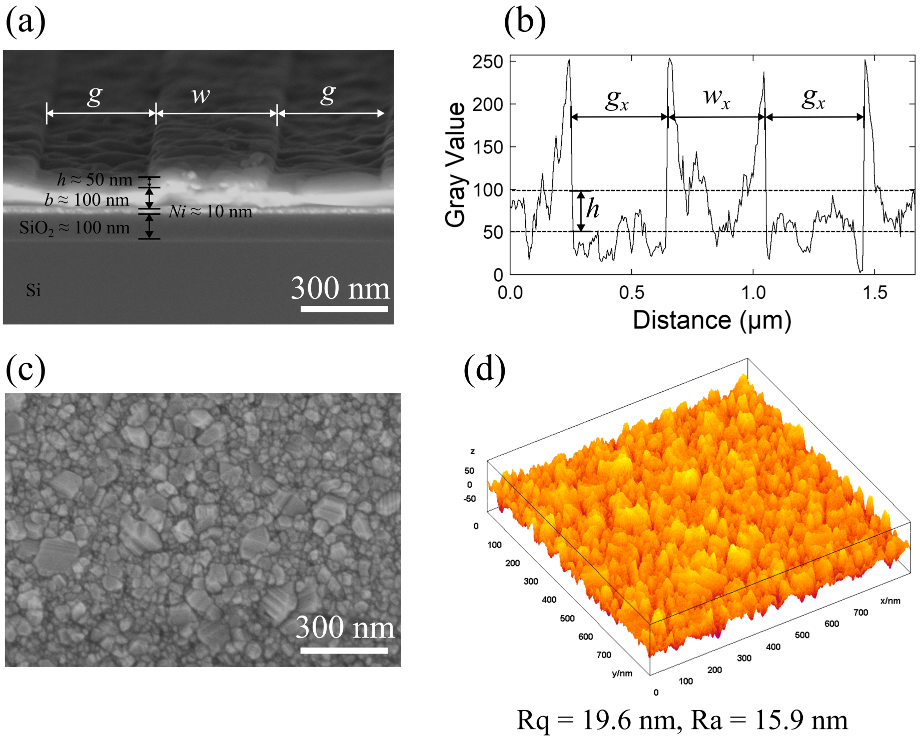

Figure 6.2.: (a) SEM cross-section of the grating structure highlighting dimensions h, b, w, and g. (b) Surface profile of the grating structure with a width w of 400 nm and a gap g of 400 nm. (c) SEM image of the silver surface created via thermal evaporation after the lift-off process. (d) Surface roughness calculated from the SEM image using ImageJ, with roughness parameters $R_q = 19.6$ nm and $R_a = 15.9$ nm. (Image from Sarapukdee, P., et al. [209], is licensed under CC BY 4.0.)

exhibit deviations from the intended values, though these variations provide insights into their influence on grating performance.

Fig. 6.2(b) and (c) illustrate the surface profile of the grating structure, showcasing the silver surface obtained via thermal evaporation and lift-off processing. The texture and uniformity of the surface are particularly emphasized.

The surface roughness, derived from SEM images via ImageJ software [210], reveals roughness parameters of $R_q = 19.6$ nm and $R_a = 15.9$ nm. Given that all samples underwent identical processing conditions, structural morphology remains consistent. Surface brightness and roughness, analyzed using SEM cross-sectional images, provide reliable data for assessing surface characteristics. This study confirms the reproducibility and reliability of the fabricated structures.

6.2. Variation of the Grating Period

This section investigates the relationship between the grating period (Λ) and plasmon excitation angles. Eq. (2.66) demonstrates that the grating period directly influences surface plasmon excitation. Determining the plasmon excitation angles is crucial for sensor applications, as the relationship between the grating period and excitation angles aids in selecting the optimal angle for specific applications.

In this experiment, seven grating structures with periods ranging from 700 to 900 nm were fabricated on the same substrate using Method A (see Sec. 5.3.1). This approach minimizes surface variations that may arise when producing multiple samples.

The grating structures were fabricated on a silicon substrate with a 98 nm SiO_2 layer, a 10 nm nickel adhesive layer, a 100 nm silver base layer, and a 50 nm grating height. These parameters were selected to determine the optimal grating thickness, which will be further discussed in Sec. 6.4. The structures were then analyzed using an optical measuring station to evaluate the coupling of incident light.

Measurements were conducted over an angular range of $\theta = 10^\circ$ to 40°, with a constant increment of $\Delta\theta = 0.2^\circ$. These angles were used to plot the reflection intensity of the reflected light. Fig. 6.4(a) illustrates the minima in reflected light intensity for different

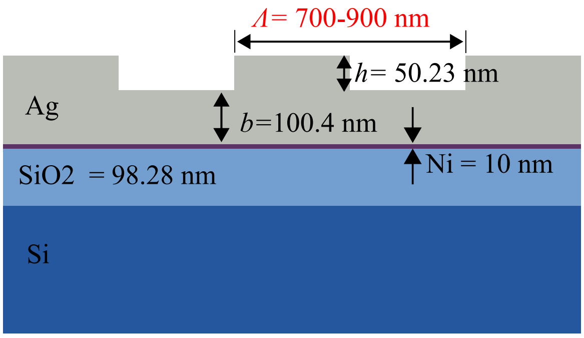

Figure 6.3.: Design of a grating structure with variable periods on a silver-based substrate with a base layer thickness of 100.4 nm and a grating height of 50.23 nm.

grating periods. At these angles, the reflected laser beam loses energy, indicating surface plasmon excitation at the silver and silicon oxide interface. The exact excitation angles and grating period measurements obtained via SEM are summarized in Tab. 6.2. The relationship between the grating period and the plasmon excitation angle, where maximum light absorption occurs, is depicted in Fig. 6.4(b).

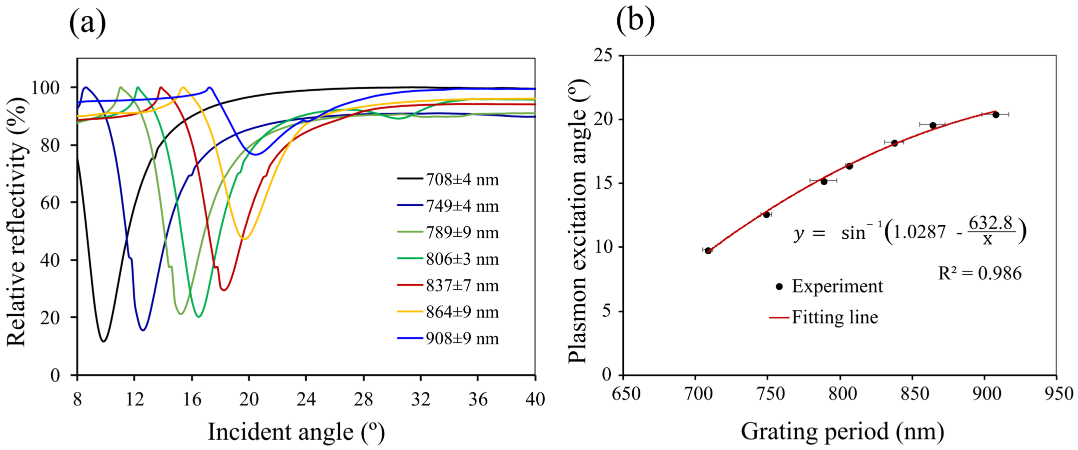

Figure 6.4.: (a) Relative reflection for grating periods between 708 nm and 908 nm, showing plasmon excitation angles within the scanning range of 8° to 40°. (b) Linear correlation between the plasmon excitation angle and grating period, with a coefficient of determination $R^2 = 0.986$. (Image from Sarapukdee, P., et al. [82], is licensed under CC BY 4.0.)

Fig. 6.4(b) shows a linear relationship between the grating period and the excitation angle at the minimum reflected light intensity, given by:

Table 6.2.: Grating period variations and corresponding plasmon excitation angles. (Adapted from Sarapukdee, P., et al. [82], licensed under CC BY 4.0.)

Grating Period (nm)	SD (nm)	Excitation Angle (°)	Relative Reflectivity (%)	FWHM (°)
708	4	9.8	11.58	5.2
749	4	12.6	15.32	3.8
789	9	15.2	21.31	3.4
806	3	16.4	20.16	3.6
837	7	18.2	29.44	3.2
864	9	19.6	47.40	3.8
908	9	20.4	76.74	3.2

$$y = \sin^{-1}\left(1.0287 + \frac{632.8}{x}\right) \tag{6.1}$$

Using this relationship, the optimal coupling angles of the grating as a function of the grating period were calculated. A curve fit using Eq. (2.67) was used to calculate the fitting parameter $\alpha = \frac{1}{n_d}\sqrt{\frac{\varepsilon_m \varepsilon_d}{\varepsilon_d + \varepsilon_d}}$ yielded a coefficient of determination $R^2 = 0.986$. The theoretical values for $n_d = 1$, $m = -15.243$, and $\varepsilon_d = 1$ resulted in a theoretical $\alpha_{\text{theory}} = 1.0287$, closely matching the experimental value of 1.0345. This strong agreement between experimental findings and theoretical predictions validates the accuracy of the model.

6.3. Comparison of Simulation and Experimental Results

The refined model was utilized to simulate the experimental conditions detailed in Sec. 6.2, wherein variations in the grating period directly influence the plasmon excitation angle. The simulation incorporated the grating period and silver layer thickness values as specified in Tab. 6.2. Furthermore, Equation (2.67) provides a means to calculate the theoretical plasmon excitation angle using the parameters $\varepsilon_m = -18.6$, $\varepsilon_d = 1$, $\Lambda = 632.8$ nm, and $n = 1$.

Fig. 6.5 presents a comparative analysis, illustrating (a) the signal graph profiles and (b) the relationship between the grating period and the plasmon excitation angle.

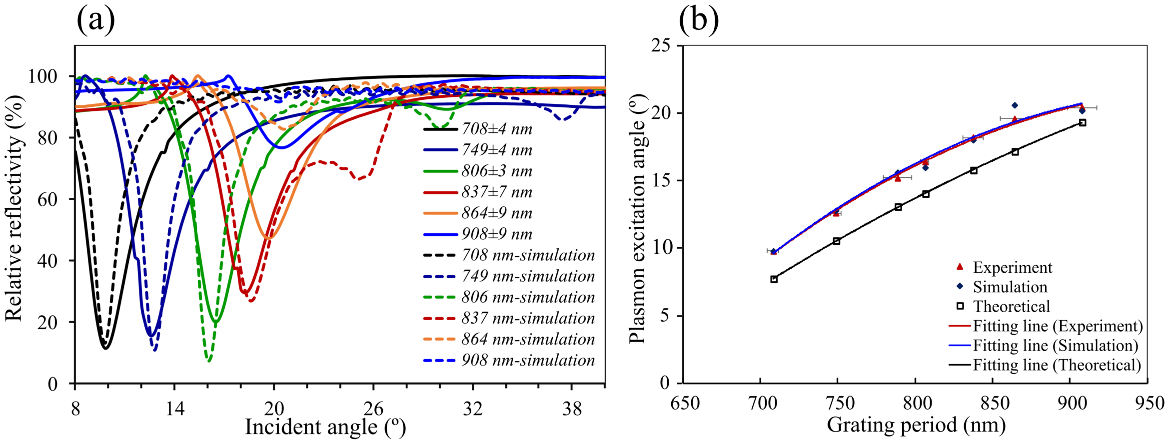

Figure 6.5.: A comparison of experimental and simulated results. (a) Dashed lines indicate simulation results, while solid lines represent experimental data. (b) The three datasets align closely, with the simulation effectively mirroring experimental trends, while the theoretical model yields slightly lower values. (Image from Sarapukdee, P., et al. [82], is licensed under CC BY 4.0.)

Table 6.3.: Comparison of plasmon excitation angles between experimental and simulation results for different grating periods. (Table from Sarapukdee, P., et al. [82], is licensed under CC BY 4.0.)

Grating Period (nm)	Plasmon Excitation Angle (°)		
	Theoretical	Experimental	Simulation
708 ±4	7.7	9.8	9.8
749 ±4	10.6	12.6	12.8
789 ±9	13.1	15.2	15.6
806 ±3	14.1	16.4	16.0
837 ±7	15.8	18.2	18.0
864 ±9	17.2	19.6	20.6
908 ±9	19.3	20.4	20.2

Tab. 6.3 consolidates the comparative results. The simulation effectively replicates both theoretical and experimental trends, particularly in reproducing sensitivity variations crucial for sensor performance evaluation. The strong agreement between experimental and simulated data underscores the reliability of the developed model. However, slight discrepancies between theoretical and experimental values may stem from simplificati-

ons inherent in theoretical modeling or experimental uncertainties. Notably, theoretical calculations, based on idealized conditions, may not always capture the complexities of real-world measurements accurately.

6.4. Variation of the Silver Thickness

In this study, variations in the silver-based layer and grating height were examined. Previous research [211] identified the optimal grating parameters as follows: a grating size of 375 nm (with a period of 750 nm), a 100 nm thick silver-based layer, and a grating height of 100 nm. However, varying the grating sizes led to observable shifts in the highest dip angle as the grating size increased.

Due to constraints in the optical measurement setup (see Appendix A.1), only angles between 10° and 40° could be measured accurately. Consequently, data below 10° could not be comprehensively plotted. To mitigate this limitation, an angular range of 15°–20° was selected to capture the full reflection signal profile while ensuring that the dip angle remains within the sensitive region for plasmonic sensing.

To investigate further, 16 structures were compared, each with a grating size $w = 400$ nm ($\Lambda = 800$ nm), while varying the silver-based layer thickness (b) between 25 and 100 nm and the grating height (h) between 25 and 100 nm. The schematic design of the samples is shown in Fig. 6.6.

Performance Evaluation

The reflection signal as a function of the excitation angle was used to evaluate the grating structure's biosensing performance. A narrow reflection dip is desirable for high sensor specificity. The full width at half maximum (FWHM) [212] was employed to quantify the signal profile's sharpness. Additionally, the relative reflection (RR) at maximum absorption was analyzed, as a lower RR indicates stronger plasmonic excitation.

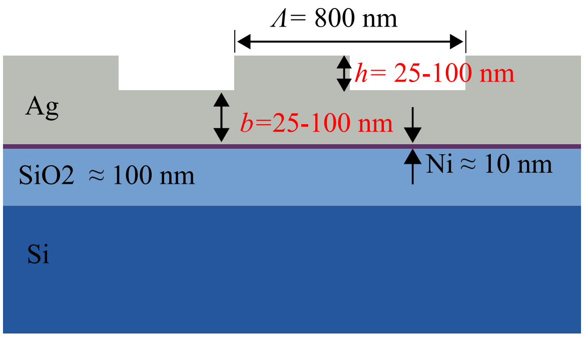

Figure 6.6.: Schematic of the grating structure with varying silver-based thickness (25 – 100 nm) and grating height (25 – 100 nm).

The results for the 16 structures with varying silver layer thicknesses ($b = 25 - 100$ nm) and grating heights ($h = 25 - 100$ nm) are summarized in Tab. 6.4 and Fig. 6.7. The findings indicate that lower relative reflection values were observed for silver layers of 75 and 100 nm, particularly when combined with grating heights of 50 nm.

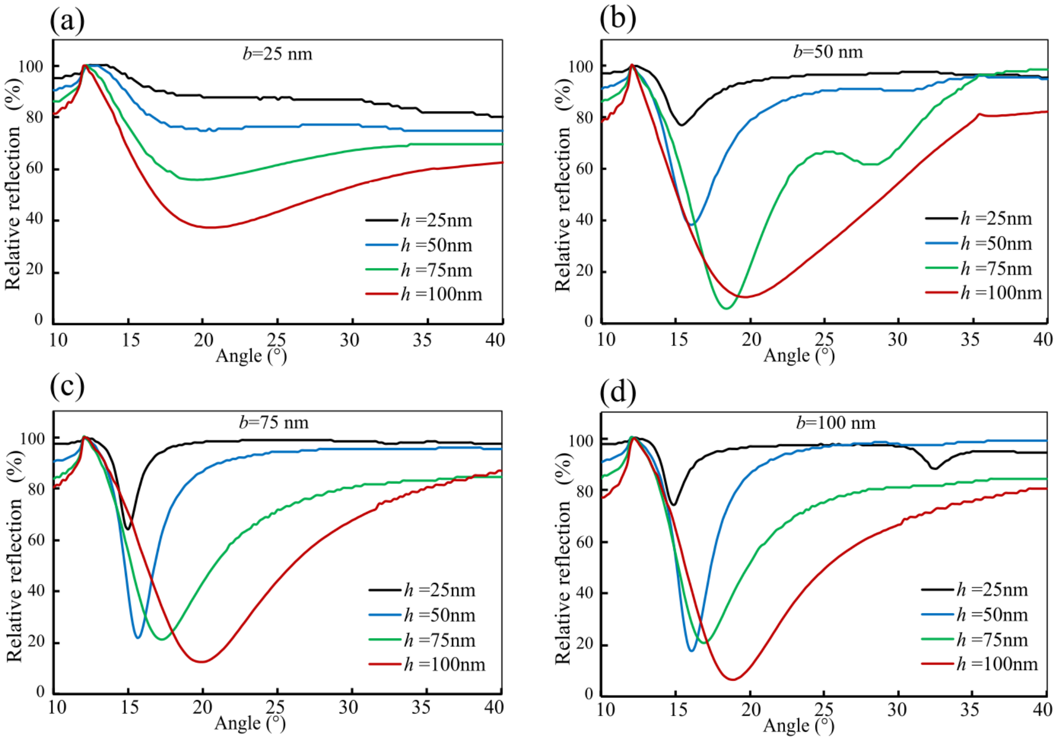

Figure 6.7.: Relative reflection of grating structures with varying silver thickness and grating height. The best performance is observed at silver thicknesses of 75 and 100 nm with a grating height of 50 nm. (Image from Sarapukdee, P., et al. [82], is licensed under CC BY 4.0.)

Table 6.4.: Results of 16 grating structures with w = 400 nm (Λ = 800 nm), varying base thickness (b) and grating height (h). Values in red indicate the highest performance.

b (nm)	h (nm)	Excitation Angle (°)	RR (%)	FWHM (°)
25	25	39.2	80.49	23.2
	50	19.8	74.80	24.8
	75	19.6	55.83	25.0
	100	20.2	37.63	25.0
50	25	15.4	76.97	3.0
	50	16.0	38.21	4.2
	75	18.4	5.76	6.4
	100	19.6	10.00	15.2
75	25	15.0	64.08	1.4
	50	15.6	21.98	2.4
	75	17.2	21.21	7.4
	100	19.8	12.57	11.0
100	25	14.8	74.53	1.6
	50	16.2	17.80	2.6
	75	17.0	20.60	6.2
	100	18.8	6.44	10.2

Note: RR = Relative reflection.

The coupling efficiency (CE) was determined by Eq. (3.5). The highest coupling efficiency of 34.21 was achieved with a base thickness of 84 nm and a grating height of 44 nm (see Fig. 6.8).

These findings indicate that a silver thickness of 75–100 nm and a grating height of 50 nm are optimal for biosensing applications.

6.5. 2D Grating Structure

A two-dimensional grating has been used in many applications, such as x-ray phase contracts [213] , super-resolution imaging [214], and switchable diffraction [215]. The use of 2D grating structures to excite surface plasmon resonances (SPR) has been a subject of significant interest and development [216]. These structures enable enhanced control

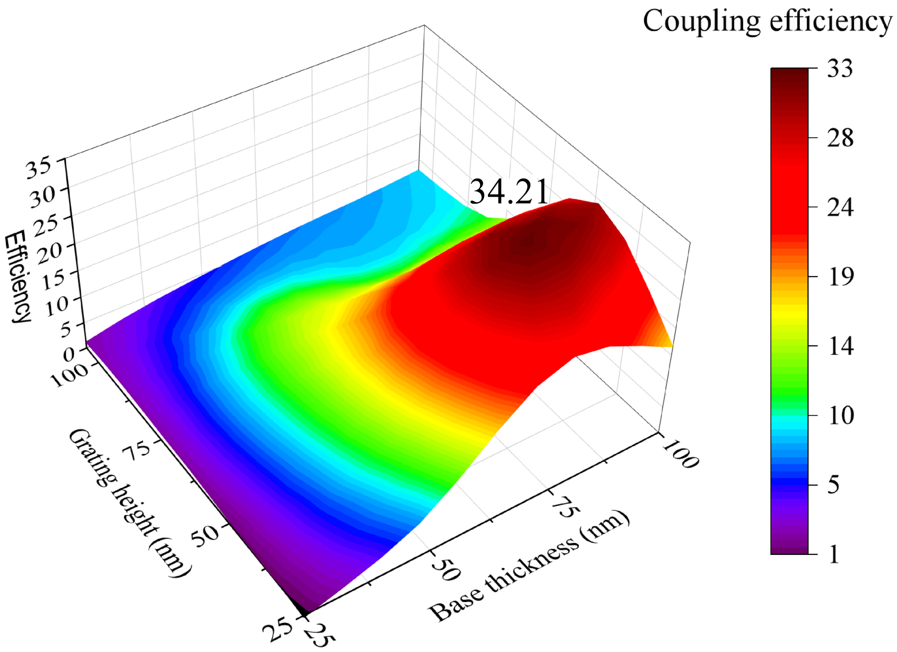

Figure 6.8.: Coupling efficiency for different grating structures. Maximum efficiency of 34.21 was achieved at a base thickness of 84 nm and a grating height of 44 nm. (Image from Sarapukdee, P., et al. [82], is licensed under CC BY 4.0.)

over plasmonic resonances by providing more degrees of freedom in tuning the spatial distribution of electromagnetic fields [217]. By manipulating both the periodicity and orientation of the grating in two dimensions, 2D gratings allow for more precise tuning of the plasmon excitation angle, which is crucial for improving sensor performance. This tunability offers greater flexibility without the need to alter other sensor components, making them ideal for a variety of sensing applications [218, 219].

In practical terms, hybrid designs incorporating metal films, dielectric layers, and 2D gratings have shown promise for refractive index sensing, supported by coupled-mode theory and finite-difference time-domain (FDTD) simulations [220]. Such structures not only improve the sensing performance but also enhance reliability. Several experimental applications have demonstrated the potential of 2D gratings, including polarization-independent filters and multi-dimensional displacement measurements [221, 222]. Furthermore, metal-assisted guided-mode resonance (MAGMR) sensors that integrate 2D gratings have outperformed conventional grating designs in terms of sensitivity, particularly across various polarization modes [223]. These advancements have been shown to offer high-resolution measurement capabilities and have applications in fields like precision positioning and machining [224].

In summary, 2D grating-based SPR systems introduce new dimensions of flexibility in plasmon excitation control, enabling better optimization of sensing performance for diverse applications. They present a versatile platform for advanced sensing, especially in fields requiring precise analyte detection and high spatial resolution.

6.5.1. Asymmetry 2D Grating Structure

This work aims to explore the excitation behavior of surface plasmon by a two-dimensional grating structure in more detail that might be applicable to apply in biosensor fields. In this work, the two-dimensional grating was designed to have the same spacing at the top and bottom with $g = 400$ nm, the same width with $w = 400$ nm, and the length of the grating body was changed as follows 400, 800, 1600, 2000 nm, resulting in a square and rectangular shape (see Fig. 6.9). The fabrication process used method A, which have a silver-based thickness of $b = 100$ nm and grating height of $h = 50$ nm. Additionally, the measurement takes place in an angular range of $\theta = 10°$ to $40°$ with a constant angle change of $\Delta\theta = 0.2°$ by using the optical measuring station. Then, the reflection and the intensity of the reflected light can be plotted with angles. To analyze the structural parameters of the final devices, optical microscopy and scanning electron microscopy (SEM) are utilized. The coupling efficiency (CE) is then derived from the characteristics of the signal by using the full width at half maximum (FWHM) of the relative reflectivity signal and the relative reflectivity.

Fig. 6.9 illustrates the experimental results of the two-dimensional grating with varying lengths of 800-2000 nm and the same width of 400 nm. Tab. 6.5 contains a full breakdown of the sizes of the produced samples, showing the particular dimensions of each grating.

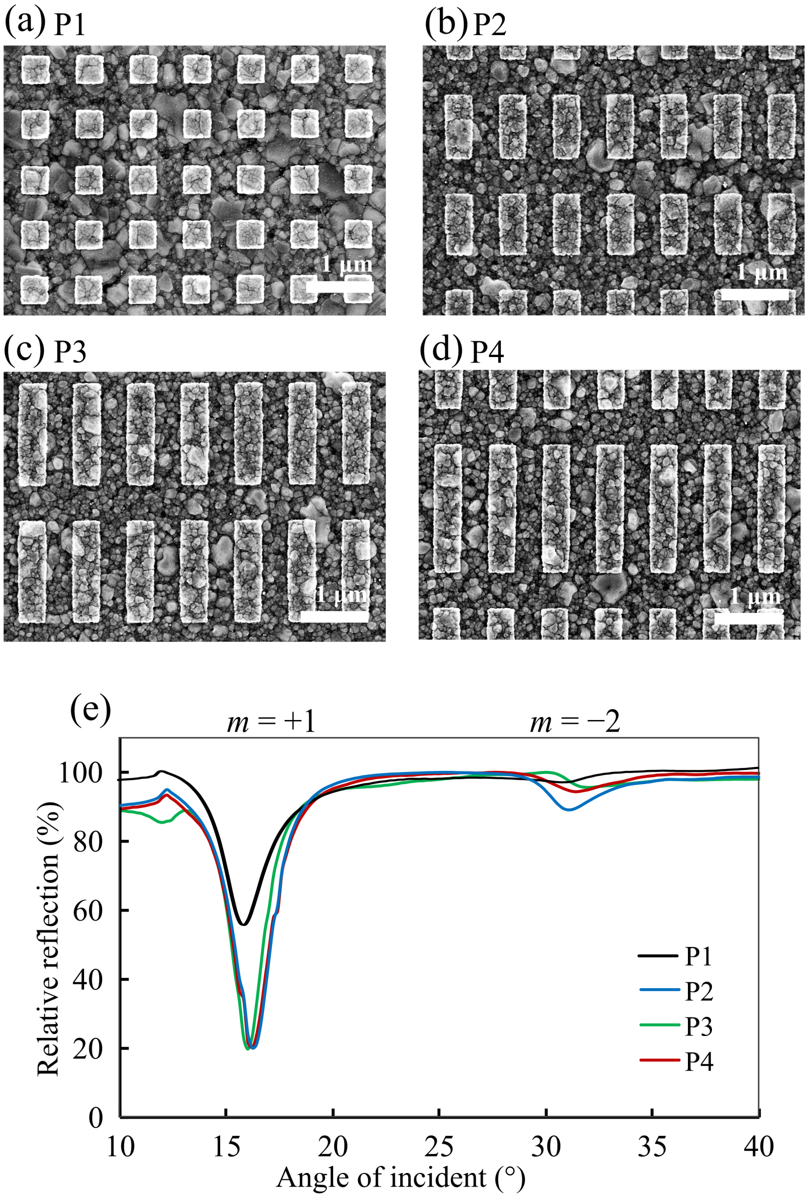

Figure 6.9.: SEM images of the manufactured two-dimensional grating structure, with the length of 400 nm(a), 800 nm(b), 1600 nm(c), 2000 nm(d) and their relative reflection results(e) that show the plasmon excitation approximately 16.2° and 31.2° for the first and second order, respectively. (Adapted from Sarapukdee, P., et al. [209], is licensed under CC BY 4.0.)

The performance of the 2D grating with varying width, w_y, is examined by plotting light reflection across different angles. The experimental results, showing the relationship between grating width, plasmon excitation angles, and coupling efficiency as a function of w_y.

Table 6.5.: Structural parameters of the grating structure and the relative reflection results show the plasmon excitation of 2D grating of sample P1-P4. Table by Sarapukdee, P., et al. [209], licensed under CC BY 4.0.

Sample	Λ_x (nm)	Λ_y (nm)	w_x (nm)	w_y (nm)	Plasmon excitation angle (°), CE +1 Order	 −2 Order
P1	807 ± 6	826 ± 8	409 ± 7	427 ± 6	16,0°, 19.6	30.8°, 0.9
P2	808 ± 6	1,373 ± 4	412 ± 8	849 ± 7	16.2°, 36.4	31.0°, 3.6
P3	811 ± 6	2,066 ± 5	426 ± 6	1,544 ± 6	16.0°, 44.6	31.4°, 0.8
P4	811 ± 7	2,451 ± 5	409 ± 8	1,933 ± 7	16.2°, 36.3	31.4°, 1.7

The experimental data offer insights into the plasmonic behavior of the 2D grating, which operates similarly to a 1D grating. Specifically, the maximum plasmon excitation angle is found to be in the range of 16.0° to 16.2° (CE = 19.6 - 44.6) for the +1 diffraction order and 30.8° to 31.4° (CE = 0.8 - 3.6) for the -2 diffraction order. These results are consistent with prior studies on silver-based 1D gratings, particularly regarding the resonance angle. However, the coupling efficiency is strongly influenced by the grating width w_y. For $w_x \geq 800$ nm, the coupling efficiency aligns with that of 1D gratings, but it significantly decreases when w_x is approximately equal to w_y.

The findings suggest that the presence of a gap in the grating structure does not notably affect the plasmon excitation angle for the +1 order when $w_y \geq 2w_x$. In contrast, for the -2 order, the best coupling efficiency is observed when the width ratio $w_y/w_x = 2$, a behavior not seen in 1D gratings.

6.5.2. Symmetry 2D Grating Structure

In this study, the grating structure was designed to be a square two-dimensional (2D) gating with the same period intended for 800 nm but varying grating widths. In e-beam lithography, dose factor techniques were used to achieve a range of grating widths, with higher energy resulting in wider gratings. The fabrication process used method A, measure the reflection and intensity of the reflected light can be plotted using angles.

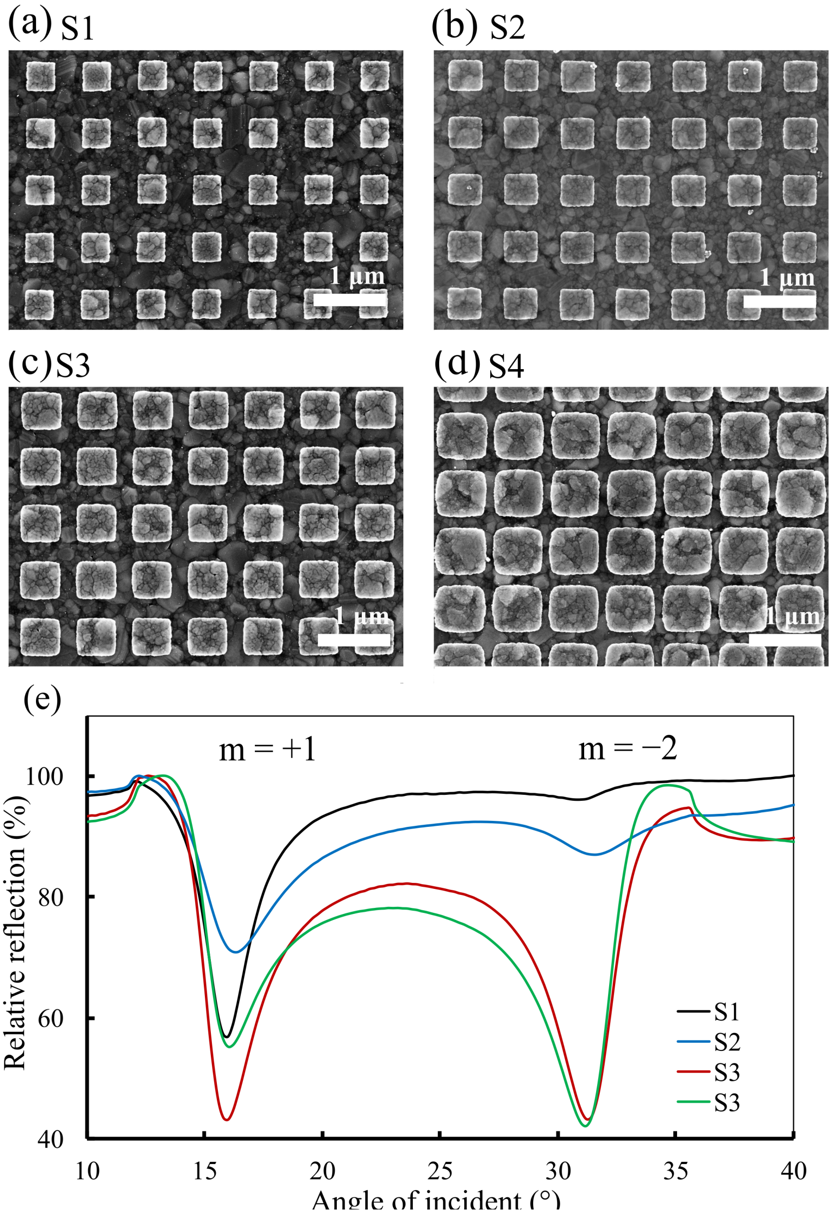

Figure 6.10.: SEM images of grating structures with the same period (Λ = 800 nm) but different grating sizes (w) of 403 nm (a), 484 nm (b), 563 nm (c), and 674 nm (d) for sample S1, S2, S3, and S4, respectively. Sample 1 (a) displays the detailed measurements of parameters (Λ and w captured by SEM. The relative reflection results (e) for samples S1-S4 exhibit plasmon excitation at approximately 16.1° and 31.2° for the +1 and −2 diffraction order, respectively. (Adapted from Sarapukdee, P., et al. [209], is licensed under CC BY 4.0.)

Tab. 6.6 provides a summary of the grating parameters for structures S1 through S4, with the corresponding relative reflection signal profiles shown in Fig. 6.10. The findings

Table 6.6.: Structural parameters of the 2D symmetry grating structure. The standard deviation of the periods is stated. (Table by Sarapukdee, P., et al. [209], licensed under CC BY 4.0.)

Sample	Λ_x (nm)	Λ_y (nm)	w_x (nm)	w_y (nm)	Plasmon excitation angle (°), CE +1 Order	 -2 Order
S1	807 ± 6	826 ± 8	409 ± 7	427 ± 6	16.0°, 19.6	30.8°, 0.9
S2	811 ± 6	828 ± 5	487 ± 4	458 ± 5	16.0°, 6.1	31.2°, 5.2
S3	816 ± 4	819 ± 5	578 ± 5	551 ± 4	16.4°, 25.9	31.6°, 16.7
S4	821 ± 10	837 ± 2	718 ± 7	689 ± 7	16.0°, 6.9	31.2°, 12.9

demonstrate that 2D grating structures significantly influence SPR characteristics, particularly in terms of excitation angles and coupling efficiencies. The systematic increase in grating periods and groove widths from S1 to S4 reflects a deliberate strategy for adjusting the plasmonic properties. While the plasmon excitation angles remain relatively consistent for the +1 order, they vary for the -2 order.

Coupling efficiencies exhibit a more complex pattern, as they do not show a straightforward relationship with grating period and groove width alone. The data reveal that increasing the grating size tends to enhance the CE for the -2 order. However, to achieve high efficiencies for both the +1 and -2orders, it is critical to optimize the grating size. Structure S3 is identified as having the most favorable dimensions, achieving high CEs of 25.9 and 16.7 for the +1 and -2 orders, respectively. This underscores the importance of fine-tuning grating dimensions to optimize SPR characteristics for various applications. Unlike 1D gratings, where the coupling efficiency for the -2 order is constrained by factors such as grating height and silver base thickness, the observed CE for both orders in 2D gratings is at a similar level. This flexibility allows for efficient use of both diffraction orders with the same grating, a capability not seen in 1D gratings.

6.6. Grating Structures for SPR with Adjustable Excitation Angle

The read-out technique in grating-based SPR systems [120, 123, 225] is typically centered on the angular modulation method, where the plasmon excitation angles before and after a sample reaction are compared. By adjusting factors such as periodicity, grating thickness, and the choice of plasmonic materials, the plasmon excitation angle can be finely tuned. However, in this approach, the plasmon excitation angle is predetermined by the grating's fabrication process, allowing only one specific angle to be excited [226, 227].

To enhance the flexibility and dynamic range of grating-based SPR sensors, advanced designs such as two-dimensional (2D) gratings [218] and gradient grating period (GGP) structures [228, 229] present alternative modes of operation. Both of these approaches allow for greater control over SPR excitation, enabling the tunability of the plasmon excitation angle without altering the sensor system's physical components.

This topic will demonstrate two techniques: rotating 2D gratings and utilizing the position on GGP to achieve an adjustable SPR angle. The use of GGP and 2D gratings in SPR systems offers new opportunities for advanced sensing applications across multiple fields. In biosensing, for instance, these designs enhance detection limits [230, 231], enable multiplexing [232], and increase the selectivity [233] for molecular interactions. Furthermore, the tunability of the plasmon excitation angle [234, 235] provides additional flexibility in optimizing sensor performance for a wide range of applications.

6.6.1. Rotating Symmetry 2D Gratings

The theory of plasmon excitation in Sec. 2.4.2 provides insight into the complex interactions within a grating structure, highlighting that for effective excitation, the incident electric field vector must precisely align with the orientation of the grating. As a result, when studying the behavior of a 1D grating structure, the sample must remain stationary to maintain the alignment between the incident light and the grating structure. However, this constraint is lifted when working with 2D gratings, which allow for rotation, enabling different effective grating periodicities to be achieved as the sample rotates in any direction. Fig. 6.11 illustrates this sample rotation and its influence on the effective Λ, facilitating the alignment of grating lines with incident light of any polarization and offering greater flexibility in exploring plasmon excitation phenomena.

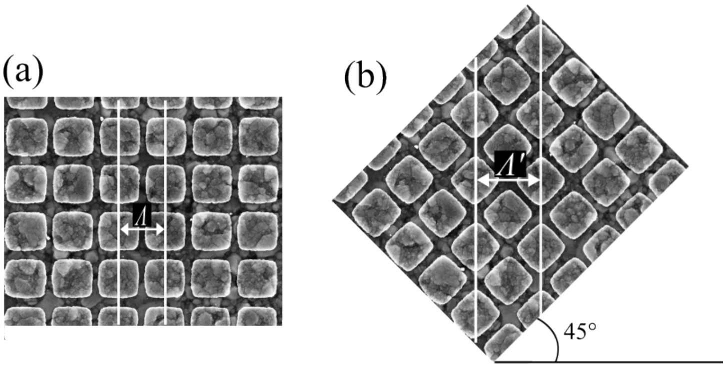

Figure 6.11.: The grating at the position of 0° (a) has period size(Λ) can represent the new grating arrangement with a new period size(Λ′) after the sample is rotated to 45° (b). (Image from Sarapukdee, P., et al. [209], is licensed under CC BY 4.0.)

To explore these unique properties, 2D grating samples (S1-S4) from Sec. 6.5.2 are used in experiments. The characterization process involves rotating the 2D grating along the z-axis at various angles (0°, 15°, 30°, 45°), providing quantitative data on how rotation impacts plasmon excitation. Fig. 6.12 presents the surface plasmon excitation profile, visually demonstrating the interaction between the 2D grating structure and the incident light wave across different rotational angles.

The experiment reveals a significant discovery: surface plasmon excitation remains efficient when the 2D grating sample is rotated in various orientations. In stark contrast, surface plasmon excitation is constrained by the fixed orientation of the grating lines in 1D gratings. The data show a gradual increase in the excitation angle, from 16° at 0° rotation to 20.8° at 45° for the +1 order. The coupling efficiency (CE) is closely tied to the grating period, as the coupling strength between light and surface plasmons at a specific wavelength scales with the grating vector [120].

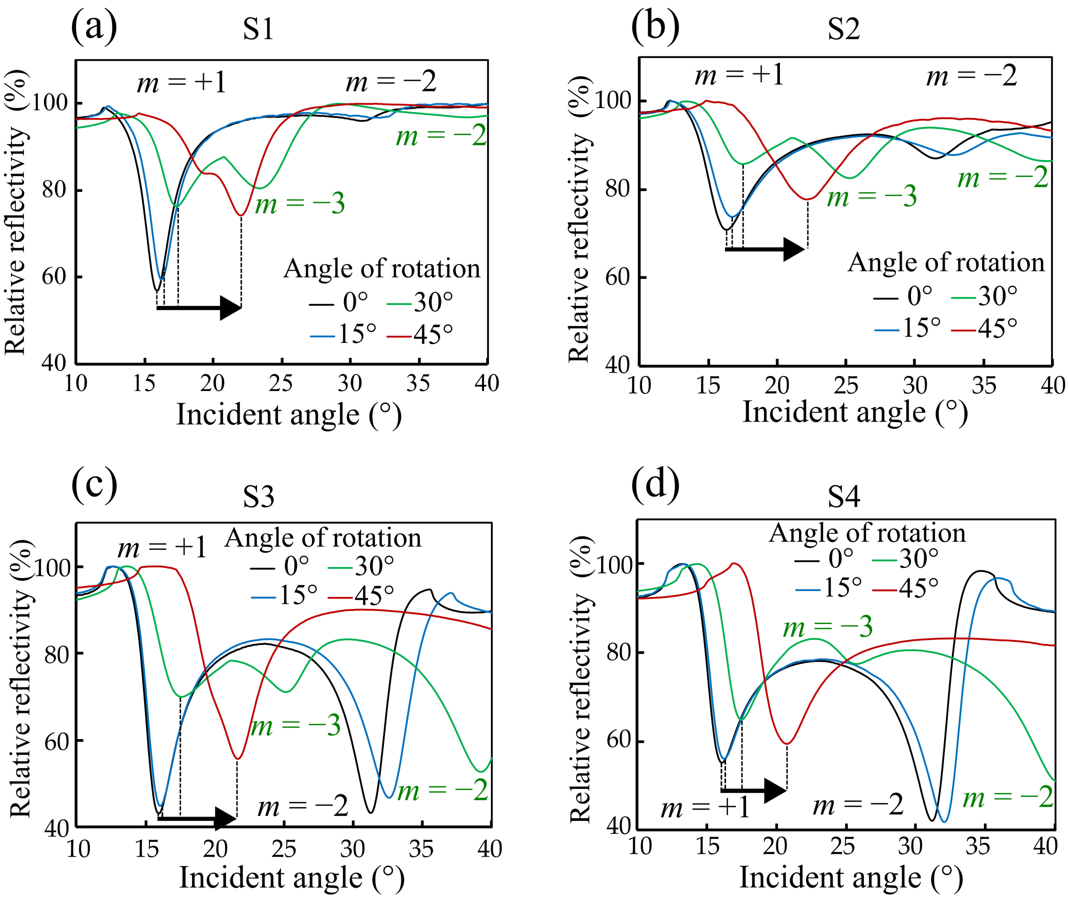

Figure 6.12.: (a-b)(S1-S4) The images illustrate the rotation of the sample during 2D grating measurements and the reflection properties of the 2D grating coupler at rotation angles between 0° and 45°. The results demonstrate that surface plasmons persist even as the sample undergoes rotation, a feature that cannot be achieved with 1D gratings. Following rotation, the plasmon excitation angle for the diffraction orders m = +1, m = −2, and m = −3 shifted to higher incident angles. This shift highlights the resilience of the plasmonic response and underscores the benefit of using 2D gratings to sustain plasmon excitation across varying rotational conditions. (Image from Sarapukdee, P., et al. [209], is licensed under CC BY 4.0.)

The largest shift in the excitation angle occurs at 45° rotation, exceeding the changes observed at other angles. This phenomenon is explained by the theoretical framework presented in [236], which outlines the rules governing grating excitation. The analysis of

Table 6.7.: Results of the plasmon excitation angle and coupling effectiveness of samples S1 to S4 with rotation angles ranging from 10° to 45°. The plasmon excitation angles are shown for +1 and −2 diffraction orders. The $m = -3$ order is seen at a rotation angle of 30°, and the analysis is presented in the summary.(Adapted from Sarapukdee, P., et al. [209], is licensed under CC BY 4.0.)

Rotation	Plasmon excitation angle (∘), Coupling efficiency (CE)							
	S1		S2		S3		S4	
	+1 Order	−2 Order	+1 Order	−2 Order	+1 Order	−2 Order	+1 Order	-2 Order
0°	16.0°, 19.6	31.2°, 0.9	16.4°, 5.9	31.8°, 3.4	16.0°, 25.9	31.2°, 15.8	16.0°, 7.2	31.2°, 12.9
15°	16.2°, 18.5	32.0°, 8.9	16.8°, 5.0	33.4°, 2.6	16.2°, 25.1	32.6°, 13.0	16.4°, 7.0	32.0°, 12.9
30°	17.4°, 5.7	38.6°, 0.4	17.4°, 2.3	40°, 1.9	17.4°, 3.9	39.2°, 9.1	17.6°, 6.1	40.0°, 9.1
		*23.2°, 3.3		*25.4°, 4.0		*25.2°, 6.8		*25.8°, 5.2
45°	20.8°, 5.2	NA, NA	22.4°, 3.7	NA, NA	21.8°, 9.4	NA, NA	20.8°, 6.2	NA, NA

∗ −3 diffraction order

these results, shown in Tab. 6.7, highlights the two diffraction orders with the highest CE. Additionally, with $m = -3$, a third diffraction order can be excited, as illustrated in Fig. 6.12. According to theory [236] and previous research, one of the main factors influencing the plasmon excitation angle is the effective periodicity and size of the grating. As expected, sample rotation introduces new grating periods, leading to significant modifications in the plasmon excitation angle.

For each rotation angle, the effective grating period can be calculated for the +1, −2, and −3 diffraction orders. Notably, for symmetric 2D gratings, the grating period generally increases with rotation. For example, at 0°, the grating periods range from 804 nm to 822 nm, while at 45°, they extend from 903 nm to 941 nm for the +1 order.

The results also demonstrate that a single 2D grating can continuously adjust the plasmon excitation angle between 16° and 40° through rotation, maintaining reasonably good coupling efficiency for the two diffraction orders over the entire range, as shown in Fig. 6.12. Interestingly, as the 2D grating is rotated, a dynamic shift in the surface plasmon excitation angle is observed. The experimental setup can detect incident angles up to 40°, which explains the absence of data for the −2 order at 45° rotation. Nevertheless, the +1 diffraction order shows a clear correlation between the plasmon excitation angle and the rotation angle, making it more useful for sensors due to its higher coupling efficiency compared to the −2 order. For the 30° rotation, two seemingly inconsistent data sets are observed, likely due to the additional resonance from the −3 order.

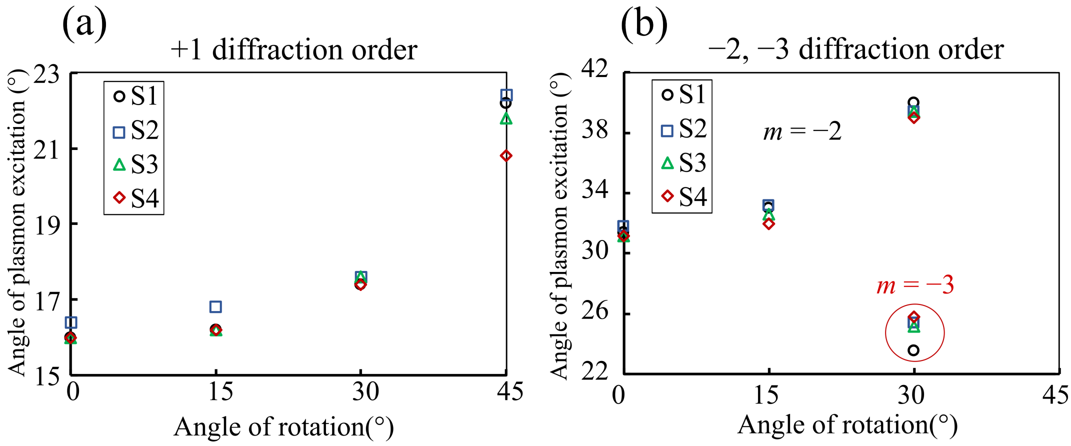

Figure 6.13.: The angle of rotation of a 2D grating correlates with the angle of plasmon excitation for +1 (a) and −2(b) diffraction orders in four separate samples (S1-S4). As the angle of rotation of the 2D grating rises, the angle of plasmon excitation also increases for both +1 and −2 orders. This shows that the plasmon excitation angle for both orders is strongly impacted by grating rotation, indicating a comparable dependence on grating orientation. (Image from Sarapukdee, P., et al. [209], is licensed under CC BY 4.0.)

Fig. 6.13 illustrates the relationship between the plasmon excitation angle and the rotation angle of the grating structure for all diffraction orders, showing a general increase in excitation angle as the rotation angle grows. At 30° rotation, the $m = -3$ order is also observed and depicted in Fig. 6.13 (b). The symmetry of the grating structure suggests that beyond 45° rotation, the configuration repeats itself, returning to its original form.

The 2D grating structure's adjustable plasmon excitation angle might improve detection accuracy in biomedical diagnostics through double-check processes [237, 238] in biomolecular interactions. Adjusting the excitation angle improves the signal-to-noise ratio for detecting low quantities of biomolecules in complex biological samples [239], leading to improved detection limits and accuracy. This may be accomplished by doing successive measurements, with one at the first excitation angle and a second after rotating the sample. This technology allows a single device to acquire two datasets, which can then be used to confirm results. Alternatively, simultaneous measurements using two light beams and detectors positioned at different angles enable real-time comparison and validation. Both techniques increase specificity, reduce false positives and negatives, and improve the reliability of biomolecular detection.

6.6.2. Utilizing the Position on Gradient Grating Structures

In the previous experiment, all samples were designed and built with a constant value for grating period length over an entire area, including 2D grating. As a consequence, the results of a surface plasmon were relatively stable. The experiments, however, demonstrated that the results of the dynamics could be found in the 2D grating by rotating a sample. Hence, this study will add more dynamic value to the investigation of the behavior of silver-based gratings by building a grating in which the length of the gap g between grating rods changes continuously along the x-axis. This grating structure is known as a gradient grating periods (GGPs). GGPs have been investigated in the context of guided-mode resonance (GMR) [228, 240]. The grating structures in this work were made with the following values: a fixed 400 nm grating size w, but the distance between the grids varies from 200 to 600 nm, a step of 1 nm every four grids, and an area size of 1.3 mm^2. With this configuration, the resulting grating period was 1000 nm at the beginning and 600 nm at the end of the grating area. The other parameters were taken from Sec. 6.2 for establishing the metal layer thickness.

To evaluate the reflectivity characteristics, an optical measurement system is employed. Notably, the laser spot used for the optical measurements is carefully placed at three distinct locations within the grating area. The laser beam is centered at 0.35 mm, 0.75 mm, and 0.95 mm from the edge that corresponds to the side of the grating with the shorter period, as shown in Fig. 6.14.

The results of the measurements reveal that when the beam spot is positioned on the left side, where the gap is smallest, the plasmon excitation angle is 14.0° with a coupling efficiency (CE) of 6.5. Referring to the relationship between the plasmon excitation angle and a constant grating period, as outlined in previous research [33], the predicted

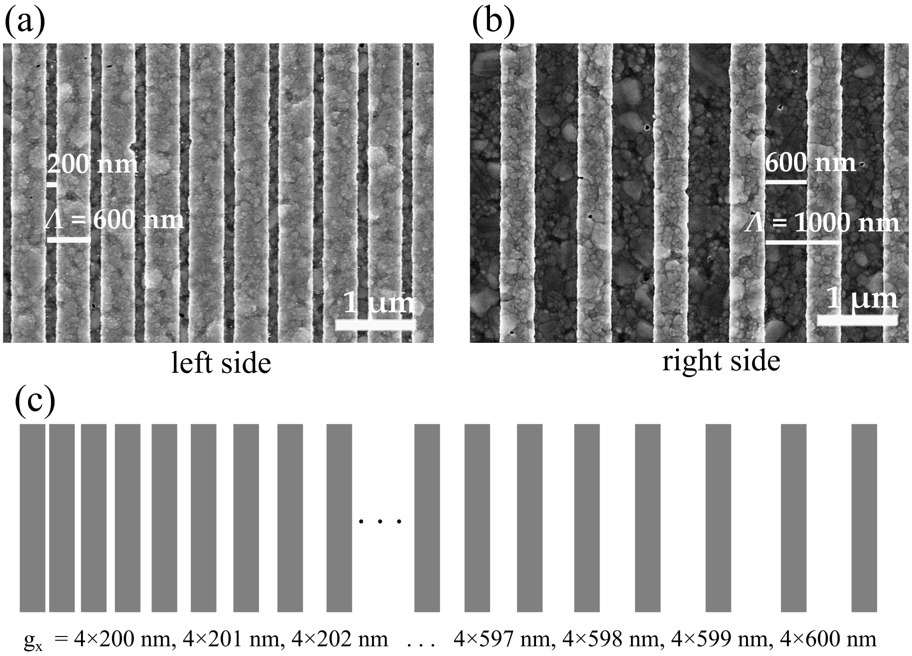

Figure 6.14.: SEM images of a manufactured gradient grating show a shorter period (a) on the right and a longer period (b) on the left. (c) The design of the sample, with different spot areas, demonstrates that the gap changes along the x-direction. (Image from Sarapukdee, P., et al. [209], is licensed under CC BY 4.0.)

plasmon excitation angle for an average grating period of 721 nm is 10.6°, compared to the measured angle of 14.0°. In the center position, the plasmon excitation angle is 19.4° with a CE of 8.9, and the calculated angle is 16.5°. On the right side, which has the largest gap, the plasmon excitation angle is 22.8° with a CE of 13.2, while the calculated angle is 20.8°. These findings are summarized in Tab. 6.8, showing a higher experimental plasmon excitation angle than predicted based on the average grating period size.

These observations suggest that as the laser beam spot moves from left to right, the plasmon excitation angle and coupling efficiency increase, in line with the growing gap size. The discrepancy between the experimental and calculated values suggests that regions with larger gaps in the gradient grating structure exert more influence on the plasmonic behavior. The experimental results consistently exhibit larger excitation angles than those expected for constant grating period sizes, likely due to the greater contribution

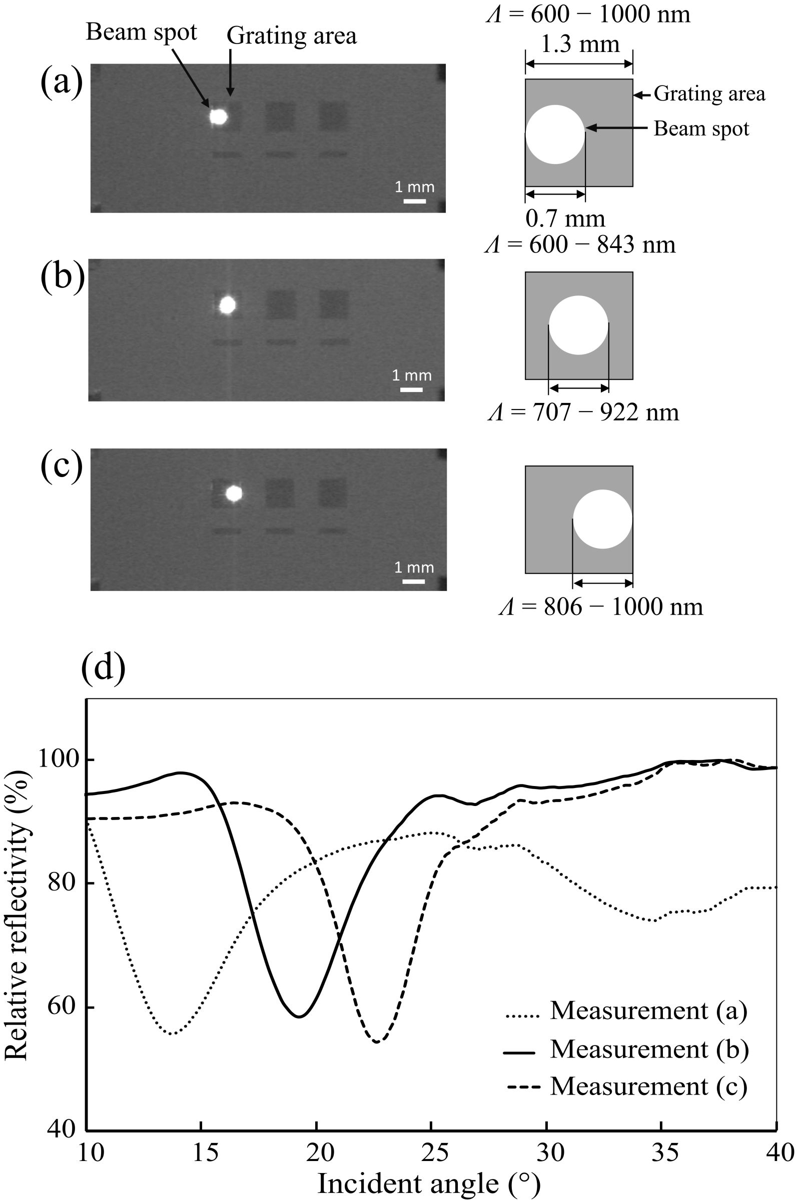

Figure 6.15.: (a-c) Images depict three distinct grating areas of the sample with the beam spot located at various points: (a) the left side with a smaller gap (grating range: Λ = 600-843 nm), (b) the middle area (grating range: Λ = 707-922 nm), and (c) the right side with a larger gap (grating range: Λ = 806-1000 nm). The bright spot indicates the beam position in each scenario. (d) The graph illustrates the plasmon excitation angles achieved from different beam spot locations on the grating, demonstrating that a single grating device can generate multiple plasmon excitation angles by shifting the beam spot position. (Adapted from Sarapukdee, P., et al. [209], is licensed under CC BY 4.0.)

Table 6.8.: Measurement results of position on gradient grating structure, (a-b) for plasmon excitation angle and coupling efficiency (CE). (Table from Sarapukdee, P., et al. [209], licensed under CC BY 4.0.)

Measurement	Λ (nm)	SPR angle (°), CE	Averaged Λ (nm)	SPR angle (°) (theory)
(a)	600-843	14.0°, 6.5	721	10.6°
(b)	707-922	19.4°, 8.9	815	16.5°
(c)	806-1000	22.8°, 13.2	903	20.8°

of larger gaps to the effective coupling of incident light to plasmon modes. This enhanced interaction underscores the role of gradient grating designs, where varying gap sizes create a more complex plasmonic response compared to uniform gratings.

However, the gradient grating's efficiency, reflected in a relative reflection of approximately 55%, is lower compared to conventional structures. The design and fabrication of a grating with multiple lengths also present challenges. Despite these limitations, the gradient grating approach introduces a novel aspect to grating design, offering a potential pathway for applications where adaptability is prioritized over uniformity.

Gradient grating structures represent a significant innovation in biosensor technology, providing unparalleled flexibility and efficiency for biomolecule detection. Traditional biosensors often require custom designs and fabrication for each target molecule, slowing down development and increasing costs. In contrast, gradient gratings, with their ability to manipulate light through varying refractive indices and adjustable excitation angles, create a versatile 'all-in-one' platform [241]. By directing light at different grating periods, users can optimize the signal-to-noise ratio across a wide range of biomolecules without constant redesigns. This adaptability is particularly advantageous for detecting biomolecules that induce large refractive index changes upon binding [242, 243], allowing for a broader detection range through simple angle adjustments. Consequently, gradient grating biosensors can accelerate research and improve productivity in biomedical diagnostics. Their ability to deliver accurate and reliable measurements across diverse applications highlights their potential to revolutionize biomolecule detection, offering more efficient and cost-effective sensing solutions.

The experimental setups discussed in this study highlight the feasibility of designing grating structures that can generate multiple plasmon excitation angles from a single grating sample. This versatility provides a significant advantage over fixed-spacing gratings, making it suitable for a broader range of applications.

This study has shown that surface plasmon polaritons can be efficiently excited using silver-based 2D grating structures. With more adjustable parameters than 1D gratings, these structures offer greater flexibility, allowing for dynamic application depending on the needs. Notably, two diffraction orders can be excited with high coupling efficiency, enabling continuous access to a range of plasmon excitation angles between 16° and 40°. Additionally, 2D gratings exhibit anisotropic behavior, which facilitates the independent measurement of strains or deformations along different axes. This is especially useful in applications like strain sensing, where distinguishing between axial and transverse strains is crucial.

Both gradient grating period (GGP) and 2D grating structures provide multi-parameter sensing capabilities, surpassing the limitations of conventional 1D gratings and traditional SPR sensing methods. These advanced grating designs pave the way for the development of high-performance, versatile, and compact optical sensors, with promising applications in areas such as biosensing, environmental monitoring, and structural health monitoring.

6.7. Measurement of Biological Samples

In this section, following an initial study on the structural properties of various grating configurations and metal layer thicknesses, the present experiment aims to demonstrate the feasibility of employing grating-coupled surface plasmon resonance (SPR) for biomolecular detection. The designed grating structure consists of a period (Λ) of 800 nm, a silver layer thickness b of 100 nm, and a grating height h of 50 nm. For biomolecular testing, protein A, a molecule purified from *Staphylococcus aureus* and human immunoglobulin G were selected. These biomolecules serve as commonly used reference models in biosensor studies [244, 245]. Fig. 6.16(a) illustrates the fundamental working principle of grating-based biological detection. In this system, the excitation of surface plasmons is influenced by variations in the permittivity of the sample medium, enabling the detection of biomolecules. Two primary detection strategies are employed:

- Antibody-based detection (Fig. 6.16(b), left): The antibody is immobilized on the grating surface to selectively bind a specific antigen present in the sample solution.
- Antigen-based detection (Fig. 6.16(b), right): The antigen is immobilized to capture a corresponding antibody.

In both cases, biomolecular interactions induce changes in the refractive index, which are detected through variations in plasmon excitation. The experimental procedure consists of three main steps:

1. Sample Preparation: Protein A (42 kD, P6031, Sigma-Aldrich, USA) and IgG (IgG; 150 kD, I4506, Sigma-Aldrich, USA) were dissolved in phosphate-buffered saline (PBS, pH 7.4, Life Technologies, UK), deposited onto the grating surface, and dried before measurement.
2. Solution Containment: A circular rod-shaped barrier was placed around the grating area to localize the solution and prevent it from spreading beyond the sensing region.
3. Microfluidic Integration: A polydimethylsiloxane (PDMS) microchannel was attached to the grating structure to facilitate controlled fluid flow during measurement.

Subsequent sections provide a detailed analysis of each experimental step and discuss the obtained results.

6.7.1. Biological Sample Measurement I

In this part, Protein A and immunoglobulin G (IgG) bind in a stoichiometric ratio of 1:2, as dictated by their respective solution concentrations [246]. Hence, Protein A was

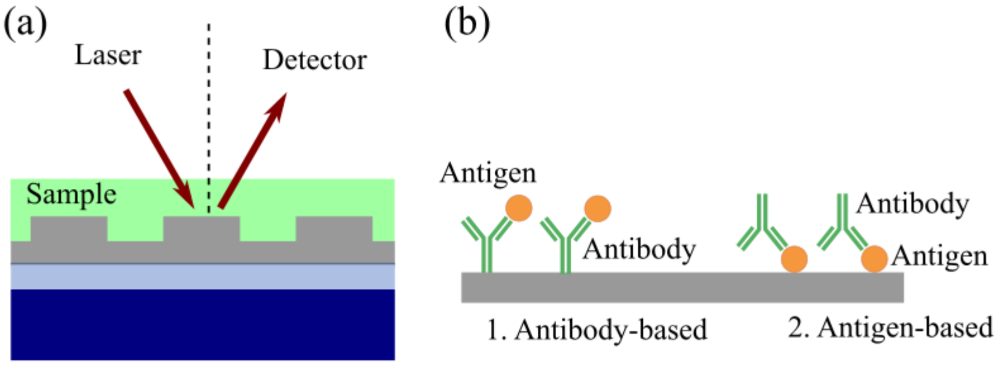

Figure 6.16.: (a) Schematic of the grating arrangement with the biological sample positioned above the metal layer. (b) Illustration of the antigen-antibody detection principles: antibody-based (left) and antigen-based (right) detection mechanisms.

prepared at a concentration of 5 μM in phosphate-buffered saline (PBS), while the IgG solution was prepared at 10 μM in PBS. Fig. 6.18 depicts the physical immobilization process on the grating structure.The detailed procedure for biomolecule detection using the grating structure, illustrated in Fig. 6.17, is outlined below:

1. Measure the baseline plasmon excitation signal from the grating structure prior to biomolecule immobilization, also referred to as the blank signal.
2. Clean the grating structure using phosphate-buffered saline (PBS), and then measure again to establish a second baseline reflecting the buffer solution environment.
3. Deposit the first biomolecule layer onto the grating. For the antibody-based approach, 5 μL of IgG solution is applied, while 5 μL of Protein A solution is used for the antigen-based approach. The samples are allowed to dry before measuring the plasmonic response, recorded as the first-layer signal.
4. Apply the second biomolecular layer onto the first layer. In the antibody-based approach, Protein A solution is deposited, whereas in the antigen-based approach, IgG solution is applied. After drying, the plasmonic response is measured, producing the second-layer signal.

5. Rinse the grating surface with DI water for two minutes and allow it to dry. The final measurement post-cleaning is recorded to assess the DI water cleaning signal.

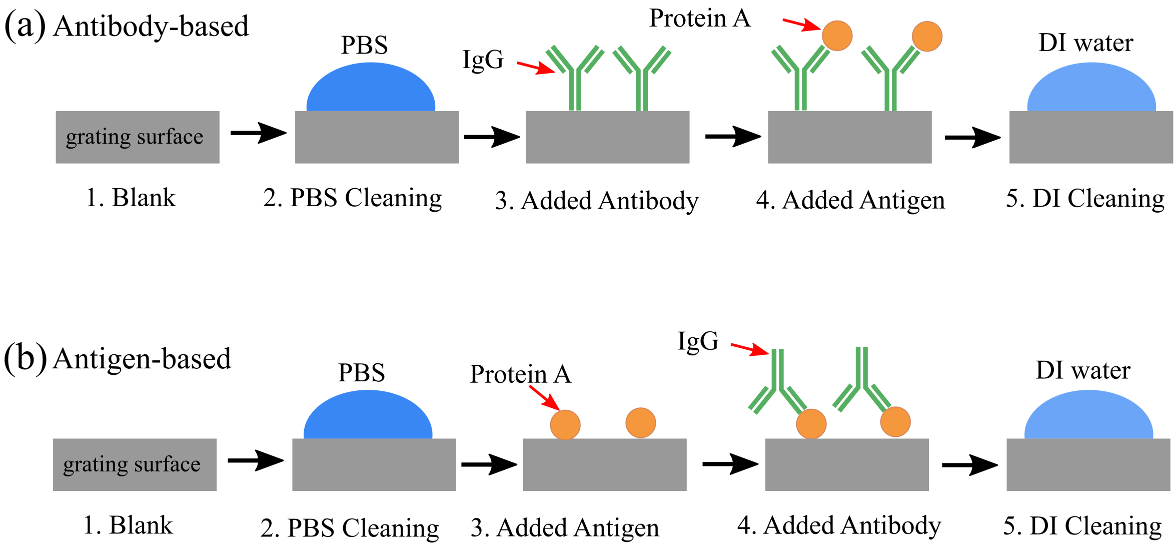

Figure 6.17.: Physical immobilization procedure for grating-coupled sensors: (a) Antibody-based approach, beginning with the IgG antibody layer followed by Protein A as the target antigen. (b) Antigen-based approach, initially immobilizing Protein A followed by IgG as the target molecule. The process concludes with DI water cleaning.

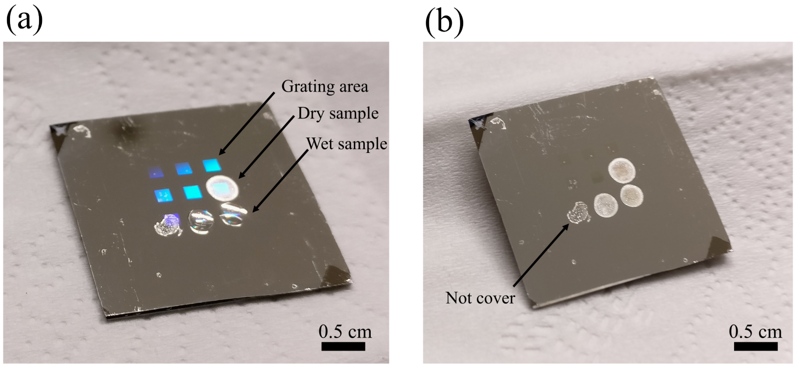

Figure 6.18.: (a) Sensor chip featuring nine grating regions designed for SPR sensing, with designated areas for wet and dry biomolecule applications. (b) Post-drying observations show uniform sample coverage except in the lower-left grating area, indicating incomplete coverage.

The data on biomolecules examined using antigen-based antibodies are presented in Tab. 6.9. Throughout the experiment, all changes occurring at each step were syste-

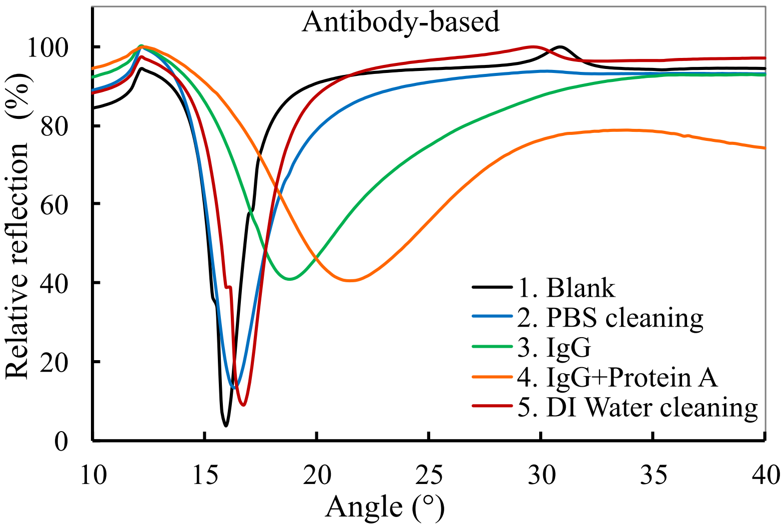

Figure 6.19.: Comparison of antibody-based antigen detection on the grating-coupled sensor against air baseline. The addition of IgG increased the plasmon excitation angle from 16.4° to 18.8°, with a further increase to 21.6° upon addition of Protein A. (Adapted from Sarapukdee, P., et al. [82], is licensed under CC BY 4.0.)

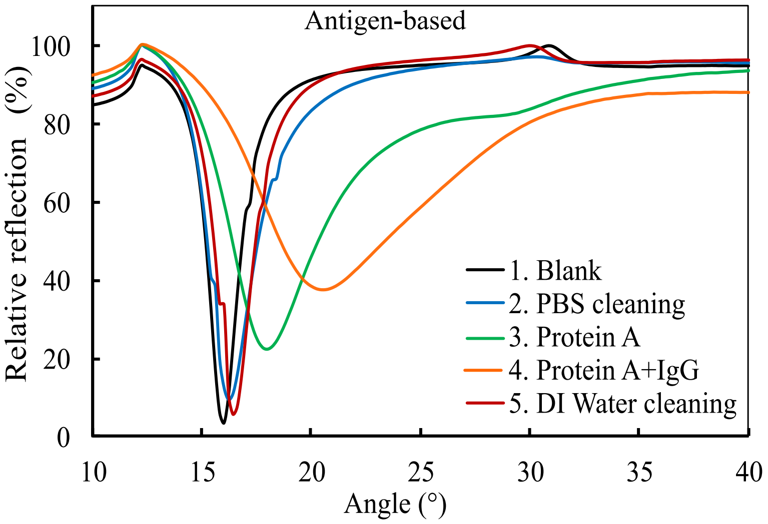

Figure 6.20.: Antigen-based measurements on the grating-coupled sensor with comparison to the air baseline. Protein A increases the plasmon excitation angle from 16.2° to 18.0°, with a subsequent increase to 20.6° after IgG application.

matically monitored. The detection of biomolecules was carried out by investigating the plasmon excitation angle of the samples, enabling the tracking of modifications in the

Table 6.9.: Results of biological testing with antibody- and antigen-based techniques.

Method	Plasmon excitation angle (°)and relative reflection(%)				
	Blank	PBS cleaning	1^{st} layer	2^{nd} layer	DI cleaning
Antibody-based	16.0°; 3.59%	16.4°, 13.32%	18.8°, 40.74%	21.6°, 40.65%	16.8°, 8.89%
Antigen-based	16.0°, 3.53%	16.2°, 9.51%	18.0°, 22.37%	20.6°, 37.51%	16.4°, 5.81%

grating structure. Fig. 6.19 and Fig. 6.20 illustrate the relative reflection chart corresponding to the plasmon excitation angle for both the antibody- and antigen-based methods, with excitation angle values detailed in Tab. 6.9.

The initial measurement was conducted using an air-based analytical layer to confirm the integrity and functionality of the grating structure. The results established a baseline signal at an excitation angle of 16° for both methods. Following this, the grating surface was cleaned with a buffer solution, which also served as a solvent for the biomolecules. This step aimed to ensure that the grating surface closely resembled the biomolecular solution environment. After PBS cleaning, the maximum plasmon excitation angle exhibited a slight increase, ranging from 16.2° to 16.4°. This shift suggests the possible formation of a thin PBS film on the grating surface, potentially influencing the analyte layer.

In the next step, the first analyte layer was deposited over the grating structure using an IgG antibody solution for the antibody-based approach and a Protein A solution for the antigen-based approach. The results indicated that the maximum plasmon excitation angles increased to 18.8° and 18.0° for IgG and Protein A, respectively. The larger shift observed for IgG can be attributed to its higher concentration, leading to a more pronounced plasmon excitation angle shift.

Subsequently, the biomolecule solution was applied as a second layer, allowed to dry, and re-measured. The results demonstrated a further shift in the plasmon excitation angle away from the baseline. Specifically, in the second layer of the Protein A experiment, the excitation angle increased to 21.6°, while in the IgG antibody experiment, it reached 20.6°. These findings confirm that the grating structure effectively differentiates analyte layers based on the plasmon excitation angle shift, which can serve as a detection indicator.

Additionally, the results suggest that the coupling between the grating and the previously deposited biomolecules was less effective. The relative reflection values for antibody- and antigen-based approaches were 40.65% and 37.51%, respectively. Despite identical total solution concentrations at the end of both experiments, the antibody-based method resulted in an excitation angle approximately 1° higher. This observation indicates that the first-layer molecules exert a greater influence on surface plasmon excitation than the second-layer molecules.

In the final step, the sample was rinsed with deionized (DI) water and re-evaluated. The results showed that the grating structure recovered its excitation angle, returning close to the PBS-washed baseline. Furthermore, Fig. 6.18 provides an image of the dried solution on the grating surface. Ideally, the solution should uniformly cover the entire grating area. However, Fig. 6.18(b) reveals potential inconsistencies in solution control within the designated area. This issue will be addressed in future experiments.

6.7.2. Biological Sample Measurement II

There was an issue with controlling the position of the liquid droplet after the experiment to measure the biomolecules on the grating structure in Sec. 6.7.1. Thus, additional bars were built around the grating structure in this experiment to keep the solvent in a specific area. The amount of solution was controlled by adding a bar around the grating area, resulting in a more consistent thickness of the substance after drying. The bar around the grating area was built by silver thermal deposition at the height of 300 nm, with a bar size of 100 nm and an average cross-section of 2.5 mm. The six grating areas were built on the same wafer, as shown in Fig. 6.21. The experimental procedure was identical to the preceding experiment in Sec. 6.7.1. Before and after the experiment, the gratings were analyzed. Before testing, biomolecules were instead prepared in this experiment as follows. In a microtube, 5 μM of IgG and 10 μM of Protein A were combined for at least one hour at 37 degrees Celsius. In order to allow the molecules to

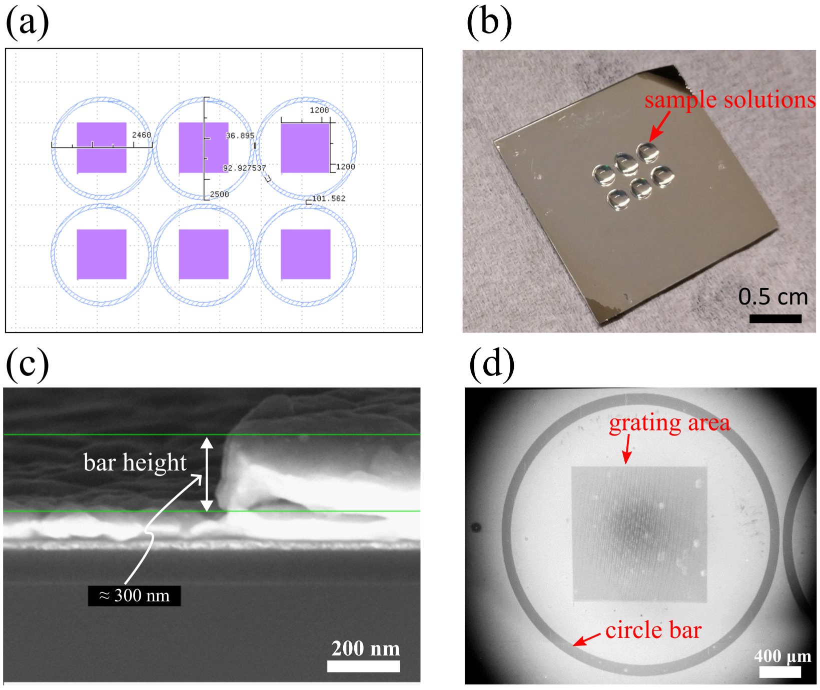

Figure 6.21.: (a) Around the six grating areas, a circle bar was designed. (b) The droplet of sample solution atop the grating structures. (c) The SEM image of the silver circle bar's cross-section measured about 300 nm in height. (d) The SEM of the grating area with the circle bar.

combine into a solution, it is necessary to permit their interaction. Then, according to the procedure, the solution was evaluated, and the angle of plasmon excitation was compared. The following are the results of this experiment: first, in Fig. 6.22, the SEM image of the grating with a bar before and after the biomolecular solution was dropped over. Fig. 6.22(a) shows the success of defining the solution's area to cover only the specified portion. The biomolecule solution dropped into the solution boundary and was found to be clearly defined in the ring. Fig. 6.22(d) depicts a layer of biomolecules adhering to the grating. Second, Fig. 6.23 illustrates the results of the relative reflection of the six grating surfaces, with angle details provided in Tab. 6.10. The measured excitation angles of all grating structures averaged 16°, with a baseline signal reflectance of 5.54%. Overall, this demonstrates that the grating structure could be successfully built according to the specified configuration. The grating structures were then tested using the prepared antigen-antibody biomolecule solutions. As a result, the plasmon excitation angle of the

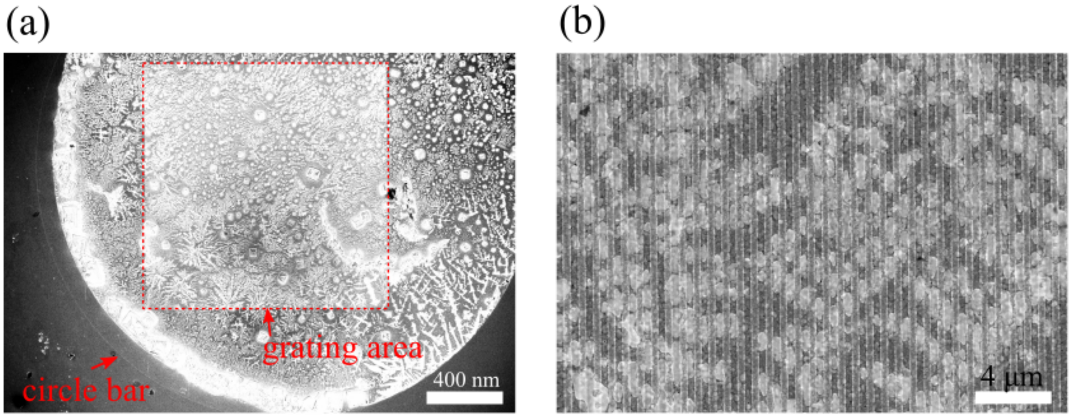

Figure 6.22.: (a) The SEM image of the grating area with added circle bar around the grating structure after the solution dried, the solution was enclosed only inside the circle region. (b) The morphology of the antigen-antibody molecules demonstrates that the molecules were successful in covering the grating structure.

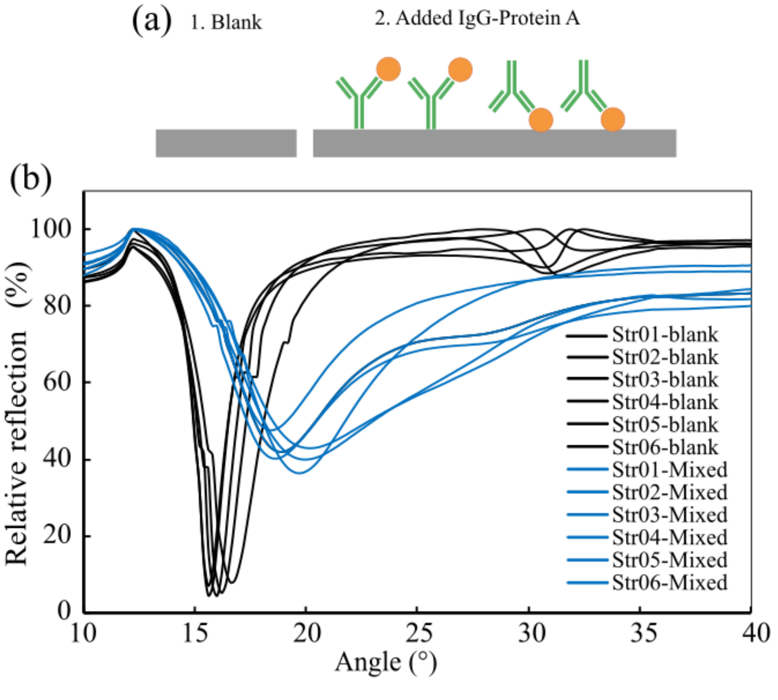

Figure 6.23.: (a) The procedure of grating structure examination of the antibody IgG combined with Protein A, and (b) the results of relative reflection of six grating structures with an added circle bar.

grating was shifted to an average of 19.3°, and the relative reflection was increased to 41.51%. Consequently, the plasmon excitation angle was shifted by an average of 3.3°

Table 6.10.: Grating structures examined the biological sample, antibody IgG combined with Protein A.

Structure	Plasmon excitation angle(°), Relative reflection (%)	
	Blank	Antiboy IgG + Protein A
1	16.0°, 4.23%	18.8°, 41.94%
2	16.2°, 5.06%	20.2°, 42.90%
3	15.6°, 4.60%	18.4°, 47.58%
4	16.0°, 4.48%	18.6°, 40.25%
5	16.6°, 7.89%	20.0°, 39.87%
6	15.6°, 6.97%	19.6°, 36.51%
Average	16.0°, 5.54%	19.3°, 41.51%
SD	0.35°, 1.39%	0.70°, 3.37%

relative to the baseline signal. In contrast, when compared to experiment Sec. 6.7.1, which was dropped by two biomolecule layers, the average plasmon excitation angle was 21.1°, a 4.8° shift over the baseline signal. In conclusion, two layers of the biomolecules solution from experiment Sec. 6.7.1 resulted in a more extensive solution than one layer from this experiment. This also explains why the final concentration of biomolecules over the grating after two drops of solution dried was greater than a single drop.

6.8. Grating-Based SPR Sensor with PDMS Microchannel

The grating structure was able to detect changes in the biomolecules layer on top of the grating structure in the grating measuring biomolecules experiments described in Sec. 6.7.1 and Sec. 6.7.2. As a result, the samples that were dried before being measured in both experiments may only be suitable for certain applications. Most biomolecules, however, are typically measured in solution form [247]. Therefore, the use of a microchannel attached to the grating structure and the sample solution feed passed through the tube to perform the biomolecule measurement was considered in this experiment. Polydimethylsiloxane (PDMS) is commonly used as the molding material for microchannels

[248] due to its flexibility, transparency, biocompatibility, gas permeability, low dielectric constant, low surface tension, and conformal contact with surfaces. These are some of the PDMS characteristics selected for rapid prototyping. PDMS is also utilized in numerous surface plasmon applications, such as biosensor microsystems [249], microchannel with embedded prism [250], biomedical applications [251], and optical fiber sensing [252]. PDMS was chosen as the microchannel material for this experiment. Sec. 5.3.2 describes the process of fabricating the microchannel with a height of 150 μm. As for the grating structures, the same configuration values as the previous experiments in Sec. 6.7.1 were used, specifically 800 nm of the grating period, 100 nm of silver-based thickness, and 50 nm of the grating height, and the experiment utilized the same optical system as the previous experiment. As shown in Fig. 6.24, the complete sensor unit, grating with microchannel, was mounted in the sample holder, and the laser spot was aligned with the grating structure. Further, the molecules in the experiment were Protein A solution at a concentration of 5 μM in pH 7.5 PBS buffer. To be specific, the practical steps were as follows. Further, the molecules in the experiment were Protein A solution at a concentration of 5 μM in pH 7.5 PBS buffer. To be specific, the practical steps were as follows.

1. The grating structure without attaching a PDMS channel was measured to be used as a baseline signal.
2. PDMS was attached to the grating substrate. Then, the grating with PDMS was measured.
3. PBS buffer solutions were injected into the microchannel, and then the grating structure was measured.
4. The protein solutions were added to force the PBS buffer out of the microchannel, replaced, and then the grating structure was measured.

Fig. 6.25 shows the result, while Tab. 6.11 provides specific details. The results indicate that the effect of the plasmon excitation angles obtained with the PDMS microchannel and without a microchannel, the grating performed identically at 16.6°, and there was a

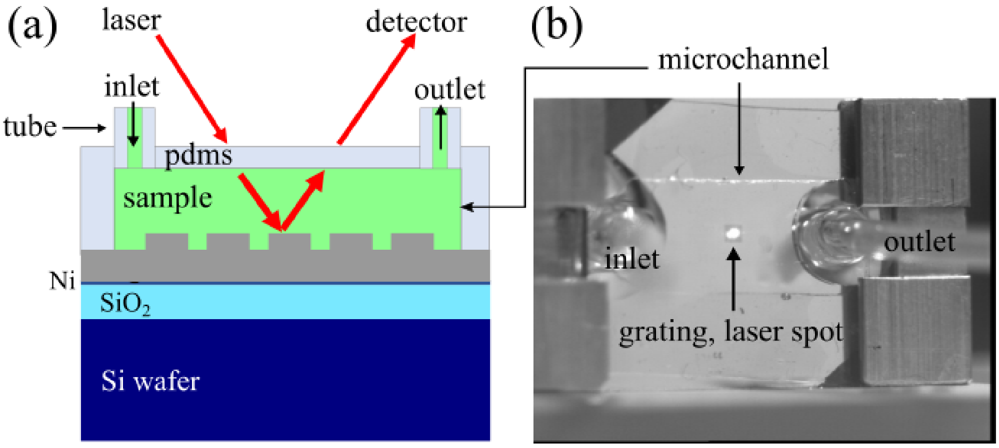

Figure 6.24.: (a) Sketch of grating structure with PDMS microchannel, and (b) the silver grating was mounted in the sample holder with laser beam alignment on the grating area. (Adapted from Sarapukdee, P., et al. [253], is licensed under CC BY 4.0.)

Table 6.11.: The result of the plasmon excitation angle of grating with PDMS microchannel measured the Protein A solution.

Configuration	Plasmon excitation angle(°), Relative reflection (%)		
	Blank	PBS	Protein A
Grating	16.6°, 23.67%	-	-
Grating with PDMS	16.6°, 23.42%	41.6°, 31.54%	43.6°, 30.37%
Sensitivity (°/RIU)		74.67	79.78

small difference in the signal after the larger scan angle after 20°. This result demonstrated that the PDMS microchannel had little effect on the detection. Consequently, this demonstrates that the decision to use PDMS as a solution-containment channel was appropriate. Following this, the buffer solution was introduced into the system. As a result, the excitation angle of plasmons shifted to 41.6° with relative reflection at 34.54%. In addition, the Protein A solution caused a further shift to 43.6° with relative reflection at 30.37%. As reported in these studies [254–257], the refractive index of PBS buffer and Protein solution were 1.3348 and 1.3384, respectively. The sensitivity of the sensor could be determined using Eq. 3.1, (41.6-16.6)/(1.3348-1.0)= 74.67; by PBS solution test and (43.6-16.6)/(1.3384-1.0)= 79.78; by Protein solution test. It can be concluded that the grating sensor with PDMS microchannel has an average sensitivity of approximately

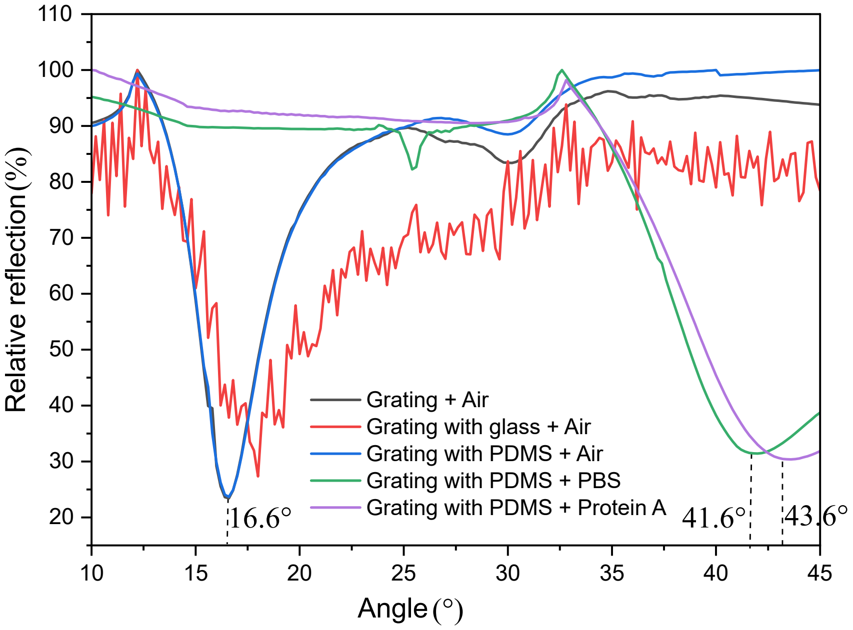

Figure 6.25.: The results display three different configurations of grating SPR sensor measurement air: a grating structure, a grating with a cover glass channel, and a grating with a PDMS microchannel. The grating with cover glass channel (black line) had an interference signal from glass reflection, while the grating with and without PDMS microchannel behaved identically at 16.6°. The plasmon excitation angle shifted from 16.6° to 41.6° when the PBS buffer solution was introduced into the system. Ultimately, the system detected an additional shift in the plasmon excitation angle to 43.6° upon injecting the Protein A solution.(Adapted from Sarapukdee, P., et al. [253], is licensed under CC BY 4.0.)

$77.23°/RIU$. This experiment ultimately demonstrated the viability of selecting PDMS as a microchannel and employed the grating structure to identify biomolecular solutions.

6.9. Long-Term Preservation

This section discusses the issues of using silver as a plasmonic material in a silver-based plasmonic grating for a biosensor. The effect of the improperly retained grating will be described first. Following that, the various methods for surface reconditioning were investigated. Finally, a surface coating method will be proposed.

6.9.1. Stability of Silver Surface

Silver is one of the best plasma materials in the visible and near-IR range [258, 259]. However, a thin silver layer degrades in the air, typically sensitive to sulfidation and can form silver sulfide [260, 261]. These effects lead directly to the surface optical properties, affecting the use of biosensor structures. In this experiment, grating structures with the following configuration were fabricated: 800 nm of the grating period, 100 nm of silver-based material, and 50 nm of grating height. These gratings were kept in a common room environment in order to be exposed to air. Next, the surface plasmon properties of the grating samples were investigated using measurements after storing the sample for 1, 5, and 8 weeks. Fig. 6.27 shows the results that when the air exposure time was increased, the plasmon excitation angle increased; the angle of the first order was shifted forward from 16° to 16.8° and 17.4 ° for one, five, and eight weeks, respectively. Similarly, for one, five, and eight weeks, the relative reflection increased from 4.05% to 5.58% and 12.83%, respectively. In contrast, for the plasmon excitation angle of the second order was shifted backward from 31.4° to 30.6° and 30.0°,for one, five, and eight weeks, respectively. Simultaneously, the relative reflection increased from 83.08% to 85.08% and 86.56% after one, five, and eight weeks. In Tab. 6.12, the comparison of measurements shows the

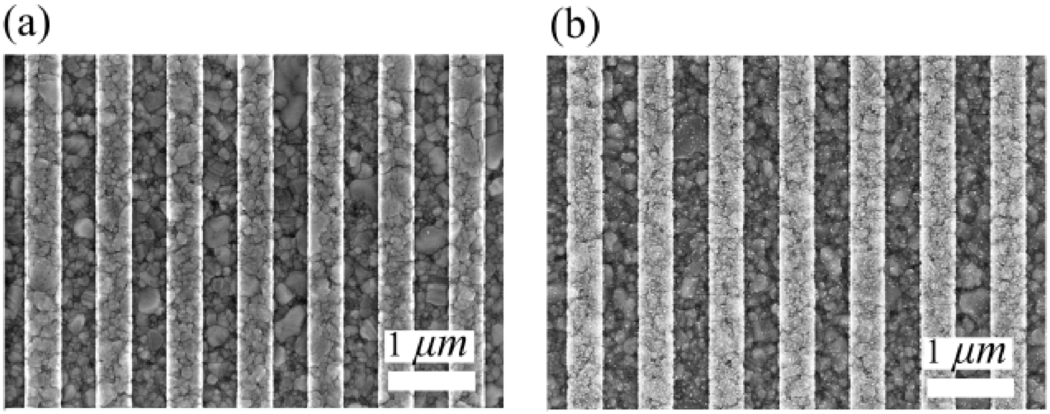

Figure 6.26.: SEM images of the silver grating, (a) the samples were kept in common room conditions for one week, and (b) the oxide particles were formed on the surface after eight weeks.

results of the plasmon excitation angle change in detail. Again, the results show that the diffraction grating structure has both first and second order. To summarize, the results of this experiment show that the silver surface reacts with air, resulting in the formation of nanoparticles on the surface, as shown in Fig. 6.26. Particles adhere to the surface of the silver grating in the SEM image. According to the literature [107], the nanoparticles could be silver oxides (Ag_2O) or silver sulfides (Ag_2S). Therefore, the protection layer on silver surfaces must be considered otherwise stored in vacuum conditions or innate air to prevent tarnishing.

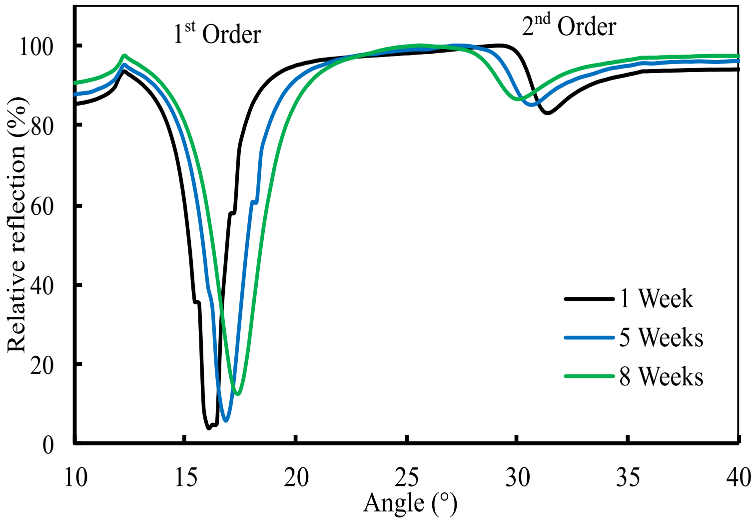

Figure 6.27.: The image shows the plasmon excitation angle of a sample stored in a common room condition for one, five, and eight weeks. The plasmon excitation angle shifts to a lower value over time, indicating a degradation of the plasmonic properties of the sample. The plasmon excitation angle for the first order shifted by approximately +0.8° at five weeks and +1.4° at eight weeks.

Table 6.12.: The sample's plasmon excitation angle after one, five, and eight weeks of storage in a common room is displayed in the result.

Duration	Plasmon excitation angle(°), Relative reflection (%)	
	1^{st} Order	2^{nd} Order
1 week	16.0°, 4.05%	31.4°, 83.08%
5 weeks	16.8°, 5.58% (+0.8°)	30.6°, 85.08% (-0.8°)
8 weeks	17.4°, 12.83% (+1.4°)	30.0°, 86.56% (-1.4°)

6.9.2. Surface Reconditioning

The tarnishing of silver-based grating couplers is most likely the result of sulfidation [260, 262, 263], but oxidation-induced corrosion must also be considered. Therefore, four distinct treatments were selected. Thermal and chemical treatments are used to remove silver oxide, and an electrochemical method for removing silver sulfide has been researched. Finally, the possibility of achieving a smoother surface by applying an additional layer of silver was investigated. Using scanning electron microscopy, the grating morphology [264–266] and surface plasmon characteristics were compared for the various treatments after treatment.

Thermal Treatment

The silver oxide is the particle's expectation on the silver grating surface. Therefore, the reaction of silver oxide is decomposed as follows the equation [267]:

$$2Ag_2O \rightarrow 4Ag + O_2 \tag{6.2}$$

The reaction occurs at high temperatures and low pressure to remove the silver oxide particle from smooth silver surfaces [268]. Previous work [269] reported that the optimum condition was reported by the preliminary experiment. Because the melting point of silver is 960.8°C [270], the temperature used to decompose the silver oxide must not be close to the melting point in order to prevent the structure from deforming. To begin the thermal treatment, the silver grating was cleaned and dried. The sample was then heated to 250°C for 60 minutes at a pressure of 1 $mTorr$ with maintained nitrogen gas. For this process, the PECVD system (PlasmaLab 80plus, Oxford Instruments) was used as a heater and pressure controller. The sample was removed and cooled to room temperature after being heated. The sample was then measured for optical properties, and the surface was examined with a scanning electron microscope. SEM images of the silver grating surface before and after thermal treatment are shown in Fig. 6.28(a, b). The

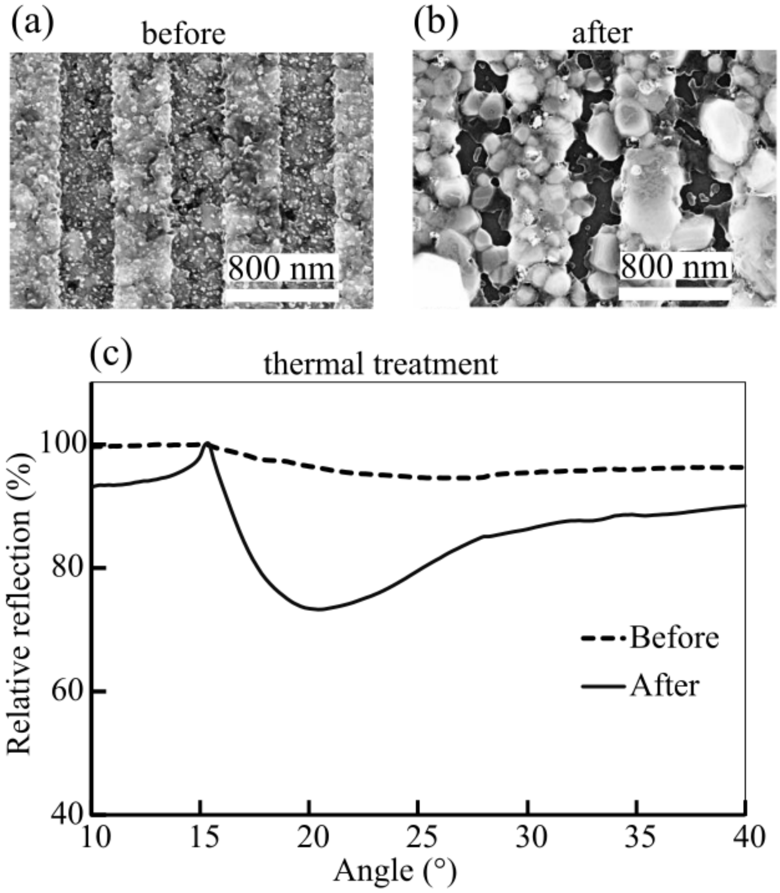

Figure 6.28.: SEM images of the grating surface before (a) and after (b) thermal treatment were compared. The samples were heated at 250°C for 60 minutes. The amount of tarnish was reduced after treatment, but the grating showed signs of deformation. (c)The relative reflection before and after thermal treatment restored the optical properties by approximately 20%. (Reprinted with permission from [271] ©Optical Society of America.)

grating structures can be seen to be slightly damaged. However, measuring the plasmon excitation angle as shows in Fig. 6.28(c), restored approximately 20% of the relative reflection.

Chemical Treatment

This chemical treatment required the removal of silver oxide from the silver surface. According to the literature [272], oxidation on a silver surface can be used as a chemical reaction to remove a tarnish using ammonia, as follows the equation:

$$Ag_2O + 4NH_3 \cdot H_2O \rightarrow 2[Ag(NH_3)_2]OH + 3H_2O. \tag{6.3}$$

The ammonia solution (25% NH_3, Sigma-Aldrich, US) was heated to 70°C to accelerate the reaction. The sample was then thoroughly cleaned with IPA and dried before being immersed in the ammonia solution for 10 minutes. The sample was then rinsed with DI water to stop the reaction before being cleaned again with IPA. Finally, the sample was allowed to dry before measuring the optical properties and inspecting the surface with a scanning electron microscope. The chemical treatment result is shown in Fig. 6.29. As can be seen, the chemical reaction results in a slight decrease in particle quantity. SEM The cleaned surface is shown in Fig. 6.29(b). Again, the relative reflection decreases by about 30% when compared to the untreated.

Electrochemical Treatment

Due to its association with atmospheric impurities, silver sulfide is the most commonly tarnished silver surface [261, 273]. The blackish film that formed made these artifacts unsuitable for optical properties. The most common method for cleaning the silver surface is electrochemical galvanic coupling with a piece of aluminum (anode), but an external power source can also be used. During the reaction, a current flows between the metals and the silver sulfide can be described by the following equation [274, 275]:

$$Ag_2S + 2Al + 3H_2O \rightarrow Ag + 3H_2S + Al_2O_3. \tag{6.4}$$

Aluminum and a sodium bicarbonate electrolyte (0.05M $NaHCO_3$, Sigma-Aldrich) were used to clean the silver surface for this treatment. During the reaction, a small current flows between the metals and the silver sulfide was reduced. Because there is insufficient information on the application of this method to thin films, different concentrations and reaction times were tested in previous work [269]. First, the sample was cleaned with IPA

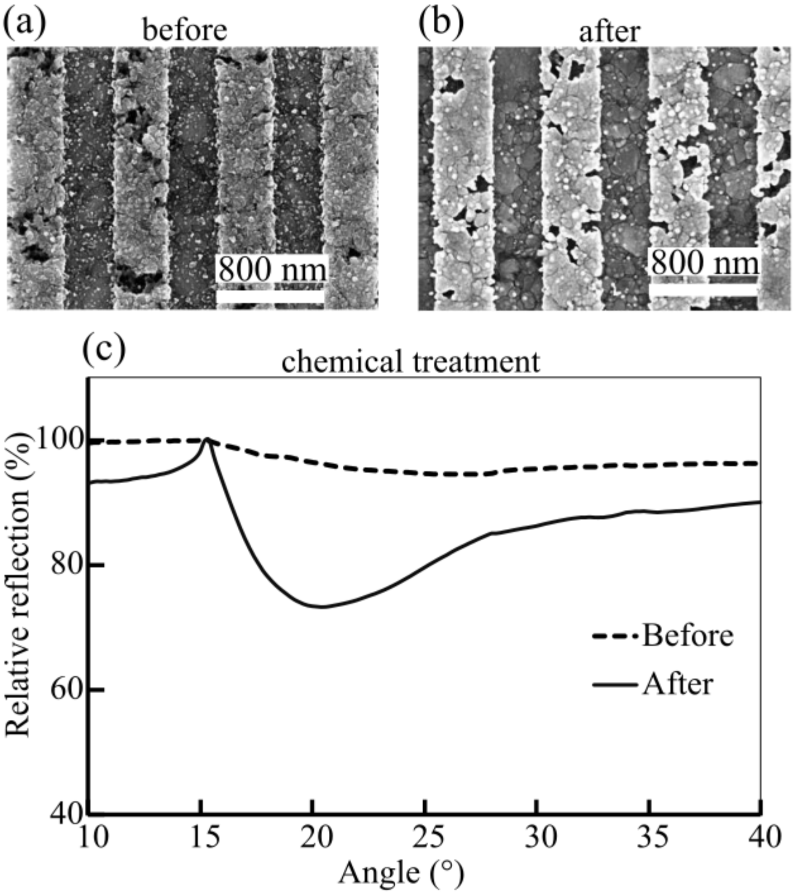

Figure 6.29.: SEM images of the grating surface were compared before (a) and after (b) chemical treatment. For 10 minutes, the sample was immersed in a 25% ammonia solution at 70°C. Following treatment, the amount of tarnish was reduced. (c)A comparison of the relative reflection results before and after the chemical treatment revealed that the relative reflection was restored by approximately 30%. (Reprinted with permission from [271] ©Optical Society of America.)

and dried. The sample was then heated on a hot plate set to 70°C. The optimal condition of $0.1MNaHCO_3$ solution at 70°C was then dropped over the sample, which contacts the aluminum foil to complete the electrochemical cell flow. Finally, the reaction was stopped in 60 seconds with deionized (DI) water. Fig. 6.30 shows the successful removal of tarnish. In addition, the treatment can restore the surface plasmon excitation curve by decreasing relative reflection by approximately 40% compared to the case without treatment.

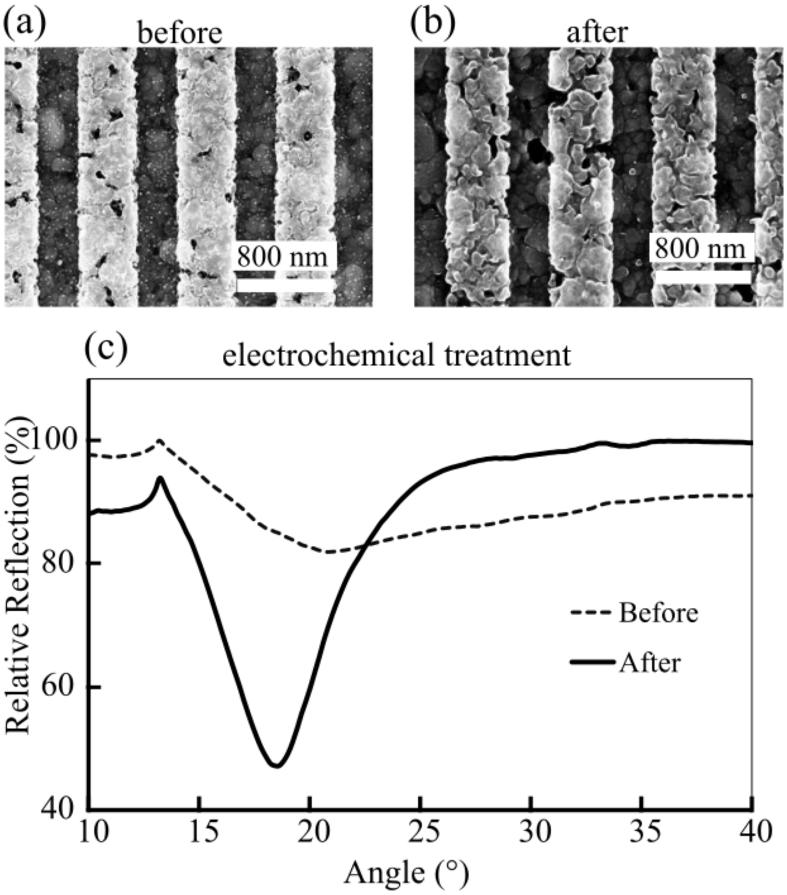

Figure 6.30.: SEM images of the grating surface were compared before (a) and after (b) electrochemical treatment. The treatment with 0.05M $NaHCO_3$ solution reduced the number of particles significantly. Before and after the electrochemical treatment, the relative reflection was restored by approximately 40%. (Reprinted with permission from [271] ©Optical Society of America.)

Silver Deposition Treatment

The final approach is based on a silver deposition treatment, which resulted in the formation of an additional thin silver film on top of the grating structure. The method used was thermal evaporation at a rate of 0.15 nm/s in a vacuum of $1.5 \times 10^{-6} mBar$. However, for 10-20 nm thicker layers, no effect on surface plasmon wave excitation was observed. A small effect from optical reflection can be seen at a thickness of 30 nm, as shown in Fig. 6.31. When compared to the untreated case, the result shows a 13% decrease in relative reflection.

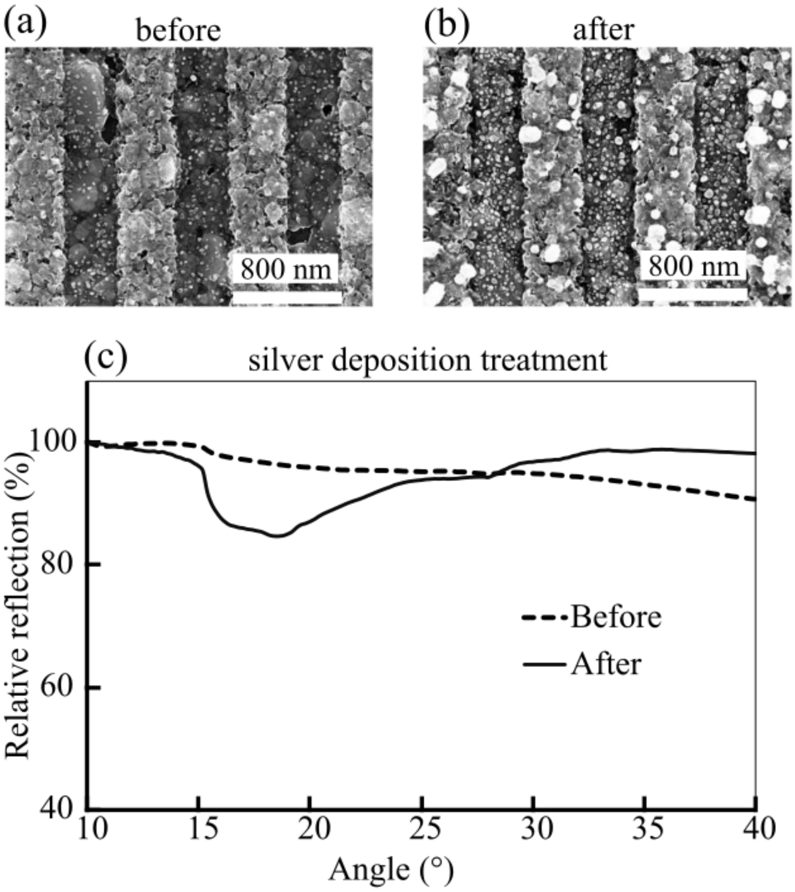

Figure 6.31.: SEM images of the grating surface were compared before (a) and after silver deposition treatment (b). A thin silver film of 30 nm was formed on top of the grating structure during the process. (c) Relative reflection before and after silver deposition was restored by approximately 13% when compared to the untreated case. (Reprinted with permission from [271] ©Optical Society of America.)

6.9.3. The Protection Against Surface Degradation

Previous experiments demonstrated that silver surface tarnish had a direct impact on grating measurements, even though the restoration techniques outlined in Sec. 6.9.2 were able to restore the optical properties. However, the restoration results were insufficient compared to before the tarnish. In this experiment, the protection thin film was used to solve the problem of corrosion by forming a protective layer on the surface. The substances being considered for use were silicon oxide (SiO_2) and silicon nitride (Si_3N_4), both of which have been studied recently [276–278] and can be deposited on a nanometer scale using the PECVD technique [279, 280]. In addition, these materials are transparent and do not block the light wave that reaches the surface. After creating a thin film, the optical properties of the samples were measured, and the SEM was used to examine the thin film layers.

Silicon Oxide Protective Layer

The first protective layer applied consists of a thin silicon oxide layer. The parameters of the process can be seen in Tab. A.2. The deposition temperature of 200°C was used to avoid the silver grating deforming. The process reaction took place on the sample's surface for 20 seconds to form a 20 nm thin silicon oxide; the process parameters can be seen in Appendix A.2. The result shows a silicon oxide layer in Fig. 6.32(a), with a layer visible above the silver layer. The curves of the silicon oxide-coated sample are shown in Fig. 6.32(b), and the angle of the plasmon excitation had shifted beyond the

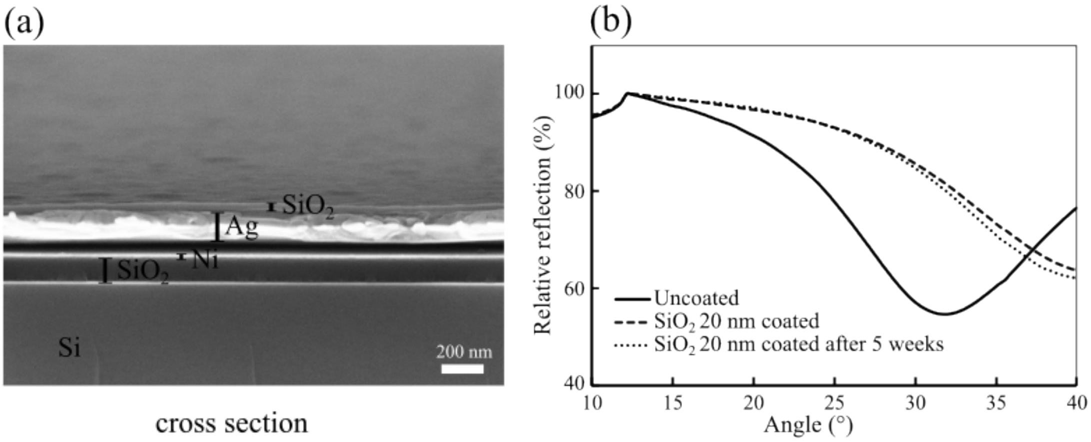

cross section

Figure 6.32.: SEM image (a) of the cross-section of a protective sample reveals the presence of silicon oxide on top of the silver layer. Graph (b) depicts the relative reflection of a grating with a silver oxide protective layer before and after silicon oxide coating in one day and after five weeks of storage in room temperature conditions. After five weeks, the silicon oxide protective layer sample demonstrates a plasmon excitation angle that has shifted by more than 40 compared to the uncoated case and has changed slightly. (Adapted from Sarapukdee, P., et al. [82], is licensed under CC BY 4.0.)

detection limit of 40, but the resulting curve trend was still visible. By representing it as an analytical layer over the grating structure, it was demonstrated that coating silicon oxide on the silver surface was successful, which can be detected by shifting the plasmon excitation angle. This experiment must be considered in terms of applying the protective layer, which can impact sensor efficiency. After that, the samples were stored in a common room for five months before being tested again. Fig. 6.32(b) shows that the results after five weeks (dash line) showed a slight change in the curves compared to the first day of coating (dot line). Furthermore, the coated sample was broken and examined under a scanning electron microscope to determine the thickness of the protective layer and the coating formed. Fig. 6.32(a) shows a silicon oxide layer with a layer visible above the silver layer.

Silicon Nitride Protective Layer

The preservation of silicon nitride is then investigated. A silicon nitride is frequently used in a preservation application. The parameters used to deposit a 20 nm silicon nitride layer have been adapted from a previous process and can be found in Appendix A.2. The process temperature is 200° C, and the sample is exposed for 10 minutes. This experiment looked into the protective layer of silicon nitride (Si_3N_4). Silicon nitride is commonly used as a protective layer in many applications [281], and it has also been studied in terms of biocompatibility, which will be useful in biosensor platforms [282–285]. The parameters for the deposition of a 20 nm thick silicon nitride layer were taken from a previous process, as shown in Tab. A.2. The process temperature was 200°C, to which the sample was exposed to silicon nitride 20 nm thickness. The sample was measured in the same manner as in the preceding experiment (Sec. 6.9.3). The process results in successfully depositing a silicon nitride layer, as shown in Fig. 6.33(a). The protective layer's thickness can be estimated to be between 10 and 30 nm. Fig. 6.33(b) shows a comparison of the optical properties of coated and uncoated gratings (b). As a result, the silicon nitride-coated plasmon excitation angle was approximately 5° different from that of uncoated. The plasmon excitation angle appears slightly lower(32° to 27°), possibly

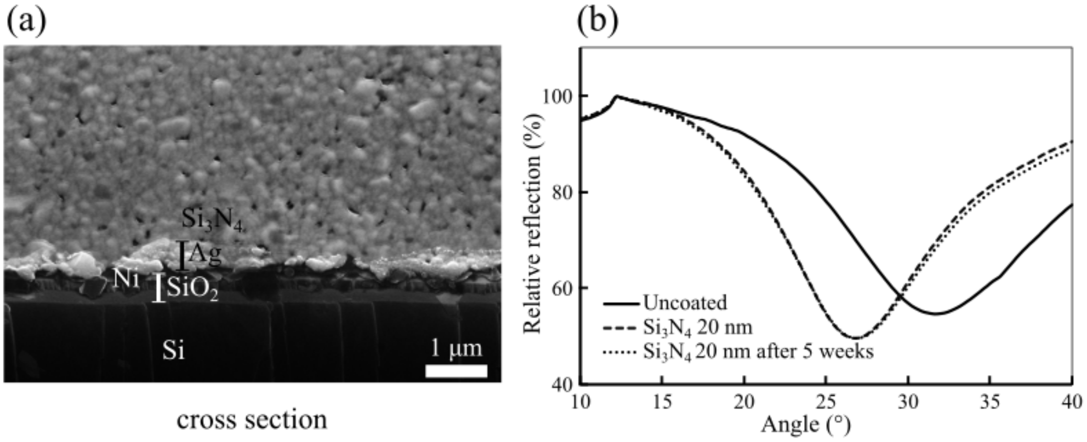

Figure 6.33.: (a) SEM image of the sample's cross-section with silicon nitride coating. The protective layer is visible on the silver surface, as can be seen. Graph (b) depicts the relative reflectance of the uncoated and coated protective layer on the first day and five weeks later. After five weeks of storage, the protective layer of silicon nitride shows minor changes in the relative reflection. Therefore, the study can conclude that silver nitride has effectively stopped the corrosion of the silver grating. (Adapted from Sarapukdee, P., et al. [82], is licensed under CC BY 4.0.)

due to the increased temperature during silicon nitride coating, which affected the grating structure. Similar to the previous comparisons, the relative reflection was measured after a 5-week storage period. Fig. 6.33(b) exhibits the results, which appear very promising because there is no visible increase in the plasmon excitation angle and relative reflection after five weeks. It can be concluded that a protective layer of a thin silicon nitride layer can prevent measurable corrosion within five weeks. Overall, this section focused on potential corrosion solutions in biosensor applications involving silver-based grating couplers. Various treatments for a tarnished surface were investigated to restore the plasmonic properties of a grating-assisted plasmonic sensor. Electrochemical treatment was the most effective method for restoring the excitation of surface plasmon waves, which is critical to the biosensor's operation. The protective layer was also examined. Given the preceding, a thin silicon oxide layer has been shown to impact the coupling properties significantly. Finally, in five weeks, a thin layer of silicon nitride was shown to protect against silver corrosion by maintaining the same plasmon excitation angle.

6.10. Inverted Grating-Based SPR Sensors

This section aims to provide argumentation and empirical evidence for using an inverted grating structure for sensing rather than the conventional configuration. This section begins with a discussion of the advantages of employing a new grating geometry, followed by sections on the simulation of an inverted grating structure, a comparison of glass substrates for inverted grating, and measurement of the inverted grating. The results could assist in determining the optimal grating geometry in terms of size, height, and silver thickness for building a new grating structure.

6.10.1. Inverted Grating Model

Experiments performed in previous section demonstrated the limitations of conventional grating structures. The conventional grating configuration exposes the grating surface directly to air and sample, which has the benefit of obtaining direct information from the sample but can also have a direct effect on the grating surface and structure. The results of the biological testing part in Sec. 6.7.1 may clarify this point with additional information. Which is after testing biomolecules on the grating structure, the intensity of the light wave was reduced. This is because the light must travel through the analyte layer before reaching the grating structure. Typically, biological samples rapidly absorb UV-VIS light [286, 287], which can reduce light intensity and sensitivity. In Sec. 6.8, an analyte solution was employed. A microchannel was utilized to hold the solution and transport it to the measurement site. It revealed that the experiment's results were more sensitive and applicable to a wider range of applications than those measured with the dry sample. Therefore, it can be concluded that the PDMS-channeled grating has a high potential for use as a biosensor chip in the real world [283, 288, 289]. When the solution carrier, a microchannel, must be adhered directly in front of the grating on the light excitation side; however, certain limitations may arise. For example, it may eliminate the measured light, particularly when a small device is required. Therefore, when designing

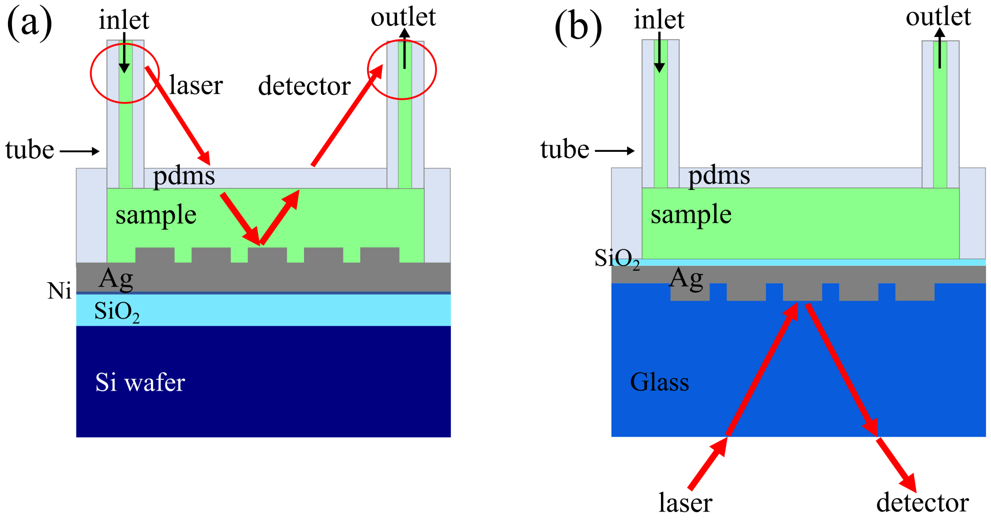

Figure 6.34.: Schematic design of using the inverted grating with PDMS microchannels. The microtube blocks the illumination light on the front side (a), while the back side (b) is advantageous for assembly. (Image by Sarapukdee, P., et al. [155] is licensed under CC BY 4.0.)

the chip, it must be ensured that the device does not obstruct the measured light when the sample rotates, which could also reduce the measured angle range. The measuring light can be blocked if the sample feeding tube is too long or rotates, as shown in Fig. 6.34(a). Moreover, Sec. 6.9.2 demonstrated the silver surface that tarnishes rapidly when exposed to air. The tarnishing on the grating surface immediately impacts the optical measurement. As a result, a protective coating is necessary. Otherwise, the sample must be stored in proper condition. As shown in Fig. 6.34(b), a periodic grating structure can be created by depositing a metal layer on a previously patterned and etched dielectric, which forms and inverts the grating structures beneath the substrate, while the analyte is placed on the backside of the grating structure. As a result, the analyte layer does not absorb the incident light. Furthermore, because the grating side is embedded in the substrate, it reduces surface exposure to air and, thus, the occurrence of tarnish. Therefore, it is possible to conclude that the inverted grating structure is more advantageous for biosensor applications. Previous research [290] suggested that the structure between heavily doped silicon and silicon substrate could be used as a diffraction grating sensor. Similarly, this work [291] demonstrated the complexities of measuring an analyte sample

Table 6.13.: Glass type and thickness details.

Glass type	Material	Thickness
Cover glass (Electron Microscopy Sciences, USA)	borosilicate glass	0.20± 0.02 mm
Borofloat (SIEGERT WAFER GmbH, GE)	borosilicate glass	0.50± 0.02 mm
Quartz 0.5 mm (GVB GmbH, GE)	Quartz glass	0.5± 0.05 mm
Quartz 1 mm (GVB GmbH, GE)	Quartz glass	1± 0.1 mm
Glass slide (SWIFT, GE)	optical glass	1± 0.1 mm

from the backside using an epoxy layer grating embedded in a glass substrate with a flat metallic surface on top. Furthermore, this study [292] employed the sol-gel technique on polymers as a silicon oxide substrate. Finally, some work has been created using a stamping process [293], which can be used on both polymers and a SiO_2 substrate [294] . Given the foregoing, it is reasonable to conclude that manufacturing work is limited and difficult.

6.10.2. Glass Substrate for Inverted Grating Structure

This experiment examined a glass to determine the best one to use as a base for the inverted grating structure. Glasses of various sizes and types were chosen for this experiment based on their commercial availability, economy, heat resistance, and corrosion resistance. Because there are many steps to the fabrication process, the substrate chosen must be suitable for the construction process. Tab. 6.13 depicts glass substrates of various materials and thicknesses. Since most commercial glass in the market is cut in the size of (2 × 2) cm, other glasses with larger sizes were thus cut to a similar size, except for the quartz glass available in (1 × 1) cm size. The samples were first cleaned with IPA and allowed to dry. The nickel was then sputtered onto the surface to form a seeding layer, followed by a smooth silver layer in the following step. Then, at a rate of 0.15 nm/s, thermal evaporation deposited a 100 nm thick silver layer over the nickel seed layer. The samples were then tested to see how light transmitted through the substrate without grating behaved. Fig. 6.35 depicts the glass testing configuration. In this test,

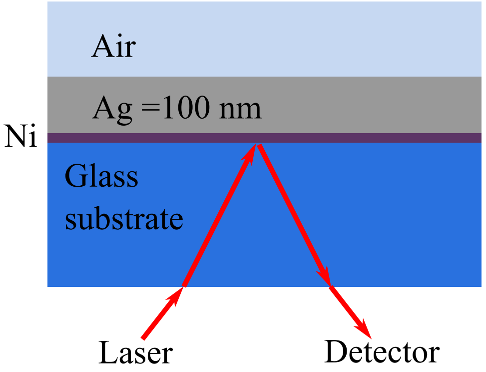

Figure 6.35.: Sketch of the structure with glass substrate.

where there is no grating structure to couple light for plasmon excitation, the reflectivity signal should be close to one hundred percent. Therefore, the reflected signal should be consistent, with no recognizable dip angles, and have a high light intensity, indicating that the glass does not absorb light. The results in Fig. 6.36 show that glass substrates with a thickness of 0.2-0.5 mm; cover glass, Boroflat, and quartz have a wave signal that can interface with the sample signal when the sensor tests a biomolecule. As a result, the reflected signals were high power because, except for quartz, the glass samples had

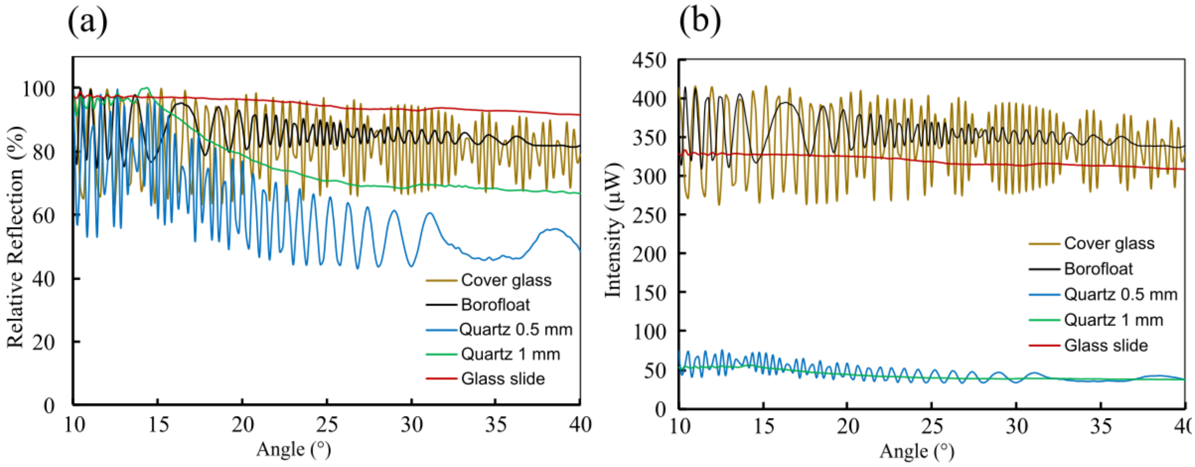

Figure 6.36.: Measurement of different types and thicknesses of glass substrates with a 100 nm silver layer on the backside, (a)the relative reflection results show a smooth signal only from glass slide (red line) and quartz 1 mm (green line). However, (b)the reflected light intensity reveals only a smooth signal with high power from the glass slide (red line). (Image from Sarapukdee, P., et al. [155], is licensed under CC BY 4.0.)

slightly absorbed the light due to the thin glass. However, the signal's vibration while scanning makes it challenging to distinguish the signal from the plasma phenomenon of the practical test. Thus, it is possible to conclude from the preliminary data that glass with a thickness of 0.2-0.5 mm was unsuitable for use as a substrate for the inverted grating structure. In contrast, the thickness of the quartz and microscope glass substrates was 1 mm. The signal from the sample with the 1 mm thick glass substrate was smooth. Furthermore, quartz 1 mm thick presented a smooth signal that began to decrease between 15° and 40°, whereas the glass slide presented a smooth signal throughout. Therefore, the 1 mm thickness of both materials demonstrated some potential for use as a substrate for the inverted grating structure. However, the 1 mm thick quartz absorbed more light than the 1 mm thick glass slide, which resulted in a lower intensity of reflected light. Since the intensity of reflected light is crucial for biosensing, it can be concluded that the 1 mm quartz glass thickness was unsuitable for the fabrication of the inverted grating structure. In contrast, only the glass slide with a 1 mm thick sample exhibited a minimal wave signal and a high power of reflected light, which, when used as a substrate for the inverted grating, has less of an effect on the investigation signal than all other types of tested glasses. Hence, it can be concluded that the 1 mm thick glass slide, among the glass substrates previously utilized, was an appropriate choice for the fabrication of an inverted grating.

6.10.3. Measuring of Inverted Grating Structure

In this experiment, an inverted grating structure with a 1 mm thick glass substrate was fabricated and measured. Fig. 6.37 reveals a sketch of the grating structure based on the fabrication parameters derived from Sec. 6.37's simulation results, with a 500 nm grating period, 30 nm of grating height, and a 50 nm thick silver layer on top. Sec. 5.3.3 described the fabrication of the inverted grating structure with a glass substrate. The inverted grating structure was then measured using an optical measurement station with a scanning angle of 10 ° to 70°. Fig. 6.38 displays the outcomes, while Tab. 6.14

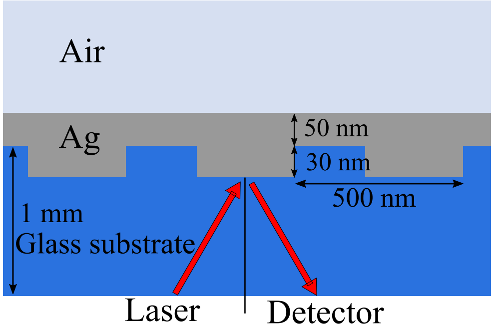

Figure 6.37.: Sketch of the inverted grating structure on a glass substrate.

provides additional information. The inverted grating production succession yield was comparatively low and inconsistent. As a result, the first-order plasmon excitation angle for each of the five structures was approximately 21.53°, and the second-order plasmon excitation angle was approximately 63°, which is too high for practical applications. Regarding the first order at 20°, the measurement from the backside would not pose as much of a problem as the measurement from the front side, even though it was nearly off from the expected angle for biosensors in the range of 10° to 20 °. Despite this, the reflectivity at the plasmon excitation angle was approximately 64% for sample E1 and considerably lower for samples E2-E6, indicating lower efficiency and consistency than conventional models. It indicates that the structure of the fabrication process should be improved. After measuring the optical properties of the grating, the grating was shattered

Table 6.14.: The inverted grating structure with a period of 500 nm, gating height of 30 nm, and a silver top layer of 50 nm present a different outcome caused by the unstable manufacturing process.

Sample	Detail	Plasmon excitation angle(°), Relative reflection (%)	
		1^{st} Order	2^{nd} Order
E1	$b = 40$ nm, $h = 20$ nm	21.8°, 94.15%	63.4°, 86.23%
E2		22.6°, 68.77%	63.0°, 93.39%
E3	$b = 50$ nm, $h = 30$ nm	22.2°, 58.37%	61.2°, 59.37%
E4		22.0°, 64.47%	60.6°, 73.43%
E5		21.4°, 92.54%	63.4°, 84.78%
E6		21.2°, 91.27%	64.0°, 77.49%
E7		21.2°, 92.20%	64.0°, 78.48%

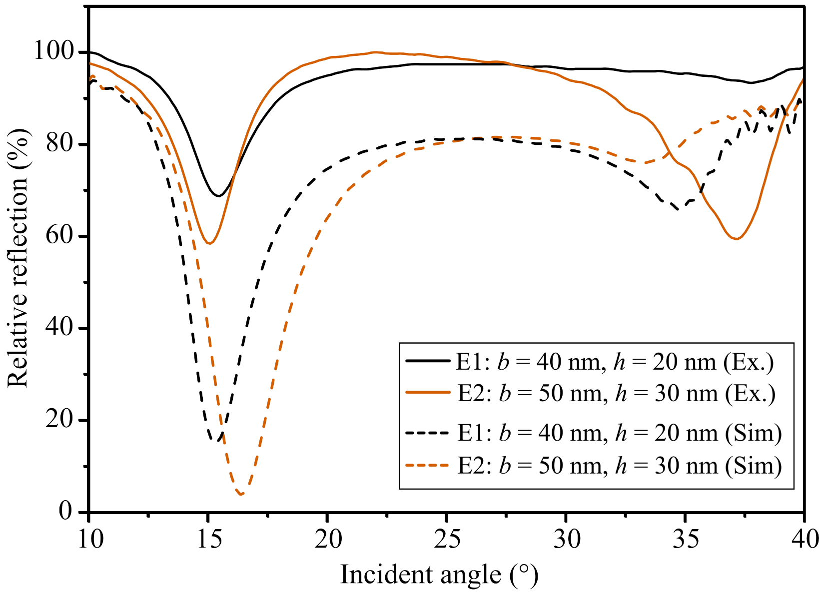

Figure 6.38.: The initial measurement of an inverted grating structure on a 1 mm thick glass substrate with a 500 nm period revealed a 30 nm grating groove height and a 50 nm silver base thickness. Additional trials resulted in a grating with a 20 nm grating groove height and a 40 nm silver base thickness. However, the results showed inconsistency, particularly in plasmon excitation angles across different grating designs. These differences indicate difficulties in properly regulating and repeating the etching processes for 20 and 30 nm grating groove height constructions. (Adapted from Sarapukdee, P., et al. [155], is licensed under CC BY 4.0.)

and measured using SEM. Fig. 6.39 features the sample sectional representation. The inverted grating structure with a lengthy etching path and a silver layer on top was manufactured successfully. The top layer of silver was peeled away, and its thickness corresponded to the grating height. However, the results demonstrated that the grating was porous due to the absence of the nickel seed layer, which may have caused interference with the analyte during the experiment. However, nickel will be investigated to produce a smoother silver layer in the following experiment.

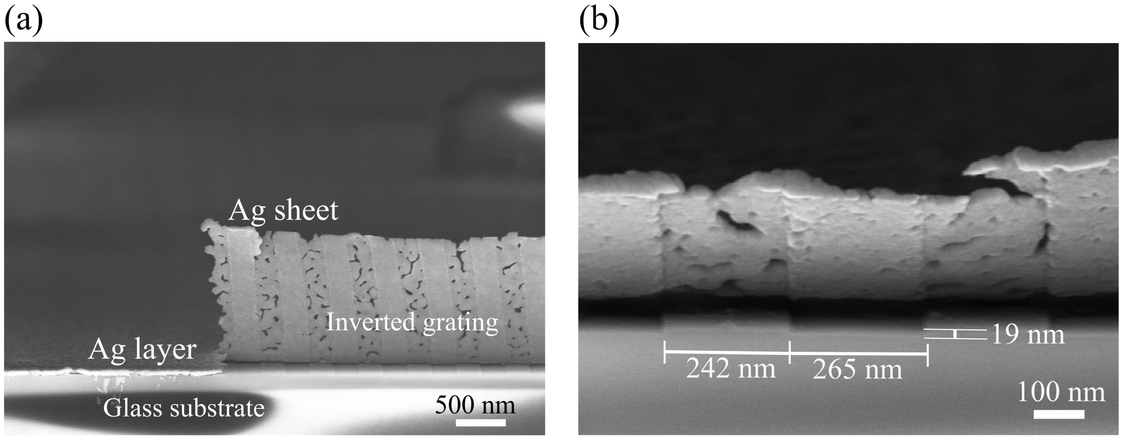

Figure 6.39.: The SEM cross-section of the inverted grating structure shows a peeling sheet of silver metal, showing porosity caused by the lack of an adhesive layer. The substrate also has an etching depth matching the grating groove height h of (20 ± 2) nm, a grating groove size of (250 ± 5 nm), and a base thickness of (40 ± 3 nm). (Image from Sarapukdee, P., et al. [155], is licensed under CC BY 4.0.)

6.10.4. Inverted Grating with Nickel Adhesive Layer

In Sec. 6.10.3, the grating was manufactured and measured. Nonetheless, the structure lacked a metal adhesive layer to enhance the adhesion of the silver layer, resulting in the silver layer's porosity. It was also discovered that the adhesion of silver was weaker than that of surfaces with a nickel adhesive layer. Sec. 5.2.2 provides information on the use of nickel to enhance the adhesion and smoothness of silver surfaces. The addition of nickel to a conventional grating structure did not significantly impact the measurements because the metal was beneath the metal side and therefore did not directly interact with the measurement light. In the inverted grating model, nickel was instead sputtered onto the glass substrate. It will cause the measuring light to reach the nickel layer before the silver grating when traveling through the substrate. The measuring light that travels through the nickel layer can reduce the light's intensity and alter the optical properties of the silver grating. Nevertheless, this inference will be confirmed by this experiment. Following the steps outlined in Sec. 5.3.3, the inverted grating was manufactured for this experiment. The first sample was constructed according to the standard procedure,

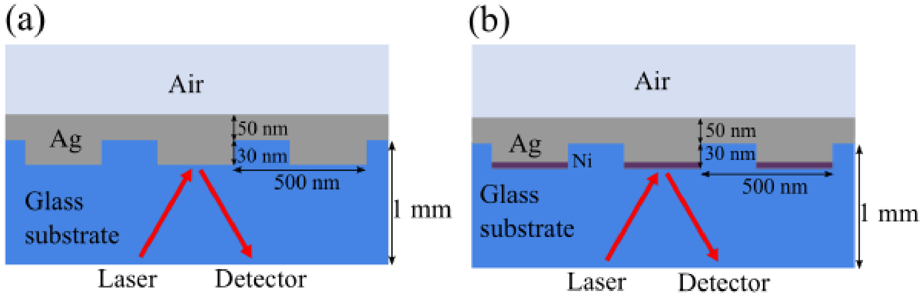

Figure 6.40.: Sketch of the inverted grating structure on a glass substrate with(a) and without(b) the nickel adhesive layer.

while the second sample was sputtered with a 10 nm nickel adhesive layer following the etching of the glass. The construction then adhered to the standard procedure. Fig. 6.40 depicts a sketch of the final product of the inverted grating with the nickel adhesive layer. Finally, the sample was measured to compare it with and without a nickel adhesive layer. Fig. 6.41 illustrates the experiment's findings. The sample without nickel had a plasmon

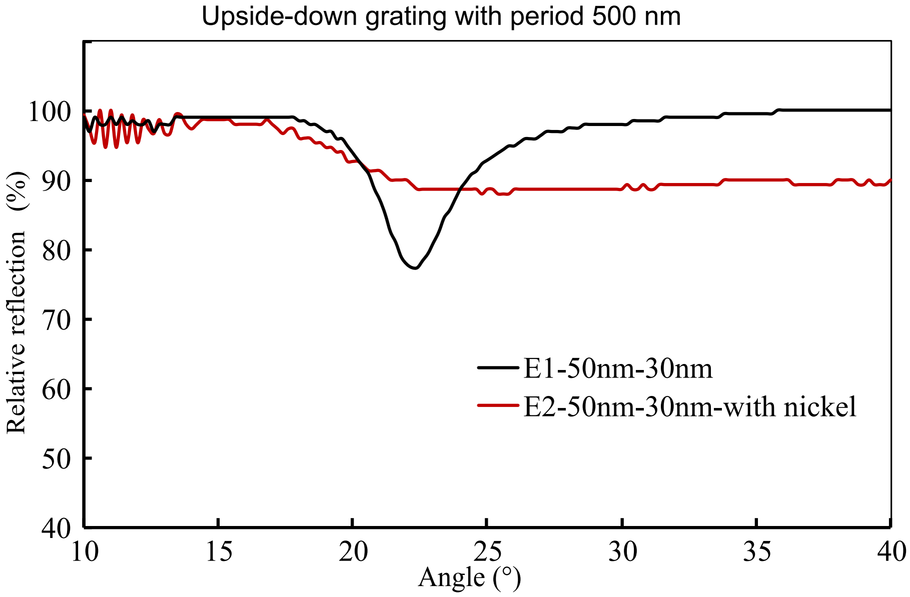

Figure 6.41.: Comparison of relative reflection of the inverted grating structure with and without a nickel adhesive layer.

excitation angle of 22.2° and a relative reflection of 77.3%, similar to the experiment in Sec. 6.10.3. On the other hand, the plasmon excitation angle was lost from the scan range of 10° to 40° in the sample with a nickel adhesive layer. As a result, the nickel layer in the inverted grating structure interfered with the plasmon excitation signal. With this issue, a new method of increasing the adhesion strength of silver deposition must be considered. Otherwise, research into a new adhesive material capable of mitigating the effects of inverted grating measurements is required. For example, these publications [295–297] have been studied from experimental characterization of evaporated and sputtered films that can be adapted for use in future work.

6.10.5. Inverted Grating with Silicon Oxide Protective Layer

The inverted grating structure was configured with a measurement light wave that reaches the grating from the bottom side, minimizing tarnishing from direct exposure to air. However, the top silver layer is still directly exposed to air, which can cause corrosion issues. Thus, the inverted grating structure was created in this experiment, and a protective layer of silicon oxide was deposited over the top of the silver surface. The optical properties of the coating and uncoated protective layers were then measured and compared. First, the inverted grating was built using the fabrication process described in Sec. 5.3.3, with a grating period of 500 nm, a grating height of 30 nm, and a silver top layer of 50 nm. Fig. 6.42 shows a sketch of the structure. Second, the optical properties were measured using the previously specified scan angle of 10° to 70°; this will be the first data. Finally, using the PECVD method, 20 nm of silicon oxide was deposited on the silver surface and measured again for the second data. Fig. 6.43 exhibits the results

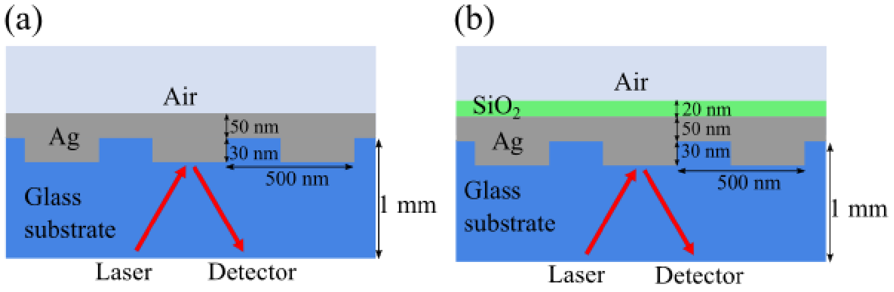

Figure 6.42.: Sketch of the inverted grating structure on a glass substrate with(a) and without(b) the silicon oxide protective layer.

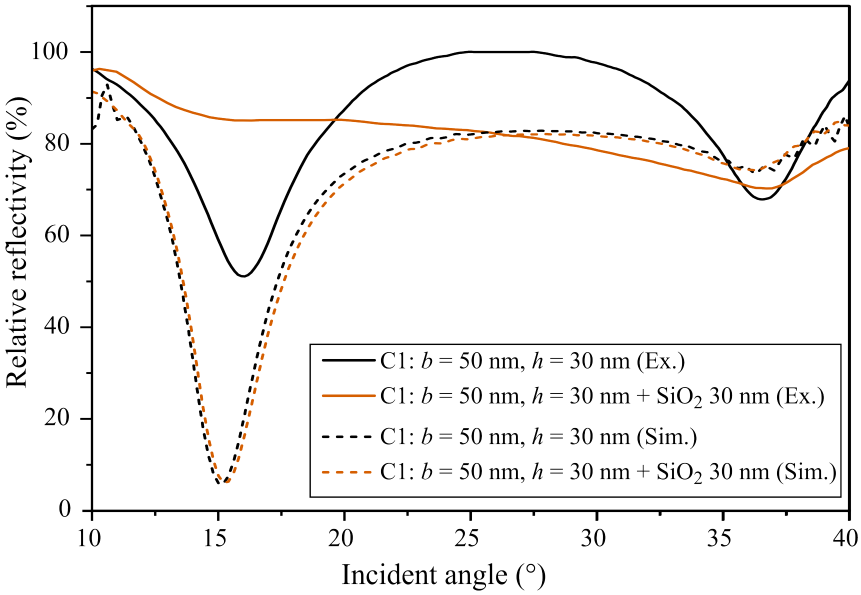

Figure 6.43.: The measurement of the inverted grating structure on a 1 mm thick glass substrate, with and without the silicon oxide protective layer. Notably, the plasmon excitation angle changed significantly following the deposition of the silicon oxide layer. This discovery implies that the high-temperature procedures involved in the deposition may have influenced the characteristics of the glass substrate and the underlying silver layer, which lacks a seed layer for regulated development. (Image from Sarapukdee, P., et al. [155], is licensed under CC BY 4.0.)

Table 6.15.: Measurement results of the inverted grating structure with and without a silicon oxide protective layer.

Sample	Plasmon excitation angle(°), Relative reflection (%)	
	1^{st} Order	2^{nd} Order
C1	23.0°, 71.98%	61.0°, 55.56%
C2	23.2°, 51.12%	59.4°, 67.98%
C1 with SiO_2	22.4°, 85.14%	60.0°, 69.30%
C2 with SiO_2	23.2°, 87.97%	60.2°, 77.44%

of the experiment, while Tab. 6.15 provides additional details. The first and second-order angles of plasmon excitation were approximately 23.1° and 60.2° with relative reflection of 61.55% and 61.77%, respectively, for the inverted grating structure lacking a silicon oxide protective layer. Comparatively, the scanning range of 10° to 70° was challenging to define for both angles on the structure with a protective layer on the surface. However, this experiment's results were consistent with the silicon oxide protective layer described in Sec. 6.9.3, in which it was determined that the plasmon excitation angle disappeared when silicon oxide was applied to the surface. The silicon oxide protective layer was, therefore, unsuitable for both conventional and inverted grating structures. In addition, the silicon nitride protective layer, which yielded positive results in prior research, should be investigated in future studies.

The unique grating structure, inverted from the conventional design, may not possess the same level of coupling efficiency, but it brings forth significant operational advantages. Its exceptional ability to mitigate surface oxidation stands out, ensuring a prolonged lifespan for the grating and rendering it suitable for diverse practical applications. In contrast to traditional plasmonic devices susceptible to corrosion, the inverted grating incorporates a protective substrate layer, reducing maintenance requirements and potentially lowering costs.

To further enhance this configuration, the incorporation of an anti-reflection layer on the glass substrate shows great potential. This innovative addition has the capacity to significantly diminish interference from the glass, thereby improving overall performance and potentially allowing for the use of thinner glass substrates. However, it is imperative to note that additional investigation and refinement are crucial. The robust adhesion of the silver layer to the glass is important, especially in demanding applications, prompting exploration into advanced fabrication techniques and materials.

Efficiency in signal detection emerges as another area ripe for improvement. While backside illumination has been explored, its dependence on complex optical systems remains a limitation. A promising avenue lies in electrical detection through integrated circuits [156] and sensors [298], streamlining the entire device. Furthermore, the integration of semiconductor nanostructures into the inverted grating introduces captivating possibilities. These nanostructures can function as highly sensitive optical sensors, offering precision and sensitivity across a spectrum of applications.

In summary, while the coupling efficiency of inverted grating structures may not yet rival conventional setups, they offer significant operational benefits and new design possibilities. Future research should focus on preventing oxidation, improving adhesion, and exploring innovative detection methods to enhance their performance.

CHAPTER 7

Summary and Outlook

Label-free detection techniques offer significant advantages for biomolecule measurements, as they eliminate the need for labeling molecules [299], such as fluorescent antibodies, proteins, amino acids, and peptides. This simplification streamlines sensor development and allows for real-time measurement of interactions, making it suitable for applications like studying association kinetics [300], rapid cancer diagnosis [301], and disease marker detection [302], as well as drug discovery [303]. Surface plasmon resonance (SPR) remains the most widely used label-free technique for monitoring biomolecular interactions in real-time [304].

Traditional SPR detectors use prism-based excitation methods [88], which, though cost-effective and simple, are not suitable for integration onto a single chip. In contrast, grating excitation offers the potential to miniaturize devices and incorporate multiple functionalities on a single chip. This study used grating-based SPR for excitation due to its advantages in reducing device size and enabling integration with other technologies, such as quartz crystal microbalance [305], electrical detectors [156], and surface-enhanced Raman scattering [306].

The FDTD method was employed to model various grating structures, exploring different sizes and thicknesses. The permittivity values used were $Air = 1$, $Ag = -19$, $Ni = -11.4$, $SiO_2 = 2.1$, and $Si = -12$. The relationship between changes in the grating period and plasmon excitation angle was calculated, with experimental results showing strong correlation, producing an R^2 value of 0.9554 when measuring the refractive index (RI) between 1.0 and 1.7. The sensitivity was approximately 20°/RIU. Additionally, the study revealed different trends for grating SPR performance across an RI range of 1.32 to 1.46. Sensitivity in the range of 1.32 to 1.37 was 22.85, 35.43°/RIU, while it increased to 35.58, 128.85°/RIU between 1.37 and 1.46.

This research successfully developed grating structures suitable for label-free biomolecule measurements. Various structures were tested, and optimal dimensions were identified: a grating period of 800 nm, a base thickness of 100 nm, and a height of 50 nm. These configurations were found to offer the best performance for biosensing applications, especially when combined with a silver layer of 100 nm thickness. Experiments with both dry and solution biomolecules, such as IgG and Protein A, demonstrated an approximate 4.8° shift in plasmon excitation angle, confirming the effectiveness of the grating.

Additionally, gradient grating periods (GGP) and 2D grating structures were explored, showing the feasibility of generating multiple plasmon excitation angles from a single grating sample. The flexibility of these structures, including the ability to excite two diffraction orders with high coupling efficiency across angles ranging from 16° to 40°, opens up possibilities for multi-parameter sensing. Their anisotropic properties allow for independent strain measurement, enhancing applications such as strain sensing and environmental monitoring.

Protein A in PBS was measured using a PDMS microchannel, yielding a sensitivity of 77.23°/RIU, indicating strong performance without assay interference. The study also addressed challenges associated with using silver as a plasmonic material, including surface tarnishing. Electrochemical methods were found to be the most effective in reconditioning the optical properties of tarnished surfaces. Among protective coatings, Si_3N_4 demonstrated better performance compared to SiO_2, with less impact on plasmon excitation angles.

The inverted grating structure was developed on a glass substrate to mitigate issues such as silver tarnishing and angle measurement constraints. A computer model guided the design, which featured a grating period of 500 nm, a grating height of 30 nm, and a 50 nm silver layer. Borosilicate glass was selected as the substrate for its low thermal expansion properties [307], with a thickness of 1 mm determined to be optimal. The inverted structure achieved plasmon excitation angles of 20° for the first-order angle and 60° for the second-order angle.

In conclusion, the study demonstrated that computer models can effectively predict the behavior of grating structures in air-based analytical environments. Experiments using multi-value RI solutions refined these models further. Long-term storage tests showed that Si_3N_4 is a superior protective layer for both conventional and inverted grating structures, reducing signal interference. While the coupling efficiency of inverted gratings is lower than that of conventional designs, they offer operational benefits, such as oxidation prevention and extended use. Further research into improving silver adhesion to glass and developing more efficient coupling techniques is recommended. Electrical detection and semiconductor-based optical sensors present exciting avenues for future investigation [158, 159, 161], as they could eliminate the need for complex optical systems in plasmon detection.

References

[1] M. Nicola, Z. Alsafi, C. Sohrabi, A. Kerwan, A. Al-Jabir, C. Iosifidis, M. Agha, and R. Agha, "The socio-economic implications of the coronavirus pandemic (covid-19): A review," *International Journal of Surgery*, vol. 78, pp. 185–193, 2020.

[2] D. C. Danko, J. Golden, C. Vorosmarty, A. Cak, F. Corsi, C. E. Mason, R. M. de Freitas, D. Nagy-Szakal, and N. B. OHara, "The challenges and opportunities in creating an early warning system for global pandemics," 2023.

[3] C. J. L. Murray, K. S. Ikuta, and et al., "Global burden of bacterial antimicrobial resistance in 2019: a systematic analysis," *The Lancet*, vol. 399, no. 10325, pp. 629–655, 2022.

[4] N. I. of Health, "Nih minority health and health disparities strategic plan 2021-2025," 1 2025.

[5] S. Paz, "Climate change: A driver of increasing vector-borne disease transmission in non-endemic areas," *PLOS Medicine*, vol. 21, no. 4, pp. 1–3, 04 2024.

[6] M. Hemdan, M. A. Ali, A. S. Doghish, S. S. A. Mageed, I. M. Elazab, M. M. Khalil, M. Mabrouk, D. B. Das, and A. S. Amin, "Innovations in biosensor technologies for healthcare diagnostics and therapeutic drug monitoring: Applications, recent progress, and future research challenges," *Sensors*, vol. 24, no. 16, 2024.

[7] M. Ramesh, R. Janani, C. Deepa, and L. Rajeshkumar, "Nanotechnology-enabled biosensors: A review of fundamentals, design principles, materials, and applications," *Biosensors*, vol. 13, 1 2023.

[8] M. G. Jiménez-Rodríguez, F. Silva-Lance, L. Parra-Arroyo, D. A. Medina-Salazar, M. Martínez-Ruiz, E. M. Melchor-Martínez, M. A. Martínez-Prado, H. M. Iqbal, R. Parra-Saldívar, D. Barceló, and J. E. Sosa-Hernández, "Biosensors for the detection of disease outbreaks through wastewater-based epidemiology," *Trends in Analytical Chemistry*, vol. 155, p. 116585, 10 2022.

[9] A. Haleem, M. Javaid, R. P. Singh, R. Suman, and S. Rab, "Biosensors applications in medical field: A brief review," *Sensors International*, vol. 2, 2021.

[10] D. Bhatia, S. Paul, T. Acharjee, and S. S. Ramachairy, "Biosensors and their widespread impact on human health," *Sensors International*, vol. 5, 1 2024.

[11] S. Gavrilaș, C. Ștefan Ursachi, S. Perța-Crișan, and F. D. Munteanu, "Recent trends in biosensors for environmental quality monitoring," *Sensors*, vol. 22, 2 2022.

[12] B. Wang, D. Huang, and Z. Weng, “Recent advances in polymer-based biosensors for food safety detection,” *Polymers*, vol. 15, 8 2023.

[13] P. Estrela, N. Bhalla, P. Jolly, N. Formisano, and P. Estrela, “Introduction to biosensors,” *Essays in Biochemistry*, vol. 60, no. 1, pp. 1–8, 06 2016. [Online]. Available: https://doi.org/10.1042/EBC20150001

[14] A. Lomae, P. Preechakasedkit, O. Hanpanich, T. Ozer, C. S. Henry, A. Maruyama, E. Pasomsub, A. Phuphuakrat, S. Rengpipat, T. Vilaivan, O. Chailapakul, N. Ruecha, and N. Ngamrojanavanich, “Label free electrochemical dna biosensor for covid-19 diagnosis,” *Talanta*, vol. 253, p. 123992, 2 2023.

[15] M. Pourmadadi, E. Rahmani, M. Rajabzadeh-Khosroshahi, A. Samadi, R. Behzadmehr, A. Rahdar, and L. F. R. Ferreira, “Properties and application of carbon quantum dots (cqds) in biosensors for disease detection: A comprehensive review,” *Journal of Drug Delivery Science and Technology*, vol. 80, 2 2023.

[16] T. Saha, R. Del Caño, K. Mahato, E. De la Paz, C. Chen, S. Ding, L. Yin, and J. Wang, “Wearable electrochemical glucose sensors in diabetes management: A comprehensive review,” *Chemical Reviews*, vol. 123, pp. 7854–7889, 6 2023.

[17] S. Nath, “Advancements in food quality monitoring: integrating biosensors for precision detection,” *Sustainable Food Technol.*, vol. 2, pp. 976–992, 2024.

[18] K. C. Honeychurch and M. Piano, “Sensors for environmental monitoring and food safety,” *Biosensors*, vol. 12, no. 6, 2022.

[19] S. Rasheed, T. Kanwal, N. Ahmad, B. Fatima, M. N. ul Haq, and D. Hussain, “Advances and challenges in portable optical biosensors for onsite detection and point-of-care diagnostics,” *TrAC - Trends in Analytical Chemistry*, vol. 173, 4 2024.

[20] A. Curulli, “Electrochemical biosensors in food safety: Challenges and perspectives,” *Molecules*, vol. 26, 5 2021.

[21] B. Acharya, A. Behera, and S. Behera, “Optimizing drug discovery: Surface plasmon resonance techniques and their multifaceted applications,” *Chemical Physics Impact*, vol. 8, 6 2024.

[22] M. A. M. Asri, A. N. Nordin, and N. Ramli, “Low-cost and cleanroom-free prototyping of microfluidic and electrochemical biosensors: Techniques in fabrication and bioconjugation,” *Biomicrofluidics*, vol. 15, 2021.

[23] J. Rainbow, E. Sedlackova, S. Jiang, G. Maxted, D. Moschou, L. Richtera, and P. Estrela, "Integrated electrochemical biosensors for detection of waterborne pathogens in low-resource settings," *Biosensors*, vol. 10, 2020.

[24] T. R. Das, S. Patra, P. P. Govender, and S. K. Shukla, *Chapter 1 - Biosensors: principle, fundamentals history, recent trends and applications.* Academic Press, 2022, pp. 1–18.

[25] E. Cesewski and B. N. Johnson, "Electrochemical biosensors for pathogen detection," *Biosensors and Bioelectronics*, vol. 159, 2020.

[26] A. K. Singh, S. Mittal, M. Das, A. Saharia, and M. Tiwari, "Optical biosensors: a decade in review," *Alexandria Engineering Journal*, vol. 67, 2023.

[27] D. Zhao, P. Xiao, X. Dong, Y. Ge, X. Guo, J. Ji, Y. Cheng, and S. Sang, "A mechanical biosensor based on membrane-mediated magneto-stress-electric coupled sensitization for human serum albumin detection," *Journal of Materials Chemistry B*, vol. 11, 2023.

[28] V. Naresh and N. Lee, "A review on biosensors and recent development of nanostructured materials-enabled biosensors," *Sensors (Switzerland)*, vol. 21, 2021.

[29] V. R. Samuel and K. J. Rao, "A review on label free biosensors," *Biosensors and Bioelectronics: X*, vol. 11, 2022.

[30] L. Huang, C. Zhang, R. Ye, B. Yan, X. Zhou, W. Xu, and J. Guo, "Capacitive biosensors for label-free and ultrasensitive detection of biomarkers," *Talanta*, vol. 266, 2024.

[31] R. Kumar, S. Agarwal, S. Pal, A. Verma, and Y. K. Prajapati, "Refractive index sensing using mxene mediated surface plasmon resonance sensor in visible to near infrared regime," *Measurement: Journal of the International Measurement Confederation*, vol. 224, 2024.

[32] F. Bonyadi, M. Kavruk, S. Ucak, B. Cetin, G. Bayramoglu, A. D. Dursun, Y. Arica, and V. C. Ozalp, "Real-time biosensing bacteria and virus with quartz crystal microbalance: Recent advances, opportunities, and challenges," *Critical Reviews in Analytical Chemistry*, 2023.

[33] C. V. Topor, M. Puiu, and C. Bala, "Strategies for surface design in surface plasmon resonance (spr) sensing," *Biosensors 2023, Vol. 13, Page 465*, vol. 13, p. 465, 4 2023.

[34] M. Sedki, Y. Chen, and A. Mulchandani, "Non-carbon 2d materials-based field-effect transistor biosensors: Recent advances, challenges, and future perspectives," *Sensors*, vol. 20, 2020.

[35] S. Akgönüllü, E. Özgür, and A. Denizli, "Recent advances in quartz crystal microbalance biosensors based on the molecular imprinting technique for disease-related biomarkers," *Chemosensors*, vol. 10, 2022.

[36] A. S. S. Vasan, D. M. Mahadeo, R. Doraiswami, Y. Huang, and M. Pecht, "Point-of-care biosensor system," *FBS*, vol. 5, no. 1, pp. 39–71, 2013.

[37] P. Sengupta, C. W. Wang, and Z. F. Ma, "Enzyme-linked immunosorbent assay (elisa) technique for food analysis," *Techniques to Measure Food Safety and Quality: Microbial, Chemical, and Sensory*, pp. 91–115, 9 2021.

[38] D. A. D. Angelis, "Fluorescence resonance energy transfer (fret)," *Molecular Analyses*, pp. 105–114, 1 2022.

[39] S. Hong, A. A. S. Samson, and J. M. Song, "Application of fluorescence resonance energy transfer to bioprinting," *TrAC - Trends in Analytical Chemistry*, vol. 122, 2020.

[40] M. G. Shemirani, M. Mohammadimasoudi, A. Goudarzi, M. Esmailpour, M. Kelishadi, H. T. Safa, I. Ahmadalidokht, F. Fotouhi-Chahouki, H. Hajghassem, and H. Shahsavarani, "A cost-effective label-free biosensor for rapid detection of multiple viral respiratory infections base on liquid crystals: Fabrication and modeling," *Biosensors and Bioelectronics*, vol. 245, 2024.

[41] M. L. Brongersma and V. M. Shalaev, "The case for plasmonics," *Science*, vol. 328, pp. 440–441, 4 2010.

[42] W. F. Stöcklein, O. Behrsing, G. Scharte, B. Micheel, A. Benkert, W. Schößler, A. Warsinke, and F. W. Scheller, "Enzyme kinetic assays with surface plasmon resonance (biacore) based on competition between enzyme and creatinine antibody," *Biosensors and Bioelectronics*, vol. 15, no. 7, pp. 377–382, 2000.

[43] D. G. Drescher, M. J. Drescher, and N. A. Ramakrishnan, "Surface plasmon resonance (spr) analysis of binding interactions of proteins in inner-ear sensory epithelia," *Methods in Molecular Biology*, vol. 493, pp. 323–343, 2009.

[44] Z. Salamon, S. Cowell, E. Varga, H. I. Yamamura, V. J. Hruby, and G. Tollin, "Plasmon resonance studies of agonist/antagonist binding to the human δ-opioid receptor: New structural insights into receptor-ligand interactions," *Biophysical Journal*, vol. 79, pp. 2463–2474, 2000.

[45] H. Zhang, L. Yang, B. Zhou, X. Wang, G. Liu, W. Liu, and P. Wang, "Investigation of biological cell–protein interactions using spr sensor through laser scanning confocal imaging–surface plasmon

resonance system," *Spectrochimica Acta Part A: Molecular and Biomolecular Spectroscopy*, vol. 121, pp. 381–386, 2014.

[46] Y. Huang, L. Zhang, H. Zhang, Y. Li, L. Liu, Y. Chen, X. Qiu, and D. Yu, "Development of a portable spr sensor for nucleic acid detection," *Micromachines*, vol. 11, no. 5, 2020.

[47] P. Singh, *Surface Plasmon Resonance: A Boon for Viral Diagnostics.* Elsevier, 2017.

[48] H. Zhao, I. I. Gorshkova, G. L. Fu, and P. Schuck, "A comparison of binding surfaces for spr biosensing using an antibody–antigen system and affinity distribution analysis," *Methods*, vol. 59, no. 3, pp. 328–335, 2013.

[49] X. Zhang, Z. Li, W. Yan, A. Li, F. Zhang, X. Li, M. Lu, and W. Peng, "Customizable miniaturized spr instrument," *Talanta*, vol. 269, p. 125440, 3 2024.

[50] V. Yesudasu, H. S. Pradhan, and R. J. Pandya, "Recent progress in surface plasmon resonance based sensors: A comprehensive review," *Heliyon*, vol. 7, p. e06321, 3 2021.

[51] H. Cai, M. Wang, J. Liu, and X. Wang, "Theoretical and experimental study of a highly sensitive spr biosensor based on au grating and au film coupling structure," *Optics Express*, vol. 30, 2022.

[52] E. G. Loewen and E. Popov, *Diffraction Gratings and Applications.* CRC Press, 10 2018.

[53] Y. Dai, H. Xu, H. Wang, Y. Lu, and P. Wang, "Experimental demonstration of high sensitivity for silver rectangular grating-coupled surface plasmon resonance (spr) sensing," *Optics Communications*, vol. 416, 2018.

[54] W. Udos, K. S. Lim, C. L. Tan, M. N. Ismail, C. W. Ooi, R. Zakaria, and H. Ahmad, "Spatial frequency spectrum of spr-tfbg: A simple spectral analysis for in-situ refractometry," *Optik*, vol. 219, 2020.

[55] E. P. Rodrigues, L. C. Oliveira, M. L. Silva, C. S. Moreira, and A. M. Lima, "Surface plasmon resonance sensing characteristics of thin copper and gold films in aqueous and gaseous interfaces," *IEEE Sensors Journal*, vol. 20, 2020.

[56] A. K. Sharma and A. K. Pandey, "Metal oxide grating based plasmonic refractive index sensor with si layer in optical communication band," *IEEE Sensors Journal*, vol. 20, 2020.

[57] X. Liu, J. Liu, H. Yang, B. Huang, and G. Zeng, "Design of a high-performance graphene/sio 2 -ag periodic grating/mos 2 surface plasmon resonance sensor," *Applied Optics*, vol. 61, 2022.

[58] Y. Tong, L. Ding, K. Han, X. Zou, S. Wang, Z. Wen, Y. Ye, and X. Ren, "Detection of carbendazim in oranges with metal grating integrated microfluidic sensor in terahertz," *Food Additives and Contaminants - Part A*, vol. 39, 2022.

[59] S. A. Maier, *Electromagnetics of Metals.* New York, NY: Springer US, 2007, pp. 5–19.

[60] H. Kocer, S. Butun, Z. Li, and K. Aydin, "Reduced near-infrared absorption using ultra-thin lossy metals in fabry-perot cavities," *Scientific Reports 2015 5:1*, vol. 5, pp. 1–6, 2 2015.

[61] M.-Y. Kao, C.-H. Hsu, Y.-Q. Huang, Y.-C. Hsu, M.-J. Liu, C.-T. Chen, P.-C. Lai, M.-Y. Lu, P.-J. Wu, and Y.-L. Chueh, "Effects of extreme ultraviolet radiation on transition metal dichalcogenides: Investigation of physical and electrical properties," *ACS Applied Electronic Materials*, vol. 6, no. 8, pp. 5640–5650, 2024.

[62] J. A. Creighton and D. G. Eadon, "Ultraviolet-visible absorption spectra of the colloidal metallic elements," *Journal of the Chemical Society, Faraday Transactions*, vol. 87, 1991.

[63] A. Kirsch and F. Hettlich, "The mathematical theory of time-harmonic maxwell's equations: Expansion-, integral-, and variational methods," *Applied Mathematical Sciences (Switzerland)*, vol. 190, pp. i–337, 2015.

[64] J. D. Jackson, *Classical Electrodynamics-Third Edition.* John Wiley and Sons, 1998.

[65] M. P. Marder, "Condensed matter physics, second edition," *Condensed Matter Physics, Second Edition*, 11 2010.

[66] R. W. Boyd, "Nonlinear optics," *Nonlinear Optics*, pp. 1–578, 2003.

[67] M. Arrayás and J. L. Trueba, "The method of fourier transforms applied to electromagnetic knots," *European Journal of Physics*, vol. 40, p. 015205, 12 2018.

[68] B. Marder, "A method for incorporating gauss' law into electromagnetic pic codes," *Journal of Computational Physics*, vol. 68, pp. 48–55, 1 1987.

[69] S. Ellipsometry, "Drude dispersion model," *Horiba Jobin Yvon*, 1900.

[70] P. B. Johnson and R. W. Christy, "Optical constants of the noble metals," *Physical Review B*, vol. 6, 1972.

[71] R. Von N. W. Ashcroft und N. D. Mermin; Holt and Winston, *Solide State Physics.* Physik in unserer Zeit, 1978, vol. 9.

[72] A. F. J. Levi, *The Lorentz oscillator model.* Morgan and Claypool Publishers, 2016.

[73] B. Saleh and M. C. Teich, *Fundamental of Photonics*, 3rd ed. John Wiley and Sons, Inc., 2019, vol. 5.

[74] E. J. Zeman and G. C. Schatz, "An accurate electromagnetic theory study of surface enhancement factors for silver, gold, copper, lithium, sodium, aluminum, gallium, indium, zinc, and cadmium," *The Journal of Physical Chemistry*, vol. 91, no. 3, pp. 634–643, 1987.

[75] N. A. Gumerov and R. Duraiswami, "Fast multipole methods for the helmholtz equation in three dimensions," *Fast Multipole Methods for the Helmholtz Equation in Three Dimensions*, 2005.

[76] E. Kretschmann and H. Raether, "Radiative decay of non radiative surface plasmons excited by light," *Zeitschrift fur Naturforschung - Section A Journal of Physical Sciences*, vol. 23, pp. 2135–2136, 1968.

[77] A. Otto, "Excitation of nonradiative surface plasma waves in silver by the method of frustrated total reflection," *Zeitschrift für Physik A Hadrons and nuclei 1968 216:4*, vol. 216, pp. 398–410, 1968.

[78] E. Devaux, T. W. Ebbesen, J. C. Weeber, and A. Dereux, "Launching and decoupling surface plasmons via micro-gratings," *Applied Physics Letters*, vol. 83, p. 4936, 2003.

[79] Y. Y. Teng and E. A. Stern, "Plasma radiation from metal grating surfaces," *Physical Review Letters*, vol. 19, p. 511, 1967.

[80] J. Jahns and S. Helfert, *Introduction to Micro- and Nanooptics.* Wiley-VCH Verlag, 2012.

[81] M. Seo, J. Lee, and M. Lee, "Grating-coupled surface plasmon resonance on bulk stainless steel," *Opt. Express*, vol. 25, no. 22, pp. 26 939–26 949, Oct 2017.

[82] P. Sarapukdee, C. Spenner, D. Schulz, and S. Palzer, "Optimizing stability and performance of silver-based grating structures for surface plasmon resonance sensors," *Sensors*, vol. 23, no. 15, 2023.

[83] T. Putnin, C. Lertvachirapaiboon, R. Ishikawa, K. Shinbo, K. Kato, S. Ekgasit, K. Ounnunkad, and A. Baba, "Enhanced organic solar cell performance: Multiple surface plasmon resonance and incorporation of silver nanodisks into a grating-structure electrode," *Opto Electron Adv*, vol. 2, no. 7, p. 190010, 2019.

[84] C. Gong and M. S. Leite, "Noble metal alloys for plasmonics," *ACS Photonics*, vol. 3, 2016.

[85] P. Nagpal, N. C. Lindquist, S. H. Oh, and D. J. Norris, “Ultrasmooth patterned metals for plasmonics and metamaterials,” *Science*, vol. 325, 2009.

[86] M. Wagner, A. Seifert, and L. M. Liz-Marzán, “Towards multi-molecular surface-enhanced infrared absorption using metal plasmonics,” *Nanoscale Horizons*, vol. 7, 2022.

[87] D. Sarid and W. A. Challener, “Plasmonic materials,” *Modern Introduction to Surface Plasmons*, pp. 283–304, 5 2010.

[88] Y. Li, *Optical Properties of Plasmonic Materials.* SPIE PRESS, 2017, pp. 1–41.

[89] C. G. Walker, J. A. Matthew, C. A. Anderson, and N. M. Brown, “An estimate of the electron effective mass in titanium nitride using ups and eels,” *Surface Science*, vol. 412-413, 1998.

[90] P. Prieto, F. Yubero, E. Elizalde, and J. M. Sanz, “Dielectric properties of zr, zrn, zr3n4, and zro2 determined by quantitative analysis of electron energy loss spectra,” *Journal of Vacuum Science and Technology A, Vacuum, Surfaces, and Films*, vol. 14, 1996.

[91] G. Soto, J. A. Díaz, and W. D. la Cruz, “Copper nitride films produced by reactive pulsed laser deposition,” *Materials Letters*, vol. 57, 2003.

[92] R. Lv, J. A. Robinson, R. E. Schaak, D. Sun, Y. Sun, T. E. Mallouk, and M. Terrones, “Transition metal dichalcogenides and beyond: Synthesis, properties, and applications of single- and few-layer nanosheets,” *Accounts of Chemical Research*, vol. 48, 2015.

[93] M. G. Blaber, M. D. Arnold, and M. J. Ford, “A review of the optical properties of alloys and intermetallics for plasmonics,” *Journal of Physics Condensed Matter*, vol. 22, 2010.

[94] P. West, S. Ishii, G. Naik, N. Emani, V. Shalaev, and A. Boltasseva, “Searching for better plasmonic materials,” pp. 795–808, 2010.

[95] P. H. Smith and H. Gurev, “Silicon dioxide as a high temperature stabilizer for silver films,” *Thin Solid Films*, vol. 45, 1977.

[96] A. A. Rifat, G. A. Mahdiraji, D. M. Chow, Y. G. Shee, R. Ahmed, and F. R. M. Adikan, “Photonic crystal fiber-based surface plasmon resonance sensor with selective analyte channels and graphene-silver deposited core,” *Sensors (Switzerland)*, vol. 15, 2015.

[97] S. N. Bonvicini and Y. Shi, “Formation and removal of alloyed bimetallic au-ag nanoparticles from silicon substrates for tunable surface plasmon resonance,” *ACS Applied Nano Materials*, vol. 5, 2022.

[98] P. J. Mok, W. Leung, K. Constant, T.-G. Kim, and K.-M. Ho, “Laser interference lithography and shadow lithography for fabricating nanowires and nanoribbons,” in *Nanowires*, A. Hashim, Ed. Rijeka: IntechOpen, 2011, ch. 21.

[99] E. Gazzola, A. Pozzato, G. Ruffato, E. Sovernigo, and A. Sonato, “High-throughput fabrication and calibration of compact high-sensitivity plasmonic lab-on-chip for biosensing,” *Optofluidics, Microfluidics and Nanofluidics*, vol. 3, 2016.

[100] D. Murugan, M. Tintelott, M. S. Narayanan, X.-T. Vu, T. Kurkina, C. Rodriguez-Emmenegger, U. Schwaneberg, J. Dostalek, S. Ingebrandt, and V. Pachauri, “Recent advances in grating coupled surface plasmon resonance technology,” *Advanced Optical Materials*, vol. 12, no. 34, p. 2401862, 2024.

[101] L. J. Guo, “Nanoimprint lithography: Methods and material requirements,” *Advanced Materials*, vol. 19, 2007.

[102] N. Kooy, K. Mohamed, L. T. Pin, and O. S. Guan, “A review of roll-to-roll nanoimprint lithography,” *Nanoscale Research Letters*, vol. 9, 2014.

[103] S. Senzaki, T. Okabe, and J. Taniguchi, “Fabrication of bifocal lenses using resin that can be processed by electron beam lithography after ultraviolet-nanoimprint lithography,” *Microelectronic Engineering*, vol. 258, 2022.

[104] N. Zhang, H. Liu, and W. Knoll, “A disposable polymer sensor chip combined with micro-fluidics and surface plasmon read-out,” *Biosensors and Bioelectronics*, vol. 24, pp. 1783–1787, 2 2009.

[105] J. S. Wi, S. Lee, S. H. Lee, D. K. Oh, K. T. Lee, I. Park, M. K. Kwak, and J. G. Ok, “Facile three-dimensional nanoarchitecturing of double-bent gold strips on roll-to-roll nanoimprinted transparent nanogratings for flexible and scalable plasmonic sensors,” *Nanoscale*, vol. 9, pp. 1398–1402, 1 2017.

[106] N. Unno and T. Mäkelä, “Thermal nanoimprint lithography—a review of the process, mold fabrication, and material,” *Nanomaterials 2023, Vol. 13, Page 2031*, vol. 13, p. 2031, 7 2023.

[107] C.-H. Lin, Y.-M. Lin, C.-C. Liang, Y.-Y. Lee, H.-S. Fung, B.-Y. Shew, and S.-H. Chen, “Extreme uv diffraction grating fabricated by nanoimprint lithography,” *Microelectronic Engineering*, vol. 98, pp. 194–197, 2012, special issue MNE 2011 - Part II.

[108] S. Long, J. Cao, Y. Wang, S. Gao, N. Xu, J. Gao, and W. Wan, “Grating coupled spr sensors using off the shelf compact discs and sensitivity dependence on grating period,” *Sensors and Actuators Reports*, vol. 2, p. 100016, 2020.

[109] X. Wang, W. Shi, R. Vafaei, N. A. Jaeger, and L. Chrostowski, “Silicon-on-insulator bragg gratings fabricated by deep uv lithography,” *2010 Asia Communications and Photonics Conference and Exhibition, ACP 2010*, pp. 501–502, 2010.

[110] C. Vieu, F. Carcenac, A. Pépin, Y. Chen, M. Mejias, A. Lebib, L. Manin-Ferlazzo, L. Couraud, and H. Launois, “Electron beam lithography: Resolution limits and applications,” *Applied Surface Science*, vol. 164, 2000.

[111] S. N. M. Bajuri, N. Hamidah, A. Halim, and J. Kangar-arau, “Pmma characterization and optimization for nano structure formation,” *1st National Conference on Electronic Design*, 2005.

[112] Y. Saito, S. Suzuki, and T. Kan, “Si grating structure for surface plasmon resonance excitation by back-side normal incidence illumination,” *Applied Physics Express*, vol. 14, 2021.

[113] C. T. DeRoo, J. Termini, F. Grisé, R. L. McEntaffer, B. D. Donovan, and C. Eichfeld, “Limiting spectral resolution of a reflection grating made via electron-beam lithography,” *The Astrophysical Journal*, vol. 904, 2020.

[114] J. Dostálek, J. Homola, and M. Miler, “Rich information format surface plasmon resonance biosensor based on array of diffraction gratings,” *Sensors and Actuators B: Chemical*, vol. 107, pp. 154–161, 5 2005.

[115] K. Tawa, F. Kondo, C. Sasakawa, K. Nagae, Y. Nakamura, A. Nozaki, and T. Kaya, “Sensitive detection of a tumor marker, alpha-fetoprotein, with a sandwich assay on a plasmonic chip,” *Analytical Chemistry*, vol. 87, pp. 3871–3876, 4 2015.

[116] K. Kintaka, K. Tawa, Y. Tatsu, J. Nishii, H. Hori, and K. Kiyosue, “Optical microscopic observation of fluorescence enhanced by grating-coupled surface plasmon resonance,” *Optics Express, Vol. 16, Issue 13, pp. 9781-9790*, vol. 16, pp. 9781–9790, 6 2008.

[117] Q. Wang, D. Zhang, Y. Qian, X. Yin, L. Wang, S. Zhang, and Y. Wang, “Research on fiber optic surface plasmon resonance biosensors: A review,” *Photonic Sensors 2024 14:2*, vol. 14, pp. 1–30, 3 2024.

[118] D. Yoo, A. Barik, F. D. León-Pérez, D. A. Mohr, M. Pelton, L. Martín-Moreno, and S. H. Oh, “Plasmonic split-trench resonator for trapping and sensing,” *ACS Nano*, vol. 15, pp. 6669–6677, 4 2021.

[119] S. Masui, S. Goda, S. Kadoya, M. Michihata, and S. Takahashi, “Grating periods measurement of multi-pitched grating using littrow configuration external cavity diode laser,” *Applied Physics Express*, vol. 14, p. 076501, 6 2021.

[120] J. Cao, Y. Sun, Y. Kong, and W. Qian, "The sensitivity of grating-based spr sensors with wavelength interrogation," *Sensors*, vol. 19, no. 2, 2019.

[121] G. Borile, S. Rossi, A. Filippi, E. Gazzola, P. Capaldo, C. Tregnago, M. Pigazzi, and F. Romanato, "Label-free, real-time on-chip sensing of living cells via grating-coupled surface plasmon resonance," *Biophysical Chemistry*, vol. 254, p. 106262, 2019.

[122] A. Sonato, M. Agostini, G. Ruffato, E. Gazzola, D. Liuni, G. Greco, M. Travagliati, M. Cecchini, and F. Romanato, "A surface acoustic wave (saw)-enhanced grating-coupling phase-interrogation surface plasmon resonance (spr) microfluidic biosensor," *Lab on a Chip*, vol. 16, pp. 1224–1233, 2016.

[123] S. Rossi, E. Gazzola, P. Capaldo, G. Borile, and F. Romanato, "Grating-coupled surface plasmon resonance (gc-spr) optimization for phase-interrogation biosensing in a microfluidic chamber," *Sensors*, vol. 18, no. 5, 2018.

[124] Y. Xu, L. Wu, and L. K. Ang, "Surface exciton polaritons: A promising mechanism for refractive-index sensing," *Physical Review Applied*, vol. 12, p. 024029, 8 2019.

[125] A. N. K. Reddy and D. K. Sagar, "Half-width at half-maximum, full-width at half-maximum analysis for resolution of asymmetrically apodized optical systems with slit apertures," *Pramana 2014 84:1*, vol. 84, pp. 117–126, 11 2014.

[126] F. Allegrini and A. C. Olivieri, *2.20 - Figures of Merit*, second edition ed. Oxford: Elsevier, 2020, pp. 441–463.

[127] M. Intelligence, "Label-free detection market - share, size and industry analysis," 2 2025. [Online]. Available: https://www.mordorintelligence.com/industry-reports/label-free-detection-lfd-market

[128] T. Mohammad, S. Ashrafi, and G. Mohanty, "Surface plasmon resonance sensors: A critical review of recent advances, market analysis, and future directions," *Plasmonics*, 123.

[129] W. Ma, L. Yang, and L. He, "Overview of the detection methods for equilibrium dissociation constant kd of drug-receptor interaction," *Journal of Pharmaceutical Analysis*, vol. 8, 2018.

[130] D. Saito and T. Nakagawa, *Surface plasmon resonance.* Elsevier, 1 2020, pp. 295–309.

[131] A. Kausaite-Minkstimiene, A. Popov, and A. Ramanaviciene, "Ultra-sensitive spr immunosensors: A comprehensive review of labeling and interface modification using nanostructures," *TrAC - Trends in Analytical Chemistry*, vol. 170, 2024.

[132] X. Li, W. Yang, H. Chen, F. Pan, W. Liu, D. Qi, S. Yu, H. Liu, X. Chai, Y. Liu, Y. Pan, and G. Wang, “Rapid screening and in vivo target occupancy quantitative evaluation of xanthine oxidase inhibitors based on drug-target binding kinetics research strategy: A case study of chrysanthemum morifolium ramat.” *Biomedicine and Pharmacotherapy*, vol. 161, p. 114379, 2023.

[133] E. Hemmerová, T. Špringer, Z. Krištofiková, and J. Homola, “Ionic environment affects biomolecular interactions of amyloid-beta: Spr biosensor study,” *International Journal of Molecular Sciences*, vol. 21, 2020.

[134] I. Moscetti, S. Cannistraro, and A. R. Bizzarri, “Surface plasmon resonance sensing of biorecognition interactions within the tumor suppressor p53 network,” *Sensors 2017, Vol. 17, Page 2680*, vol. 17, p. 2680, 11 2017.

[135] O. R. Bolduc and J. F. Masson, “Advances in surface plasmon resonance sensing with nanoparticles and thin films: Nanomaterials, surface chemistry, and hybrid plasmonic techniques,” *Analytical Chemistry*, vol. 83, pp. 8057–8062, 11 2011.

[136] C. Fenzl, C. Genslein, C. Domonkos, K. A. Edwards, T. Hirsch, and A. J. Baeumner, “Investigating non-specific binding to chemically engineered sensor surfaces using liposomes as models,” *Analyst*, vol. 141, 2016.

[137] J. Visentin, L. Couzi, C. Dromer, M. Neau-Cransac, G. Guidicelli, V. Veniard, K. N. le Coniat, P. Merville, C. D. Primo, and J. L. Taupin, “Overcoming non-specific binding to measure the active concentration and kinetics of serum anti-hla antibodies by surface plasmon resonance,” *Biosensors and Bioelectronics*, vol. 117, 2018.

[138] D. M. Kim, J. S. Park, S. W. Jung, J. Yeom, and S. M. Yoo, “Biosensing applications using nanostructure-based localized surface plasmon resonance sensors,” *Sensors 2021, Vol. 21, Page 3191*, vol. 21, p. 3191, 5 2021.

[139] G. Doria, J. Conde, B. Veigas, L. Giestas, C. Almeida, M. Assunção, J. Rosa, and P. V. Baptista, “Noble metal nanoparticles for biosensing applications,” *Sensors*, vol. 12, 2012.

[140] J. Langer, S. M. Novikov, and L. M. Liz-Marzán, “Sensing using plasmonic nanostructures and nanoparticles,” *Nanotechnology*, vol. 26, no. 32, p. 322001, jul 2015.

[141] C. F. A. Negre and C. G. Sánchez, *Optical Properties of Metal Nanoclusters from an Atomistic Point of View.* New York, NY: Springer New York, 2013, pp. 105–157.

[142] K. A. Willets and R. P. V. Duyne, “Localized surface plasmon resonance spectroscopy and sensing,” *Annual Review of Physical Chemistry*, vol. 58, pp. 267–297, 2007.

[143] E. Petryayeva and U. J. Krull, “Localized surface plasmon resonance: Nanostructures, bioassays and biosensing—a review,” *Analytica Chimica Acta*, vol. 706, pp. 8–24, 2011.

[144] N. G. Bastús, J. Piella, and V. Puntes, “Quantifying the sensitivity of multipolar (dipolar, quadrupolar, and octapolar) surface plasmon resonances in silver nanoparticles: The effect of size, composition, and surface coating,” *Langmuir*, vol. 32, 2016.

[145] A. Kuzminova, P. Solař, P. Kúš, and O. Kylián, “Double plasmon resonance nanostructured silver coatings with tunable properties,” *Journal of Nanomaterials*, vol. 2019, 2019.

[146] L. L. Sun, Y. S. Leo, X. Zhou, W. Ng, T. I. Wong, and J. Deng, “Localized surface plasmon resonance based point-of-care system for sepsis diagnosis,” *Materials Science for Energy Technologies*, vol. 3, 2020.

[147] Z. Fan, Z. Geng, W. Fang, X. Lv, Y. Su, S. Wang, and H. Chen, “Smartphone biosensor system with multi-testing unit based on localized surface plasmon resonance integrated with microfluidics chip,” *Sensors (Switzerland)*, vol. 20, 2020.

[148] G. A. Lopez, M. C. Estevez, M. Soler, and L. M. Lechuga, “Recent advances in nanoplasmonic biosensors: Applications and lab-on-a-chip integration,” *Nanophotonics*, vol. 6, 2017.

[149] P. Yu, L. V. Besteiro, Y. Huang, J. Wu, L. Fu, H. H. Tan, C. Jagadish, G. P. Wiederrecht, A. O. Govorov, and Z. Wang, “Broadband metamaterial absorbers,” *Advanced Optical Materials*, vol. 7, 2019.

[150] S. Unser, I. Bruzas, J. He, and L. Sagle, “Localized surface plasmon resonance biosensing: Current challenges and approaches,” *Sensors*, vol. 15, 2015.

[151] M. P. Mcoyi, K. T. Mpofu, M. Sekhwama, and P. Mthunzi-Kufa, “Developments in localized surface plasmon resonance,” *Plasmonics 2024*, pp. 1–40, 11 2024.

[152] J. Li, Z. Lou, and B. Li, “Nanostructured materials with localized surface plasmon resonance for photocatalysis,” *Chinese Chemical Letters*, vol. 33, 2022.

[153] S. Long, E. Wang, M. Wu, H. Zhu, N. Xu, Y. Wang, and J. Cao, “Sensing absorptive fluids with backside illuminated grating coupled spr sensor fabricated by nanoimprint technology,” *Sensors and Actuators A: Physical*, vol. 337, p. 113416, 2022.

[154] M. Oshita, S. Suzuki, K. Masamoto, and T. Kan, "Detection of backside coupled propagating surface plasmon resonance on the sidewall of a wafer," *AIP Advances*, vol. 13, p. 10, 11 2023.

[155] P. Sarapukdee, D. Schulz, and S. Palzer, "Concept, simulation, and fabrication of inverted grating structures for surface plasmon resonance sensors," *Journal of Sensors and Sensor Systems*, vol. 13, no. 2, pp. 157–166, 2024.

[156] Y. Saito, Y. Yamamoto, T. Kan, T. Tsukagoshi, K. Noda, and I. Shimoyama, "Electrical detection spr sensor with grating coupled backside illumination," *Optics Express*, vol. 27, p. 17763, 2019.

[157] T. Kan, Y. Saito, and S. Suzuki, "Backside illumination spr generating structure for efficient light coupling," in *2021 IEEE 34th International Conference on Micro Electro Mechanical Systems (MEMS)*, 2021, pp. 933–936.

[158] S. Pi, X. Zeng, N. Zhaug, D. Ji, H. Soug, S. Jiang, and Q. Gan, "Dielectric-grating-coupled surface plasmon resonance for ultrasensitive sensing," *Frontiers in Optics 2016 (2016), paper JW4A.30*, p. JW4A.30, 2016.

[159] W.-K. Kuo, J. Tongpakpanang, P.-H. Kuo, and S.-F. Kuo, "Implementation and phase detection of dielectric-grating-coupled surface plasmon resonance sensor for backside incident light," *Optics express*, vol. 27, p. 3867, 2019.

[160] S. Hageneder, S. Fossati, N.-G. Ferrer, N.-G. Ferrer, B. Güngörmez, B. Güngörmez, S. K. Auer, S. K. Auer, J. Dostalek, and J. Dostalek, "Multi-diffractive grating for surface plasmon biosensors with direct back-side excitation," *Optics Express, Vol. 28, Issue 26, pp. 39770-39780*, vol. 28, pp. 39 770–39 780, 2020.

[161] N. C. Lindquist, T. W. Johnson, J. Jose, L. M. Otto, and S. H. Oh, "Ultrasmooth metallic films with buried nanostructures for backside reflection-mode plasmonic biosensing," *Annalen der Physik*, vol. 524, pp. 687–696, 2012.

[162] A. K. Ghosh, S. Sarkar, L. J. Nebel, O. Aftenieva, V. Gupta, O. Sander, A. Das, J. Joseph, S. Wießner, T. A. König, and A. Fery, "Exploring plasmonic resonances toward "large-scale" flexible optical sensors with deformation stability," *Advanced Functional Materials*, vol. 31, p. 2101959, 7 2021.

[163] D. Geilfuss, R. Boukherroub, J. Dostalek, W. Knoll, J.-F. Masson, A. J. Baeumner, and S. Szunerits, "Can classical surface plasmon resonance advance via the coupling to other analytical approaches?" *Frontiers in Analytical Science*, vol. 2, p. 1091869, 12 2022.

[164] T. Vandenryt, A. Pohl, B. Van Grinsven, R. Thoelen, W. De Ceuninck, P. Wagner, and J. Opitz, “Combining electrochemical impedance spectroscopy and surface plasmon resonance into one simultaneous read-out system for the detection of surface interactions,” *Sensors*, vol. 13, no. 11, pp. 14 650–14 661, 2013.

[165] Y. Ajiki, T. Kan, K. Matsumoto, and I. Shimoyama, “Electrically detectable surface plasmon resonance sensor by combining a gold grating and a silicon photodiode,” *Applied Physics Express*, vol. 11, p. 022001, 2018.

[166] A. Shakoor, B. C. Cheah, D. Hao, M. Al-Rawhani, B. Nagy, J. Grant, C. Dale, N. Keegan, C. McNeil, and D. R. S. Cumming, “Plasmonic sensor monolithically integrated with a cmos photodiode,” *ACS Photonics*, vol. 3, no. 10, pp. 1926–1933, 2016.

[167] S. Patskovsky, A. M. Dallaire, and M. Meunier, “Electrochemical surface plasmon resonance sensing with absorptive redox mediator film,” *Sensors and Actuators B: Chemical*, vol. 222, pp. 71–77, 1 2016.

[168] P. Aspermair, U. Ramach, C. Reiner-Rozman, S. Fossati, B. Lechner, S. E. Moya, O. Azzaroni, J. Dostalek, S. Szunerits, W. Knoll, and J. Bintinger, “Dual monitoring of surface reactions in real time by combined surface-plasmon resonance and field-effect transistor interrogation,” *Journal of the American Chemical Society*, vol. 142, no. 27, pp. 11 709–11 716, 2020.

[169] L. Wen, L. Liang, X. Yang, Z. Liu, B. Li, and Q. Chen, “Multiband and ultrahigh figure-of-merit nanoplasmonic sensing with direct electrical readout in au-si nanojunctions,” *ACS Nano*, vol. 13, no. 6, pp. 6963–6972, 2019, pMID: 31180202.

[170] R. Kuroki, S. Suzuki, S. Yasunaga, M. Oshita, and T. Kan, “Grating-based surface plasmon resonance sensor for visible light employing a metal/semiconductor junction for electrical readout,” *IEEE Sensors Journal*, vol. 22, no. 23, pp. 22 557–22 563, 2022.

[171] J. Li, L. Shi, Y. Ma, Y. Ran, Y. Liu, and J. Wang, “Efficient and stable implementation of rcwa for ultrathin multilayer gratings: T-matrix approach without solving eigenvalues,” *IEEE Antennas and Wireless Propagation Letters*, vol. 20, no. 1, pp. 83–87, 2021.

[172] W. Zhang, G. Liu, J. Bi, K. Bao, and P. Wang, “In-situ and ultrasensitive detection of mercury (ii) ions (hg2+) using the localized surface plasmon resonance (lspr) nanosensor and the microfluidic chip,” *Sensors and Actuators A: Physical*, vol. 349, p. 114074, 2023. [Online]. Available: https://www.sciencedirect.com/science/article/pii/S0924424722007099

[173] Y. J. Wei, Y. N. Zhao, X. Zhang, X. Wei, M. L. Chen, and X. W. Chen, "Biochemical analysis based on optical detection integrated microfluidic chip," *TrAC - Trends in Analytical Chemistry*, vol. 158, 2023.

[174] X. Ou, P. Chen, and B. F. Liu, "Optical technologies for single-cell analysis on microchips," *Chemosensors*, vol. 11, 2023.

[175] Y. Liu and X. Zhang, "Microfluidics-based plasmonic biosensing system based on patterned plasmonic nanostructure arrays," *Micromachines*, vol. 12, 2021.

[176] M. Soler, A. Belushkin, A. Cavallini, C. Kebbi-Beghdadi, G. Greub, and H. Altug, "Multiplexed nanoplasmonic biosensor for one-step simultaneous detection of chlamydia trachomatis and neisseria gonorrhoeae in urine," *Biosensors and Bioelectronics*, vol. 94, pp. 560–567, 2017.

[177] C. Xiao, J. Eriksson, A. Suska, D. Filippini, and W. C. Mak, "Print-and-stick unibody microfluidics coupled surface plasmon resonance (spr) chip for smartphone imaging spr (smart-isrp)," *Analytica Chimica Acta*, vol. 1201, p. 339606, 4 2022.

[178] O. Tokel, U. H. Yildiz, F. Inci, N. G. Durmus, O. O. Ekiz, B. Turker, C. Cetin, S. Rao, K. Sridhar, N. Natarajan, H. Shafiee, A. Dana, and U. Demirci, "Portable microfluidic integrated plasmonic platform for pathogen detection," *Scientific Reports 2015 5:1*, vol. 5, pp. 1–9, 3 2015.

[179] F. Tian, C. Liu, J. Deng, and J. Sun, "Microfluidic separation, detection, and engineering of extracellular vesicles for cancer diagnostics and drug delivery," *Accounts of Materials Research*, vol. 3, pp. 498–510, 5 2022.

[180] "Microfluidic surface plasmon resonance sensors: From principles to point-of-care applications," *Sensors*, vol. 16, 2016.

[181] B. Liedberg, C. Nylander, and I. Lunström, "Surface plasmon resonance for gas detection and biosensing," *Sensors and Actuators*, vol. 4, pp. 299–304, 1983.

[182] "Research advances on surface plasmon resonance biosensors," *Nanoscale*, vol. 14, 2022.

[183] P. Steglich, G. Lecci, and A. Mai, "Surface plasmon resonance (spr) spectroscopy and photonic integrated circuit (pic) biosensors: A comparative review," *Sensors*, vol. 22, 2022.

[184] A. Djaileb, B. Charron, M. H. Jodaylami, V. Thibault, J. Coutu, K. Stevenson, S. Forest, L. S. Live, D. Boudreau, J. N. Pelletier, and J.-F. Masson, "A rapid and quantitative serum test for sars-cov-2 antibodies with portable surface plasmon resonance sensing," 4 2020.

[185] J. N. Yih, Y. M. Chu, Y. C. Mao, W. H. Wang, F. C. Chien, C. Y. Lin, K. L. Lee, P. K. Wei, and S. J. Chen, “Optical waveguide biosensors constructed with subwavelength gratings,” *Applied Optics, Vol. 45, Issue 9, pp. 1938-1942*, vol. 45, pp. 1938–1942, 2006.

[186] K. M. Arif, J. Potgieter, and O. Diegel, “Simulation of nanoparticle enhanced diffraction grating biosensor using dda,” in *2013 IEEE 4th International Conference on Photonics (ICP)*, 2013, pp. 265–267.

[187] A. Sathukarn, C. J. Yi, S. Boonruang, M. Horprathum, K. Tantiwanichapan, K. Prasertsuk, C. Thanapirom, W. Kusolthossakul, and K. Kasamsook, “The simulation of a surface plasmon resonance metallic grating for maximizing thz sensitivity in refractive index sensor application,” *International Journal of Optics*, vol. 2020, 2020.

[188] K. S. Yee, “Numerical solution of initial boundary value problems involving maxwell’s equations in isotropic media,” *IEEE Transactions on Antennas and Propagation*, vol. 14, pp. 302–307, 1966.

[189] J. B. Schneider, *Introduction to the FDTD Method.* GitHub, 2011, pp. 33–73.

[190] J. P. Berenger, “A perfectly matched layer for the absorption of electromagnetic waves,” *Journal of Computational Physics*, vol. 114, pp. 185–200, 1994.

[191] F. M. Johar, S. N. Salleh, F. A. Azmin, B. H. Ahmad, and M. M. Shukor, “A review of method in fdtd for the analysis of oblique incident plane wave on periodic structures,” *International Journal of Engineering and Technology (IJET)*, vol. 5, no. 5, 2013.

[192] O. Zhernovaya, O. Sydoruk, V. Tuchin, and A. Douplik, “The refractive index of human hemoglobin in the visible range,” *Physics in Medicine and Biology*, vol. 56, no. 13, p. 4013, jun 2011.

[193] V. V. Tuchin, *Tissue Optics: Light Scattering Methods and Instruments for Medical Diagnosis.* Society of Photo-Optical Instrumentation Engineers (SPIE), 2015.

[194] I. J. Bigio and S. G. Bown, “Spectrroscopic sensing of cancer and cancer therapy: Current status of translational research,” *Cancer Biology and Therapy*, vol. 3, no. 3, pp. 259–267, 2004, pMID: 15107613.

[195] G. J. Tearney, M. E. Brezinski, J. F. Southern, B. E. Bouma, M. R. Hee, and J. G. Fujimoto, “Determination of the refractive index of highly scattering human tissue by optical coherence tomography,” *Opt. Lett.*, vol. 20, no. 21, pp. 2258–2260, 1995.

[196] J. Wang, Z. Deng, X. Wang, Q. Ye, W. Zhou, J. Mei, C. Zhang, and J. Tian, “Measurement of the refractive index of hemoglobin solutions for a continuous spectral region,” *Biomed. Opt. Express*, vol. 6, no. 7, pp. 2536–2541, Jul 2015.

[197] O. Sydoruk, O. S. Zhernovaya, V. V. Tuchin, and A. Douplik, “Refractive index of solutions of human hemoglobin from the near-infrared to the ultraviolet range: Kramers-Kronig analysis,” *Journal of Biomedical Optics*, vol. 17, no. 11, p. 115002, 2012.

[198] L. Xia, S. Yin, H. Gao, Q. Deng, and C. Du, “Sensitivity enhancement for surface plasmon resonance imaging biosensor by utilizing gold-silver bimetallic film configuration,” *Plasmonics*, vol. 6, pp. 245–250, 2011.

[199] M. B. Hossain, M. M. R. Khan, M. S. Rahman, S. S. B. Badrudduza, M. M. Sabiha, and M. M. Rana, “Graphene-mos2-au-tio2-sio2 hybrid spr biosensor: A new window for formalin detection,” *Journal of Materials and Applications*, vol. 8, pp. 51–58, Nov 2019.

[200] A. Verma, A. Prakash, and R. Tripathi, “Sensitivity enhancement of surface plasmon resonance biosensor using graphene and air gap,” *Optics Communications*, vol. 357, pp. 106–112, 2015.

[201] L. Kong, J. Lv, Q. Gu, Y. Ying, X. Jiang, and G. Si, “Sensitivity-enhanced spr sensor based on graphene and subwavelength silver gratings,” *Nanomaterials*, vol. 10, pp. 1–12, 2020.

[202] C. Hu and D. Liu, “High-performance grating coupled surface plasmon resonance sensor based on al-au bimetallic layer,” *Modern Applied Science*, vol. 4, pp. 8–13, 2010.

[203] A. Bijalwan and V. Rastogi, “Sensitivity enhancement of a conventional gold grating assisted surface plasmon resonance sensor by using a bimetallic configuration,” *Applied Optics*, vol. 56, p. 9606, 2017.

[204] A. Dhibi, M. Khemiri, and M. Oumezzine, “Theoretical study of surface plasmon resonance sensors based on 2d bimetallic alloy grating,” *Photonics and Nanostructures - Fundamentals and Applications*, vol. 22, pp. 1–8, 2016.

[205] A. Bijalwan and V. Rastogi, “Gold–aluminum-based surface plasmon resonance sensor with a high quality factor and figure of merit for the detection of hemoglobin,” *Applied Optics*, vol. 57, p. 9230, 2018.

[206] M. Bachman, “Rca-2 silicon wafer cleaning,” *INRF application note*, vol. 2, 1999.

[207] H. Liu, B. Wang, E. S. Leong, P. Yang, Y. Zong, G. Si, J. Teng, and S. A. Maier, "Enhanced surface plasmon resonance on a smooth silver film with a seed growth layer," *ACS Nano*, vol. 4, pp. 3139–3146, 2010.

[208] "E-beam resist ar-p 632 series," 2023. [Online]. Available: https://www.allresist.com/portfolio-item/e-beam-resist-ar-p-632-series/

[209] P. Sarapukdee, D. Schulz, and S. Palzer, "Grating structures for silver-based surface plasmon resonance sensors with adjustable excitation angle," *Sensors 2024, Vol. 24, Page 4538*, vol. 24, p. 4538, 7 2024.

[210] J. Schindelin, I. Arganda-Carreras, E. Frise, V. Kaynig, M. Longair, T. Pietzsch, S. Preibisch, C. Rueden, S. Saalfeld, B. Schmid, J.-Y. Tinevez, D. J. White, V. Hartenstein, K. Eliceiri, P. Tomancak, and A. Cardona, "Fiji: an open-source platform for biological-image analysis," *Nature methods*, vol. 9, no. 7, pp. 676–682, 2012.

[211] J. Schmitz, "Entwicklung eines neuartigen verfahrens zur herstellung von optischen kopplerstrukturen für plasmonische wellenleiter," *Masterarbeit, Technische Universität Dortmund*, 2015.

[212] M. H. Weik, *full-width at half-maximum.* Boston, MA: Springer US, 2001, pp. 661–661.

[213] M. Zakharova, V. Vlnieska, H. Fornasier, M. Börner, T. dos Santos Rolo, J. Mohr, and D. Kunka, "Development and characterization of two-dimensional gratings for single-shot x-ray phase-contrast imaging," *Applied Sciences 2018, Vol. 8, Page 468*, vol. 8, p. 468, 2018.

[214] K. Wu and G. P. Wang, "Two-dimensional fibonacci grating for far-field super-resolution imaging," *Scientific Reports 2016 6:1*, vol. 6, pp. 1–8, 2016.

[215] M. Wahle, K. Brassat, J. Ebel, J. Bürger, J. K. N. Lindner, H.-S. Kitzerow, R. K. Komanduri, W. M. Jones, C. Oh, and M. J. Escuti, "Two-dimensional switchable blue phase gratings manufactured by nanosphere lithography," *Optics Express, Vol. 25, Issue 19, pp. 22608-22619*, vol. 25, pp. 22 608–22 619, 2017.

[216] A. Philip and A. R. Kumar, "Two-dimensional materials and their role in sensitivity enhancement of surface plasmon resonance based biosensor," *TrAC Trends in Analytical Chemistry*, vol. 171, p. 117497, 2024.

[217] A. Warren, M. Alkaisi, and C. Moore, "Design of 2d plasmonic diffraction gratings for sensing and super-resolution imaging applications," in *2020 IEEE International Instrumentation and Measurement Technology Conference (I2MTC)*, 2020, pp. 1–6.

[218] P. Urbancova, M. Goraus, D. Pudis, P. Hlubina, A. Kuzma, D. Jandura, J. Durisova, and P. Micek, “2d polymer/metal structures for surface plasmon resonance,” *Applied Surface Science*, vol. 530, p. 147279, 2020.

[219] A. Zięba, K. Hreczycho, M. Sikora, A. Chudzyńska, P. Korzec, and S. Patela, “Multi-axis diffraction gratings,” *Optical Materials*, vol. 137, p. 113606, 2023.

[220] X. Zhu and B. Wang, “Hybrid nanostructure with two-dimensional grating for resonance waves self-referenced sensing,” *Applied Physics Letters*, vol. 123, no. 20, p. 202202, 11 2023. [Online]. Available: 10.1063/5.0167370

[221] D. Wang, Q. Wang, and Z. Zhan, “Polarization-independent filter based on 2-d crossed grating under oblique incidence,” *IEEE Photonics Journal*, vol. 10, no. 5, pp. 1–9, 2018.

[222] P. Wei, X. Lu, D. Qiao, L. Zou, X. Huang, J. Tan, and Z. Lu, “Two-dimensional displacement measurement based on two parallel gratings,” *Review of Scientific Instruments*, vol. 89, no. 6, p. 065105, 06 2018.

[223] V. Pandey and S. Pal, “Optimization of two-dimensional metal-assisted guided mode resonance based structures for sensing applications in the visible region,” *Photonics and Nanostructures - Fundamentals and Applications*, vol. 43, p. 100901, 2021.

[224] Y. Ban, G. Zhao, H. Liu, Z. Zhang, B. Chen, B. Lu, and H. Liu, “Two-dimensional grating interferometer with nanometer accuracy,” *AIP Advances*, vol. 13, no. 12, p. 125125, 12 2023. [Online]. Available: 10.1063/5.0179173

[225] G. Janith, H. Herath, N. Hendeniya, D. Attygalle, D. Amarasinghe, V. Logeeshan, P. Wickramasinghe, and Y. Wijayasinghe, “Advances in surface plasmon resonance biosensors for medical diagnostics: An overview of recent developments and techniques,” *Journal of Pharmaceutical and Biomedical Analysis Open*, vol. 2, p. 100019, 2023.

[226] J. Homola, I. Koudela, and S. S. Yee, “Surface plasmon resonance sensors based on diffraction gratings and prism couplers: sensitivity comparison,” *Sensors and Actuators B: Chemical*, vol. 54, no. 1, pp. 16–24, 1999.

[227] L. Ávalos, A. González-Alcalde, E. Chaikina, E. García-Guerrero, A. Maradudin, and E. Méndez, “Excitation of plasmonic and photonic modes in metallic lamellar gratings,” *Optics Communications*, vol. 500, p. 127324, 2021.

[228] H.-Y. Hsu, Y.-H. Lan, and C.-S. Huang, “A gradient grating period guided-mode resonance spectrometer,” *IEEE Photonics Journal*, vol. 10, no. 1, pp. 1–9, 2018.

[229] C.-T. Hsiung and C.-S. Huang, “Refractive index sensor based on a gradient grating period guided-mode resonance,” *IEEE Photonics Technology Letters*, vol. 31, no. 3, pp. 253–256, 2019.

[230] Y. Cai, Y. Huang, K. Zhu, and H. Wu, “Symmetric metasurface with dual band polarization-independent high-q resonances governed by symmetry-protected bic,” *Opt. Lett.*, vol. 46, no. 16, pp. 4049–4052, Aug 2021.

[231] Q. Ji, Y. Zhang, Y. Zhang, and Z. Liu, “Chemical vapour deposition of group-vib metal dichalcogenide monolayers: engineered substrates from amorphous to single crystalline,” *Chem. Soc. Rev.*, vol. 44, pp. 2587–2602, 2015.

[232] A. Bobrovsky, V. Shibaev, B. Ostrovskii, M. Cigl, V. Hamplová, and A. Bubnov, “Photo- and electro-controllable 2d diffraction gratings prepared using electrohydrodynamic instability in a nematic polymerizable mixture,” *J. Mater. Chem. C*, vol. 11, pp. 11 379–11 391, 2023.

[233] A. John-Herpin, A. Tittl, and H. Altug, “Quantifying the limits of detection of surface-enhanced infrared spectroscopy with grating order-coupled nanogap antennas,” *ACS Photonics*, vol. 5, no. 10, pp. 4117–4124, 2018, pMID: 30828588.

[234] W. Fei, X. Jiang, L. Dai, W. Qiu, Y. Fang, D. Li, J. Hu, and Q. Zhan, “Polarization-selective narrow band dual-toroidal-dipole resonances in a symmetry-broken dielectric tetramer metamaterial,” *Opt. Express*, vol. 31, no. 6, pp. 9608–9619, Mar 2023.

[235] W.-K. Kuo and C.-J. Hsu, “Two-dimensional grating guided-mode resonance tunable filter,” *Opt. Express*, vol. 25, no. 24, pp. 29 642–29 649, Nov 2017.

[236] S. Bellucci, O. Vernyhor, A. Bendziak, I. Yaremchuk, V. M. Fitio, and Y. Bobitski, “Characteristics of the surface plasmon–polariton resonance in a metal grating, as a sensitive element of refractive index change,” *Materials*, vol. 13, no. 8, 2020.

[237] W. Yue, C. Tang, C. Wang, C. Bai, S. Liu, X. Xie, H. Hua, Z. Zhang, and D. Li, “An electricity-fluorescence double-checking biosensor based on graphene for detection of binding kinetics of dna hybridization,” *RSC Adv.*, vol. 7, pp. 44 559–44 567, 2017.

[238] S. Zhang, M. Sun, X. Wang, J. Wang, Z. Jia, X. Lv, and X. Huang, “Spectral-free double light detection of dna based on a porous silicon bragg mirror,” *Sensors*, vol. 22, no. 18, 2022.

[239] A. Abumazwed, W. Kubo, C. Shen, T. Tanaka, and A. G. Kirk, "Projection method for improving signal to noise ratio of localized surface plasmon resonance biosensors," *Biomed. Opt. Express*, vol. 8, no. 1, pp. 446–459, Jan 2017.

[240] C.-W. Huang, C.-W. Kao, C.-C. Yin, J.-J. Lin, T.-C. Kao, and Y.-J. Hung, "Optical spectrometer based on continuously-chirped guided mode resonance filter," *Optics Express, Vol. 26, Issue 21, pp. 27515-27527*, vol. 26, pp. 27 515–27 527, 2018.

[241] R. Vinoth, P. Sangavi, T. Nakagawa, M. Jayaraman, and A. V. Mohan, "All-in-one microfluidic device with an integrated porous filtration membrane for on-site detection of multiple salivary biomarkers," *Sensors and Actuators B: Chemical*, vol. 379, p. 133214, 2023.

[242] T. McGrath, J. Buijs, A. Huet, P. Delahaut, C. Elliott, and M. Mooney, "Assessment of a multiplexing high throughput immunochemical spr biosensor in measuring multiple proteins on a single biosensor chip," *Sensors and Actuators B: Chemical*, vol. 186, pp. 423–430, 2013.

[243] A. Jones, L. Dhanapala, R. N. T. Kankanamage, C. V. Kumar, and J. F. Rusling, "Multiplexed immunosensors and immunoarrays," *Analytical Chemistry*, vol. 92, no. 1, pp. 345–362, 2020, pMID: 31726821.

[244] M. Marian and W. Seghezzi, *Chapter 4 - Novel Biopharmaceuticals: Pharmacokinetics, Pharmacodynamics, and Bioanalytics*, L. M. Plitnick and D. J. Herzyk, Eds. San Diego: Academic Press, 2013.

[245] S. U. Trivedi, C. Miao, J. E. Sanchez, H. Caidi, A. Tamin, L. Haynes, and N. J. Thornburg, "Development and evaluation of a multiplexed immunoassay for simultaneous detection of serum igg antibodies to six human coronaviruses," *Scientific Reports 2019 9:1*, vol. 9, pp. 1–8, 2019.

[246] L. Yang, M. E. Biswas, and P. Chen, "Study of binding between protein a and immunoglobulin g using a surface tension probe," *Biophysical Journal*, vol. 84, p. 509, 2003.

[247] F. Bragheri, R. Martínez Vázquez, and R. Osellame, *Chapter 12.3 - Microfluidics*, ser. Micro and Nano Technologies, T. Baldacchini, Ed. William Andrew Publishing, 2020.

[248] M. P. Wolf, G. B. Salieb-Beugelaar, and P. Hunziker, "Pdms with designer functionalities—properties, modifications strategies, and applications," *Progress in Polymer Science*, vol. 83, pp. 97–134, 2018.

[249] L. M. Lechuga, K. Zinoviev, L. Fernández, J. Elizalde, O. E. Hidalgo, and C. Dominguez, "Biosensing microsystem platforms based on the integration of Si Mach-Zehnder interferometer, microfluidics and grating couplers," in *Silicon Photonics IV*, J. A. Kubby and G. T. Reed, Eds., vol. 7220, International Society for Optics and Photonics. SPIE, 2009, p. 72200L.

[250] Y. Kazama, E. T. Carlen, A. van den Berg, and A. Hibara, "Top-and-side dual-view microfluidic device with embedded prism," *Sensors and Actuators B: Chemical*, vol. 248, pp. 753–760, 2017.

[251] T. Fujii, "Pdms-based microfluidic devices for biomedical applications," *Microelectronic Engineering*, vol. 61-62, pp. 907–914, 2002.

[252] A. Polynkin, M. Mansuripur, N. Peyghambarian, and P. Polynkin, "Evanescent field-based optical fiber sensing device for measuring the refractive index of liquids in microfluidic channels," *Optics Letters, Vol. 30, Issue 11, pp. 1273-1275*, vol. 30, pp. 1273–1275, 2005.

[253] P. Sarapukdee, D. Schulz, and S. Palzer, "Silver-based plasmonic grating with pdms microchannel for biological sensors," *Proceedings*, vol. 97, no. 1, 2024.

[254] C. Y. Tan and Y. X. Huang, "Dependence of refractive index on concentration and temperature in electrolyte solution, polar solution, nonpolar solution, and protein solution," *Journal of Chemical and Engineering Data*, vol. 60, pp. 2827–2833, 2015.

[255] J. Vörös, "The density and refractive index of adsorbing protein layers," *Biophysical journal*, vol. 87, pp. 553–561, 2004.

[256] R. Barer and S. Tkaczyk, "Refractive index of concentrated protein solutions," *Nature 1954 173:4409*, vol. 173, pp. 821–822, 1954.

[257] G. E. Perlmann and L. G. Longsworth, "The specific refractive increment of some purified proteins," *J. Amer. Chem. Soc.*, vol. 70, p. 2719, 1948.

[258] P. Berini, R. Charbonneau, N. Lahoud, and G. Mattiussi, "Characterization of long-range surface-plasmon-polariton waveguides," *Journal of Applied Physics*, vol. 98, p. 043109, 2005.

[259] A. S. Baburin, A. M. Merzlikin, A. V. Baryshev, I. A. Rodionov, I. A. Ryzhikov, and Y. V. Panfilov, "Silver-based plasmonics: golden material platform and application challenges [invited]," *Optical Materials Express, Vol. 9, Issue 2, pp. 611-642*, vol. 9, pp. 611–642, 2019.

[260] D. K. Burge, J. M. Bennett, R. L. Peck, and H. E. Bennett, "Growth of surface films on silver," *Surface Science*, vol. 16, pp. 303–320, 1969.

[261] G. V. Naik, V. M. Shalaev, A. Boltasseva, G. V. Naik, V. M. Shalaev, and A. Boltasseva, “Alternative plasmonic materials: Beyond gold and silver,” *Advanced Materials*, vol. 25, pp. 3264–3294, 2013.

[262] S. JL, “Determination of surface-film thickness from shift of optically excited surface plasma resonance,” *JOSA, Vol. 60, Issue 1, pp. 49-53*, vol. 60, pp. 49–53, 1970.

[263] J. Payer and H. Kim, “The tarnish process of silver in h2s environments,” *Corros Sci Technol*, vol. 5, pp. 206–212, 2006.

[264] M. G. Dowsett, A. Adriaens, M. Soares, H. Wouters, V. V. Palitsin, R. Gibbons, and R. J. Morris, “The use of ultra-low-energy dynamic sims in the study of the tarnishing of silver,” *Nuclear Instruments and Methods in Physics Research Section B: Beam Interactions with Materials and Atoms*, vol. 239, pp. 51–64, 2005.

[265] A. Mansingh and N. Mehan, “Study of tarnished films formed on silver by exposure to h2s with the surface-plasmon resonance technique,” *Applied Optics, Vol. 39, Issue 28, pp. 5214-5220*, vol. 39, pp. 5214–5220, 2000.

[266] J. Ortíz-Corona, J. L. Ruvalcaba-Sil, E. Casanova-González, and F. J. Rodríguez-Gómez, “Surface analysis of the tarnishing layer in silver alloys,” *MRS Advances*, vol. 2, pp. 3983–3989, 2017.

[267] B. V. L’vov, “Kinetics and mechanism of thermal decomposition of silver oxide,” *Thermochimica Acta*, vol. 333, pp. 13–19, 1999.

[268] P. J. Herley and E. G. Prout, “The thermal decomposition of silver oxide,” *Journal of the American Chemical Society*, vol. 82, pp. 1540–1543, 2002.

[269] M. Pech, “Surface reconditioning and passivation of silver based plasmonic grating-coupled sensors,” Technische Universität Dortmund, 2018.

[270] A. D. Kirshenbaum, J. A. Cahill, and A. V. Grosse, “The density of liquid silver from its melting point to its normal boiling point 2450°k,” *Journal of Inorganic and Nuclear Chemistry*, vol. 24, pp. 333–336, 1962.

[271] P. Sarapukdee, M. Pech, and D. Schulz, “Surface reconditioning of silver-based gratings for surface plasmon biosensors,” *Biophotonics Congress 2021 (2021), paper DTu1A.2*, p. DTu1A.2, 4 2021. [Online]. Available: https://opg.optica.org/abstract.cfm?uri=BODA-2021-DTu1A.2

[272] M. Montazer, F. Alimohammadi, A. Shamei, and M. K. Rahimi, “In situ synthesis of nano silver on cotton using tollens’ reagent,” *Carbohydrate Polymers*, vol. 87, pp. 1706–1712, 2012.

[273] J. Novakovic, P. Vassiliou, and E. Georgiza, “Electrochemical cleaning of artificially tarnished silver,” *Int. J. Electrochem. Sci*, vol. 8, pp. 7223–7232, 2013.

[274] M. C. Bernard, E. Dauvergne, M. Evesque, M. Keddam, and H. Takenouti, “Reduction of silver tarnishing and protection against subsequent corrosion,” *Corrosion Science*, vol. 47, pp. 663–679, 2005.

[275] T. Palomar, B. R. Barat, E. García, and E. Cano, “A comparative study of cleaning methods for tarnished silver,” *Journal of Cultural Heritage*, vol. 17, pp. 20–26, 2016.

[276] T. Shikama, Y. Sakai, and M. Okada, “Silicon oxide coatings as protection against corrosion,” *Thin Solid Films*, vol. 145, pp. 89–97, 1986.

[277] R. G. Munro and S. J. Dapkunas, “Corrosion characteristics of silicon carbide and silicon nitride,” *Journal of Research of the National Institute of Standards and Technology*, vol. 98, p. 607, 1993.

[278] V. T. Vu, T. T. Dinh, N. T. Pham, T. T. Nguyen, P. T. Nguyen, and H. T. To, “Evaluation of the corrosion inhibiting capacity of silica/polypyrrole-oxalate nanocomposite in epoxy coatings,” *International Journal of Corrosion*, vol. 2018, 2018.

[279] A. Delimi, Y. Coffinier, B. Talhi, R. Boukherroub, and S. Szunerits, “Investigation of the corrosion protection of siox-like oxide films deposited by plasma-enhanced chemical vapor deposition onto carbon steel,” *Electrochimica Acta*, vol. 55, pp. 8921–8927, 2010.

[280] Y. Pan, H. Liu, Z. Wang, J. Jia, and J. Zhao, “Optical constant and conformality analysis of sio2 thin films deposited on linear array microstructure substrate by pecvd,” *Coatings 2021, Vol. 11, Page 510*, vol. 11, p. 510, 2021.

[281] A. E. Kaloyeros, Y. Pan, J. Goff, and B. Arkles, “Review—silicon nitride and silicon nitride-rich thin film technologies: State-of-the-art processing technologies, properties, and applications,” *ECS Journal of Solid State Science and Technology*, vol. 9, p. 063006, 2020.

[282] Z. Shi, Y. Wang, C. Du, N. Huang, L. Wang, and C. Ning, “Silicon nitride films for the protective functional coating: blood compatibility and biomechanical property study,” *Journal of the mechanical behavior of biomedical materials*, vol. 16, pp. 9–20, 2012.

[283] K. Alsabbagh, T. Hornung, A. Voigt, S. Sadir, T. Rajabi, and K. Länge, “Microfluidic impedance biosensor chips using sensing layers based on dna-based self-assembled monolayers for label-free detection of proteins,” *Biosensors*, vol. 11, 2021.

[284] X. Wei, V. Q. Do, S. V. Pham, D. Martins, and Y. A. Song, “A multiwell-based detection platform with integrated pdms concentrators for rapid multiplexed enzymatic assays,” *Scientific Reports 2018 8:1*, vol. 8, pp. 1–11, 2018.

[285] J. Liu, I. Jasim, Z. Shen, L. Zhao, M. Dweik, S. Zhang, and M. Almasri, “A microfluidic based biosensor for rapid detection of salmonella in food products,” *PLOS ONE*, vol. 14, p. e0216873, 2019.

[286] E. Hemmer, F. Vetrone, and K. Soga, “Lanthanide-based nanostructures for optical bioimaging: Small particles with large promise,” *MRS Bulletin*, vol. 39, pp. 960–964, 2014.

[287] S. Soltani, A. Ojaghi, and F. E. Robles, “Deep uv dispersion and absorption spectroscopy of biomolecules,” *Biomedical Optics Express*, vol. 10, p. 487, 2019.

[288] S. Mi, J. Xia, Y. Xu, Z. Du, and W. Sun, “An integrated microchannel biosensor platform to analyse low density lactate metabolism in hepg2 cells in vitro,” *RSC Advances*, vol. 9, pp. 9006–9013, 2019.

[289] H. Gao, C. Yan, W. Wu, and J. Li, “Application of microfluidic chip technology in food safety sensing,” *Sensors*, vol. 20, no. 6, 2020.

[290] W. DiPippo, B. J. Lee, K. Park, C. Y. Yang, E. Brooks, Y. Li, P. Denny, C. M. Ho, F. Qi, W. Shi, L. Wolinsky, B. Wu, D. T. W. Wong, and C. D. Montemagno, “Design analysis of doped-silicon surface plasmon resonance immunosensors in mid-infrared range,” *Optics Express, Vol. 18, Issue 18, pp. 19396-19406*, vol. 18, pp. 19 396–19 406, 2010.

[291] S. Joseph, S. Sarkar, and J. Joseph, “Grating-coupled surface plasmon-polariton sensing at a flat metal–analyte interface in a hybrid-configuration,” *ACS Applied Materials and Interfaces*, vol. 12, pp. 46 519–46 529, 2020.

[292] J. Vörös, J. J. Ramsden, G. Csúcs, I. Szendro, S. M. D. Paul, M. Textor, and N. D. Spencer, “Optical grating coupler biosensors,” *Biomaterials*, vol. 23, pp. 3699–3710, 2002.

[293] J. Dostálek, J. Homola, and M. Miler, “Rich information format surface plasmon resonance biosensor based on array of diffraction gratings,” *Sensors and Actuators B: Chemical*, vol. 107, pp. 154–161, 2005.

[294] S. Zhao, Q. Zhang, Y. Lv, and X. Wang, “An hf-free etching of sio2 for soft lithography,” *IEEE Transactions on Nanotechnology*, vol. 15, pp. 666–670, 2016.

[295] S. Stempfhuber, N. Felde, S. Schwinde, M. Trost, P. Schenk, S. Schröder, and A. Tünnermann, "Influence of seed layers on optical properties of aluminum in the uv range," *Optics Express*, vol. 28, p. 20324, 2020.

[296] J. C. Taylor, "Platinum metallization on silicon and silicates," *Journal of Materials Research*, vol. 36, pp. 211–234, 2021.

[297] P. Schmitt, S. Stempfhuber, N. Felde, A. V. Szeghalmi, N. Kaiser, A. Tünnermann, and S. Schwinde, "Influence of seed layers on the reflectance of sputtered aluminum thin films," *Opt. Express*, vol. 29, no. 13, pp. 19 472–19 485, Jun 2021.

[298] J. Lin, C. Li, C.-C. Chang, T.-H. Tsai, D. Zito, and S.-F. Chang, "Editors' choice—review—semiconductor integrated radar for sensing applications," *ECS Journal of Solid State Science and Technology*, vol. 7, no. 7, p. Q3126, apr 2018.

[299] S. Ray, G. Mehta, and S. Srivastava, "Label-free detection techniques for protein microarrays: Prospects, merits and challenges," *PROTEOMICS*, vol. 10, no. 4, pp. 731–748, 2010.

[300] D. Wassaf, G. Kuang, K. Kopacz, Q. L. Wu, Q. Nguyen, M. Toews, J. Cosic, J. Jacques, S. Wiltshire, J. Lambert, C. C. Pazmany, S. Hogan, R. C. Ladner, A. E. Nixon, and D. J. Sexton, "High-throughput affinity ranking of antibodies using surface plasmon resonance microarrays," *Analytical Biochemistry*, vol. 351, pp. 241–253, 2006.

[301] C. Campagnolo, K. J. Meyers, T. Ryan, R. C. Atkinson, Y. T. Chen, M. J. Scanlan, G. Ritter, L. J. Old, and C. A. Batt, "Real-time, label-free monitoring of tumor antigen and serum antibody interactions," *Journal of Biochemical and Biophysical Methods*, vol. 61, pp. 283–298, 2004.

[302] C. Lausted, Z. Hu, and L. Hood, "Quantitative serum proteomics from surface plasmon resonance imaging," *Molecular and Cellular Proteomics*, vol. 7, pp. 2464–2474, 2008.

[303] D. R. Shankaran, K. V. Gobi, and N. Miura, "Recent advancements in surface plasmon resonance immunosensors for detection of small molecules of biomedical, food and environmental interest," *Sensors and Actuators B: Chemical*, vol. 121, pp. 158–177, 2007.

[304] E. Zeidan, C. L. Kepley, C. Sayes, and M. G. Sandros, "Surface plasmon resonance: a label-free tool for cellular analysis," *Nanomedicine (London, England)*, vol. 10, pp. 1833–1846, 2015.

[305] A. Bund, A. Baba, S. Berg, D. Johannsmann, J. Lüibben, Z. Wang, and W. Knoll, "Combining surface plasmon resonance and quartz crystal microbalance for the in situ investigation of the electropolymerization and doping/dedoping of poly(pyrrole)," *The Journal of Physical Chemistry B*, vol. 107, pp. 6743–6747, 2003.

[306] P. I. Nikitin, A. A. Beloglazov, M. V. Valeiko, J. A. Creighton, and J. D. Wright, “Silicon-based surface plasmon resonance combined with surface-enhanced raman scattering for chemical sensing,” *Review of Scientific Instruments*, vol. 68, p. 2554, 1998.

[307] S. J. Park and M. K. Seo, “Element and processing,” *Interface Science and Technology*, vol. 18, pp. 431–499, 2011.

List of Figures

List of Tables

APPENDIX A

Appendix

A.1. Structure of the Measuring Station

At the University of Hagen's well-appointed optical laboratory [211], reflection experiments were conducted. The equipment has been adapted from prototypes in order to be suitable for this task. Based on the area of the grating structure, the structure has dimensions of approximately (1.2 × 1.2) mm. For the laser light to irradiate the grating structure, it must possess the following properties:

1. A grating structure converts only TM-polarized light into surface plasmons because its polarization is perpendicular to the y-plane of the grating.
2. The beam diameter $< (1 \times 1) mm$ should not exceed the grating area, so the surrounding unstructured silver surface will reflect the beam unaffected and directly into the detector. As a result, the reflection may not form adequately.
3. The optimal state would be a beam cross-section with a constant intensity distribution.

The 632.8 nm helium-neon gas laser (05-LHP-151, Melles Griot, JP) with an integrated polarizer was utilized to polarize the light output. Therefore, the laser was only needed to set the correct polarization direction for axial rotation. Using a neutral filter (ND filter), the power of the laser beam was decreased from 10 mW to 1 mW in order to avoid damaging a biological sample due to its excessive intensity. The beam's intensity distribution was approximately Gaussian in cross-section, with a spot diameter of about 3 mm. For filtering and beam adjustment, the beam was manipulated using the configuration depicted in Figure A.1. First, a convex lens (f = 30cm) was utilized to focus the laser's beam.

A pinhole diaphragm was positioned in the spotlight of the lens to intercept unwanted beam portions. The lens situated behind serves as a collimator. Using the distance between the lens and probe in the experimental setup, we can establish a 1 ± 0.2 mm beam cross-section behind the lens. A light source, a probe, and a detector must be positioned in relation to one another for optical measurement. The beam from the fixed light source directly strikes the sample. Thus, the sample reflected the beam onto the detector (ANDO, Ando Electric Co., Ltd., JP). As shown in Figure A.1, if the reflection angle of the sample is to be adjusted, the sample itself becomes double ($\theta_{detector} = 2\theta_{sample}$). The laser's position remains unchanged. As the sample rotated, the exit angle of the reflected beam was also altered. Therefore, the detector must be rotated in a double-angle circular path around the center of the sample. An automated solution was implemented as it was difficult to manually adjust the position and angle of the sample and the detector with a high angular resolution. This straightforward dependence on the angle of rotation is a mechanical coupling. For the rotary motion to occur, an actuator was required. Step-

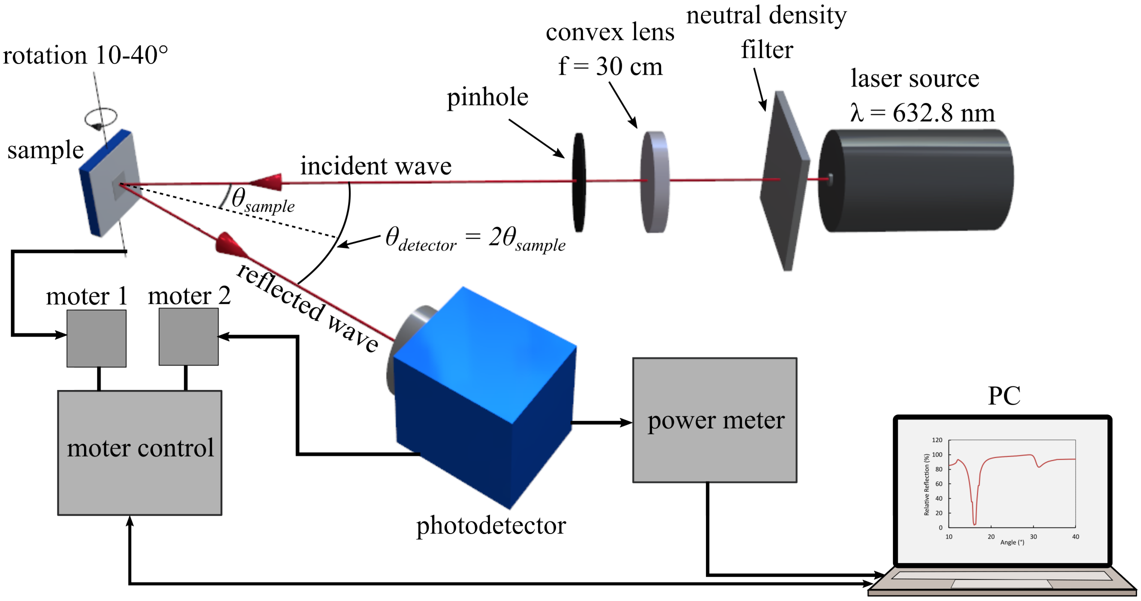

Figure A.1.: The optical measurement setup excites the grating couple with incident light of 632.8 nm wavelength supplied by a HeNe laser passing through a pinhole and a convex lens with a 30 cm focal length. The optical power sensor detected the light reflection. (Image from Sarapukdee, P., et al. [253], is licensed under CC BY 4.0.)

ping motors (Type ST4209M1704, Nanotec Electronic GmbH, GE) with the maximum number of poles were optimal for precise positioning. Torque was required because the motor's sole function was positioning. There was a control unit box (SMCI33-2, Nanotec Electronic GmbH, GE) for controlling stepper motors that were connected to a personal computer (PC) via a universal serial bus (USB) port. On the PC, a LabView program (National Instruments, US) was used to control sample positioning. The angular resolution of the selected conventional stepper motor is 0.9°. Therefore, each revolution has 400 steps. Consequently, when measuring or rotating the sample and detector, the angles should be approached with a maximum precision of 0.1°. However, this was not directly possible due to the stepper motor's resolution. The mechanical ratio of 1:9 between the stepper motor and a sample was required to adjust the resolution. Also driven by the stepper motor is the detector. The intermediate shaft also enabled the detector's required ratio of 2:9 to be achieved. The specimen holder aligned the specimen with the incidence plane of light. This was micrometer-adjustable in all spatial directions (x-, y-, and z-direction). The micrometer adjustment has the benefit that the location of the structure does not need to be precisely in the middle of the sample. Figure A.2 examines

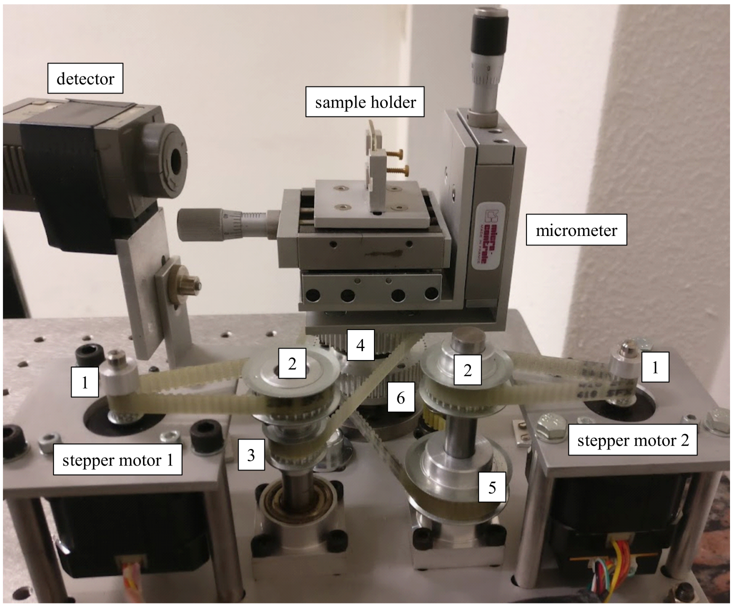

Figure A.2.: Step gear with a step belt is located at points 1-6. For numbers 1, 2, 3, 5, and 6, the corresponding numbers of teeth are 10, 30, 20, 60, 40, and 60.

the translation of the belt transmission's angular resolution in considerable detail. The resolution of the stepper motor is 0.9°. Due to the 1: 3 ratio, the intermediate axle can move with 0.3° of precision (number 1 and 2). With a different gear ratio, the desired angular resolution of 0.1° between the intermediate axis and the samples was achieved (number 3 and 4). Since the detector must spin twice as fast as the sample, the pinion on the intermediate axis has exactly twice as many teeth as the pinion driving the sample (number 5 and 6). With this configuration, the incident wave will be blocked by the optical detector housing, which limits the resolution to 0.1° and the angle scanning to begin at 10°. This constraint suggests that reliable measurements within a limited range of angles are possible, but that in order to prevent interference from the optical detector housing, initial measurements must start at 10 degrees. This will guarantee correct data collection and processing.

A.2. Process Recipes

Grating Structure; Method A

Process flow of method A, thickness 100 nm, 50 nm

Substrat: Si-Wafer 4"

Pretreat sample

- Cleaning RCA
- Grow up oxide 100 nm
- Wafer cutting into (2 × 2) cm
- Label sample
- Cleaning RCA, dry

Nickel layer sputtering (dNi): thickness 5-10 nm

- Ar-Flow: 25 sccm, P = 500 W, p = 10 mTorr, Step time 10 sec.

Silver Thermal Vapor Deposition

- Thickness 100 nm, rate 0.15 nm/s

Ebeam Resist : Thickness 400 nm

- Heating: hot plate 180°C, 90 sec
- Chemical Type: PMMA 950K 4% , Allresist 679.04
- Spins : 4000 rpm, 60 sec, upm = 2000 rpm/sec
- Softback: hot plate 180°C, 90 sec

Electron Beam Lithography

- Writing field (WF): 100 μm, Structure size: (1200×1200) μm
- Beam energy : 10 keV, Aperture: 30 μm, Dose: 55 $\mu m/cm^2$

Chemical Development

- Development: 45 sec, 3:1 2-Propanol (90 ml): (30 ml) Deionized water
- Stop reaction : 60 seconds, 2-Propanol

Silver Thermal Vapor Deposition

- Thickness 50 nm, rate 0.15 nm/s

Lift-Off

- Acetone with 80% of ultrasonic power, 15 min

Cleaning

- 2-Propanol with 80% of power, 2 min

Grating Structure; Method B

Process flow of method B, thickness 100 nm, 50 nm

Substrat: Si-Wafer 4"

Pretreat sample

- Cleaning RCA
- Grow up oxide 100 nm
- Wafer cutting into size (2 × 2) cm
- Label sample
- Cleaning RCA, dry

Nickel layer sputtering (dNi): thickness 5-10 nm

- Ar-Flow: 25 sccm, P = 500 W, p = 10 mTorr, Step time 10 sec.

Ebeam Resist : Thickness 400 nm

- Heating: hot plate 180°C, 90 sec
- Chemical Type: PMMA 950K 4% , Allresist 679.04
- Spins : 4000 rpm, 60 sec, upm = 2000 rpm/sec
- Softback: hot plate 180°C, 90 sec

Electron Beam Lithography

- Writing field (WF): 100 μm, Structure size: (1200×1200) μm
- Beam energy : 10 keV, Aperture: 30 μm, Dose: 55 $\mu m/cm^2$

Chemical Development

- Development: 45 sec, 3:1 2-Propanol (90 ml): (30 ml) Deionized water
- Stop reaction : 60 seconds, 2-Propanol

Silver Thermal Vapor Deposition

- Thickness 50 nm, rate 0.15 nm/s

Lift-Off

- Acetone with 80% of sonicator power, 15 min

Cleaning

- 2-Propanol with 80% of sonicator power, 2 min

Silver Thermal Vapor Deposition

- Thickness 100 nm, rate 0.15 nm/s

Cleaning

- 2-Propanol with 80% of sonicator power, 2 min

Grating Structure with Circle Bar

Process flow of grating with a circle bar, thickness 100 nm, 50 nm, bar 300 nm

Substrat: Si-Wafer 4"

Pretreat sample

- Cleaning RCA
- Grow up oxide 100 nm
- Wafer cutting into size (2 × 2) cm
- Label sample
- Cleaning RCA, dry

Nickel layer sputtering (dNi): thickness 5-10 nm

- Ar-Flow: 25 sccm, P = 500 W, p = 10 mTorr, Step time 10 sec.

Silver Thermal Vapor Deposition

- Thickness 100 nm, rate 0.15 nm/s

Photoresist (dResist) : 400 nm

- Heating: hot plate 180°C, 90 sec
- Chemical Type: PMMA 950K 4% , Allresist 679.04
- Spins : 4000 rpm, 60 sec, upm = 2000 rpm/sec
- Softback: hot plate 180°C, 90 sec

Electron Beam Lithography

- Writing field (WF): 100 μm, Structure size: (1200×1200) μm
- Beam energy : 10 keV, Aperture: 30 μm, Dose: 55 $\mu m/cm^2$

Chemical Development

- Development: 45 sec, 3:1 2-Propanol (90 ml): (30 ml) Deionized water
- Stop reaction : 60 seconds, 2-Propanol

Silver Thermal Vapor Deposition

- Thickness 50 nm, rate 0.15 nm/s

Lift-Off

- Acetone with 80% of ultrasonic power, 15 min

Cleaning

- 2-Propanol with 80% of power, 2 min

Ebeam Resist : Thickness 400 nm

- Heating: hot plate 180°C, 90 sec
- Chemical Type: PMMA 950K 4% , Allresist 679.04
- Spins : 4000 rpm, 60 sec, upm = 2000 rpm/sec

- Softback: hot plate 180°C, 90 sec

Electron Beam Lithography

- Writing field (WF): 100 μm, Structure size: (1200×1200) μm
- Beam energy : 10 keV, Aperture: 30 μm, Dose: 55 $\mu m/cm^2$

Chemical Development

- Development: 45 sec, 3:1 2-Propanol (90 ml): (30 ml) Deionized water
- Stop reaction : 60 seconds, 2-Propanol

Silver Thermal Vapor Deposition

- Thickness 400 nm, rate 0.2 nm/s

Lift-Off

- Acetone with 80% of ultrasonic power, 20 min

Cleaning

- 2-Propanol with 80% of power, 2 min

Inverted Grating Structure

Process of upside-down grating, silver base thickness 50 nm, grating height 30 nm

Substrate: Glass substrate

- Cleaning RCA
- Substrate cutting into size (2 × 2) cm
- Label sample
- Cleaning RCA, dry

Ebeam Resist (dResist) : 400 nm

- Heating: hot plate 180°C, 90 sec
- Chemical Type: PMMA 950K 4% , Allresist 679.04
- Spins : 4000 rpm, 60 sec, upm = 2000 rpm/sec
- Softback: hot plate 180°C, 90 sec

Conductive Resist (dResist) : 60 nm

- Heating: hot plate 150°C, 120 sec
- Chemical Type: Electra 92, Allresist 5090
- Spins : 2000 rpm, 60 sec, upm = 1000 rpm/sec
- Softback: hot plate 90°C, 120 sec

Electron Beam Lithography

- Writing field (WF): 100 μm, Structure size: (1200×1200) μm

- Beam energy : 10 keV, Aperture: 30 μm, Dose: 55 $\mu m/cm^2$

Chemical Development

- Development: 45 sec, 3:1 2-Propanol (90 ml): (30 ml) Deionized water
- Stop reaction : 60 seconds, 2-Propanol

Dry etching: depth 30 nm

- Gas: O_2, Ar, CH_3 1, 10, 10 sccm
- RF power: 150 w, 2 min; 30 nm

Silver Thermal Vapor Deposition 1

- Thickness 30 nm, rate 0.15 nm/s

Lift-Off

- Acetone with 80% of ultrasonic power, 15 min

Cleaning

- 2-Propanol with 80% of power, 2 min

Silver Thermal Vapor Deposition 2

- Thickness 50 nm, rate 0.15 nm/s

Silver Deposition on Glass Substrate

The process of silver deposition on glass substrate with parameters

Resize sample and cleaning	Substrate thickness of G1: 0.08 - 0.12 mm
	Substrate thickness of G2: 0.13 - 0.17 mm
	Substrate thickness of G3: 0.16 - 0.19 mm
	Substrate thickness of G4: 0.19 - 0.23 mm
	Substrate thickness of G5: 0.45 - 0.50 mm
	Substrate thickness of G6: 1.00 - 1.20 mm
Sputtering of nickel	Layer thickness: 15 nm
	Process gas flow: 25 sccm
	Sputtering power: 500 W
	Process pressure: 10 mTorr
	Step time: 10 sec
Thermal evaporation of silver	Evaporation rate: 0.18 nm/s
	Layer thickness: 20 | 50 | 100 | 150 nm
	Step time for 20 nm: 0 h 2 m 35 s
	Step time for 50 nm: 0 h 6 m 30 s

	Step time for 100 nm: 0 h 9 m 30 s
	Step time for 150 nm: 0 h 15 m 00 s
Deposition of SiO_2	Layer thickness: 100 nm
	Process gas flow of SiH_4/Ar_2: 400 sccm
	Process gas flow of N_2O: 710 sccm
	HF power: 150 W
	Process pressure: 10 mTorr
	Process temperature: 350 °C
	Step time: 0h 1m 12s

Silicon Oxide Protection Layer

Parameters used in the SiO_2 deposition

Time	20 seconds
Temperature	200°C
$SiH_4/Ar_2\%$	40 sccm
N_2O	710 sccm
Pressure	1000 mTorr
HF Power	150 W

Silicon Nitride Protection Layer

Parameters used in the Si_3N_4 deposition

Step 1: $N2$ Plasma

Time	60 seconds
Temperature	200°C
N_2 flow rate	500 sccm
Pressure	500 mTorr
HF Power	HF Power 300 W

Step 2: Si_3N_4 deposition

Time	90 seconds
Temperature	200°C
$SiH_4/Ar_2\%$ flow rate	400 sccm
NH_3 flow rate	20 sccm

N_2 flow rate	600 sccm
Pressure	1000 mTorr
HF Power	40 W, Pulse Time 10
LF Power	50 W LF, Pulse Time 2
Step 3: N_2 **Plasma**	
Time	60 seconds
temperature	200°C Table temperature
N_2 flow rate	250 sccm
Pressure	500 mTorr
HF power	150 W

A.3. Simulation Results of the Inverted Grating Model

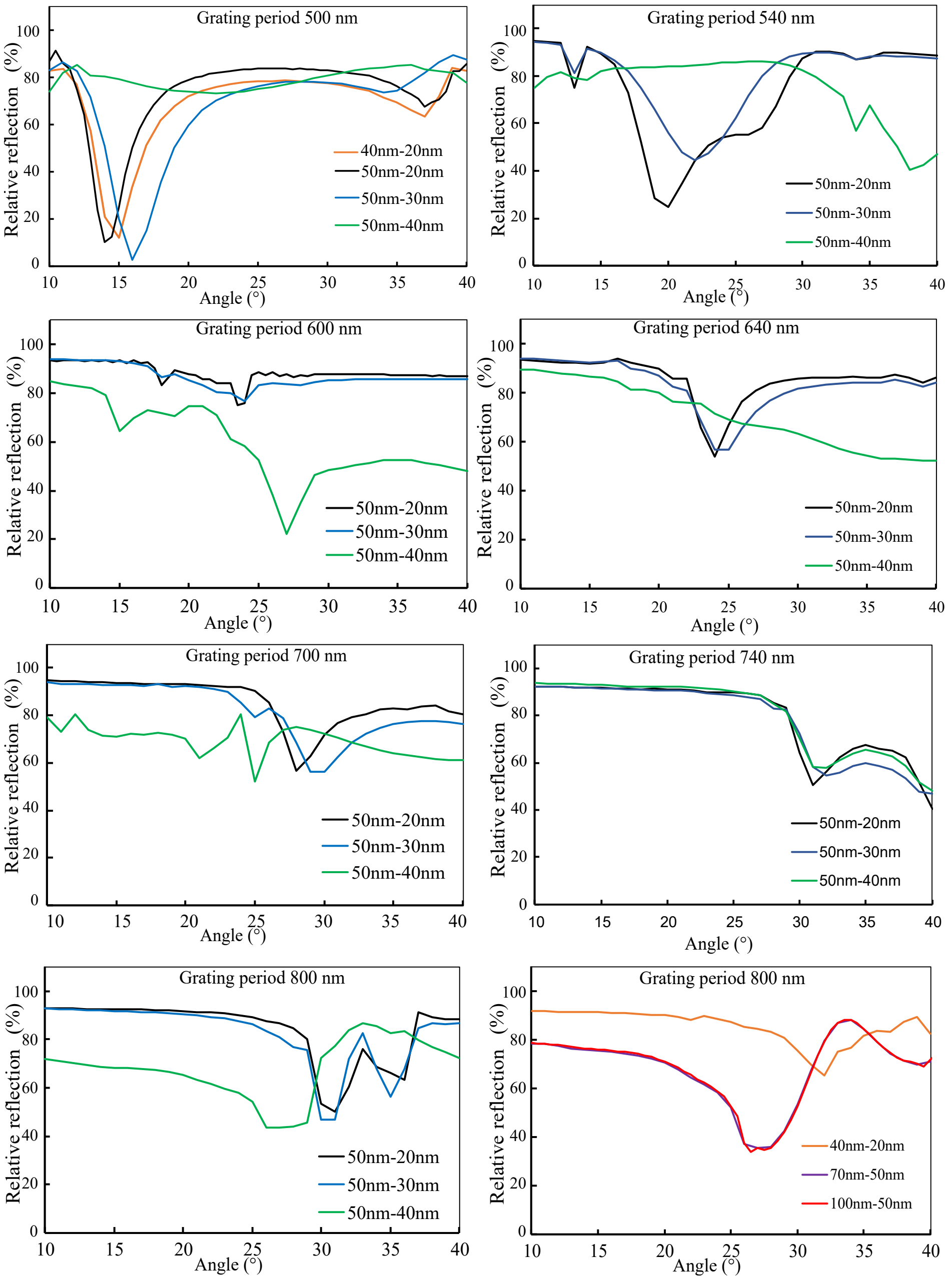

Figure A.3.: Simulation results of the upside-down grating model, the grating period range of 500-800 nm, the grating height range of 20-40 nm, and silver layer on the top thickness of 40-100 nm

Abbreviations

Physical Constants

Symbol	**Name**	**Value / Units**
ε_0	Vacuum permittivity	8.854×10^{-12} F/m
μ_0	Vacuum permeability	1.257×10^{-6} H/m
c_0	Speed of light in vacuum	2.998×10^{8} m/s
e	Elementary charge	1.602×10^{-19} C
m	Electron mass	9.109×10^{-31} kg
π	Pi (circle constant)	≈ 3.1416

Symbols and Variables

Symbol	**Description**	**Units / Type**
$\mathbf{E}$	Electric field vector	V/m
$\mathbf{D}$	Electric displacement field	$\mathrm{C/m^2}$
$\mathbf{H}$	Magnetic field strength	A/m
$\mathbf{B}$	Magnetic flux density	T
$\mathbf{J}$	Current density	$\mathrm{A/m^2}$
ρ	Charge density	$\mathrm{C/m^3}$
σ	Electrical conductivity (can be ω-dependent)	S/m
χ	Electric susceptibility	Dimensionless
ε	Relative permittivity (dielectric function)	Dimensionless / Complex
μ	Relative permeability	Dimensionless
ω	Angular frequency	rad/s
τ	Scattering time / Relaxation time	s

γ_d	Damping rate ($= 1/\tau$)	1/s
ω_p	Plasma frequency	rad/s
λ_p	Plasma wavelength	m
λ	Wavelength of light	m
$n(\omega)$	Complex refractive index	Dimensionless
κ	Extinction coefficient	Dimensionless
β	Propagation constant	1/m
$\mathbf{k}_0$	Wave number in vacuum	1/m
$\mathbf{k}, \mathbf{k}_m$	Wave vectors	1/m
Λ	Grating period	m
θ	Incidence angle	rad or deg
θ_m	Diffraction angle (order m)	rad or deg
ν	Frequency	Hz
$\Delta\nu$	Spectral width	Hz
ω_{sp}	Surface plasmon resonance frequency	rad/s
ε_1, ε_2	Dielectric constants (metal, dielectric)	Dimensionless / Complex
β_{SPP}	Propagation constant for SPP	1/m
α	Attenuation coefficient	1/m
d_1, d_2	Penetration depth in dielectric and metal	m
χ_m	Residual susceptibility (high-frequency)	Dimensionless
κ	Elastic constant in Lorentz model	N/m

Abbreviations

CMOS	Complementary Metal Oxide Semiconductor
CAD	Computer-Aided Design
Chem FET	Chemical Field-effect transistor
DNA	Deoxyribonucleic acid

DAC	Digital-Analog-Converter
FDTD	Finite-difference time-domain
FET	Field-effect transistor
GGPs	Gradient grating periods
ISFET	Ion Sensitive Field-effect transistor
LSPP	Localized Surface Plasmon Polaritons
LSPR	Localized Surface Plasmon Resonance
LPCVD	Low pressure chemical vapor deposition
NIR	Near-infrared
PECVD	Plasmaenhanced chemical vapor deposition
PDMS	Polydimethylsiloxane
PMMA	Polymethylmethacrylat
QCM	Quartz Crystal Microbalance
RIE	Reactive-ion etching
RIU	Reflective index unit
RPM	Revolutions per minute
FMHM	Full width at half maximum
SEM	Scanning electron microscope
SPP	Surface Plasmon Polaritons
SPR	Surface plasmon Resonance
SERS	Surface-Enhanced Raman Scattering
TEOS	Tetraethyl orthosilicate
TE mode	Transverse electric mode
TM mode	Transverse magnetic mode

Publications

Peer-reviews journal contributions

- P. Sarapukdee, D. Schulz, S. Palzer,“Grating Structures for Silver-Based Surface Plasmon Resonance Sensors with Adjustable Excitation Angle ”, Sensors 2024, 24(14). DOI: 10.3390/s24144538.

- P. Sarapukdee, D. Schulz, S. Palzer,“Concept, Simulation, and Fabrication of Inverted Grating Structures for Surface Plasmon Resonance Sensors”, J. Sens. Sens. Syst., 13, 157–166, 2024. DOI: 10.5194/jsss-13-157-2024.

- P. Sarapukdee, C. Spenner, D. Schulz, S. Palzer,“Optimizing stability and performance of silver-based grating structures for surface plasmon resonance sensors”, Sensors 2023, 23(15), 6743. DOI: 10.3390/s23156743.

- K. Chauyod, S. Rattanavarin, P. Sarapukdee, S. Porntheeraphat, K. Sritunyalucksana, and N. Khemthongcharoen, “Bacillus velezensis suppression on the growth of Vibrio parahaemolyticus causing acute hepatopancreatic necrosis disease in marine shrimp”, Journal of Applied Aquaculture, pp. 1–15, 2022. DOI: 10.1080/10454438.2022.2105672.

- N. Srisuai, S. Boonruang, M. Horprathum, P. Sarapukdee, S. Denchitcharoen, “Growth of highly uniform size-distribution ZnO NR arrays on sputtered ZnO thin film via hydrothermal with PMMA template-assisted”, Materials Science in Semiconductor Processing, Volume 105, 2020, 104736. DOI: 10.1016/j.mssp.2019.104736.

Conference contributions

- P. Sarapukdee, C. Spenner, D. Schulz, and S. Palzer, Simulation Environment for Optimized Grating-Based Plasmon Couplers”, EUROSENSORS XXXVII Conference 2025., 7-10 September 2025, Wrocław, Poland. DOI: .

- P. Sarapukdee, D. Schulz, S. Palzer, Silver-based plasmonic grating with PDMS microchannel for biological sensors”, EUROSENSORS XXXV Conference, 10–13 September 2023, Lecce, Italy, Proceedings 2024, 97(1), 192. DOI: 10.3390/proceedings2024097192.

- J. Kneer, P. Sarapukdee, S. Palzer, “Collective Effects of Copper(II)Oxide layers for selective mono-nitrogen oxide sensing, The 19th International Meeting on Chemical Sensors”, IMCS2023 (IMCS2023), 4-8 August 2023, Changchun,China.

- P. Sarapukdee, M. Pech, D. Schulz, “Surface Reconditioning of Silver-Based Gratings for Surface Plasmon Biosensors”, Biophotonics Congress 2021, 12–16 April 2021, Washington, DC, United States. DOI: 10.1364/BODA.2021.DTu1A.2.

- C. Spenner, P. Sarapukdee, H. Kleene, K. Kallis, D. Schulz, “Analysis of SiO2- and MgF2-Based Surface Plasmon Resonance Sensors”, 26th International workshop on the optical wave and waveguide theory and numerical modeling OWTNM, 2018, Bad Sassendorf, Germany.

Supervised thesis

- Roma Dhar, “Development of an Inkjet Process for the Deposition of Gas Sensitive Nanoparticles on Microstructures, Master thesis”, Professur Sensorik, Technische Universität Dortmund, 20.07.2023.

- Gobinath Navaneethakrishnan, “Simulation of Hot Plate Based Microsensors”, Master thesis, Professur Sensorik, Technische Universität Dortmund, 05.06.2023.

- Arne Delfs, “Inkjet-Technologie zum Abscheiden homoge-ner Schichten von gassensitiven Nanoparti-keln auf Mikrostrukturen”, Bachelorarbeit, Professur Sensorik, Technische Universität Dortmund, 11.11.2022.

- Marc Beuel, “Fabrication and analysis of a surface plasmon resonance spectroscopy sensor chip employing grating coupling and PDMS fluidic channels as well as recommissioning of a laser direct writing lithography system”, Master thesis, Department of Electrical Engineering and Computer Science, Münster University of Applied Sciences, 14.01.2019.

- Christoph Kleinhans, “Numerische Optimierung und Herstellung optischer Kopplerstrukturen für plasmonische Wellenleiter mittels FDTD-Verfahren in Python”, Master thesis, Technische Universität Dortmund, Lehrstuhl für hochfrequenztechnik, 17.12.2018.

- Mathias Pech, “Surface reconditioning and passivation of silver-based plasmonic grating-coupled sensors”, Bachelor thesis, Technische Universität Dortmund, Lehrstuhl für Intelligente Mikrosysteme, 30.07.2018.

- Wladimir Plotnikov, “Analyse der Auswirkung unterschiedlicher Metall- und Isolatorstärken auf die Eigenschaft von plasmonischen Gitterkopplern”, Bachelor thesis, Lehrstuhl für Intelligente Mikrosysteme, Technische Universität Dortmund, 05.07.2018.

- Maik Aßhoff, “Experimentelle Untersuchung der optischen Anregung von Oberfl¨achen-Plasmonen in gitterperiodischen Strukturen”, Bachelor thesis, Lehrstuhl für hochfrequenztechnik, Technische Universität Dortmund, 01.10.2017.

- Tommy Doi Phat Luong, “Optimierung plasmonischer Kopplerstrukturen mittels geometrischer Parametervariation”, Bachelor thesis, Lehrstuhl für Intelligente Mikrosysteme, Technische Universität Dortmund, 13.10.2016.

Acknowledgments

I would like to extend my heartfelt gratitude to all those who have played a significant role in making my thesis journey a success.

First and foremost, I am immensely grateful apl. Prof. Dr.-Ing. Dirk Schulz, Dr.-Ing. Klaus Kallis, Dr. Romuald Jolivot and Dr. Waleed Mohammed for granting me the invaluable opportunity to pursue my studies at the Faculty of Electrical Engineering and Information Technology, TU-Dortmund. Your guidance and support have been instrumental in shaping my academic path.

I am incredibly grateful to Prof. Stefan Palzer, PhD (Cantab), whose patience, guidance, and unwavering assistance were pivotal in shaping the outcome of this thesis. Your mentorship has been an immense source of knowledge and inspiration for me. Without you, this couldn't be possible. More than that, I am incredibly grateful for the incredible opportunity to be a part of your professorship.

I am grateful to my colleagues at Professorship for Sensors, including Dr.-Ing. Michael Jakubowsky, Dr.-Ing. Álvaro Ortiz Pérez for your invaluable support and time dedicated to reading and providing feedback on my thesis, Manuela Meyer, Gabriel Rodríguez Gutiérrez, Olga Ivanova, Kaiqi Wu, Moritz Berger, Iris Wolff, Ulrich Marggraf, Ulrich Müller-Confurius, thank you for a warm welcome as an integral part of our team and your unwavering commitment and assistance throughout this journey.

I must also express my sincere appreciation to the entire TU-Dortmund University's IMS and MNE group, including Prof. Dr.-Ing. Stefan Tappertzhofen, Marion Brünninghaus-Willmes, Philipp Czyba, Dr.-Ing. Evelyn Drabiniok, Dr.-Ing. Jakob Zimmermann, Dr.-Ing. Sven Ebschke, Dr.-Ing. Friederike Giebel, Karola Kolander, Ulrike Lippe, Dr.-Ing. Andre Löochte, Ashutosh Loyalka, Dr.-Ing. Dominik Merten, Dr.-Ing. Remigius Poloczek, Achim Wiggershaus, Thomas Seiler, André Kosak, Raphael Ahlmann, Sarah Emily Beck, and Julian Liedtke for their warm hospitality and unwavering assistance whenever I needed it. I am thankful to each one of them for their collaboration and also the HFT group, including Christian Spenner, Mathias Pech, and Wladimir Plotnikov for their incredible work.

A particular thanks goes to my Thai colleagues and friends, notably Dr. Numfon Khemthongcharoen, Santi Rattanavarin, Kondee Chauyod, Dr. Nantarat Srisuai for their support since the beginning.

A special thank goes to the Micro- and Nanophotonics group at the Fernuniversität Hagen for generously allowing me to utilize their optics lab to characterize the sensor chip. Your support in this regard was invaluable to the success of my research.

I am also deeply indebted to my friends and family, whose unwavering support and encouragement throughout my study abroad journey made it possible for me to overcome challenges and achieve my goals. Your belief in me kept me going during difficult times, and I will always cherish your support.

Furthermore, my heartfelt gratitude goes to my beloved wife, Dr.-Ing. Wiriya Puntub, whose unwavering support and understanding have been the backbone of my success. Your encouragement and belief in me have been a constant source of motivation.

Finally, I would like to acknowledge the support of the Erasmus Mundus grant and the National Electronics and Computer Technology Center in Thailand for providing me with the scholarship that made this academic journey possible. Your support has been instrumental in shaping my academic and personal growth.

To everyone mentioned above and to those not explicitly named, but who have contributed to my academic journey in any way, thank you. This thesis would not have been possible without the collective support and encouragement of all these remarkable individuals.

Dortmund in February 2025
Pongsak Sarapukdee

From Electromagnetic Theory to Experimental Validation

The advancement of label-free biosensing is vital for real-time diagnostics and healthcare applications. This thesis focuses on grating-based Surface Plasmon Resonance (SPR) as a compact and integrable alternative to prism-based systems. Theoretical modeling, numerical simulations, and experimental validation are carried out to optimize grating geometries and material configurations. Various designs, including one-dimensional, two-dimensional, gradient, and inverted gratings, are fabricated and integrated with microfluidic channels for real-time sensing. Biosensing experiments demonstrate reliable detection of biomolecular interactions, confirming the potential of grating SPR for developing miniaturized, CMOS-compatible, and high-sensitivity biosensors suitable for future diagnostic platforms.